Effect of Carbon Segregation and Carbide Precipitation on the Mechanical Response of Martensite

by

Guillaume Badinier

M.Sc Materials Science, Ecole des Mines de Saint-Etienne, 2008

A THESIS SUBMITTED IN PARTIAL FULFILLMENT
OF THE REQUIREMENTS FOR THE DEGREE OF

Doctor of Philosophy

in

THE FACULTY OF GRADUATE STUDIES
(Materials Engineering)

The University Of British Columbia
(Vancouver)

March 2013

© Guillaume Badinier, 2013

Abstract

The influence of carbon distribution and carbide precipitation on the mechanical properties of the as-quenched and quenched and tempered 300M martensitic steel has been investigated. The microstructure, investigated by transmission electron microscopy (TEM) and three dimensional atom probe tomography (APT) was found to be relatively homogeneous in the as-water-quenched state, but significantly evolved upon tempering and variation of quench rate. This evolution included carbon segregation to dislocations and grain boundaries and carbide precipitation. A simple mean-field precipitation model assuming heterogeneous nucleation onto the dislocations proved to satisfactorily capture the evolution of precipitation upon tempering at 120°C and 150°C. The material was found to behave, mechanically, as a composite and in accordance, the Bauschinger stress-strain behaviour was successfully modeled using a continuous Masing model. This model, when related to the microstructure, showed that the composite behaviour arose from the mechanical contrast between the laths, this being controlled by the local dislocation density and carbon segregation and/or precipitation onto them. Carbon segregation and carbide precipitation were observed to have a direct impact on α' in the Taylor-like equation that was shown to control the local yield stress within the laths. When applied to martensites containing various amount of carbon, the model allowed for an empirical assessment of the effect of the nominal carbon content on α, which was found to be linearly dependent on the nominal carbon content.

Preface

The majority of the experimental work presented in this thesis has been carried out in the Department of Materials Engineering at the University of British Columbia between January 2009 and October 2012. This included all the experimental design, material heat treatment and mechanical testing. Part of the microstructure characterization, however, has been performed through collaborations with other universities and with the ArcelorMittal Research Centre in Maizieres-les-Metz, France. In all of these experiments (described below) the author planned the experiments, prepared the samples for measurement and carried out the analysis on the raw datasets.

Transmission electron microscopy was performed in collaboration with Dr. X. Wang at McMaster University (Canada). The majority of observations were made during a visit of the author in August 2011. During this visit the author worked directly with Dr. Wang on the microscope to perform the observations. A small number of subsequent observations were made by Dr. X. Wang alone. The interpretation and quantitative analysis of these images were made, however, by the author.

Electron back-scatter diffraction measurements were made with Dr. D. Barbier at ArcelorMittal Research Centre (France) during a visit of the author to this lab in April 2011. While Dr. Barbier operated the microscope and provided the raw experimental data, all analysis and interpretation was performed by the author.

Finally, three dimensional atom probe tomography experiments were performed in collaboration with Mr. V. Bilyk and Dr. X. Sauvage at the Université de Rouen (France). Approximately 40% of the experimental data

presented in this thesis were collected during visits of the author in April 2010, April 2011 and December 2011 . The other experimental data was collected by Dr. X. Sauvage between and after these visits. Three of the experimental datasets collected as part of this thesis were also used by Mr. Bilyk in his Masters thesis dissertation at the Université de Rouen. These datasets, as well as all of the other atom probe tomography data presented in this thesis, have been completely re-analyzed (from the raw experimental data) by the author. Those datasets previously used by Mr. Bilyk are referenced to his Masters thesis in the body of this document.

Table of Contents

Abstract . . . . . **ii**

Preface . . . . . **iii**

Table of Contents . . . . . **v**

List of Tables . . . . . **ix**

List of Figures . . . . . **xii**

Acknowledgments . . . . . **xxix**

Dedication . . . . . **xxxii**

1 Introduction **1**

2 Literature Review **3**

2.1 An overview of the microstructure of ferrous martensite . 3

2.1.1 As-quenched martensite 4

2.1.2 Aged and tempered martensite 17

2.1.3 Effect of plastic deformation on the microstructure of martensite 32

2.1.4 Summary: microstructure of as-quenched, aged and tempered martensite 33

2.2 Mechanical properties of martensite 34

2.2.1 Lath boundary strengthening 34

2.2.2 Solid solution hardening 36
2.2.3 Hardening by spinodal decomposition 37
2.2.4 Precipitation hardening 40
2.2.5 Mechanisms of plastic deformation in martensite . 40
2.2.6 Internal stresses 46
2.2.7 Effect of dynamic strain aging on work hardening . 46
2.2.8 Fracture of martensite 49
2.3 Summary of the literature review 51

3 Scope and Objectives 52

4 Experimental Methodology 54
4.1 Materials studied 54
4.2 Sample design 55
4.2.1 Introduction 55
4.2.2 Sample dimensions and mechanical testing 56
4.2.3 Strain measurement 57
4.3 Heat treatment 63
4.3.1 Formation of martensite via quenching 64
4.3.2 Aging and tempering of martensite 68
4.4 Microstructure characterization tools 68
4.4.1 Sample preparation 69
4.4.2 Calorimetry measurements 72
4.4.3 Electron microscopy 72
4.4.4 Atom probe tomography 72
4.5 Analysis of atom probe tomography data 76
4.5.1 Carbon composition in the matrix 76
4.5.2 Mean distance between carbon segregated regions . 78
4.5.3 Maximum composition and thickness of carbon segregated regions 79
4.5.4 Statistical analysis 80
4.6 Summary 80

5 Microstructure Characterization of 300M Steel 81
5.1 Introduction 81
5.2 Calorimetry 82
5.3 Electron microscopy 84
5.3.1 As-quenched martensite 84
5.3.2 Influence of cooling rate 92
5.3.3 Evolution of the microstructure with tempering . . 93
5.4 Measurement of carbon distribution by atom probe tomography 100
5.4.1 Introduction 100
5.4.2 As-quenched martensite 103
5.4.3 Effect of cooling rate 106
5.4.4 Evolution of the microstructure with tempering . . 112
5.5 Discussion 123
5.5.1 Microstructures of as-quenched martensites 123
5.5.2 Effect of tempering on the microstructure of water-quenched specimens 131
5.6 Summary 141

6 Mechanical Properties: Monotonic Loading 143
6.1 Introduction 143
6.2 Monotonic torsion testing of the as-quenched and tempered steel 143
6.3 Effect of cooling rate on work hardening and yielding of the 300M martensite 153
6.4 Discussion 156
6.4.1 Evolution of fracture behaviour on tempering . . . 156
6.4.2 Plastic deformation: yielding and work hardening behaviour 158
6.5 Conclusion 165

7 A Composite Model for the Room Temperature Mechanical Response of Martensite 167

7.1 Introduction 167
7.2 Measuring the Bauschinger effect in martensite 169
7.3 Interpreting the Bauschinger effect via a continuous Masing model 171
7.3.1 Continuous distribution of yield stress and the macroscopic monotonic stress-strain response 171
7.3.2 Internal stresses and prediction of the Bauschinger effect 173
7.3.3 Introduction of a localization parameter: effect of non-uniform strain 178
7.4 Application: modelling the Bauschinger effect of martensite 178
7.5 Discussion 185
7.5.1 Application of model to other steel grades 198
7.6 Conclusion 201

8 Conclusion 203
8.1 Summary and key results 203
8.2 Future work 205

Bibliography 207

Appendices 222

Appendix A Measurement of the Ms Temperature by Dilatometry 223

Appendix B Finite Element Analysis of a Torsion Test on a Tubular Specimen 225

Appendix C Precipitation Model 227
C.1 Nucleation and growth 227
C.2 Growth and coarsening 229

Appendix D Measurement of the Back-Stress 230

List of Tables

Table 2.1 Stages of aging and tempering in ferrous martensites. . 30

Table 2.2 Phenomena contributing to the strength of a 0.1 wt% C (4310) and a 0.4 wt% C (4340) as-quenched lath martensite, according to Leslie and Sober [90]. 47

Table 4.1 Chemical composition of the 4340-300M material (wt%). 55

Table 4.2 Relative abundances of nickel isotopes. The values are used to estimate the contribution of Ni_58 to the Fe_58 peak in the mass spectrum. 75

Table 5.1 Phenomena occurring during tempering of martensite according to the calorimetry result, interpreted based on the work of Han *et al.* [47]. The question mark indicates that the upper limit for retained austenite decomposition could not be measured due to the limited temperature range of the apparatus. 83

Table 5.2 Choice of tempering conditions of 300M steel based on calorimetry measurements and technique of invesigation. All conditions refer to material that was water quenched. The 'x' symbol signifies that the technique was used, and the '–' symbol means that the technique was not used. 'Mon. Tors.' means that a specimen of the condition was tested in monotonic torsion and 'Bausch.' means that a specimen of the condition was tested in strain reversal test. 'TEM' stands for 'transmission electron microscopy' and 'APT' for 'three dimensional atom probe tomography'. 84

Table 5.3 Tempering conditions investigated by transmission electron microscopy. 93

Table 5.4 Carbide number density N as a function of assumed foil thickness t. 98

Table 5.5 Evolution of the average carbide diameter, number density and volume fraction with tempering. The number density is estimated assuming an average TEM sample thickness of 100 nm. The carbide size for the specimen tempered one hour at 350°C was only approximately estimated. The number density and volume fraction was not estimated in this case. 99

Table 5.6 Chemical composition obtained by APT, compared to the bulk composition. All the values are in at%. 102

Table 5.7 Conditions selected for atom probe tomography. The volume analyzed and average carbon composition are indicated. The nominal carbon composition of the 300M steel was 1.76 at%C. 'WQ' designates the as-water-quenched sample and 'HeQ' designates as-helium-quenched samples. 'RT' means room temperature. * Samples also studied by Mr. Bilyk during his Master's thesis [138]. 103

Table 5.8 Summary of the three dimensional atom probe results. The thickness t of the segregations and the mean distance λ between two nearest segregations are presented. The carbon composition of the matrix and the carbon-rich regions are also indicated. 126
Table 5.9 Summary of the microstructural observations revealing the effect of cooling rate. 130
Table 5.10 Summary of the microstructural observations revealing the effect of cooling rate. 133
Table 5.11 Summary of the inputs used for the modelling of precipitation and segregation. 137

Table 6.1 Fracture stress (σ_f) as a function of tempering temperature and time. All the specimens failed in a brittle intergranular manner along the prior austenite grain boundaries. 147
Table 6.2 Mechanical properties of 300M martensite as a function of tempering. 149

Table 7.1 Parameters used in the log-normal distributions. The subscript 'f' refers to the forward direction whereas the subscript 'r' refers to the reverse direction. 183
Table 7.2 Solid solution strengthening predicted using equation 7.25 and based on the amount of carbon in solid solution predicted by the precipitation model. 191
Table 7.3 Scale and shape parameters used in the log-normal distributions used to fit the mechanical behaviour of specimens tempered up to one hour at 150°C. The $\alpha'(C)$ parameter extracted is also indicated. 196

List of Figures

Figure 2.1 Schematic view of the different length-scales in the case of lath martensite, a) Size of the actual part, b) Optical micrograph showing the prior austenite grain size, c) Transmission electron micrograph showing the lath size and d) 3D atom probe tomography showing the solute spacing (only carbon atoms are represented). 4

Figure 2.2 Optical micrograph of a) lath martensite and b) plate martensite, from ref. [10]. In b), retained austenite appears in light gray whereas martensite appears in dark gray. In a), no retained austenite is visible. 5

Figure 2.3 Schematic view of a) the Bain transformation where black circles represent atom positions in a bcc lattice whereas white circles represent atom positions in a fcc lattice, and b) tetragonality induced by foreign atoms (in black) located on z-type interstitial sites of a bcc lattice. 6

Figure 2.4 Schematic evolution of the free energies of austenite and martensite with temperature. The Ms and T_0 temperatures are represented. Reproduced from ref. [5] 8

Figure 2.5 Evolution of the Ms temperature, fraction of lath martensite and volume of retained austenite with carbon content, from ref. [8]. 9

Figure 2.6 Dark field micrograph showing the films of retained austenite (in white) between the laths in medium carbon low alloyed ferrous martensite, from ref. [20]. 10
Figure 2.7 Lath width distribution determined by carbon replica and thin foil analysis. From ref. [26]. 12
Figure 2.8 Hardness as a function of distance from specimen surface in as-quenched 4315 low carbon martensite. Plotted from values given in ref. [33]. 14
Figure 2.9 3D atom probe results on as-quenched martensite aged a few hours at room temperature due to specimen preparation, containing a) 0.1 wt% C, box length 210 nm, b) 0.2 wt% C , box length 230 nm, and c) 0.5 wt% C, box length 220 nm. Only carbon atoms are represented. From ref. [35]. 16
Figure 2.10 Typical wavelengths measured by selected area diffraction pattern analysis and atom probe analysis, a) initial wavelength as a function of nominal carbon content and b) evolution of the wavelength with aging time at room temperature for two different martensites. From ref. [44]. 18
Figure 2.11 [100] electron diffraction pattern showing the diffuse spikes around fundamental spots, obtained after aging a Fe-21 wt% Ni-1 wt% C martensite at room temperature for 26 minutes. The diffuse spikes are due to lattice elastic distortions induced by the modulated structure. From ref. [44]. 19
Figure 2.12 Dark field electron micrograph obtained using the diffuse spikes around 002 fundamental spot of a 1.1 wt% C martensite. Clusters appear in white. From ref. [46]. . . . 20
Figure 2.13 Evolution of the modulated structure of a Fe-21wt% Ni-1wt% C martensite with aging time at room temperature, (a) 5.5 hours, (b) 2 days and (c) 48 days. Additional contrast is attributed to lattice dislocations. From ref. [44]. 21

Figure 2.14 Evolution of the minimum and maximum carbon concentration measured by atom probe analysis during aging at room temperature of an initially virgin Fe-21wt% Ni-1wt% C martensite. Reproduced from ref. [44]. 22
Figure 2.15 Typical resistivity curve obtained on tempering virgin lath or plate martensite. Interpretation of the changes is indicated. From ref [42]. 24
Figure 2.16 Relative resistivity curves measured at 77 K, as a function of time at indicated temperature for as-quenched plate and lath 0.4 wt% C martensites. The relative resistivities above one for the plate martensites indicate that the beginning of the spinodal decomposition occured during heating of the samples. Reproduced from ref. [12] and [44]. 29
Figure 2.17 Retained austenite volume fraction, measured by X-ray diffraction, as a function of time upon tempering at indicated temperature a 0.3 wt% C lath martensite. From ref. [21]. 31
Figure 2.18 0.2% yield stress, measured at room temperature, of as-quench low carbon lath martensites. For carbon contents between 0 and 0.1 wt%, the quench was not fast enough and the microstructure consisted in a mixture of massive ferrite and lath martensite. Reproduced from ref. [24]. 35
Figure 2.19 0.6% yield stress, measured at -196°C, after tempering virgin plate martensite at indicated temperature for one hour. Area 1 shows strengthening due to the tweed-like structure, whereas area 2 shows the softening due to precipitation of transition carbides. Reproduced from ref. [94]. 39
Figure 2.20 Engineering stress-strain curves of 3 martensitic steels, as-quench (in oil), containing 0.3 wt% C (4330), 0.4 wt% C (4340) and 0.4 wt% C (4350), from ref. [102]. . . . 42

Figure 2.21 Work hardening rate as a function of strain for specimens tempered at 175°C for 10 minutes, from ref. [102]. Note the logarithmic scales. 43
Figure 2.22 Elastic limit and 0.2% yield stress of a low alloyed 0.4 wt% C martensite as a function of tempering temperature, with a holding time of one hour. Reproduced from ref. [103]. 44
Figure 2.23 Residual stresses as a function of distance from quench surface in a 0.9 wt% C martensite, for different tempering temperatures (tempering time was one hour). Reproduced from ref. [37]. 45
Figure 2.24 0.6% yield stress of a virgin 0.18 wt% C martensite as a function of temperature for two different strain rates. The temperature range where unstable flow occurred is indicated. Reproduced from ref. [113]. 48

Figure 4.1 Longitudinal cross section of a tubular sample (dimensions expressed in mm). 57
Figure 4.2 Method used by Davis to calculate the strains from a speckle pattern (continued), d) corrected image with attached undeformed grid (note the coarse window size), e) corrected image with deformed grid, and f) calculated shear strain field. The shear strain is averaged over the area within the black rectangle on f)). 60
Figure 4.3 Elastic portion of a typical stress strain curve measured on 300M martensitic steel. The strain was measured using the DIC set-up. 61
Figure 4.4 Shear strain versus time obtained by digital image correlation. 62
Figure 4.5 Equivalent stress-strain curves of a 0.15 wt% C tested in tension (red curve) and the same material tested in torsion using the system developed as part of this project. . . 63

Figure 4.6 Temperature profiles recorded during the heat treatment of a tubular specimen a) full temperature profile, b) close-up to show the cooling rates, c) instantaneous cooling rate (note the logarithmic scale) and d) cross section of a tubular sample showing where the thermocouples TC1 and TC2 were attached. 65

Figure 4.7 Vickers hardness as a function of the distance from the center of the specimen. The edge of the torsion sample's gauge length is at 3 mm from the centre and is indicated by the dotted line. 66

Figure 4.8 Comparison of the cooling rates obtained with water and helium gas. a) temperature versus time curve, and b) cooling rate versus temperature curve. Note the logarithmic scale in b). 67

Figure 4.9 Schematic of the set-up used in the Gleeble to anneal the strips. Samples were clamped into copper grips and a quenching system was installed and the hose was fixed so that the quenchant (water or helium gas) hit the sample in the centre during the quench. The area where temperature and cooling rate were homogeneous is delimited schematically by the two red vertical bars. 69

Figure 4.10 Comparison of the cooling rates obtained on the thin-walled torsion samples and on the sheet samples. a) Temperature versus time, and b) instantaneous cooling rate as a function of temperature. 70

Figure 4.11 Typical mass spectrum recorded during atom probe tomography measurements. a) Global mass spectrum showing major peaks (indicated), b) and c) close-ups to reveal peaks corresponding to other chemical elements. . . . 74

Figure 4.12 Focus on C_{12}^{2+} peak in the mass spectrum presented in figure 4.11(a). The interval over which the spectrum is integrated to estimate the number of noise atoms is indicated. It has the same length as the carbon interval. . 77

Figure 4.13 Carbon composition linear profile showing three carbon segregated regions. 78
Figure 4.14 Example of a typical linear carbon composition profile obtained across a carbon segregated region. 79

Figure 5.1 Heat flow recorded on heating an as-quenched 4340 sample from room temperature to 280°C at a speed of 2°C per minute. Each peak is reflecting the occurrence of a particular phenomenon (see text). 83
Figure 5.2 EBSD map following cleaning (using grain dilation) to remove non-indexed points, coloured based on the orientation of the grains parallel to the plane of observation. Several prior austenite grains are highlighted, the extent of the prior austenite grains having been determined based on the orientation relationship between austenite and the martensite formed within that prior austenite grain. If the prior austenite grain is enveloped properly then a specific pattern for the orientations of the martensite laths is revealed. This is illustrated for the highlighted grain where the inset $\{001\}_{\alpha'}$ pole figure shows the features characteristic of the orientation relationship between different martensite variants and the prior austenite grain. . . . 86
Figure 5.3 EBSD map using inverse pole figure colouring (as in figure 5.2) but presented without grain dilation to remove non-indexed points (non-indexed points are black). Comparison between feature size in this map with TEM observations reveals that the EBSD map misses measuring the finest features (laths) within the microstructure. Other aspects of the microstructure can also be revealed however. A packet boundary separating two packets of laths each sharing the same orientation relationship (red and blue) with the prior austenite is shown. Also highlighted is the extent of a prior austenite grain. 87

Figure 5.4 Experimental ⟨001⟩ martensite poles plotted in the austenite reference system. The orientations of the prior austenite grains were found by manually comparing the ideal positions of the ⟨001⟩ martensite poles assuming Kurdjumov-Sachs (blue circles) and Nishiyama-Wassermann (red circles) orientation relationships. The high degree of correspondence between the experimental data and the ideal orientations shows that the determination of the extent of the prior austenite grain boundaries is excellent. 88

Figure 5.5 Montage of several low magnification TEM pictures showing an overview of the microstructure of the as-quenched material. 89

Figure 5.6 High magnification view of typical features in martensite a) Bright field image of a lath area, b) corresponding dark field image highlighting retained austenite, c) diffraction pattern showing extra spots due to retained austenite, d) bright field image of twinned area, e) corresponding dark field, and f) diffraction pattern. 90

Figure 5.7 Method for determining the lath size distribution a) raw bright field image of a lath area in the as-quenched specimen, and b) corresponding analyzed image. The length of each red segment was measured. 91

Figure 5.8 Distribution of lath sizes determined from the TEM picture of the as-quenched material, and log-normal fit. The mean value and standard deviation of the log-normal distribution was 0.19 μm and 0.22 μm, respectively. . . 91

Figure 5.9 Typical selected area diffraction pattern obtained with the electron beam parallel to $[100]_{\alpha'}$. The superlattice reflections corresponding to a CoN_2-type structure are indicated by arrows. The white circle corresponds to $(210)_{\eta}$. 93

Figure 5.10 Carbide precipitation in the sample slowly quenched to room temperature. a) Bright field image of a small laths area showing small carbides (in black), b) diffraction pattern showing faint extra spots due to η-carbides, c) bright field image of a large laths area showing small carbides (in black), and d) diffraction pattern showing extra spots due to η-carbides. Note the difference in intensity of the spots. 94

Figure 5.11 Typical microstructures observed by transmission electron microscopy on a specimen tempered one hour at 120°C. a) Bright field image of a large lath, b) corresponding diffraction pattern showing extra spots (highlighted in red) due to the presence of η-carbides, c) Bright field image of many small laths and d) corresponding diffraction pattern showing only spots due to bcc iron. 96

Figure 5.12 Electron micrograph showing precipitation in fine laths of martensite. a) Bright field image, b) dark field image highlighting transition carbides, and c) corresponding diffraction pattern with η-carbides diffraction spots highlighted. In b), 1 indicates intra-lath precipitation, and 2,3 and 4 indicate precipitation along lath boundaries. . . 97

Figure 5.13 Example of an image analysis performed on the microstructure tempered at 120°C for five hours a) raw image and b) image showing the method for determining the carbide size, which was estimated based on an the average of the long and short axis of the red ellipses. 99

Figure 5.14 Carbides size distributions as a function of tempering conditions. a) 120°C one hour, b) 120°C three hours, c) 120°C five hours, d) 120°C 8 hours and e) 150°C one hour. Lognormal fits are represented in red. 101

Figure 5.15 Electron micrograph of the microstructure after tempering at 350°C for 1 hour a) bright field and b) corresponding dark field. 102

Figure 5.16 Three dimensional APT volume obtained on as-quenched specimens, $8 \times 8 \times 240$ nm^3, 7×10^5 atoms. 104

Figure 5.17 a) Image of a representative volume of dimensions $8 \times 8 \times 230$ nm^3 (only carbon atoms are represented), and b) linear profile of the carbon composition along the length of the volume in a). The composition was sampled using small volumes of $8 \times 8 \times 2$ nm^3 (represented in blue in a)) which were moved along the length with a step size of 1 Å. The error bar is indicated on the figure. 105

Figure 5.18 Carbon composition distribution obtained experimentally (gray rectangles) compared to a Bernoulli distribution (red line), for the as-quenched specimen. The total volume sampled is $8 \times 8 \times 230$ nm^3. A random spatial distribution of carbon should result in the measured histogram matching the Bernoulli distribution. 106

Figure 5.19 Three dimensional APT volumes obtained on as-helium-quenched specimens. a) Sample 1, $42 \times 42 \times 72$ nm^3, 3.3×10^6 atoms, and b) Sample 2, $28 \times 28 \times 56$ nm^3, 9.5×10^5 atoms. 107

Figure 5.20 Three dimensional atom probe measurement of the carbon composition profile in the sample shown in figure 5.19(a). a) image of a representative volume of dimensions $8 \times 8 \times 64$ nm^3 (only carbon atoms are represented), and b) linear profile of the carbon composition along the length of the volume in a). The error bar is indicated in the figure. 109

Figure 5.21 Three dimensional atom probe measurement of the carbon composition profile in the sample shown in figure 5.19(b). a) image of a representative volume of dimensions $8 \times 8 \times 50$ nm^3 (only carbon atoms are represented), and b) linear profile of the carbon composition along the length of the volume in a). The error bar is indicated in the figure. 110

Figure 5.22 Equiaxed carbon-rich region observed in the as-helium-quenched sample. a) Three dimensional volume, $5 \times 5 \times 15$ nm^3 showing the equiaxed carbon-rich region, b) same as in a) but tilted 90° with respect to the length axis, and c) linear carbon composition profile obtained along the length of the box. 111

Figure 5.23 Close view of region '1' indicated in figure 5.19(b), and b) linear profile of the carbon composition along the length of the volume in a). The error bar is indicated in the figure. 112

Figure 5.24 Equiaxed carbon-rich region '2' observed in sample 2 of the as-helium-quenched condition. a) Three dimensional volume, $4 \times 4 \times 15$ nm^3 showing the equiaxed carbon-rich region, b) same as in a) but tilted 90° with respect to the length axis, and c) linear carbon composition profile obtained along the length of the box. 113

Figure 5.25 a) Carbon composition distribution obtained in sample 1 (the sampled volume had dimensions $24 \times 24 \times 60$ nm^3), and b) same as in a) for sample 2 (the sampled volume had dimensions $18 \times 18 \times 50$ nm^3). 114

Figure 5.26 Reconstructed volume obtained on the specimen tempered one hour at 120°C. The total number of atoms detected was 8.5×10^5. 115

Figure 5.27 Reconstructed volume obtained on the specimen tempered 8 hours at 120°C. The total number of atoms detected was 21.8×10^6. 116

Figure 5.28 a) Carbon-rich region '1' singled out in a box having dimensions $60 \times 60 \times 20$ nm^3, and b) linear carbon composition profile along the length of the box shown in a). 117

Figure 5.29 Two views of region '1' showing a roughly equiaxed particle. 118

Figure 5.30 Example of an equiaxed carbon-rich region observed in a specimen water-quenched and tempered 8 hours at 120°C. a) Three dimensional volume, $5 \times 5 \times 15$ nm^3 showing the equiaxed carbon-rich region, b) same as in a) but tilted 180°with respect to the length axis, and c) linear carbon composition profile obtained along the length of the box. 119

Figure 5.31 Linear carbon-rich region observed in a specimen water-quenched and tempered 8 hours at 120°C. a) Three dimensional volume, $8 \times 8 \times 30$ nm^3 showing the linear carbon-rich region, and b) same as in a) but tilted 180°with respect to the length axis. 120

Figure 5.32 Reconstructed volume obtained on the specimen tempered one hour at 150°C. The total number of atoms detected was 1.7×10^6. 121

Figure 5.33 Equiaxed carbon-rich region labeled '1' in figure 5.32. a) Three dimensional volume, $5 \times 5 \times 12$ nm^3 showing the equiaxed carbon-rich region, b) same as in a) but tilted 180°with respect to the length axis, and c) linear carbon composition profile obtained along the length of the box. 122

Figure 5.34 Reconstructed volume obtained in a specimen tempered one hour at 150°C. a) Three dimensional volume, $12 \times 12 \times 63$ nm^3 showing the flat carbon-rich region (3×10^5 atoms were detected), b) same as in a) but tilted 180° with respect to the length axis, and c) linear carbon composition profile obtained across region '1'. 124

Figure 5.35 Reconstructed volume obtained in a specimen tempered one hour at 150°C. a) Three dimensional volume, $4 \times 4 \times 15$ nm^3 showing the equiaxed carbon-rich region, b) same as in a) but tilted 180°with respect to the length axis, and c) linear carbon composition profile obtained along the length of the box shown in a) and b). 125

Figure 5.36 Diffusion distance as a function of total martensite fraction. AQ designates the as-water-quenched specimen and HeQ the as-helium-quenched specimen. 129
Figure 5.37 a) Bright field, and b) dark field TEM images revealing the non-homogeneous distribution of carbides within a single lath after tempering for 1 hour at 150°C. 132
Figure 5.38 A comparison between model prediction (lines) and experimentally measured, a) precipitate radii, and b) precipitate volume fraction at 120°C and 150°C. Also presented (c) is the predicted evolution of the carbon in solid solution as a function of aging time. The calculations were performed using the parameters listed in table 5.11 and a dislocation density of $\rho = 3 \times 10^{15}$ m^{-2}. The error bars in a) represent the incertitude on the foil thickness. . . 138
Figure 5.39 Effect of dislocation density on precipitation predicted by the model on tempering at 120°C. a) Volume fraction of precipitates as a function of tempering time, b) precipitate radii, and c) carbon in solid solution. 139
Figure 5.40 Effect of dislocation density on precipitation predicted by the model on tempering 5 hours at 120°C. a) Volume fraction of precipitates as a function of dislocation density, b) precipitate radii, and c) carbon in solid solution. . . . 140
Figure 5.41 Model predictions for the a) volume fraction of precipitates and b) carbon remaining in solid solution for three different values of the dislocation density, after tempering at 350°C. 141

Figure 6.1 Equivalent stress-strain curves, up to fracture of a) all the conditions where ductility was observed, and b) a selection of conditions that exhibited brittle intergranular fracture. 144

Figure 6.2 Summary of fracture behaviour as determined by observation of the fracture surface of samples as a function of tempering condition (cf. figure 6.3), particularly highlighting conditions at the transition between brittle and ductile behaviour. The blue line roughly separates intergranular brittle fracture from ductile fracture and passes through those conditions leading to an intermediate fracture condition. 145

Figure 6.3 Typical fracture surfaces observed in the SEM for samples in the a) as-water quenched and b),c) tempered conditions. The fracture surface appears intergranular with facet sizes consistent with the prior austenite grain size. b) Fracture surface obtained for intermediate tempering conditions. The features on the fracture surface are difficult to identify but roughly correspond to the expected dimensions of laths [160]. c) Fully ductile shear fracture obtained from samples temperature at high temperatures and/or long times. 146

Figure 6.4 Measured evolution of in intergranular fracture stress with tempering at 80°C, 100°C and 120°C. Also plotted are the predicted kinetics of fracture strength evolution based on the assumption that the fracture strength evolves linearly with the degree of segregation to the grain boundary as predicted by the McLean equation (equation 6.1). Each curve corresponds to a different tempering time where the curves have been made to pass through the first data point in the case of each tempering condition. It can be seen that the rate of fracture stress evolution changes much more rapidly than this simple model would predict. . 148

Figure 6.5 Evolution of the 0.2% yield stress with time, at different temperatures. 150

Figure 6.6 Typical normalized work hardening rate obtained on a specimen tempered one hour at 150°C, showing the three different regimes (see text). 151

Figure 6.7 Normalized work hardening as a function of applied stress a) full curves and b) zoom-in to show the monotonic decrease of work hardening with tempering temperature and/or time. Note that, for clarity, not all the conditions are presented on the graphs. 152

Figure 6.8 Influence of the cooling rate on the mechanical properties of martensite. a) equivalent stress strain curves up to fracture, and b) corresponding work hardening rate as a function of applied stress. 155

Figure 6.9 Mechanical properties of strain-aged specimens after two different pre-deformations. The material was tempered 5 hours at 120°C, plastically deformed, re-tempered 3 hours at 120°C and subsequently redeformed. 159

Figure 6.10 Rate sensitivity tests performed in the 300M martensite tempered one hour at 150°C. a) Comparison of monotonic stress-strain curves performed at $\sim 10^{-3}$ s^{-1} and $\sim 10^{-4}$ s^{-1}. b) The change in flow stress following a jump from $\sim 10^{-4}$ s^{-1} to $\sim 10^{-3}$ s^{-1}. 161

Figure 6.11 Stress-angular rotation graph showing the typical response of the material to a sudden increase in strain rate. The upper and lower increases in flow stress corresponding to figure 6.10(b) are indicated. 162

Figure 7.1 Equivalent stress-strain curves obtained during Bauschinger trials on the 300M martensite a) tempered three hours at 120°C, b) tempered five hours at 120°C, c) tempered one hour at 150°C, d) tempered one hour at 350°C, and e) helium gas-quenched. The level of forward pre-strain is indicated. 170

Figure 7.2 Schematic of a stress-distribution function showing the amount of material that has yielded after straining to a strain $\overline{\epsilon} = \frac{\sigma_l}{E}$. 173
Figure 7.3 Optimal scale (m) and shape (s) parameters for different values of β obtained by fitting the Masing model to the forward stress-strain response of a sample tempered at 150°C for one hour. 179
Figure 7.4 Masing fits of the Bauschinger response of martensite after tempering a) 3 hours at 120°C, b) 5 hours at 120°C, c) 1 hour at 150°C, and d) 1 hour at 350°C. e) As-helium-quenched. 181
Figure 7.5 a) Stress-distribution functions used for fitting the stress-strain curves in the forward direction, and b) same as in a) for the reverse direction. 182
Figure 7.6 a) Masing fit of the Bauschinger stress-strain behaviour of as-helium-quenched specimens obtained after modifying the stress-distribution function to fit the reverse stress-strain curve. b) Forward and reverse stress-distributions. c) and d) Same as in a) and b) for specimens tempered one hour at 350°C. 184
Figure 7.7 a) Masing fit of the tensile behaviour of as-quenched low carbon martensite, b) stress-distribution function used to fit the stress-strain curve in a), and c) dislocation density distribution estimated based on the stress-distribution plotted in b). 187
Figure 7.8 Precipitation (σ_{ppt}, solid line) and solid solution (σ_{fr}^{C}, dashed line) strengthening as a function of time and dislocation density, upon tempering at 120°C. The gray curves correspond to $\rho = 10^{14}$ m^{-2}, the red curves to $\rho = 3\times10^{15}$ m^{-2} and the dark blue curves to $\rho = 10^{16}$ m^{-2}. 189
Figure 7.9 Diagram showing the different steps used for the determination of the stress-distribution functions plotted in figure 7.10. 190

Figure 7.10 a) Predicted stress-distributions corresponding to the different contributions after tempering one hour at 120°C. b) Evolution of the predicted overall stress-distributions with tempering at 120°C. 192
Figure 7.11 Predicted stress-distribution functions for $n = 1$ and $n = 2$ after tempering 14 hours at 120°C. 192
Figure 7.12 Predicted stress-strain curve (red line) compared to the experimental stress-strain curve obtained on specimens tempered one hour at 150°C. 194
Figure 7.13 Masing fits of the Bauschinger response of martensite after tempering a) 3 hours at 120°C, b) 5 hours at 120°C, c) 1 hour at 150°C, and d) 1 hour at 350°C. e) As-helium-quenched. 195
Figure 7.14 Typical stress-distribution function obtained for solid solution strengthening. 196
Figure 7.15 Masing model applied to the Bauschinger behaviour of a) an as-quenched 0.15 wt% C martensite, and b) an as-quenched 0.24 wt% C martensite. c) Masing model applied to as-quenched martensites containing various amount of carbon (the value of α' used is also indicated). . . . 200

Figure A.1 Dilatation-temperature curve measured during the heat treatment. 224

Figure B.1 Von Mises equivalent stress in the outer and inner fibers of a tubular specimen pulled in torsion. 226

Figure D.1 Example of a stress strain curve obtained in a Bauschinger trial and plotted in terms of cumulative strain and absolute stress. The data extracted to calculate the different Bauschinger effect parameters are indicated. 231

Figure D.2 Evolution of the back-stress as a function of forward pre-strain for each condition a) after tempering 3 hours at 120°C, b) after tempering 5 hours at 120°C, c) after tempering 1 hour at 150°C, d) after tempering 1 hour at 350°C, and e) in the as-helium-quenched condition. . . 232
Figure D.3 Comparison of the back-stress in the conditions studied here. 233

Acknowledgments

Here I was at the end of America – no more land – and now there was nowhere to go but back.
— Jack Kerouac

We arrived in Vancouver on January 9, 2009 (foggy day), we were naive and young and ready to enjoy our very first steps in North America, land of freedom, peace & love, and Starbucks coffee. The landing was rough, Co was unemployed during the first three months and the perspective of staying in Vancouver was decreasing as time went by. For some unknown reasons, we made it (too long to explain in detail here) and I feel that I need to acknowledge the key people that helped make the past four years a journey we will remember for the rest of our lives.

I would like to thank Prof. Chad Sinclair for his (never failing) encouragement, support, patience and enthusiasm during the course of my Ph.D. I have learned a lot with you, and that's what matters the most. I am also indebted to Prof. David Embury for the many fruitful (long) discussions about my project (or sometimes French politics). Many thanks to Dr. Olivier Bouaziz, Dr. Sébastien Allain and Dr. Mohamed Gouné for the interest they showed in my studies, and for the very fruitful technical discussions.

I couldn't have done this without numerous external collaborations. I would like to thank Dr. Xavier Sauvage and Mr. Vincent Bilyk for their help with three dimensional atom probe experiments at the Université de Rouen, and Prof. Hatem Zurob and Dr. Xiang Wang for their help with transmission electron microscopy at McMaster University. I owe you all a

great deal of the success of this work!

I can't leave this section without praising the wonderful job done by Ross McLeod and his (dream) team (Carl and Dave) in making those famous torsion grips and the torsion samples. Their work is the definitive proof that the old alchemist theory (turning iron into gold) is, indeed, true.

The organization of the internal defense was a mess (again it's too long to explain here). Prof. Jean-Hubert Schmitt, you were a wonderful last-minute substitute examiner. I hope you enjoyed the Canadian wine (sorry I kept the French wine for Chad).

Those lines are the final lines of a long process which sometimes drove me into craziness, the ever-lasting search of what makes sense, the mind being focused on things, beauty, equations, emptiness, fear, sadness and in the end, eternity. Visions of a better world, Neal Cassady walking along the rail tracks under the hot Mexican sun, talking like a madman, burning, reciting poetry, the angels dance in the sky. Thanks a lot Kerouac.

My deepest thanks go to the gang of old aristocrats of the mighty AMPEL lab (Vancouver, BC), Guillaume (du Lefebvrier), Thomas (de la Garcinière), Guilhem (de la Martinière), Ludi (de la Chauvière) for the 'soirées mémorables' on Friday nights, which were often joined by Jenny and Tegar (love you guys). I already miss the bad beer of Vancouver, the discussions, the laughs, the madness. Yann and Virginia, I will always remember the lengthy discussion on quantum physics the night before my internal defense. Thanks also to David, you were the cohesive force during the early years of the group (thanks for your help in FF119). Cheers everybody!

Special thanks to Guilhem and Tom who were the greatest hosts I could have hoped for during my last two months in Vancouver.

Many thanks to our families for their love and support during the time we spent in Canada. Sylvie and Michel, thanks for believing in us!

This work is dedicated to Colette, I couldn't have done this without you. My love for you extends beyond the mountains of the North shore, beyond the Rockies, beyond the stars. What about walking through life together?

Now that all this belongs to the past, 'Let's have a drink and smoke a

cigarette' [1].

[1] Wes Anderson's 'The Darjeeling Limited' (2007).

To Colette,

Chapter 1

Introduction

Martensitic steels are interesting for a wide range of applications because they are easy to produce, are low cost and exhibit a very high strength (up to 2.5 GPa in some grades, compared to an expected theoretical shear strength of 8 GPa for iron [1]). This allows manufacturers to use martensitic grades for aircraft landing gears and anti-intrusion bars in cars, applications where very high strength are required. A recent article in The New York Times pointed out how high strength steels are strategic for car manufacturers to meet crash and fuel standards [2]. Low carbon martensitic steels are used for anti-intrusion parts in automobiles because they present an excellent strength/cost ratio. A limitation to the use of martensitic grades arises from the complex relationship between processing and properties. In some cases, martensitic steels can exhibit brittle fracture, and even spontaneous fracture if processing is not done properly. There is therefore a need to understand the link between structure and properties in martensitic steels in order to develop grades having the best combinations strength and elongation. For many steel companies, the current target is to develop steels with strengths of 2 GPa and reasonable ductility. In addition, recent progress made in the development of compositionally graded steels [3] has revived the interest in understanding the deformation mechanisms of martensite. The design of these steels, having a core made of monolithic martensite, will be aided by having a better understanding of the martensitic core.

From a scientific standpoint, ferrous martensite has received considerable attention for many years not only because of a lack of understanding of the origins of its incredible strength, but also because of the complexity of its microstructure and properties. Strength in these steels has been attributed to precipitation hardening, solid solution hardening, size effects, interaction between dislocations and interstitial atoms and even fluctuations of carbon concentrations on a very fine scale. Though the microstructure of martensite has been heavily studied, a lot of questions remain concerning its mechanical properties in general, and its response to complex loading paths in particular. A quick survey of the literature shows a distinct lack of combined microstructure/mechanical properties studies. The mechanical response from careful tests can give a lot of information about the internal stress state, induced by the different microstructures (lath size, amount of carbon in solid solution, carbides volume fraction, size and shape).

In this work, the influence of carbon redistribution on the mechanical properties of martensite has been investigated. The studied material was a 300M silicon-modified martensitic steel supplied by Goodrich (Canada). The samples were heat treated to obtain fully martensitic microstructures. In certain cases they were also tempered at low temperature (at or below 350°C) to vary the carbon distribution. Experimentally, the material has been characterized with the view to linking the microstructure to specific strengthening mechanisms.

This thesis starts by a survey of the literature, aimed at clarifying the microstructure, plasticity and fracture of ferrous, thermal martensite. It continues with a description of the experimental methodology used in the project. Then, a study of the microstructure followed by the bulk mechanical properties and their evolution with tempering is presented. Finally, the Bauschinger effect of martensite is assessed. Those results are used to develop a composite model to link the microstructure to the mechanical properties.

Chapter 2

Literature Review

In this section, the microstructure and the mechanical properties of ferrous martensite are reviewed starting with as-quenched martensite, and its evolution with aging and tempering. The thermodynamics and kinetics of the martensitic transformation are briefly reviewed (the interested reader is directed to the comprehensive review by Olson and Cohen [4]).

Following this, proposed explanations for the mechanical properties of martensite are presented.

2.1 An overview of the microstructure of ferrous martensite

Ferrous martensite is a metastable product of iron obtained after quenching from austenite at high temperature to room temperature. The transformation from austenite to martensite results in a complex microstructure having different features at different length scales (figure 2.1). The review starts with a description of the microstructure of as-quenched martensite and its evolution with aging and tempering. The typical length-scales of the microstructure are highlighted as these length-scales are important for interpreting the bulk mechanical properties of martensite.

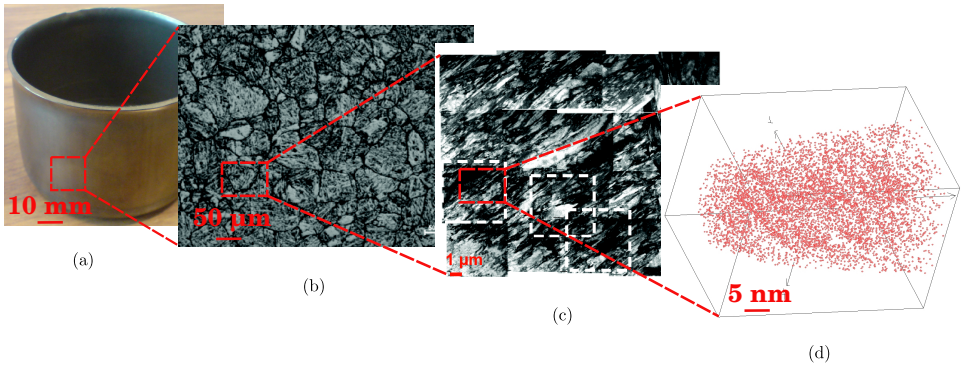

Figure 2.1: Schematic view of the different length-scales in the case of lath martensite, a) Size of the actual part, b) Optical micrograph showing the prior austenite grain size, c) Transmission electron micrograph showing the lath size and d) 3D atom probe tomography showing the solute spacing (only carbon atoms are represented).

2.1.1 As-quenched martensite

Basic concepts and nomenclature

Martensitic transformations are displacive, meaning that no long range diffusion of atoms occurs during the transformation. Consequently the product (martensite) has the same composition as the parent (austenite) phase. The transformation requires both a change in volume as well as a large shear to convert the face centered cubic (fcc) structure to the body centered tetragonal (bct) structure. In the phenomenological theory of martensite, the transformation is imagined to occur by a combination of a lattice transformation strain plus a lattice invariant shear, the latter being thought to occur by dislocation slip or deformation twinning, depending on the critical temperature below which the transformation can proceed, the so-called martensite-start (Ms) temperature [5]. Depending on whether the martensite is accommodated by twinning or slip, the morphology of the microstructure changes [6]. In the following, the terminology established by a round-robin study published by Krauss and Marder [7] is adopted. Low Ms

twinned martensites are named *plate martensite* whereas high Ms needle-shaped martensites are named *lath martensite*. As pointed out by Speich and Leslie [8], and Magee and Davies [9], the transition between lath and plate martensite is not sharp, meaning that mixed lath/plate microstructures exist. Those martensites will be referenced as *mixed martensite*. The difference in microstructure between plate and lath can be seen in the light microscope, as shown by Magee and Davies [9]. In the former case, coarse plates of martensite are formed and electron microscopy analysis shows that each plate is heavily twinned around its center line (midrib, figure 2.2). In the latter case, packets of fine parallel laths form within the austenite.

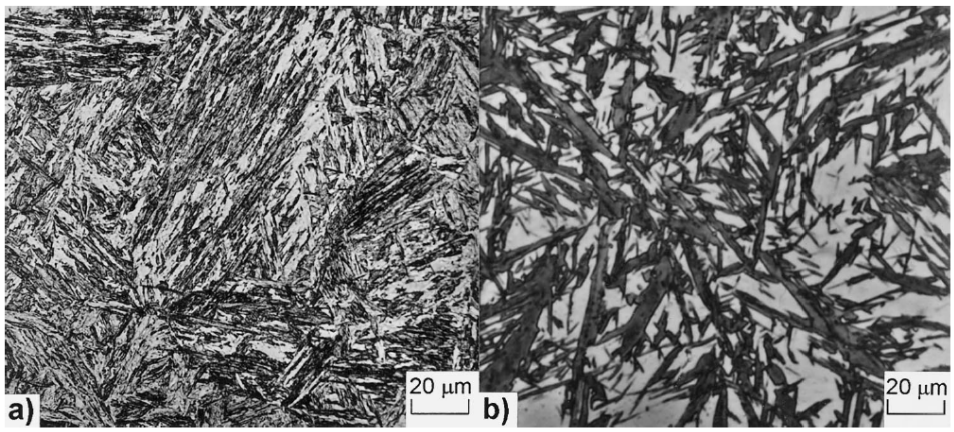

Figure 2.2: Optical micrograph of a) lath martensite and b) plate martensite, from ref. [10]. In b), retained austenite appears in light gray whereas martensite appears in dark gray. In a), no retained austenite is visible.

From austenite to martensite: the Bain transformation

Bain proposed a simple path for forming a body center cubic (bcc) martensite from face centered cubic (fcc) austenite [11] (figure 2.3(a)) by means of compression in the [001] direction and expansion in the [110] and $[\bar{1}10]$ directions. A consequence of this is that carbon is inherited into one set of octahedral interstitial sites in the bct lattice. Since the carbon occupies

one of the three possible types of interstitial site in the bcc lattice, a tetragonality should be observed. Experimentally, however, no tetragonality is observed in plain low carbon martensite, a result probably due to the segregation of carbon atoms to lattice defects (lath boundaries, dislocations) during the quench [12], a phenomenon called *auto-tempering*. Tetragonality is observed in as-quenched martensites formed around or below room temperature where the thermal mobility of interstitials is greatly reduced, limiting the redistribution of interstitials during the quench. The amount of tetragonality, as measured experimentally by the ratio $\frac{c}{a}$, where c is the lattice parameter in the [001] direction and a is the lattice parameter in the [110] and $\left[\bar{1}10\right]$ directions (figure 2.3(b)), is a linear function of the carbon content [13]:

$$\frac{c}{a} = 1.000 + 0.045(wt\%C) \tag{2.1}$$

Where c and a have the same definitions as above.

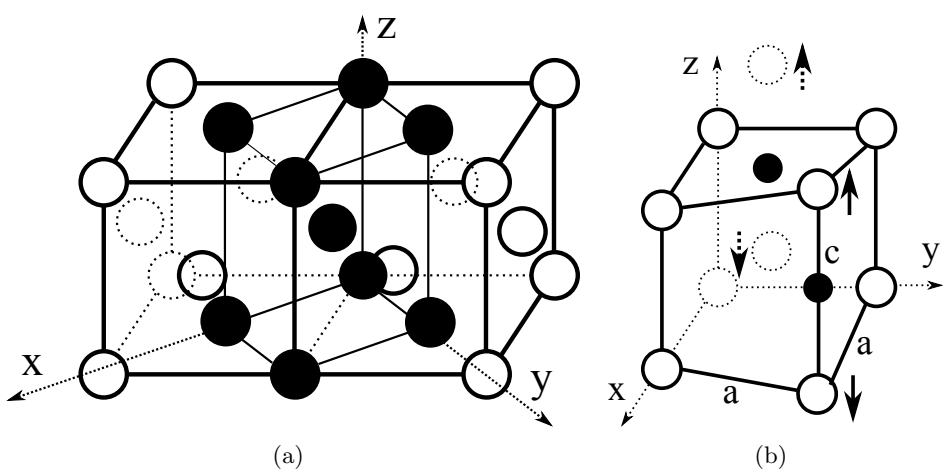

Figure 2.3: Schematic view of a) the Bain transformation where black circles represent atom positions in a bcc lattice whereas white circles represent atom positions in a fcc lattice, and b) tetragonality induced by foreign atoms (in black) located on z-type interstitial sites of a bcc lattice.

Volume fraction of martensite and Ms temperature

Both lath and plate martensite are formed via an athermal process where the volume fraction of product transformed is only a function of temperature, not time. An empirical equation linking the volume fraction of martensite to temperature below Ms has been determined by Koistinen and Marbuger. By carefully measuring the amount of retained austenite in different alloys, after quenching at different temperatures (room temperature and below), the authors showed that the volume fraction of martensite transformed was a function of the difference between the Ms temperature and the lowest temperature reached during the quench [14]:

$$V_{\alpha'}(T_q) = 1 - \exp(-\alpha(Ms - T_q)) \tag{2.2}$$

Where $V_{\alpha'}$ is the volume fraction of martensite at the end of the quench, Ms is the martensite start temperature of the material and T_q is the lowest temperature reached during the quench.

Martensite does not start to form at the temperature T_0, where the free energy for the transformation from austenite to martensite is zero. Instead, it starts to form at a slightly lower temperature, the so-called Ms temperature (see figure 2.4). This is due to dissipative effects, like the creation of interfaces between martensite and the austenite matrix, or the plastic deformation needed in the transformation process. The free energy change which corresponds to the temperature difference between T_0 and Ms constitutes the driving force for the transformation [5].

The Ms temperature of a particular alloy is a function of its chemical composition. For instance, Ishida calculated the following dependence of the Ms temperature on alloying elements [15]:

$$Ms(^\circ C/wt\%) = 545 - 330C - 14Cr - 23Mn - 5Mo - 13Ni - 7Si \tag{2.3}$$

Where the elemental symbols represent the weight percentage of elements (only the influence of major alloying elements are shown, for the complete equation see ref. [15]). Equation 2.3 shows the dominant effect of carbon in

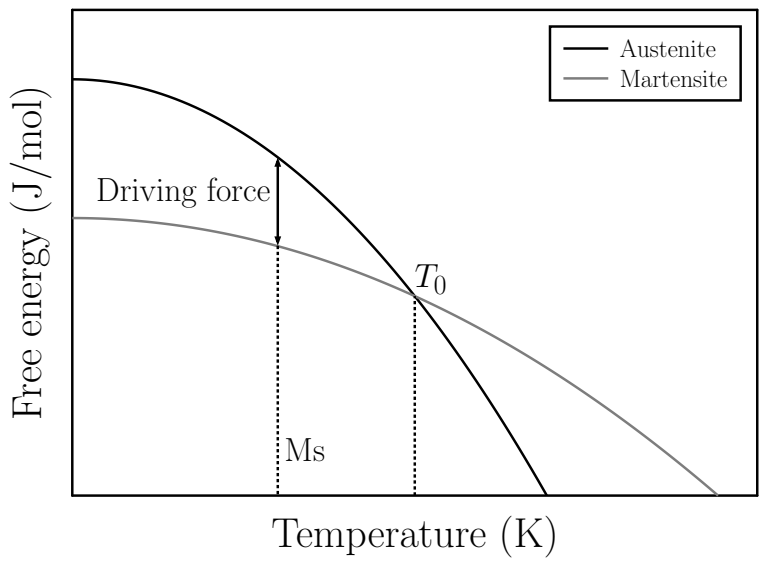

Figure 2.4: Schematic evolution of the free energies of austenite and martensite with temperature. The Ms and T_0 temperatures are represented. Reproduced from ref. [5]

influencing the Ms temperature.

Volume fraction of retained austenite

Equation 2.2 shows that the martensitic reaction does not necessarily go to completion, leading to some retained austenite after quenching. This has been experimentally verified in various plain carbon martensites [8] (figure 2.5). Inserting the values of Ms for plain carbon martensites given by Greninger and Troiano [16] in eq. 2.2 gives a reasonable estimate of the amount of retained austenite found experimentally at room temperature (20°C) by Marder and Krauss [17]. Moreover, for a martensite having a Ms temperature of -35°C, e.g. Winchell and Cohen [13], equation 2.2 gives 17% retained austenite, a value quite close to the 20% found experimentally [13]. Therefore, Koistinen and Marburger's empirical model seems to be reliable for determining the amount of retained austenite for martensites having a wide range of Ms temperatures. Not captured by this relation, however,

is the observation that the amount of retained austenite is dependent on the quench rate. This was reported by Sherman *et al.*, who observed more retained austenite in a slowly cooled (55°C/s) specimen compared to a fast quenched specimen (560°C/s) [18]. The authors explained this result as a consequence of the rejection of carbon atoms at the austenite-martensite interface in slowly cooled specimens. This is drastically inhibited as the cooling rate is increased. Morito *et al.* also recorded a carbon enrichment in thin films of inter-lath retained austenite, a phenomenon that was attributed to auto-tempering and/or room temperature aging [19].

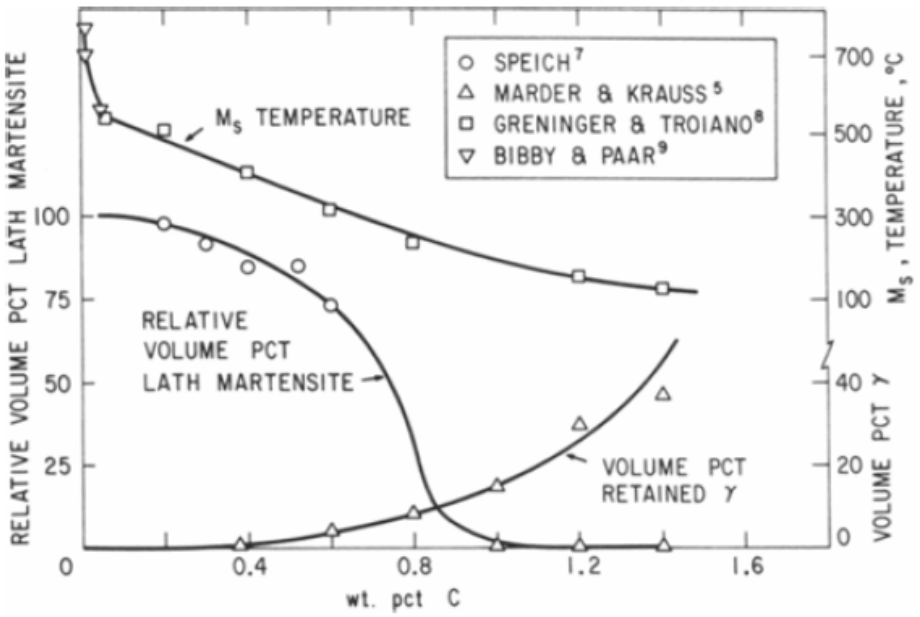

Figure 2.5: Evolution of the Ms temperature, fraction of lath martensite and volume of retained austenite with carbon content, from ref. [8].

In specimens containing less than 10% retained austenite, direct observation of the austenite is not possible in the optical microscope. Electron microscopy has revealed that austenite is retained as thin films (10 nm in thickness) along lath boundaries [20–22] (figure 2.6). The mechanical and thermal stability of the retained austenite films will be discussed in section

2.2.

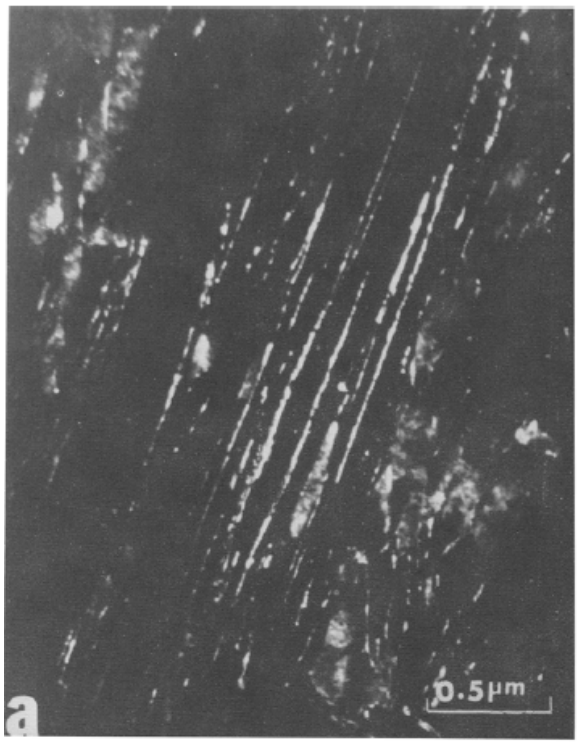

Figure 2.6: Dark field micrograph showing the films of retained austenite (in white) between the laths in medium carbon low alloyed ferrous martensite, from ref. [20].

Effect of alloying elements on microstructure

As was already pointed out, it is possible to change the microstructure of martensite from lath to plate by adjusting the Ms temperature via alloying additions (e.g nickel). Magee and Davies, using alloys with various carbon and nickel contents, were able to obtain lath and plate martensites, and mixed martensite with different fractions of plates relative to laths [9]. From their experimental work, they observed that a full lath martensite was

obtained if the carbon content of the alloy was given by:

$$wt\%C \leq 0.6 - 0.02(wt\%Ni) \tag{2.4}$$

Whereas a full plate martensite was obtained for carbon contents given by:

$$wt\%C \geq 1.05 - 0.04(wt\%Ni) \tag{2.5}$$

The condition for having full plate martensite (equation 2.5) in plain carbon steels (without alloying elements) correlates well with the results reported by Speich and Leslie [8]. However, equation 2.4 seems to provide a small overestimate since Speich and Leslie measured around 20% of twinned areas in a plain 0.6 wt% C martensite.

The microstructure in lath martensite is somewhat more complicated than that in plate martensite. A prior austenite grain contains several packets, a packet being a group of laths having a similar crystallographic orientation separated by low angle boundaries [17, 23]. The size of a packet is a direct function of the prior austenite grain size. Speich and Warlimont found an average lath thickness of 0.25 μm, independent of carbon content for carbon contents above 0.05 wt% [24]. Marder and Krauss however, noted that a broad range of lath sizes exist in a typical martensitic microstructure the range being between 0.025 μm and 2.25 μm [25]. These authors also noted that martensite contains a significant fraction of laths having thickness below 100 nm, a result later confirmed by Apple *et al.* [26] (figure 2.7). By videorecording the austenite to martensite phase transformation, they observed that the fine laths were formed in an austenite matrix mechanically constrained by the already formed, bigger laths, so that the fine laths tend to appear after the large laths during the transformation. The effect of lath size on bulk mechanical response has not been extensively studied, though a Hall-Petch effect due to lath boundaries has been previously suggested as a contributor to the strength of martensite [27].

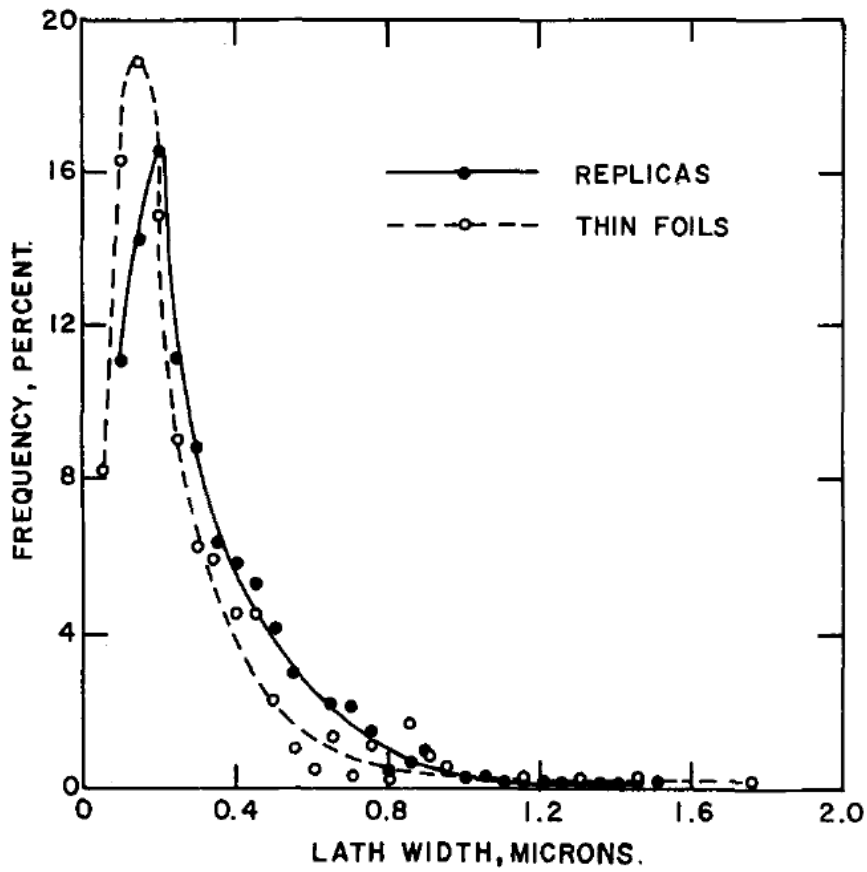

Figure 2.7: Lath width distribution determined by carbon replica and thin foil analysis. From ref. [26].

Dislocation substructure

The dislocation substructure in lath and plate martensites has been studied by Wayman and co-workers, by means of transmission electron microscopy [23, 28, 29]. They found a higher dislocation density in lath martensite compared to the untwinned region of a plate martensite by roughly an order of magnitude (5×10^{14} m^{-2} in the former case compared to 7×10^{13} m^{-2} in the latter case). They also showed that, in both cases most of the dislocations were screw in character. Such high dislocation densities are consistent with the more recent results of Morito *et al.* [30] obtained from lath martensites.

Morito *et al.* also reported a small dependency of the dislocation density on the nominal carbon content, but for all the martensites investigated, the dislocation density remained lower than 5×10^{15} m^{-2}. Sandvik and Wayman observed irregularities of dislocation arrangements between laths with an increase in dislocation density in the vicinity of the retained austenite [23]. Consistent with the view of Thomas [20], they proposed that part of the dislocation substructure was due to plastic accommodation in martensite induced by mechanical constraints from neighboring austenite during the phase transformation.

Carbon redistribution during quenching

Significant carbon redistribution (and even carbide precipitation [31]) can occur during quenching if the Ms temperature is well above room temperature [12]. This phenomenon can be enhanced by a low quench rate and the use of large samples [32, 33]. This phenomenon, called *auto-tempering*, has been known for decades but has been difficult to quantify because in some cases the redistribution can occur with a scale of $\sim$ 10 nm. Recent advances in experimental techniques such as three dimensional atom probe tomography have allowed more quantitative measurements of this phenomenon [34–36].

Aborn studied the effect of sample size on auto-tempering. In low alloyed low carbon (0.13 wt%) 1013 steel, he found that thick (1/8 inch) samples exhibited a more advanced state of precipitation compared to thin samples (1/32 inch), after austenitizing and quenching in ice brine (a cooling rate of $\sim$ 500°C/s) [33]. Moreover, no precipitation was observed near the surface (i.e. the area which experienced the fastest cooling rate). The same effects were observed on a 4315 steel that contained more alloying elements. This effect was also quantified by a decrease in mid-thickness hardness with increasing sample diameter (figure 2.8). As shown in figure 2.8, the effects on the mechanical properties of the resulting product could be potentially significant. If we consider that the hardness value is approximately 3 times the yield stress, a decrease of 35 Hv would induce a decrease of around

100 MPa in yield stress. Moreover, quench gradients along the thickness of the specimens give rise to residual internal stresses that also influence the mechanical properties of the material [37].

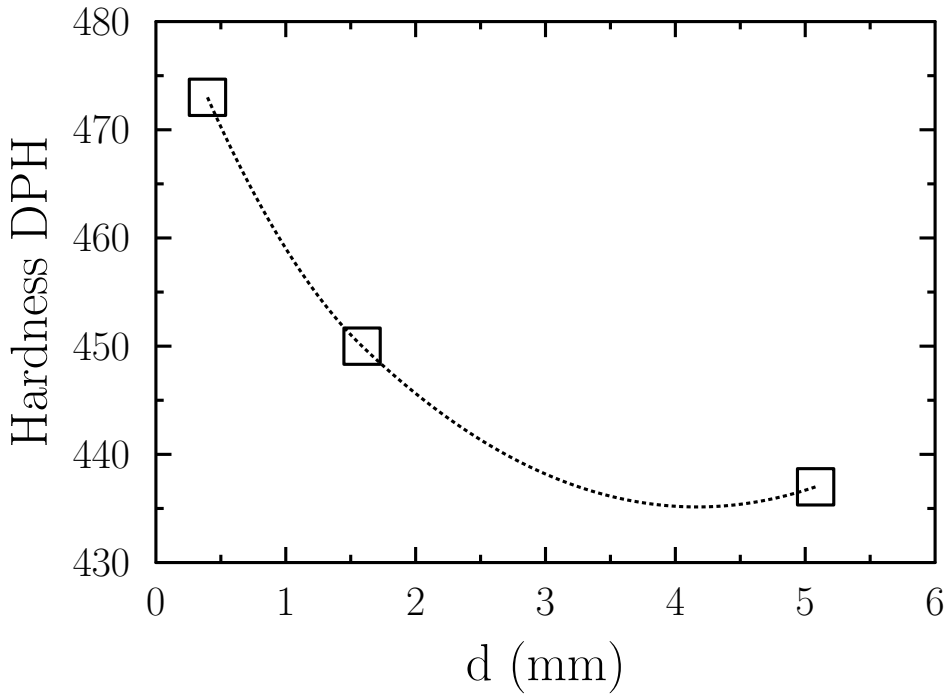

Figure 2.8: Hardness as a function of distance from specimen surface in as-quenched 4315 low carbon martensite. Plotted from values given in ref. [33].

Speich showed that very thin specimens (0.25 mm) prevented carbide precipitation during quenching, even in low carbon steels [12]. However, Speich calculated that carbon redistribution to lattice defects such as dislocations or lath boundaries could easily occur during the quench, especially for low carbon, high Ms temperature martensites. This idea was supported by internal friction and electrical resistivity measurements, according to which 80 to 90% of the carbon atoms were found to be segregated to lattice defects upon completion of the quench, in a 0.2 wt% C martensite. Kalish and Roberts, using a theoretical approach, confirmed Speich's experimental

results, although in their model they only considered dislocations, and no other types of defects (laths, twins, prior austenite grain boundaries) [38]. Using field ion microscopy, Miller *et al.* found evidence of carbon segregation to twin boundaries in a low Ms Fe-Ni-C martensite, aged several hours at room temperature [39]. More recently, Hutchinson *et al.* using 3D atom probe tomography, observed segregation on both planar and linear defects, in as-quenched martensites containing different amount of carbon (from 0.1 wt% to 0.5 wt%) [35]. Although the nature of the defects could not be assessed with certainty, the distance between the two planar defects recorded was comparable to the lath width (figure 2.9). The linear appearance of some segregation was attributed to Cottrell atmosphere around dislocations. Statistical analysis showed that the carbon was more homogeneously distributed in higher carbon martensites than in lower carbon martensites. This might be expected given the effect of carbon on the Ms temperature of steels and on carbon diffusion in martensite [40]. The maximum carbon concentration in the segregated regions was between 2 at% C and 3 at% C in all cases, and regardless of the type of segregation (linear or planar). Unfortunately, neither the cooling rate nor the area in which atom probe or electron microscopy samples were extracted (near the surface or near the core) was specified in the case of the work reported in [35], making the comparison between the results difficult. Nevertheless, it is clear from the considerations presented above that many as-quenched martensites are already decomposed during the quench and subsequent aging at room temperature, the extent of decomposition being a function of the Ms temperature. Finally, as equation 2.2 states, the volume fraction of martensite formed during quenching is a function of temperature. A consequence of this is that a bulk martensitic material contains martensite formed at a range of temperatures, and therefore having experienced a range of auto-tempering. As noted earlier, the coarsest laths tend to form earliest (highest temperature) and therefore are expected to have undergone more auto-tempering than the fine laths formed at lower temperature. Though difficult to assess, this might be an important source of mechanical heterogeneities in the as-quenched material.

From the above discussion, it is clear that the microstructure of as-

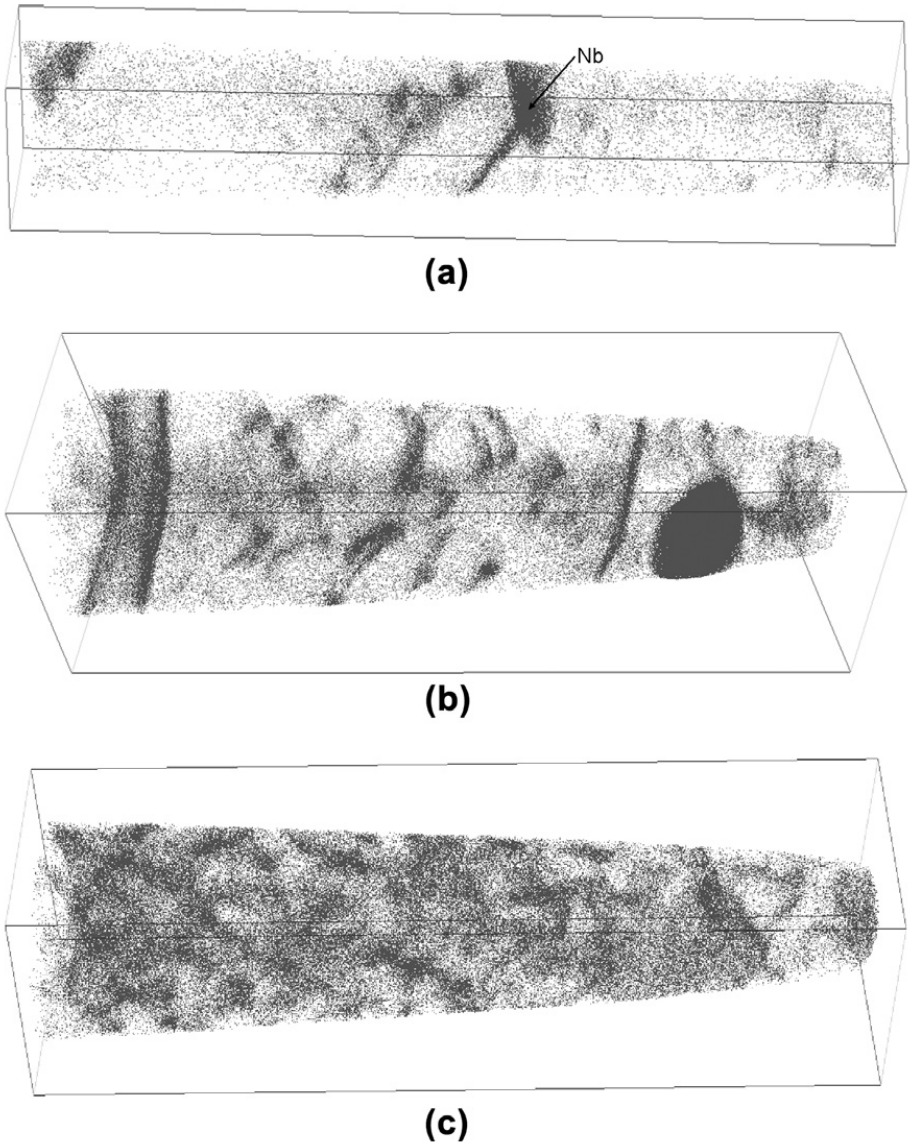

Figure 2.9: 3D atom probe results on as-quenched martensite aged a few hours at room temperature due to specimen preparation, containing a) 0.1 wt% C, box length 210 nm, b) 0.2 wt% C , box length 230 nm, and c) 0.5 wt% C, box length 220 nm. Only carbon atoms are represented. From ref. [35].

quenched martensite is complex, and encompasses fine scale features that are difficult to quantify, but are nevertheless essential for understanding the relation between strength and structure. This complex material becomes even more complex when it is tempered, as described in the next section.

2.1.2 Aged and tempered martensite

In this section the classical distinction between 'Aging' and 'Tempering' is adopted. Aging refers to phenomena occurring *below* 100°C (i.e. a temperature range in which there is carbon movement but no precipitation of transition carbides), while tempering refers to annealing at temperature *above* 100°C where precipitation of iron carbides occurs [8, 41–43]. In what follows, aging and tempering are treated separately, although some overlap exists between the two processes, as will be highlighted later. In each subsection, various aspects are treated, mainly kinetics and microstructural evolution.

Formation of structural modulations in carbon concentration

It is well known that substantial changes happen when as-quenched martensite is held at low temperatures, even below room temperature in low Ms martensites. This was first reported by Winchell and Cohen, who described a concomitant increase in hardness and electrical resistivity unpon aging virgin martensite between -60°C and 100°C [13]. Since then, considerable effort has been made to try to characterize the microstructural changes occurring on aging at low temperature (from -60°C to 100°C). A variety of experimental techniques have been used in this regard, including transmission electron microscopy [44–47], X-ray diffraction [48, 49], Mössbauer spectroscopy [50–54], differential scanning calorimetry [47, 55, 56], electrical resistivity [42, 44], field ion microscopy [39, 57] and, more recently, three dimensional atom probe tomography [34]. Though the exact nature of the microstructural changes is still a matter of debate, especially due to conflicting conclusions drawn from Mössbauer and atom probe analysis, it is clear that low temperature aging leads to significant carbon segregation.

This occurs through cluster formation and formation of a modulated structure [46] of carbon rich regions having a maximum composition of approximately 10 at% C. This has been observed after aging for 1000 hours at room temperature (see figure 2.14) [34, 44]. Detailed studies of this modulated structure show that it consists of a periodic arrangement of regions of low and high carbon concentration. The initial wavelength of the modulated structure depends on the nominal carbon content, but is of the order of 1 to 5 nm (figure 2.10(a)) [44, 45]. Differential scanning calorimetry and Mössbauer spectrometry studies suggest that clustering and the formation of the modulated structure are controlled by carbon diffusion. This has been determined based on the fact that the measured activation energies for these processes are comparable to the activation energy for carbon diffusion in ferrite [55, 58].

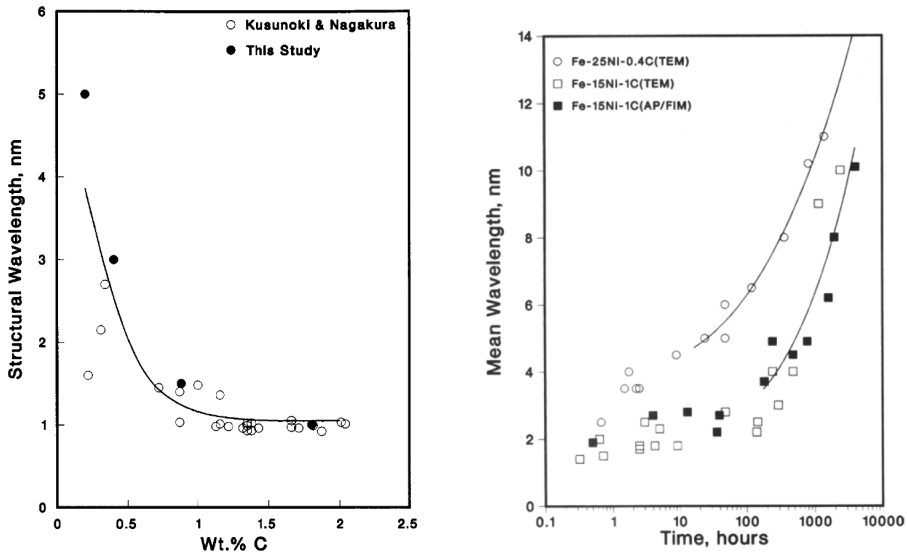

(a) (b)

Figure 2.10: Typical wavelengths measured by selected area diffraction pattern analysis and atom probe analysis, a) initial wavelength as a function of nominal carbon content and b) evolution of the wavelength with aging time at room temperature for two different martensites. From ref. [44].

Specific details about the sequence of aging and tempering in plain carbon martensites have been discussed by Nagakura *et al.* [46], with a particular emphasis on the interpretation of transmission electron microscopy diffraction patterns. The authors were able to obtain virgin martensite in plain carbon steel by carefully controlling the heat treatment and specimen preparation. Thin specimens (0.1 mm thick) were used, ensuring a fast, homogeneous quench rate along the thickness of the material in order to avoid auto-tempering. After the quench in ice brine, specimens were immediately transfered into liquid nitrogen to avoid room temperature aging. By this careful procedure they were able to interpret the microstructure evolution upon low temperature aging, starting from a microstructure as homogeneous in carbon distribution as possible. In electron diffraction patterns, they observed diffuse spikes (figure 2.11) around fundamental spots at temperature as low as 270 K (-3°C). As the temperature was raised, satellite spots ap-

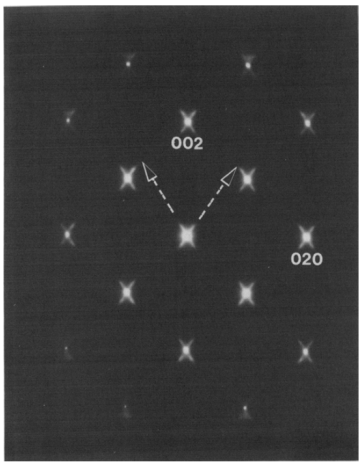

Figure 2.11: [100] electron diffraction pattern showing the diffuse spikes around fundamental spots, obtained after aging a Fe-21 wt% Ni-1 wt% C martensite at room temperature for 26 minutes. The diffuse spikes are due to lattice elastic distortions induced by the modulated structure. From ref. [44].

peared at the tips of the diffuse spikes, at temperatures up to 360 K (87°C). The appearance of diffuse spikes was ascribed to carbon cluster formation

at low temperature (below 270 K), the size of the clusters was estimated by dark field imaging and found to be 10 Å (figure 2.12). The spacing between clusters was estimated to be between 6 and 8 nm. The appearance of satellite spots was ascribed to the rearrangement of the clusters to form a modulated structure, as described by Taylor *et al.* [44] and Kusunoki and Nagakura [45]. The modulated structure has been described as 'tweed-like' because of the contrast observed in transmission electron microscopy (in black are the carbon-rich regions and in white are the carbon-depleted regions) induced by the modulated structure (see figure 2.13). The temperature range over which the 'tweed-like' structure is observed in the electron microscope is consistent with the work of Han *et al.* [47] and Taylor *et al.* [44]. However, Taylor and Cohen later pointed out that satellite spots were never observed in aging Fe-Ni-C martensites [43].

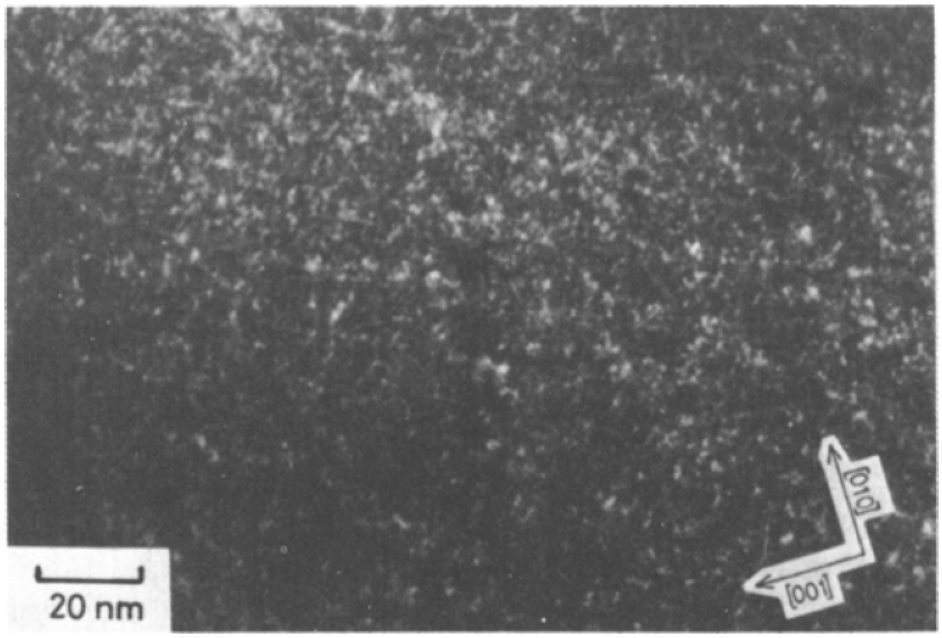

Figure 2.12: Dark field electron micrograph obtained using the diffuse spikes around 002 fundamental spot of a 1.1 wt% C martensite. Clusters appear in white. From ref. [46].

The modulated structure (figure 2.13) has been observed during aging of

both virgin, low Ms plate martensites [44, 47] and lath martensites [42, 44–46], although it seems that some specific conditions (small sample thickness, quenched into ice brine, careful control of specimen preparation, and/or lower Ms achieved with some nickel addition) were required to observe it in the case of lath martensite. Taylor *et al.* [44] argued that the forma-

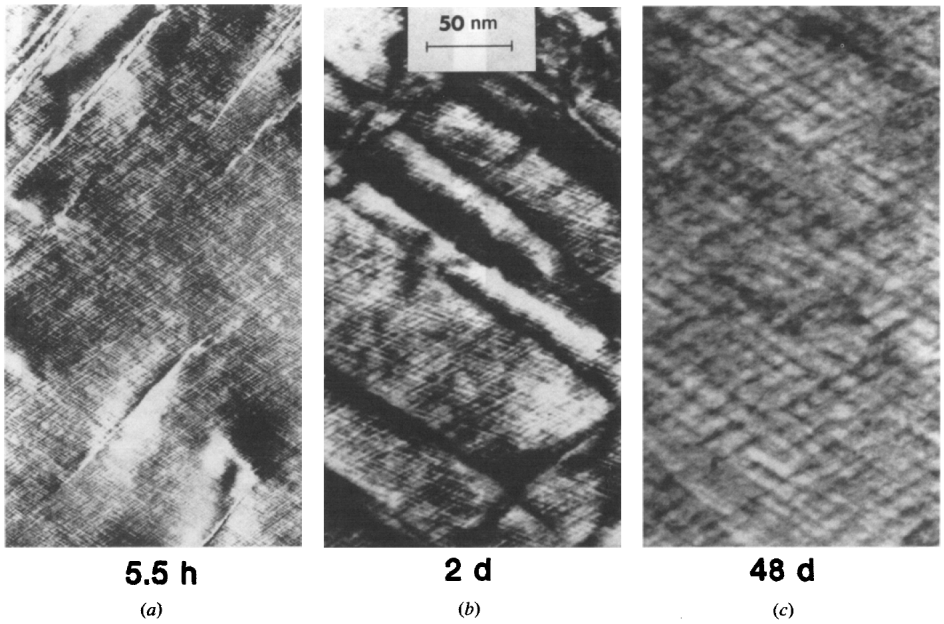

Figure 2.13: Evolution of the modulated structure of a Fe-21wt% Ni-1wt% C martensite with aging time at room temperature, (a) 5.5 hours, (b) 2 days and (c) 48 days. Additional contrast is attributed to lattice dislocations. From ref. [44].

tion of the periodic modulated structure followed a spinodal decomposition process, consistent with the thermodynamic calculation of Ren and Wang [59]. According to Taylor *et al.* [44], the main experimental features in support of this view were the periodicity of the modulations and the continuous increase in compositional amplitude with aging time (figure 2.14). The authors also observed a coarsening stage of the modulation where the wavelength increased to 10 nm (figure 2.10(b)) before carbide precipitation. They finally made the point that, given the concentration of the carbon-rich re-

gions (measured by atom probe), those regions might actually correspond to a carbide having the stoichiometry $Fe_{16}C_2$, isomorphous to the well-known α"-$Fe_{16}N_2$ found in iron-nitrogen martensite. However, detailed high resolution electron microscopy [47] and synchrotron radiation diffraction analysis [49] of the aging sequence in virgin martensite ruled out this possibility. The diffraction experiments conducted by Van Genderen *et al.* [49] showed no evidence of diffraction peaks due to a α" superstructure.

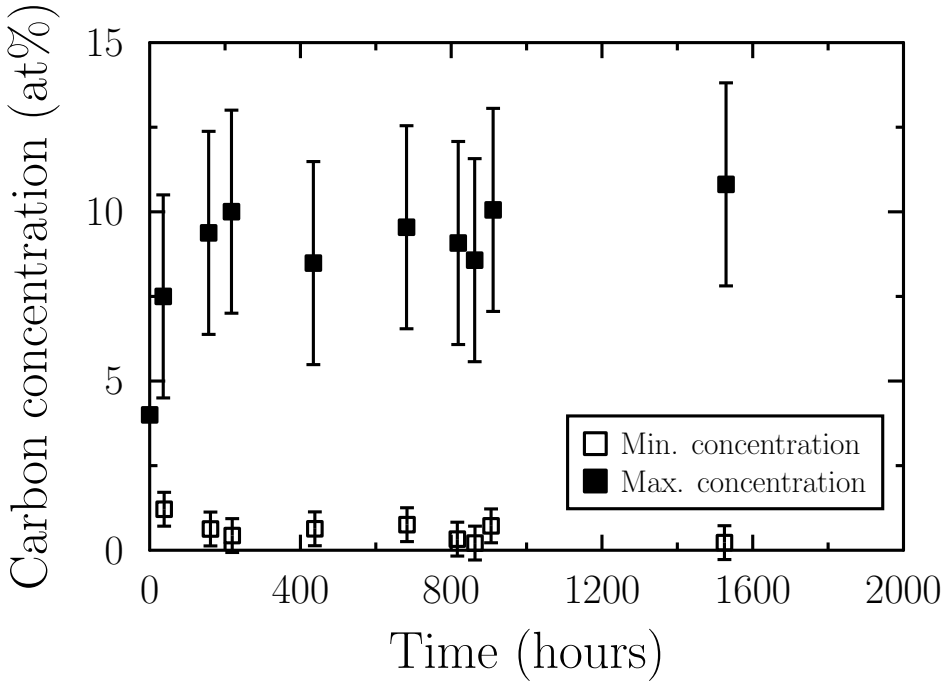

Figure 2.14: Evolution of the minimum and maximum carbon concentration measured by atom probe analysis during aging at room temperature of an initially virgin Fe-21wt% Ni-1wt% C martensite. Reproduced from ref. [44].

Carbon segregation to defects

As noted earlier, Speich has suggested that most, if not all, defects such as dislocations and twin boundaries are fully saturated with carbon following

quenching [12]. This has been supported by the more recent observations with three dimensional atom probe made by Miller *et al.* [39, 57] and Wilde *et al.* [60]. Olson and Cohen have pointed out however that, although carbon segregation to lattice defects might be active during aging of virgin or fresh martensites, clustering of carbon atoms should be the dominant mechanism up to the later stages of the aging process [41]. Support for this comes from the fact that low Ms martensites, regardless of the microstructure (lath or plate) exhibit a peak in resistivity upon aging for short time at low temperature (figure 2.15). Since segregation to lattice defects, according to Speich's measurements, produces a decrease in resistivity, the resistivity peak has been attributed to carbon clustering [43]. This peak can be explained by the large lattice strains created by the carbon clusters (see Taylor and Cohen's review for details about the physics underlying this statement [43]). Secondly, the diffusion distances involved in the segregation mechanism are much greater than the distances involved in the spinodal process. If we consider a typical dislocation density for martensite of 10^{15} m^{-2}, the average distance between two dislocations is 32 nm. This should be compared with a wavelength of approximately 10 nm observed for the modulated structure. If, however, due to large specimen dimensions, a low cooling rate, or a high Ms temperature, all the carbon atoms are segregated to lattice defects during the quench, then the occurrence of a modulated structure upon aging is highly improbable. The lack of the modulated structure in those particular conditions has been attributed to the absence of hardness and resistivity peaks during aging of low and medium plain carbon martensites. Speich did record however a small increase in hardness (40 Hv), but no increase in resistivity, after aging one hour at 100°C. Unfortunately no explanation for this behaviour was given [12]. Therefore, in the case of low Ms martensite, both phenomena (carbon clustering *and* carbon segregation to lattice defects) can occur concurrently. Indeed, Cheng *et al.*, in studying the evolution of the lattice parameter with aging temperature and time of a high carbon martensite (5.1 at% C or 1.1 wt% C) deduced from the decrease of the unit cell volume recorded that 0.2 at% C was segregated to lattice defects [48]. The remaining carbon, they argued, followed a clustering/ordering process as

described above. However, as Olson and Cohen stated, the balance between those two phenomena is still not well understood [41].

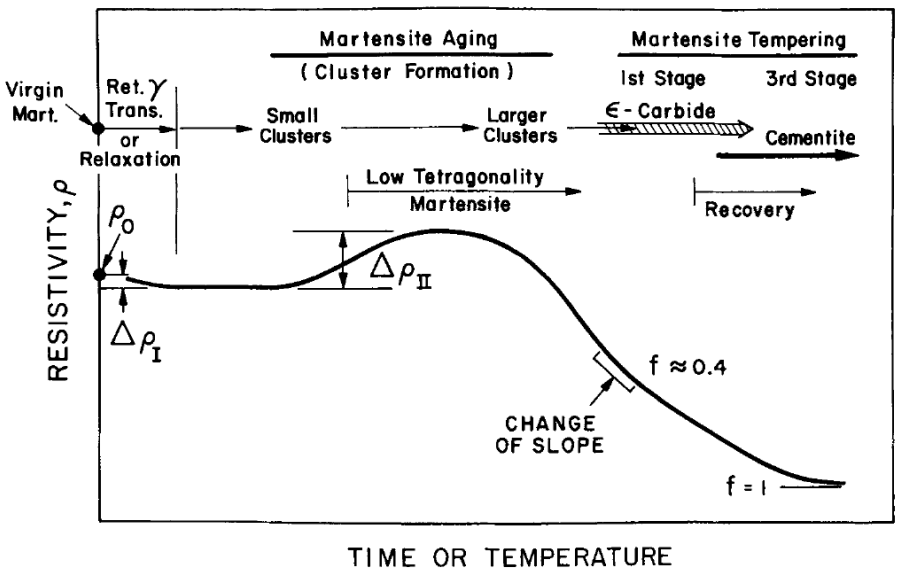

Figure 2.15: Typical resistivity curve obtained on tempering virgin lath or plate martensite. Interpretation of the changes is indicated. From ref [42].

Studies of the kinetics of the aging behaviour described above are scarce mainly because of the rather small scale at which these phenomena occur, and because some overlap can occur, leading to ambiguity when bulk, macroscopic measurements like electrical resistivity or dilatometry are used. On the theoretical side, however, Cottrell and Bilby developed a model for the segregation of carbon to a dislocation [61], for short aging times,

$$f = 3(\frac{\pi}{2})^{\frac{1}{2}}\rho(\frac{ADt}{kT})^{\frac{2}{3}} \tag{2.6}$$

Where f is the fraction of interstitial segregated, ρ is the dislocation density, D is the diffusion coefficient, t is the time, T is the temperature, k is the Boltzmann constant, and A is a parameter derived from the interaction energy between a carbon atom and a dislocation. Harper later generalized

Cottrell and Bilby's result by accounting for carbon depletion in the matrix [62]:

$$f = 1 - \exp(-3(\frac{\pi}{2})^{\frac{1}{2}}\rho(\frac{ADt}{kT})^{\frac{2}{3}}) \tag{2.7}$$

The segregation kinetics, as described by Cottrell and Bilby have been observed by Waterschoot *et al.* in an 0.8 wt% C martensite on aging at 80°C [63]. They also measured an activation energy for segregation close to the value for carbon diffusion in ferrite. There appears to have been no studies of the kinetics of the formation of the modulated structure occuring in martensite.

Transition carbide precipitation

Tempering at a temperature higher than 80°C leads to further changes in the microstructure, the first of which is transition carbide precipitation (also called the first stage of tempering). Sherman *et al.* pointed out that the beginning of transition carbide precipitation overlapped with the end of coarsening of the modulated microstructure [42]. Two different crystal structures have been proposed for transition carbides. Jack proposed a hexagonal structure, which he named *ϵ-carbide* having a stoichiometry of $Fe_{2.4}C$ [64], whereas Hirotsu and Nagakura proposed an orthorhombic structure which they named *η-carbide* [65], having a stoichiometry of Fe_2C. The orientation relationship measured by Jack was:

$$(011)_{\alpha'} \| (0001)_{\epsilon} \tag{2.8}$$

$$(101)_{\alpha'} \| (10\overline{1}1)_{\epsilon} \tag{2.9}$$

And the relationship measured by Hirotsu and Nagakura was:

$$(010)_{\alpha'} \| (110)_{\eta} \tag{2.10}$$

$$[100]_{\alpha'} \parallel [001]_{\eta} \tag{2.11}$$

The stoichiometries proposed above have, however, been questioned in view of more recent atom probe measurements during the first stage of tem-

pering. Olson and Cohen emphasized that there was a continuous evolution of the maximum carbon concentration recorded, from the 10 at% detected in the carbon clusters, to 25 at% found in Fe_3C cementite [41]. The exact structure and range of composition of these transition carbides remains an open question.

Transition from the modulated structure to carbide precipitation

Again, different theories exist in the literature to explain the transition from the modulated structure to the precipitation of transition carbides. Taylor *et al.* suggested that the transition carbides nucleated heterogeneously on the carbon-rich regions formed during the spinodal decomposition [66], whereas Génin proposed that there was an *in situ* transformation of the carbon-rich regions into transition carbides via an ordering of the carbon atoms *inside* those regions [50, 67]. In these studies, no nucleation of transition carbides on lattice defects such as grain boundaries or dislocations was reported, contrary to earlier experimental work where precipitation of transition carbides was seen along dislocation lines [65, 68]. However, in the latter studies, the transition between the modulated structure and transition carbides was not carefully investigated, and it is possible that the precipitation process was already well advanced (microstructures were observed after tempering at 120°C for a minimum of one day), and that some coarsening had already occurred. Moreover, these studies were made on lath martensite (partially twinned) which contains a higher dislocation density than its plate counterpart, and were probably already partially decomposed during the quench. In fact, it is not clear at all whether or not the occurrence of a modulated structure is a *necessary* condition for the occurrence of transition carbide precipitation. One interesting observation made by Hirotsu and Nagakura during the first stage of tempering of a 0.45 wt% C plain carbon martensite, is that precipitation of transition carbides did not happen in the fine laths [68], suggesting that, locally, the density of defects was high enough to trap all the carbon atoms and prevent precipitation. This result shows that in some cases, precipitation can be quite heterogeneous throughout the mi-

crostructure. This constrasts with Taylor *et al.*'s observation that in plate martensite, precipitation of transition carbides is approximately homogeneous [66].

Competition between segregation and carbide precipitation

In contrast to these studies on medium to high carbon martensites, it is now well recognized that below a certain carbon content (0.2 wt% C), tempering high Ms, plain carbon (lath) martensites does not lead to transition carbide precipitation [12, 69, 70], because the dislocation density is usually high enough to trap all the carbon atoms, and because the binding energy between a carbon atom and a dislocation is higher than the binding energy of a carbon atom in a transition carbide [38, 71, 72]. In those steels, the microstructure starts to evolve at higher temperature (around 200°C), where cementite starts to precipitate. However, Barton observed precipitation of transition carbides in a low Ms (-10°C) 25 wt% Ni 0.1 wt% C internally twinned martensite [73] and Sherman *et al.* also observed the aging sequence discussed above followed by precipitation of transition carbides in rapidly quenched high Ms (180°C) 18 wt% Ni 0.1 wt% C lath martensite [42]. Both results suggest that the precipitation of transition carbides is not influenced by the microstructure (lath vs. plate), although some in-depth characterization of the microstructure, and in particular a reliable measure of the defect density, would be required to draw an unambiguous conclusion. If, in Speich's 0.1 wt% C plain carbon (lath) martensite, the precipitation of transition carbide is prevented due to a high density of dislocations (or defects) capable of trapping all the carbon atoms, the same phenomenon should happen in Sherman's 0.1 wt% C lath martensite. The discrepancy between Speich and Sherman *et al.*'s results can only be resolved if one assumes that in Sherman's martensite, the density of defects is lower than in Speich's martensite. According to Kalish and Cohen's theoretical calculations, a dislocation density of 10^{15} m^{-2} can only trap 0.01 wt% C but a dislocation density of 10^{16} m^{-2} is sufficient to trap 0.1 wt% C [71]. Even though a value of 10^{16} m^{-2} for the dislocation density seems possible in mar-

tensite given Speich's electrical resistivity measurements, numerous direct measurements in electron microscopy indicate that the average dislocation density in a 0.1wt% C martensite is close to 10^{15} m^{-2} [30, 74, 75]. In this case the dislocation density should not be able to remove a carbon concentration of 0.1 wt% from solid solution. It must be noted, however, that Kalish and Cohen's theory only considers linear defects (e.g. dislocations), ignoring planar defects such as lath boundaries and twins.

So far, no mention has been made of the substitutional alloying elements. Norstrom showed that, at equal carbon content, the dislocation density was lower in Mn bearing martensite than in plain carbon martensite [75]. The discrepancy mentioned above should be further investigated on this basis.

Speich produced an intriguing observation of resistivity on aging of a 0.4 wt% C plain carbon martensite [12]. On aging at 50°C, the decrease in resistivity was not as steep as in the lower carbon martensites investigated in his study, and unlike the virgin plate martensites, no resistivity peak was observed (figure 2.16). One explanation for this behaviour would be that *both* segregation to lattice defects (which induces a resistivity decrease) *and* spinodal decomposition (which induces a resistivity increase) are active. Upon further tempering, the modulated structure leads to transition carbide precipitation as discussed by Taylor *et al.* [44], and the resulting microstructure consists of a mixture of carbon segregated to lattice defects and transition carbides. Sherman *et al.* also pointed out that segregation to lattice defects should be observed in low Ms plate martensites but, given the resistivity and hardness behaviour of those alloys, this effect should not be dominant in the aging/tempering process [42]. The fact that no hardness peak upon aging is observed in plain 0.4 wt% C martensite seems to indicate that the strengthening due to the spinodal decomposition is balanced by a softening of some kind.

The four stages of tempering

Tempering is commonly separated into four stages, each stage being associated with a particular phenomena. As summarized in table 2.1, the first

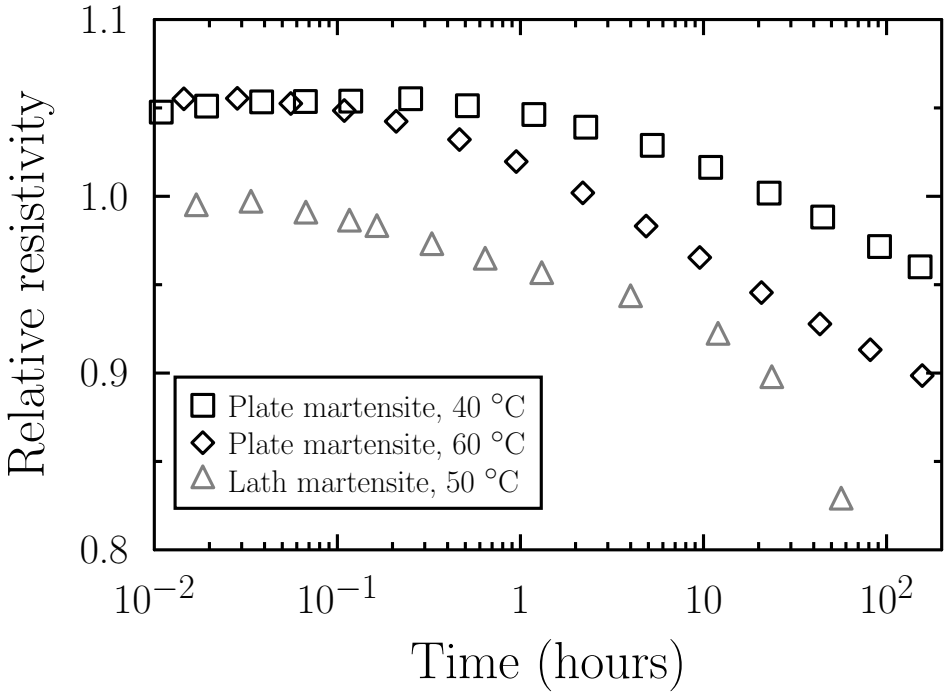

Figure 2.16: Relative resistivity curves measured at 77 K, as a function of time at indicated temperature for as-quenched plate and lath 0.4 wt% C martensites. The relative resistivities above one for the plate martensites indicate that the beginning of the spinodal decomposition occured during heating of the samples. Reproduced from ref. [12] and [44].

stage of tempering is associated with the precipitation of transition carbides, the second stage is associated with the decomposition of retained austenite into ferrite and cementite, the third stage is associated with the precipitation of cementite, and the fourth stage is associated with the coarsening of cementite, the recovery of the dislocation substructure, and eventually recrystallization of the ferrite.

Kinetics of the first stage of tempering

The kinetics of the first stage of tempering have been studied in detail by Cohen and co-workers [69, 76]. The activation energy measured was found

Tempering stage	Phenomenon	Temperature Range
A1	Cluster formation + segregation	-60°C - 0°C
A2	Ordering + segregation	0°C - 80°C
T1	Precipitation of ϵ or η-carbides	80°C - 150°C
T2	Transf. of retained γ	150°C - 250°C
T3	Precipitation of θ	150°C - 700°C
T4	Coarsening, recovery, recrystallization	400°C - 700°C

Table 2.1: Stages of aging and tempering in ferrous martensites.

to be higher than the activation energy for carbon diffusion in iron (110 kJ/mol, compared to 84 kJ/mol in iron) and the time exponent was found to be about 1/3 [76]. Hillert later pointed out that the activation energy for carbon diffusion in martensite should be higher than in ferrite due to tetragnoality induced by the carbon atoms [40]. The same activation energy and time exponent were found by Waterschoot *et al.* on tempering of an 0.8 wt% C martensite [63].

Transformation of retained austenite

As mentioned earlier, the martensitic transformation is rarely complete, and some retained austenite is often present between the laths. Upon tempering at 200°C or higher, the retained austenite transforms into ferrite and cementite. This stage is known as the second stage of tempering. Sarikaya *et al.* [21] were able to observe the decomposition of retained austenite into ferrite and cementite, with various tempering times at different temperatures. Using X-ray diffraction, they followed the kinetics of the reaction and found that the transformation was complete after 1 hour at 250°C. An investigation of the same kind was performed by Horn and Ritchie on a silicon-modified 4340 martensitic steel [77]. After quenching the material in oil at room temperature, the material contained 6% of retained austenite. After a tempering at 500°C for one hour, all the retained austenite had transformed. Also, the amount of retained austenite in a slowly cooled

specimen was found to be significantly higher (18%).

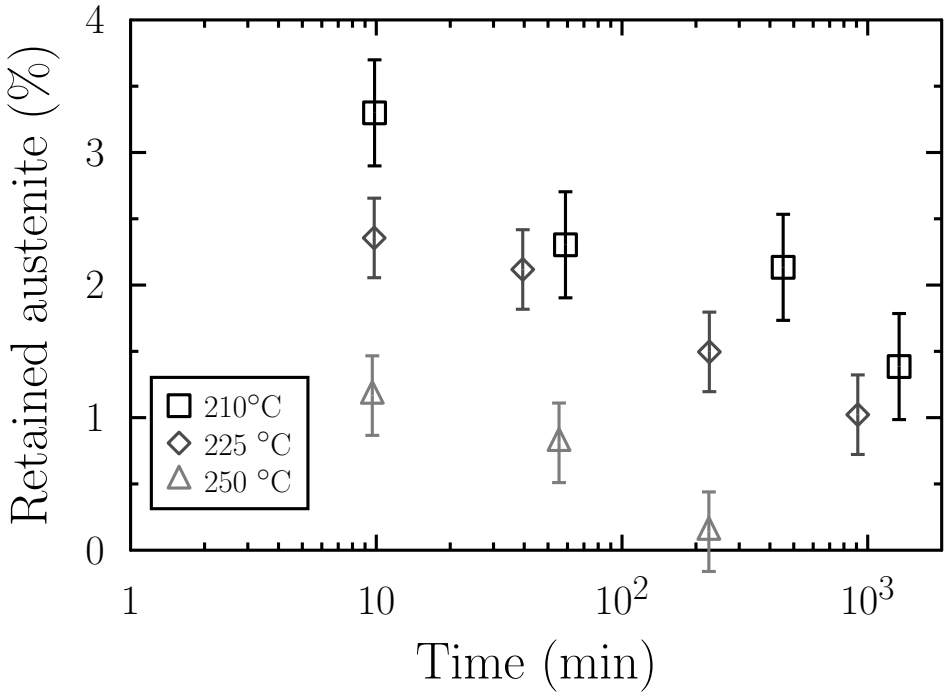

Figure 2.17: Retained austenite volume fraction, measured by X-ray diffraction, as a function of time upon tempering at indicated temperature a 0.3 wt% C lath martensite. From ref. [21].

Precipitation of cementite and spheroidization

Upon further tempering (third stage), the very small transition carbides dissolve, and are replaced by rod-shaped cementite (Fe_3C), which has an orthorhombic crystallographic structure), with a very high aspect ratio. Cementite tends to spheroidize when the time and temperature of tempering are increased. The last stage of tempering leads to the formation of a fine cell structure due to the growth of the laths [78], and eventually to a fully recrystallized structure of equiaxed ferrite and spheroidized cementite.

Role of alloying elements

The possible role of substitutional elements on modifying the defect content of as-quenched martensite was highlighted earlier. Substitutional elements can have other important effects on the process of tempering. Silicon is perhaps the most studied substitutional alloying element as it has often been used to delay precipitation, and particularly the transformation of retained austenite. This has been used to suppress the so-called 'temper embrittlement' encountered in low alloyed martensitic steels [77, 79, 80]. Altstetter *et al.* [80] showed that silicon addition delayed the temperatures at which transformation of retained austenite and precipitation of cementite occur. Transition carbides in alloys containing silicon were found to be stable up to higher temperature [80], a conclusion shared by Miyamoto *et al.* [81]. The latter authors also reported that silicon addition had a significant influence on the growth of cementite, a phenomenon ascribed to the redistribution of silicon atoms between cementite and ferrite.

2.1.3 Effect of plastic deformation on the microstructure of martensite

It has been earlier proposed that the binding energy of a carbon atom to the core of a dislocation can be stronger than the binding energy of a carbon atom in an iron carbide. From this consideration alone, it might be expected that plastic deformation, accompanied by an increase of the dislocation density, should influence the precipitation behavior of martensite. By observing the precipitation behavior of as-quenched (in ice brine) and subsequently deformed (in compression) medium carbon (0.47 wt% C and 0.74 wt% C) martensites, Wilson clearly showed that transition carbide precipitation was inhibited, if not suppressed in certain cases [82]. The distribution of total carbon content between dislocations and precipitates, Wilson noted, depends on the dislocation density, a phenomenon later confirmed experimentally by Breyer and Polakowski who studied a 0.4 wt% C martensite. By using tapered samples, they showed that the amount of precipitation was a function of the amount of plastic deformation, and therefore of the

dislocation density [83].

A physically based model was developed by Kalish and Cohen [71] to quantify this phenomenon. Based on the work of Cochardt *et al.* who calculated the interaction energy of carbon atoms with a dislocation as a function of the distance from the core [84], they estimated that a dislocation density of 2×10^{16} m^{-2} was enough to trap all carbon atoms in steels up to 0.2 wt% C. Since dislocation densities of this order of magnitude have been estimated to exist in as-quenched martensite [12], Kalish and Cohen's model would also provide a theoretical explanation of why ϵ-carbide precipitation is not observed in low carbon (up to 0.2 wt% C) martensites.

Wilson [82], and Stephenson and Cohen [85] also observed the tempering behaviour of martensites that were tempered prior to plastic deformation. In this case, it was demonstrated that re-dissolution of previously precipitated carbides (transition carbides and even cementite in Wilson's case) occurred, either during or after plastic deformation. This possibility is also supported by Kalish and Cohen's theoretical treatment.

2.1.4 Summary: microstructure of as-quenched, aged and tempered martensite

The literature has been surveyed to highlight the current knowledge of the microstructure of as-quenched, aged and tempered martensite. The description of the as-quenched microstructure has been found to be a challenge, since it depends strongly on thermal processing (e.g. cooling rate). Many studies have pointed to microstructural heterogeneities in as-quenched martensite. It has, for example, been reported that finer laths contained a higher dislocation density than larger laths. These differences in dislocation densities could affect the extent of auto-tempering, aging and tempering.

Aging and tempering lead to further modifications of the microstructure. The fine scale processes associated with aging are still not well understood, especially for lath martensite. In particular, it is not known whether the modulated structure forms invariably in lath martensite upon aging. The evolution of the microstructure is more well-understood, although some questions remain. A few studies of the precipitation behaviour of martensite

have highlighted heterogeneities in the tempering process. For example, in low temperature tempered martensites, the fine laths were reported not to contain precipitated carbides, whereas the large laths did contain precipitated carbides.

2.2 Mechanical properties of martensite

In this section, the literature concerning the mechanical properties of ferrous martensite is surveyed. Different aspects of strengthening will be treated, such as grain size strengthening, solid solution strengthening, precipitation strengthening and work hardening. Then, some comments are made on the possible influence of internal stresses on the mechanical response of martensite. Dynamic effects such as dynamic strain aging will also be briefly mentioned. Given that the focus of this thesis is the plastic response of martensite only a brief review of fracture will be given, the reader being pointed to previous reviews on this subject [10, 86].

2.2.1 Lath boundary strengthening

As has been pointed out in section 2.1, the microstructure of martensite is complex, with features existing on a wide range of lengthscales that could impact the bulk mechanical behaviour. Grange [87] showed that the yield strength of a variety of martensitic steels followed Hall-Petch relationship, when the prior austenite grain size was used as the grain size. However, Christian pointed out that this could be an indirect effect since the lath size should depend on the prior austenite grain size as well [27].

The strength given by the microstructure alone is difficult to assess because it is difficult to produce martensite with no carbon by simply quenching the material. However, Vyhnal and Radcliffe were able to produce lath martensite containing no carbon by heat treating the material under hydrostatic pressure [88]. They measured an increase in hardness compared to the same material annealed under atmospheric pressure. This is probably due to the refined lath structure (compared to equiaxed ferrite). This result has been recently confirmed by Kang *et al.* [89]. If one converts the hardness

measurements obtained on these carbon free martensites (218 HV [89] and ≈ 200 HV [88]) into an equivalent 0.2% offset yield stress using Speich and Warlimont's calibration curve [24], the result gives 500 MPa and 430 MPa, respectively. The yield stress estimated in this way is very close to the value obtained by extrapolating the results of Chilton and Kelly [31] and Speich and Warlimont [24] to zero carbon (≈ 415 MPa, as seen in figure 2.18).

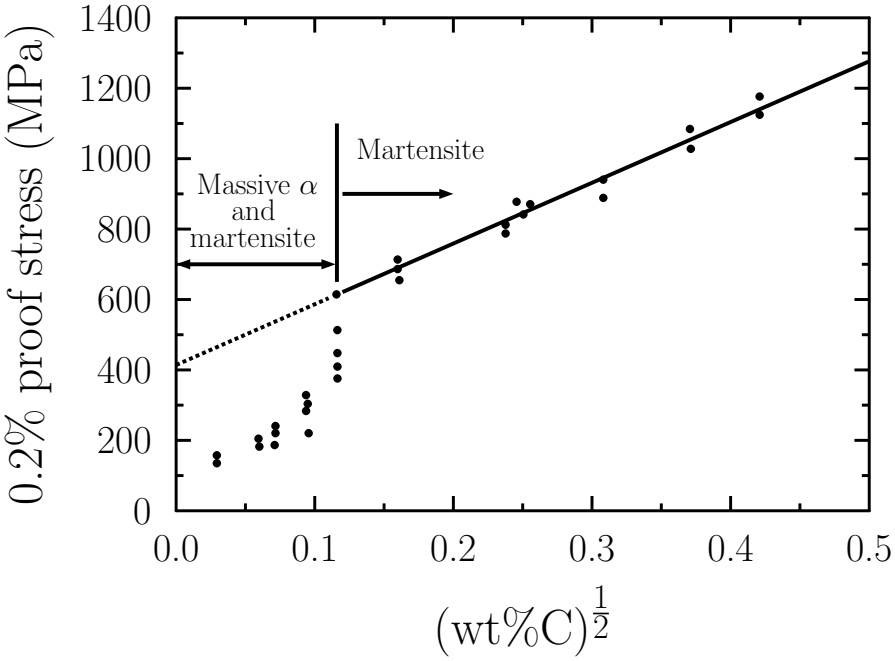

Figure 2.18: 0.2% yield stress, measured at room temperature, of as-quench low carbon lath martensites. For carbon contents between 0 and 0.1 wt%, the quench was not fast enough and the microstructure consisted in a mixture of massive ferrite and lath martensite. Reproduced from ref. [24].

A lath structure can also be produced by shock-loading an Interstitial Free (IF) steel, as demonstrated by Leslie and Sober [90]. In this case, the hardness of the material was 230 HV, a result quite close to those of Vyhnal and Radcliffe [88] and Kang *et al.* [89]. However, the 0.2% offset yield stress measured by Leslie and Sober [90] was somewhat higher (670 MPa, measured

by tensile testing at room temperature) than the approximate value given by the method described above for 'carbon free' martensite. Indeed, the authors pointed out that shock-loaded iron, because of a higher dislocation density and possibly twins, would give an upper limit for the strength of 'carbon free' martensite. Since the dislocation density was, however, not measured by the authors, the additional strength due to the dislocation density could not be assessed.

From the above considerations, the lath structure seems to contribute about 500-600 MPa to the 0.2% offset yield stress of lath martensite. In theory, this result is true only for lath martensite. Nevertheless, Chilton and Kelly's work has shown that, at equal carbon content, the yield strength of martensite is negligibly affected by the nature of the substructure (lath, plate, or a mixed).

2.2.2 Solid solution hardening

Alloying elements such as manganese, silicon and nickel are routinely added to martensitic steels, in small quantities (less than 2 wt%), for various purposes. These combined with carbon in solid solution provide solid solution hardening to martensite. Given the complexity of martensite, on one hand, and the various effects of alloying elements on the other hand, it is often hard to determine precisely the hardening provided by substitutional elements. Moreover, most of the studies on the solid solution in martensite deal with the effect of carbon due to the much larger effect of carbon on a per at% basis compared to substitutional elements. Nevertheless, effects have been reported for substitutional solid solution hardening. For instance, Shih *et al.* observed that adding 1.5 wt% silicon hardened martensite by about 140 MPa [79]. For other elements like nickel, some scatter exists in the literature. For instance, Speich and Swann [91] found that the yield stress increased linearly with the square root of the nickel content, while Radcliffe and Schatz [92] found the hardness of iron nickel alloys quenched into liquid nitrogen to be independent of nickel content over the range 4-33 at% nickel.

The solution hardening of carbon atoms has been extensively studied, several studies showing a linear dependence of the 0.2% offset yield stress to the square root of carbon concentration. This is consistent with the theory developed, for instance, by Fleischer [93]. Speich and Warlimont found the following empirical equation for plain Fe-C martensites [24]:

$$\sigma_y(0.2\%) = 415 + 1725(wt\%C)^{\frac{1}{2}} \tag{2.12}$$

Where $\sigma_y(0.2\%)$ is the 0.2% yield stress and $wt\%$ is the carbon concentration of martensite. A plot of $\tau = 1/2 \times \sigma_y(0.2\%)$ vs. $wt\%C$ gives a slope of approximately $G/15$ (where G is the shear modulus and τ is an estimate of the equivalent shear stress based on $\sigma_y(0.2\%)/2$). This is the value predicted by Fleischer's theory. Nevertheless, this good correlation seems rather coincidental for two reasons. First, the martensite formed in plain carbon steel is probably strongly auto-tempered (giving a non homogenous distribution of carbon atoms) and second, the arbitrary choice of a 0.2% offset, instead of the proportionality limit, to measure the yield stress relies on the crude assumption that carbon in solid solution does not influence significantly the intial work hardening.

One way of reducing (or suppressing) the extent of auto-tempering relies on studying alloys with Ms temperatures below room temperature. Winchell and Cohen designed low Ms temperature martensites with varying carbon content by adjusting the nickel content to obtain a Ms of -35°C for each alloy [13]. They found a linear dependence of the 0.6% yield stress with the cubic root of the carbon concentration, but other workers pointed out that their data could be described with a square root dependence, with a slope between $G/15$ and $G/20$ depending on the testing temperature. In this case, the results are more reliable since the martensites were much more homogenous in terms of carbon concentration.

2.2.3 Hardening by spinodal decomposition

Low Ms martensites in the as-quenched condition should have microstructures that are simpler than those in high Ms alloys. Correspondingly, the

aging phenomenon should also be easier to control. Fe-Ni-C martensites exhibit a strengthening when aged at low temperature to produce the tweed-like structure (introduced in section 2.1.2) [94] by spinodal decomposition. Two slightly different theoretical treatments associated to periodic fluctuations in lattice strain have been developed by Cahn [95] and by Ardell [96] who found the following results (see [43]):

$$\Delta\tau = K_1 A^2 (\frac{\lambda}{\Gamma}) \tag{2.13}$$

$$\Delta\tau = K_2 A^{5/3} (\frac{\lambda}{\Gamma})^{2/3} \tag{2.14}$$

Where $\Delta\tau$ is the increment in shear stress, K_1 and K_2 are constants, A is the compositional amplitude, λ is the wavelength of the periodic strain fluctuation and Γ is the line tension of a dislocation. Thus, the strengthening increases with both the amplitude and the wavelength of the spinodal decomposition, which correlates well the results of Eldis and Cohen [94] (figure 2.19).

Chilton and Kelly [31] also reported a strengthening due to low temperature aging (between 20°C and 100 °C) in low Ms twinned martensite, which qualitatively corresponds to the strengthening observed by Eldis and Cohen [94]. Moreover, they reported that the microstructure, observed by transmission electron microscopy, did not reveal any trace of carbide precipitation prior to the peak hardness, which would suggest that the microstructure was only spinodally decomposed, as in Eldis and Cohen's case. However, high Ms lath martensite was reported not to age harden at all when aging was performed in the same temperature range. Investigation of the microstructure showed that the material was auto-tempered (carbides were present after the quench). This was later confirmed by Speich, although he recorded a small increase in hardness in a 0.18wt% martensite after aging at 100°C for 1 hour [12]. Speich's explanation of this was that in high Ms lath martensite, all the carbon is segregated to lattice defects and is in energetically favorable position, so that no further decomposition is observed during aging at low temperature. The hardness drop measured after tempering at higher

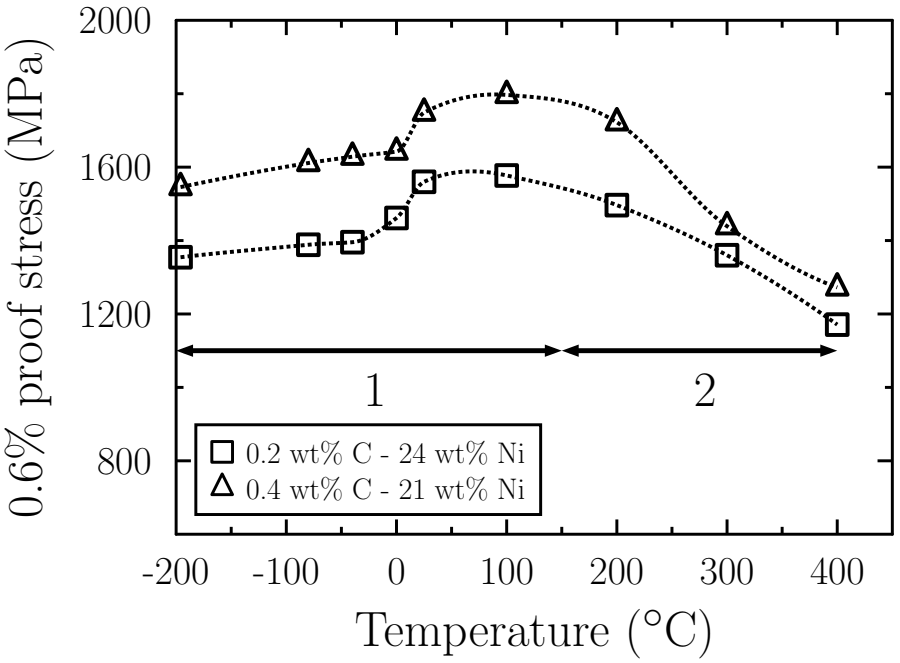

Figure 2.19: 0.6% yield stress, measured at -196°C, after tempering virgin plate martensite at indicated temperature for one hour. Area 1 shows strengthening due to the tweed-like structure, whereas area 2 shows the softening due to precipitation of transition carbides. Reproduced from ref. [94].

temperature corresponds to cementite precipitation.

From these remarks, it can be concluded that spinodal decomposition hardening is unlikely to be a strengthening mechanism in high Ms lath martensitic steels. The resulting strength of the product is therefore a combination of solid solution strengthening (if some carbon is retained in solid solution), the contribution of the substructure (dislocations, lath, twins and grain boundary strengthening) and a strengthening due to precipitation and/or segregation of carbon atoms to lattice defects. The contribution of the latter is extremely difficult to assess, partly because characterizing the extent of segregation requires the microstructure to be observed at the atomic scale, which can be a challenging task.

2.2.4 Precipitation hardening

Precipitation strengthening is a thoroughly addressed topic in materials science, in a variety of systems [96]. The case of tempered martensite has, however, been poorly studied. It appears that no detailed study focusing on the influence of transition carbides on the mechanical properties (yield strength, tensile strength, work hardening) exists in the literature. It is not known, for instance, if the transition carbides are shearable precipitates or non-shearable precipitates, or both (depending on their size).

One exception to the above statement is the work of Malik and Lund [97]. This work aimed at linking the evolution of the 0.2% yield stress with microstructural evolution (e.g. cementite precipitation and dislocation density) during tempering. The mean distance between carbides was measured on transmission electron micrographs on microstructures tempered between 250°C and 550°C. The contribution of carbide precipitation strengthening to the 0.2% yield stress was evaluated using a modified Orowan equation. The evolution of the dislocation density was also measured by X-ray diffraction analysis. The authors found that the evolution of the 0.2% yield stress could be linked to the microstructure (e.g. average carbide spacing L and dislocation density) reasonably well. In their view, no extra contribution of the lath substructure was needed to explain the evolution of the 0.2% yield stress.

The influence of those microstructural features on the work hardening of tempered martensite was, however, not assessed. This remains an open question.

2.2.5 Mechanisms of plastic deformation in martensite

In martensite, both slip and twinning have been observed as deformation mechanisms, the mode of deformation depending strongly on the nature of martensite, i.e. lath or plate. Magee and Davies [9] were able to systematically obtain lath, plate and mixed martensites by varying Ni additions to change the Ms temperature of the alloys. They observed the nature of deformation (at room temperature) by optical metallography on specimens

polished prior deformation, and they drew the following conclusions:

1. In low carbon plate martensites, deformation at room temperature occurs mainly by wavy dislocation slip, although the proportion of twinning in the deformation process increases gradually with carbon content. Above 0.4 wt% of carbon, deformation was reported to occur exclusively by twinning, as also reported by Richman [98],

2. In lath martensite (up to $\sim$ 0.6 wt% C), deformation occurs by dislocation slip,

3. In mixed microstructures with a carbon concentration above 0.4 wt%, deformation occurs by twinning in the lenticular parts of the microstructure, and by wavy slip in the laths.

The above mentioned experiments consisted of observing the surface relief caused by slip bands and/or twins in coarse martensitic crystals on polished specimen surfaces. A more detailed study has been performed by Swarr and Krauss, who studied the structure of deformed (at room temperature) low carbon (0.2 wt% C), lath-type, martensite by means of transmission electron microscopy, both in the as-quenched condition and after tempering at elevated temperature (400°C for 1 minute) [99]. A striking observation was the difference of dislocation arrangement with increasing deformation when the starting state was an as-quenched martensite or a tempered martensite [99]. In the former case, dislocations tended to arrange in cells within the laths, whereas, in the latter case, the dislocations remained more uniformly distributed (the latter result correlates well with the findings of Embury *et al.* on tempered maraging steel [100]). After deformation of the as-quenched specimen, the cell size was observed to be between 20 nm and 140 nm, with an average of 60 nm. As a matter of comparison, the average cell size measured after wire drawing iron to an equivalent strain of 6 was 40 nm [101].

Few studies concerning the work hardening rate of martensitic steels are available in the literature. In most cases, the mechanical properties are characterized in terms of yield strength (measured using an offset strain, typically

0.2%), ultimate tensile strength (UTS) or hardness value. Notable exceptions are the above mentioned work of Swarr and Krauss, and the work of Saeglitz and Krauss, the latter focusing on as-quenched and low temperature tempered martensites containing 0.3 wt% C to 0.5 wt% C [102]. A general feature of their results is the continuous nature of the stress-strain curve (figure 2.20), a feature also observed in 'carbon free' martensite obtained by shock loading IF steel [90]. In all the conditions investigated by Seaglitz and

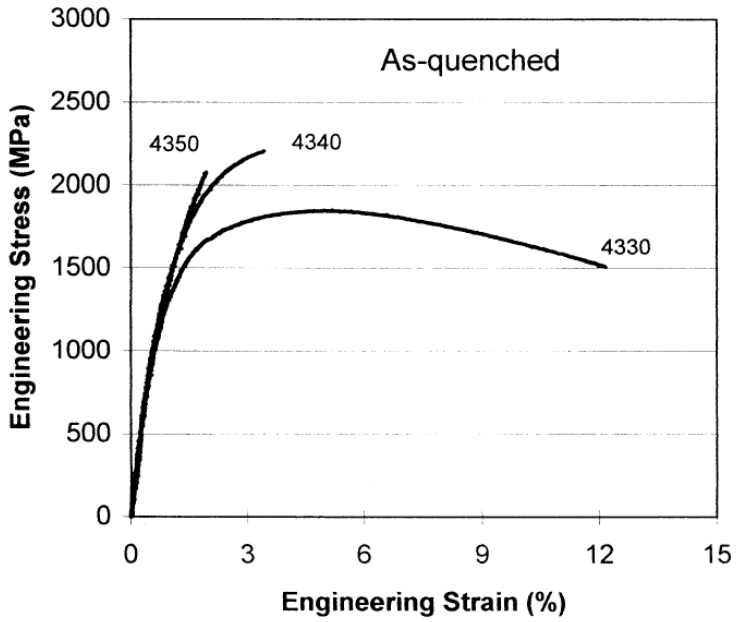

Figure 2.20: Engineering stress-strain curves of 3 martensitic steels, as-quench (in oil), containing 0.3 wt% C (4330), 0.4 wt% C (4340) and 0.4 wt% C (4350), from ref. [102].

Krauss, the work hardening rate was an increasing function of the nominal carbon content of the steel (figure 2.21). Full analysis of the effect of carbon in solid solution on the work hardening rate in the as-quenched specimens was prevented due to the fact that high carbon martensite (with carbon content above 0.5 wt% C) fails in a brittle fashion at room temperature, with no apparent plastic deformation. For a given tempering treatment the higher work hardening rate in specimens of higher nominal carbon content was at-

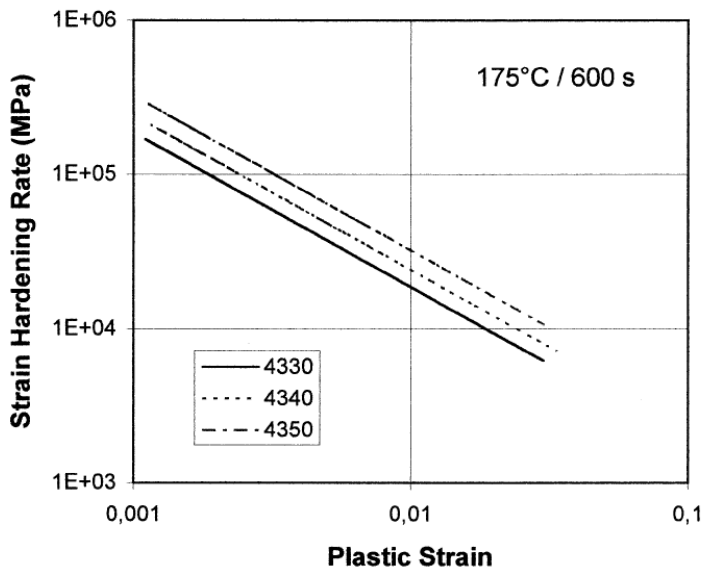

Figure 2.21: Work hardening rate as a function of strain for specimens tempered at 175°C for 10 minutes, from ref. [102]. Note the logarithmic scales.

tributed to a reduction of the dislocation mean free path via an increase in the transition carbide density. The work hardening rate was found to vary exponentially with strain in all cases, highlighting the parabolic nature of the stress-strain curve. For a given chemical composition, increasing the tempering treatment (temperature and/or time) decreases the work hardening rate, an effect which was attributed to the coarsening of transition carbides (hence increasing the dislocation mean free path). Since some carbon remained in solid solution after low temperature aging, the possibility of a contribution due to dynamic strain aging was proposed, but no estimation of this contribution, nor further study on the subject was made.

The 'roundness' of the stress-strain curve, revealing the absence of a marked yield point, has been attributed to a complex set of internal stresses induced by the quenching process and the phase transformation [90, 103]. Muir *et al.* showed that the elastic limit (or proportional limit) of quenched

and low tempered martensitic steels was significantly lower than the 0.2% yield strength of the material [103]. However, they remarked that the elastic limit of the material gradually increased with tempering temperature, as seen in figure 2.22. They interpreted this result as an effect of internal stress relaxation during tempering. Zaccone and Krauss, on the other hand, argued that stress-induced transformation of retained austenite contributes to the low elastic limits recorded in low alloyed martensitic steels [104].

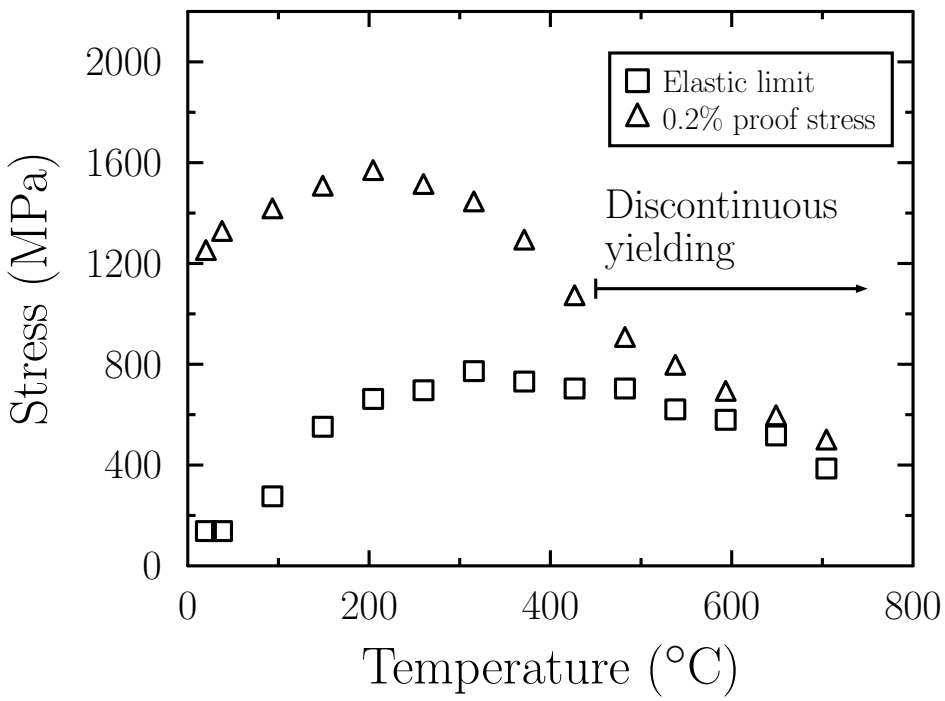

Figure 2.22: Elastic limit and 0.2% yield stress of a low alloyed 0.4 wt% C martensite as a function of tempering temperature, with a holding time of one hour. Reproduced from ref. [103].

However, neither Muir *et al.* nor Zaccone and Krauss discussed the importance of specimen size in this regard. Both groups used large specimens (6 mm in diameter), so that gradients of microstructure, due to gradients of cooling rate between the outer surface and the center of the specimens, could also have a significant effect on the apparent elastic limit. Indeed,

Snyder [37] observed by X-ray diffraction that the surface of large samples quenched from austenite to form martensite were in residual tension, the core being in residual compression (see figure 2.23). Snyder also found that those macroscopic residual stresses were relaxed after tempering one hour between 200°C and 500°C. The relaxation was the highest after tempering at the highest temperature.

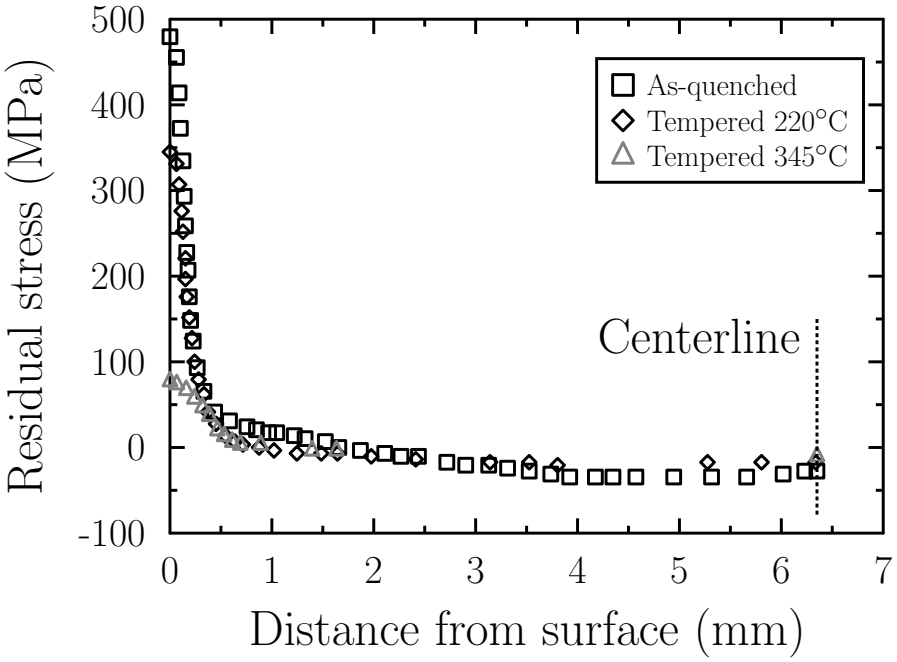

Figure 2.23: Residual stresses as a function of distance from quench surface in a 0.9 wt% C martensite, for different tempering temperatures (tempering time was one hour). Reproduced from ref. [37].

Other studies available in the literature have suggested the existence of quenched-in internal stresses in martensite. Balliett and Krauss [105] and Taylor *et al.* [66] observed significant stress relief on the surface of pre-polished specimens, after tempering at low temperature (between 150°C and 200°C). Those experiments show that internal stresses were present in the as-quenched martensite, and that low temperature tempering could relax them.

Optical microscopy investigation of the surfaces showed that the scales involved in the stress relief process were similar to the plate thickness. This showed that internal stresses existed between plates of martensite. Brown *et al.* [106] also demonstrated that stresses could be relaxed after low temperature tempering. However, no study was performed to measure those internal stresses.

2.2.6 Internal stresses

One way to observe internal stresses is by performing Bauschinger tests [107]. The asymmetry between the forward and reverse flow curves gives a measure of the magnitude of internal stresses [107].

Although several researchers have mentioned the possibility that significant internal stresses may exist in martensite [25, 66, 90, 106, 108], no in-depth study has been proposed to assess them. Vicente Alvarez *et al.* [109] tried to measure internal stresses in martensite using strain reversal (Bauschinger) tests, but their analysis was done on highly tempered martensite (at 685°C for 20 minutes). The microstructure of this material was closer to a mixture of ferrite and cementite than to the tempered martensite of interest here [110]. Yan also proposed a study of the Bauschinger effect in spring steels [111], but the microstructures of the material tested is unclear, and the Bauschinger results are difficult to rely on.

2.2.7 Effect of dynamic strain aging on work hardening

Another contribution to work hardening could come from dynamic effects such as dynamic strain aging. The importance of this effect can be revealed by varying the strain rate in mechanical testing. Leslie and Sober did an extensive study on the strength of ferrite and (lath) martensite, varying the composition, temperature and strain rate [90]. In as-quenched martensites containing between 0.1 wt% C and 0.3 wt% C, they did observe a negative strain rate sensitivity at room temperature, and below a critical strain rate that appeared to depend on the nominal carbon content. Above this critical strain rate, the strain rate sensitivity was positive. However, for an unknown

reason, the strain rate sensitivity of the 0.4 wt% C martensite was null at room temperature (but, as put forward by the authors, the scatter in the mechanical properties was greater in this case). Below room temperature, the strain rate sensitivity showed two distinct regimes in all cases: it was close to zero at low strain rates, and slightly positive at larger strain rates (above 10^{-3}-10^{-2} s^{-1}). Leslie and Sober's results emphasized the non negligible contribution of dynamic effects (Snoek ordering or Cottrell locking) to the total strength of as-quenched martensite, at room temperature. This contribution was roughly estimated as lying between 200 MPa and 280 MPa, independantly of the nominal carbon content (see table 2.2). However, this value might be a lower bound estimate of the dynamic effects since in the high Ms commercial steels tested most of the carbon atoms are segregated to static dislocations [112, 113]. For instance, in analysing the dynamic effects in a high Ms, auto-tempered, commercial martensite containing 0.2 wt% C, Owen and Roberts found that it behaved like a low Ms, virgin 0.08 wt% C martensite (obtained in the Fe-Ni-C system) [112]. However, no clear explanation was provided in regards to the change in strain rate sensitivity (from negative to positive) as the strain rate was raised.

AISI 4310 (MPa)	**Component**	**AISI 4340 (MPa)**
620	Fine structure	620
205	Dynamic strain aging	205
345	Work hardening	240
	Segregation of C atoms during the quench	760
	Solid solution	415
1170	0.2% offset yield strength	2240

Table 2.2: Phenomena contributing to the strength of a 0.1 wt% C (4310) and a 0.4 wt% C (4340) as-quenched lath martensite, according to Leslie and Sober [90].

The negative strain rate sensitivity was shown more accurately in low Ms, 'virgin' martensites with both lath [112, 113] and plate [114–116] mi-

crostructures, where the complexity due to auto-tempering does not arise (figure 2.24). As several authors have pointed out, it is striking to note the

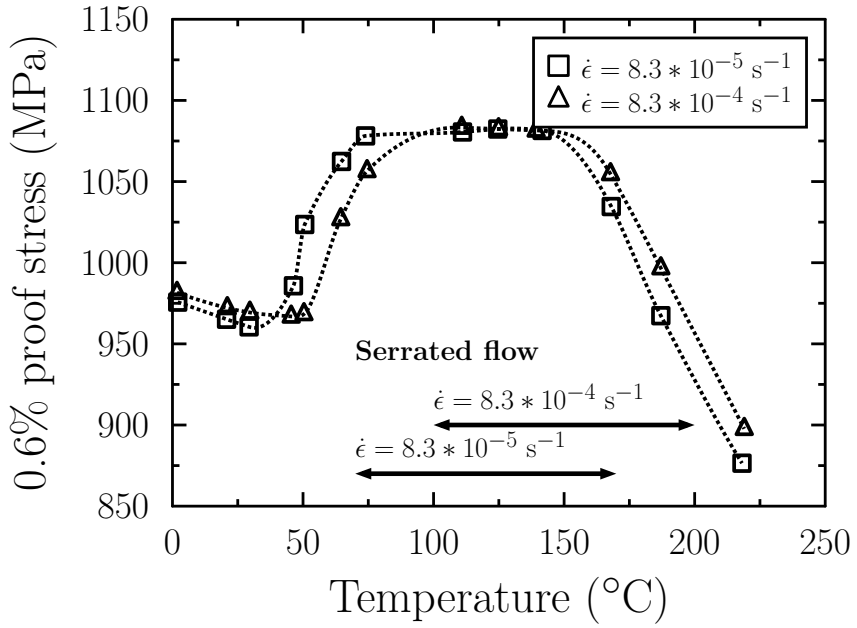

Figure 2.24: 0.6% yield stress of a virgin 0.18 wt% C martensite as a function of temperature for two different strain rates. The temperature range where unstable flow occurred is indicated. Reproduced from ref. [113].

continuous character of the stress-strain curve of martensitic steels, even in a range of temperatures where the material exhibits negative strain-rate sensitivity [90, 108, 113]. Indeed, jerky flow (characteristic of Snoek ordering) is never observed in martensite, although a Snoek peak is detected, at around 220K, in internal friction experiments [117–119]. This temperature corresponds well to the onset of Snoek ordering in the static strain-aging experiments mentioned earlier. The reason for the non appearance of a macroscopic effect (jerky flow) due to Snoek ordering similar to what is observed in α-iron, for instance, is not well established. Presumably, quenched-in internal stresses could mask the effect and induce the observed continuous stress-strain curve [90]. Nevertheless, in support of the view that dynamic

Snoek ordering does contribute to the strength of martensite at low temperature (i.e. at or below room temperature), Hyspecká *et al.* showed that experimentally determined strain-rate sensitivities are in accordance with theories developed by Eshelby [120] and Schoeck and Seeger [121].

At fixed strain rate, as the the testing temperature is raised, serrated flow, induced by Cottrell atmosphere drag on the moving dilocations, occurs. This phenomenon seems to be present in virgin lath and plate martensites [112, 115], and in commercial auto-tempered low-carbon martensite [122], although differences between the two kind of martensites were detected and attributed to auto-tempering during the quench [112]. As highlighted by Owen and Roberts [112, 113], the onset of serrated flow depends on the strain rate and on the testing temperature, and the activation energy associated is close the the activation energy for carbon diffusion in ferrite.

2.2.8 Fracture of martensite

The mechanisms of fracture of martensite have received broad attention over the years, especially in regards to the so-called temper embrittlement phenomenon [20, 21, 77, 123–126]. The treatment of such a phenomenon lies beyond the scope of this study. However, we will draw attention to the mechanisms controlling fracture in as-quenched and low temperature tempered martensite. Since review papers summarizing abundant data on the subject are available [10, 86], we choose to highlight only some of the key ideas.

It is generally admitted that increasing the carbon content in martensite increases its sensitivity to quench embrittlement. Martensites containing more than 0.5 wt% C are brittle at room temperature in the as-quenched state [10, 108]. Those martensites present intergranular (along the prior austenite grain boundaries) fracture surfaces, and fail before any plasticity can occur [10]. The sensitivity to quench embrittlement has been linked to cementite precipitation on the austenite grain boundaries, which occurred either during cooling from austenitizing temperature during the heat treatment, or during the austenitization itself. The negative effect produced

by increasing the phosphorous content has been explained by the capacity of phosphorus to enhance cementite precipitation. Therefore, phosphorus was seen to have an indirect effect on the quench embrittlement sensitivity of high carbon steels [10]. However, as pointed out by Bandyopadhyay and McMahon, precipitation of cementite must not be the only reason for embrittlement in martensite [126]. Indeed, it seems that both precipitation of cementite *and* segregation of impurities such as alloying elements might be responsible for a decrease in cohesive strength of prior austenite grain boundaries. Varying the alloying elements in a 0.4 wt% C alloy, the authors showed a clear decrease of the fracture strength in bending test with increasing content of manganese, silicon, phosphorus and sulfur. This result suggests that, in addition to cementite precipitation, segregation of impurties during austenitizing also weakens the cohesive strength of austenite grain boundaries. This effect has also been suggested as one of the controlling mechanisms by Horn and Ritchie in relation to temper martensite embrittlement, where the material exhibits intergranular fracture [77]. Furthermore, Ritchie *et al.* have shown evidence of a loss of ductility (and toughness) in as-quenched 4340 martensite after austenitizing at 1200°C, step cooling to 870°C, and oil quenching, compared to the same material austenitized at 1200°C and quenched directly in oil [127]. Ritchie *et al.*'s result seems to account for detrimental effects of segregation of impurities during austenitizing on the mechanical properties of the material.

Below 0.5 wt% C, and for tempering treatments that do not lead to temper embrittlement, martensites are ductile at room temperature, although, in the case of an as-quenched 4340 martensite, signs of brittleness have been observed (fracture before necking in uniaxial tension and cleavage facets on the fracture surface) [102]. This observation was associated with dynamic strain aging [102]. However, full ductility was recovered after tempering at low temperature (150°C and above). Lower carbon martensites were fully ductile in any case, fracture occurring through the classic process of void nucleation, growth and coalescence [10, 108]. Close investigation of the micromechanisms of fracture revealed the dominent role of second phase particles (distribution, size and shape) in the nucleation of microvoids [10].

2.3 Summary of the literature review

This literature review has highlighted some key points on the microstructure and mechanical properties of ferrous martensite. The microstructure of lath martensite shows a hierarchy in terms of lengthscales. The prior austenite grain boundaries (about 30 μm) encompass packets (about 3 μm) of fine parallel laths (0.2 μm). Within the laths, a high density of dislocations (about 10^{15} m^{-2}) sets another typical lengthscale. In the as-quenched state, most of the carbon is segregated to lattice defects (lath/grain boundaries, dislocations), and the remaining carbon sits in solid solution. This is due to auto-tempering during the quench, an effect which appears to be unavoidable (to some extent), even with high quench rates. Tempering the as-quenched microstructure leads to further modification of the carbon distribution. Segregation to lattice defects is enhanced and precipitation of transition carbides occurs. Further tempering leads to the decomposition of retained austenite and precipitation of cementite.

The mechanical properties are less well-understood. In general, the evolution of the 0.2% offset yield stress, ultimate tensile stress and/or hardness is only qualitatively assessed, and few studies focus on the evolution of work hardening with microstructure. Even though it has been pointed out in a number of studies that internal stresses can contribute to a large part of the high work hardening rate observed, little effort has been dedicated to experimentally evaluate them. In particular, no study dedicated to the measurement of the proportion of kinematic hardening (hardening due to internal stress generation) contributing to the total hardening of the material has been reported in the literature.

Chapter 3

Scope and Objectives

The previous chapter has shown that a fully physical model linking microstructure and mechanical properties does not exist for martensitic steels. It was shown that ferrous martensite exhibits a high rate of work hardening but to date the mechanisms controlling this are not well understood.

The objective of this project has been to model the work hardening response of martensitic steels for low strain rate, room temperature deformation. In this work, as-quenched and quenched and tempered 0.4 wt% C martensite has been studied. Tempering has been used to vary the carbon in solid solution, carbon segregation to defects and carbide precipitation.

The microstructure has been quantified (particularly at the nanometric scale) and an attempt has been made to model the carbon redistribution occurring on tempering with a focus on carbide precipitation. The mechanical properties have been measured in torsion testing on tubular specimens. In addition to monotonic torsion tests, strain reversal torsion tests have been performed to quantify the Bauschinger effect. Both types of test were used to validate the underlying physical assumptions of the work hardening model developed in this work.

This project is part of a larger collaboration on developing strong, ductile martensitic steels and involves strong collaborations with the ArcelorMittal Global Research Centre in France (electron back-scattered diffraction experiments), McMaster University (transmission electron microscopy char-

acterization) and the Université de Rouen (three dimensional atom probe tomography observations).

Chapter 4

Experimental Methodology

Pop art is for everyone.
— Andy Warhol

This chapter describes the key experimental techniques used in this thesis. First, the material studied as part of this thesis is presented. Next, sample design, mechanical testing and heat treatment procedures are discussed. Finally, a brief description of the tools used for microstructure characterization are described.

4.1 Materials studied

A 300M (silicon modified) steel (see chemical composition in table 4.1) was used in this thesis. This steel contains 1.67 wt% Si compared to 0.3 wt% Si found in the standard 4340 alloys. As silicon strongly affects precipitation kinetics its addition is important for interpreting the microstructure evolution observed in this work. Given the chemical composition of this alloy, it has an expected Ms temperature of 290°C [15], and upon quenching to room temperature it is expected to contain $\sim 5\%$ retained austenite [12].

The 300M steel was received from Goodrich Canada in the form of a wrought cylinder having the dimensions of 25 centimeters in diameter and 50 centimeters in length. The material is zone refined and thus contains low impurity levels and high chemical and microstructural homogeneity in the

as-received state.

C	Mn	Mo	Cr	Ti	Ni	Nb	Si	Al	V	Fe
0.39	0.65	0.34	0.72	0.002	1.75	0.007	1.67	0.1	0.06	bal.

Table 4.1: Chemical composition of the 4340-300M material (wt%).

Because of the importance of the Ms temperature in this work, a dilatometry experiment was performed to experimentally measure it. The Ms temperature measured this way (see appendix A) was 282°C.

4.2 Sample design

4.2.1 Introduction

Significant effort was expanded to develop a highly controlled method for the preparation and testing of samples in this thesis. As was shown in chapter 2, most of the mechanical property testing on martensitic steels has been by tensile, compressive of hardness testing. The first two test methods require relatively large cross sections that can lead to temperature and cooling rate gradients across the width and/or thickness of the sample. This can lead to undesirable variations in the microstructure (due to auto-tempering) and type I internal stresses [37]. Tensile tests are further limited by the onset of tensile instability (necking). Hardness measurements give no information on the work hardening response of the material.

A further consideration in the design of these experiments was the desire to quantify the Bauschinger effect in homogeneous martensitic samples where the effect of the complex martensitic microstructure on the work hardening response could be assessed. The above features (auto-tempering gradients, residual stresses) would have a strong and undesirable effect on the Bauschinger effect.

For the above reasons it was decided to develop a procedure for performing torsion tests on hollow tubular samples. In this case, tensile and compressive instabilities can be avoided, allowing the straining of the ma-

terial to the point of fracture, and the unambiguous measurement of the Bauschinger effect in strain reversal tests. Moreover, these samples were designed to allow for the production of homogeneous microstructures having a minimum of cooling rate variation within the sample, and a nearly 'virgin' martensitic structure. By performing heat treatment on the thin-walled tubular samples in a Gleeble 3500 thermomechanical simulator, cooling rates of up to 1000°C/s are achievable.

4.2.2 Sample dimensions and mechanical testing

The torsion samples' dimensions were scaled from Lindholm specimens suitable for performing high quality torsion testing [128, 129]. The sample design is represented in figure 4.1. The wall thickness was small enough (0.6 mm) to minimize stress and strain variations across it during torsion testing. To further check this, finite element calculations were performed, as described in appendix B, using a constitutive law that mimicked the mechanical response of a typical quenched and tempered 300M sample. Those calculations showed that the variation of stress across the tube wall increased to a maximum of 16% during the elastic portion of the loading. This variation began to decrease as the material yielded. When the inner tube wall was at a stress of 1800 MPa, for instance, the stress differential across the tube wall was found to be 6%.

The samples were mechanically tested at room temperature in an Instron 8874 servohydraulic tension/torsion machine equipped with Wavematrix control software. Grips with a collet system were designed and adapted to the machine to enhance the alignment between the top and bottom grips. The alignment was checked with a dial gage prior to testing. During a rotation of 30 degrees of the top grip, no more than 0.06 mm of axial displacement was recorded. The tests were run at an angular velocity of 0.05°/s, which gives an equivalent strain rate of approximately $1.3 \times 10^{-3}\mathrm{s}^{-1}$. The samples were held under 0.3 kN tension, equivalent to 20 MPa axial stress. This was done to mimic the conditions of a free end torsion test, since this stress is much lower than the yield stresses observed (2200 MPa) [102].

The resulted torque was recorded during the test and the shear stress was calculated (in MPa) as [129]:

$$\tau_m = 1000 \frac{M\langle r \rangle}{\frac{\pi}{2}(r_o^4 - r_i^4)} \tag{4.1}$$

Where M is the measured torque expressed in N.m and r_o and r_i are the outer and inner radii expressed in mm.

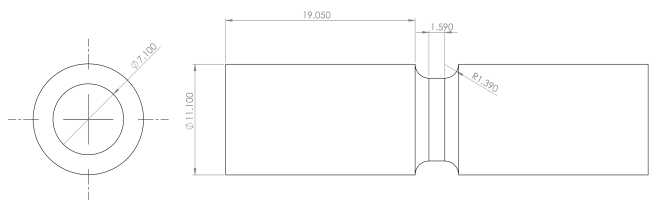

Figure 4.1: Longitudinal cross section of a tubular sample (dimensions expressed in mm).

4.2.3 Strain measurement

The accurate measurement of strain during the torsion tests is a challenge given that the small strain elasto-plastic response is of interest. Due to the finite stiffness of the load frame, the imposed angular velocity was not found to give a highly accurate measure of sample strain. It was therefore decided to use a non-contact measurement technique involving digital image correlation (DIC). A commercial DIC system was used for both image acquisition during testing and for the post processing of the images. The LaVision Davis software [130] was coupled to two synchronized digital cameras having a maximum acquisition rate of 10 Hz. The cameras were mounted on a single rigid rail and brought as close to the sample surface as possible. Lighting was provided by a tungsten halogen lamp mounted on a rig, the height of which could be adjusted. The DIC system was coupled to the torsion load frame by a BNC-BNC cable so as to allow for the synchronization of image acquisition with the imposed stress. In this case the image acquisition was triggered by the load frame and the level of stress at the

point of image acquisition imprinted onto each image. An image acquisition frequency of one hertz was found to provide a good compromise between time for post processing and strain resolution.

DIC has become a relatively widely used technique for the full-field measurement of displacement and strain in two and three dimensions (see [131–133] for a detailed description of the history and state-of-the-art for this technique). The calculation of displacement via DIC involves the quantitative comparison of two images taken before (reference image) and after deformation. These images need to have a quasi-random surface pattern with distinct features that can be easily identified. These images are divided into a regular grid, the grid intersections being the locations where the displacements and strains are eventually evaluated. A square region of pre-defined size is next defined around each grid point in the reference image. This subset of the reference image is then quantitatively compared (via cross-correlation [131]) to boxes of the same size in the deformed image and the correlation between the boxes in the reference image and the boxes in the deformed image are compared to find the box in the deformed image that has the highest degree of correlation with the reference image. The centroid of the box with the highest correlation in the deformed image is then considered to give the displacement of the centroid of the original grid point. This is then repeated for each grid point in the reference image leading to a spatial map of displacement over the sample surface. From this displacement map the strains can be calculated as the gradients of the displacement field.

In the present situation, the surface of the sample is curved and thus a binocular stereoimage technique has been used to obtain displacements on the surface of the sample in three-dimensional space [131]. Calibration of the setup is performed using a regular grid positioned at different distances and angles with respect to the cameras so as to [131, 134],

- rectify the pairs of images
- correct for lens distortion
- triangulate the three-dimensional position of a point from the stereo

projections

Following this calibration, the procedure for computing the displacement and strain at the grid points is identical to that described above. It is important to note that even in the three-dimensional stereoimaging DIC case, displacements are measured only on the surface of the object and thus a full three dimensional strain tensor cannot be calculated.

The practical resolution of the DIC technique for the determination of displacement depends on many parameters, including (but not limited to) the initial calibration, the sample surface quality, lighting and the size of the interrogation region used for performing the image correlation [133]. Thus, while the theoretical resolution of the technique may be sub-pixel, the ability to achieve a specific resolution should be expected to vary from experiment to experiment. With this in mind the experiments were performed here holding the conditions of the experiments as constant as possible.

In the present experiments the goal was to determine the average shear strain in the gauge section of the torsion samples and not to obtain maps of the spatial variation of strain across the sample surface. With this in mind the grid used for the displacement measurements was chosen to be relatively coarse. This provides an advantage in terms of resolving small displacements since a relatively large area around each grid point can be used for performing the correlation between images leading to smaller uncertainty in the correlation [131].

Figure 4.2 shows the grid (red) that was selected for the processing both before and after deformation. The dark/light contrast on the surface of the sample was introduced by first spray painting the surface white then applying fine droplets of black paint using an airbrush. To choose the number of grid points to use for calculating the displacement field, a first calculation was run with a large grid size and the displacement field obtained. The same calculation was performed several times, each time the grid size being reduced until it was found that the displacement field within the gauge section did not change. It was generally found that using $\sim$ 10 to 20 grid points across the gauge section provided a good compromise for the mea-

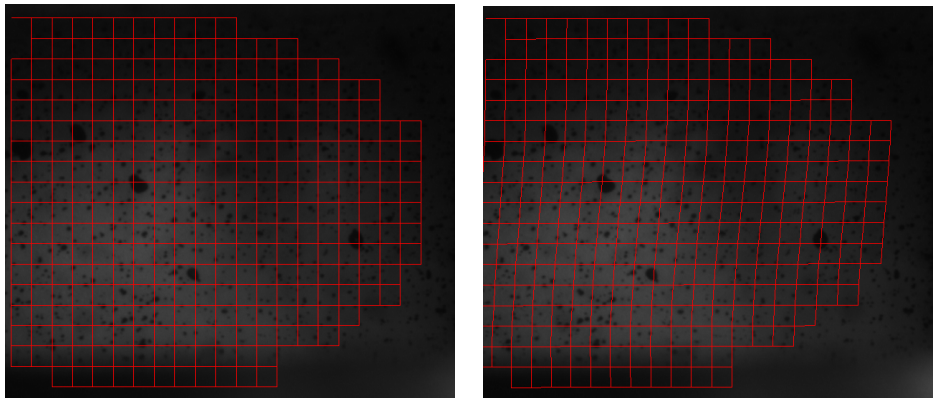

(a) (b)

Figure 4.2: Method used by Davis to calculate the strains from a speckle pattern (continued), d) corrected image with attached undeformed grid (note the coarse window size), e) corrected image with deformed grid, and f) calculated shear strain field. The shear strain is averaged over the area within the black rectangle on f)).

surements. Using fewer grid points led to the region outside of the gauge section influencing the strain measurements within the gauge section. This was clearly seen as no distinct constant displacement/strain region could be discerned along the length of the gauge section. The exact number of grid points selected for the measurements depended on the quality of the random features on the samples and, particularly, the lighting. Providing uniform and equal lighting over the sample surface was challenging in these cases due to the curvature of the sample surface and the short gauge length of the sample. Image processing was applied within the Davis software to reduce intensity variations as much as possible prior to performing the image correlation. From the final displacement map, the strains were calculated over the interrogation volume and average values were calculated from a box containing $\sim 10 \times 5$ grid points at the centre of the gauge section.

To provide a measure of the ability of this technique to achieve high displacement resolution, an experiment was performed where a sample was

loaded elastically and the strains measured using DIC. The resulting elastic loading curve is shown in Figure 4.3. It can be seen that the elastic response is linear ($R^2 = 0.9977$), having a slope $\mu = 79$ GPa. This compares very well against the expected shear modulus of iron, $\mu = 78$ GPa [135] . Moreover, it can be seen that the increment of measured shear strain was $\sim \Delta\gamma = 4.5 \times 10^{-4}$, this providing an estimate of the achievable strain resolution in the measurements made here.

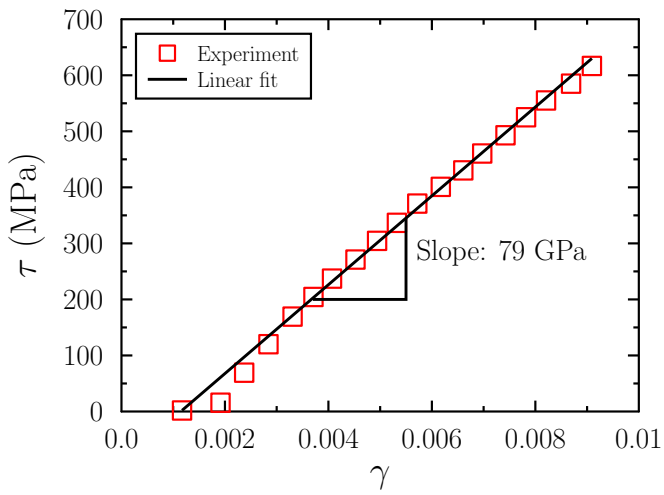

Figure 4.3: Elastic portion of a typical stress strain curve measured on 300M martensitic steel. The strain was measured using the DIC set-up.

To allow for the direct comparison with tension and compression test results, the measured shear stress and shear strain have been reported here as von Mises equivalents,

$$\sigma_{eq} = \sqrt{3}\tau \tag{4.2}$$

$$\epsilon_{eq} = \frac{\gamma}{\sqrt{3}} \tag{4.3}$$

Where σ_{eq} and ϵ_{eq} are the equivalent stress and equivalent strain, respectively, and τ and γ are the shear stress and engineering shear strain, respectively.

Strictly, the conversion of shear stress and shear strain to von Mises equivalent stress and strain should only be applicable within the fully plastic portion of the stress strain curve. However, in this thesis the conversion was made to the whole data-set including the elastic portion of the curve. It is, however, expected that the conversion of the elastic portion of the curve in this way will give results close to the expected response. Converting the elastic behaviour in shear ($\tau = \mu\gamma$) to tension using von Mises equivalent gives $\sigma_{eq} = 3\mu\epsilon_{eq}$, leading to $\mu = \frac{1}{3}E$. This value is only 12.5% larger than the expected value $\mu \approx \frac{3}{8}E$.

As a first check of the technique, the shear strain γ determined by Davis was plotted versus time (see figure 4.4). The figure shows that after a transition regime, the strain rate is constant and is 1.6×10^{-3} s^{-1} in shear, which is close to the theoretical shear strain rate that would be obtained given the dimensions of the sample and the imposed displacement rate (2.2×10^{-3} s^{-1}).

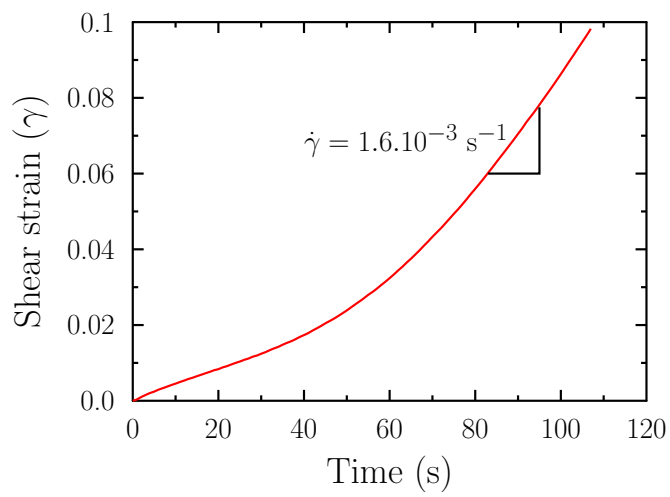

Figure 4.4: Shear strain versus time obtained by digital image correlation.

Finally, a test was performed where a torsion test and a tensile test were performed on the same material and the von Mises equivalent stress-strain curves compared. A tubular specimen taken from a 0.15 wt% C steel was

annealed in the Gleeble (see section 4.3 for details of the procedure) and quenched to obtain a martensitic microstructure. The specimen was tested in torsion up to fracture, and was compared to a tensile test obtained on the same material [1]. To compare the two curves, the shear stress-shear strain curve was transformed into von Mises equivalent stress and strain curve using equations 4.2 and 4.3. As shown in figure 4.5, the results compare well with each other. As expected, the von Mises equivalent stress-strain curve calculated from the torsion test predicts a higher apparent modulus than the tensile test (by approximately 10.8%).

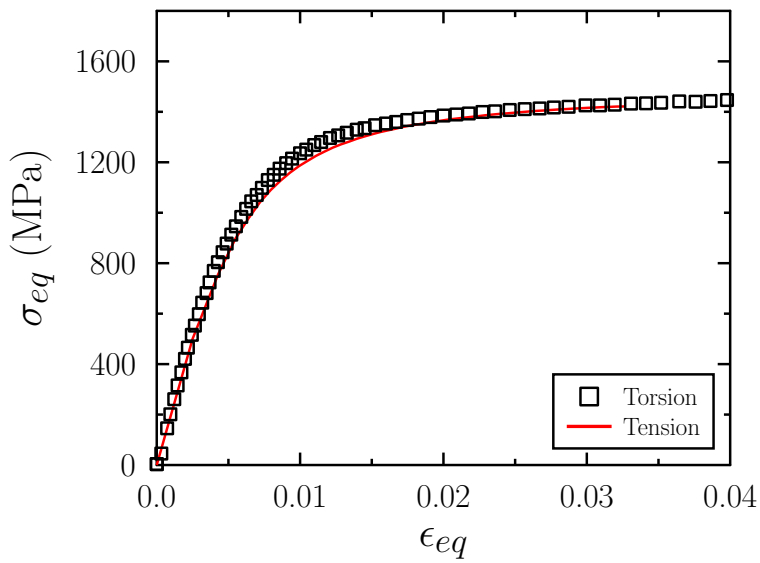

Figure 4.5: Equivalent stress-strain curves of a 0.15 wt% C tested in tension (red curve) and the same material tested in torsion using the system developed as part of this project.

4.3 Heat treatment

As mentioned above, the tubular samples designed for this study were also designed to facilitate the well controlled formation of martensite in the gauge

[1] The tensile data were supplied by Dr. S.Allain at ArcelorMittal Research Centre (France).

section of the samples. Further annealing (aging and tempering) was performed on these samples after quenching. In this section the heat treatment procedures are described.

4.3.1 Formation of martensite via quenching

The ends of the tubular torsion samples were designed so as to fit into the end quench unit of the Gleeble 3500 thermomechanical simulator. To obtain a martensitic microstructure they were heated resistively to 900°C at a speed of 10°C/s, held at 900°C for 5 minutes and water quenched to room temperature by forcing pressurized water through the samples. The heat treatments were performed under high vacuum (the pressure in the chamber was lower than 2×10^{-3} mtorr). The austenitizing temperature and time were chosen so as to avoid excessive grain growth. Metallography following quenching showed the austenite grain size to be about 30 microns. Given the sample wall thickness, this grain size ensured that there were at least twenty austenite grains through the wall thickness. Optical microscopy observations were also used to confirm that there was no sign of decarburization due to this heat treatment.

The quench from 900°C to room temperature was completed in approximately 1.5 seconds, giving an average cooling rate of 600°C/s (see figure 4.6). The cooling rate, however, decreases between the Ms temperature and room temperature.

Due to the resistive heating of samples in the Gleeble, the temperature being controlled only at the centre of the sample, a temperature gradient exists between the centre and the ends of the specimens. To examine this further, the temperature was recorded both on the center of the gauge length of the sample (TC1 in figure 4.6) and on the shoulder (TC2 in figure 4.6). This was done to ensure that martensite was formed over a large portion of the sample. The concern was that softer non-martensitic regions in the grips could plastically deform during subsequent mechanical testing. Figure 4.6(a) shows that during austenitization the temperature measured at the shoulder of the specimen was 870°C, 30°C less than the temperature at the

sample center, but still high enough for the shoulder to be in the austenite region of the phase diagram. Figure 4.6(d) shows that the cooling rate in the shoulder of the specimen was slightly lower than at the center. This was due to the larger thickness of the tube wall at this point. Nevertheless, the cooling rate was high enough to avoid the formation of ferrite during cooling. For all subsequent heat treatments on tubular specimens, the temperature was recorded only at the center of the specimens, and no extra thermocouple was attached to the shoulders.

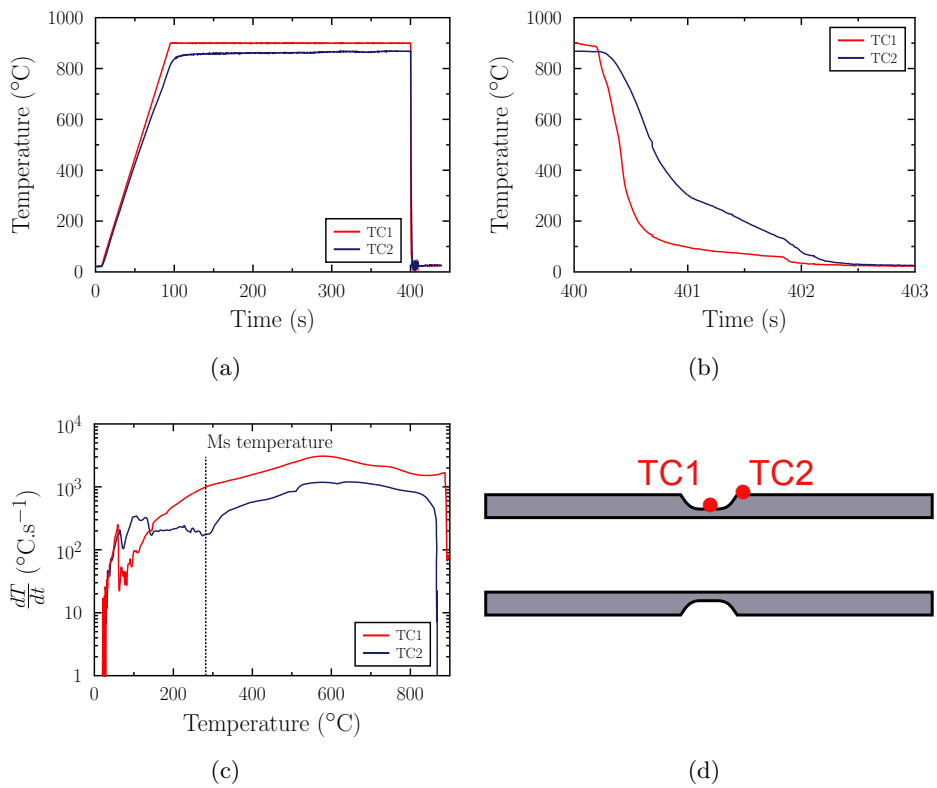

Figure 4.6: Temperature profiles recorded during the heat treatment of a tubular specimen a) full temperature profile, b) close-up to show the cooling rates, c) instantaneous cooling rate (note the logarithmic scale) and d) cross section of a tubular sample showing where the thermocouples TC1 and TC2 were attached.

To confirm the presence of martensite outside of the gauge section, a sample was cut in half along its axis of symmetry and Vickers microhardness measurements were made along the length, with an applied force of 1 kg. The results, plotted in figure 4.7, show that the microstructure is homogeneous, at least mechanically, up to a distance of 4 mm away from the center of the specimen, i.e. it has transformed to martensite on a length sufficient enough for subsequent mechanical testing.

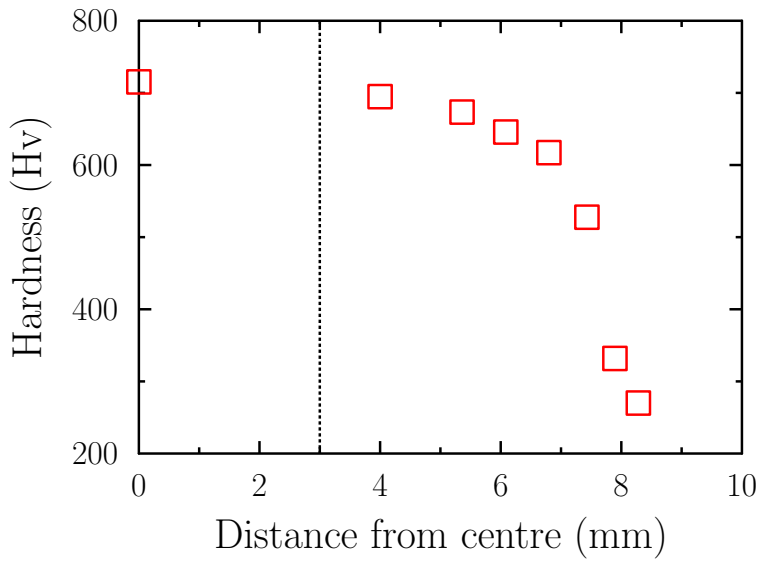

Figure 4.7: Vickers hardness as a function of the distance from the center of the specimen. The edge of the torsion sample's gauge length is at 3 mm from the centre and is indicated by the dotted line.

In order to check the influence of auto-tempering on the mechanical properties of the material, some samples were also prepared after cooling at a slower rate. This was done by replacing water by helium gas as a cooling medium. In this case, the quench was completed in approximately 50 seconds (see figure 4.8), giving an average cooling rate of 18°C/s. As with water quenching the cooling rate drastically decreased below the Ms temperature. Differentiating the temperature-time curves presented in figure 4.8(a) allowed for an instantaneous measurement of the cooling rates

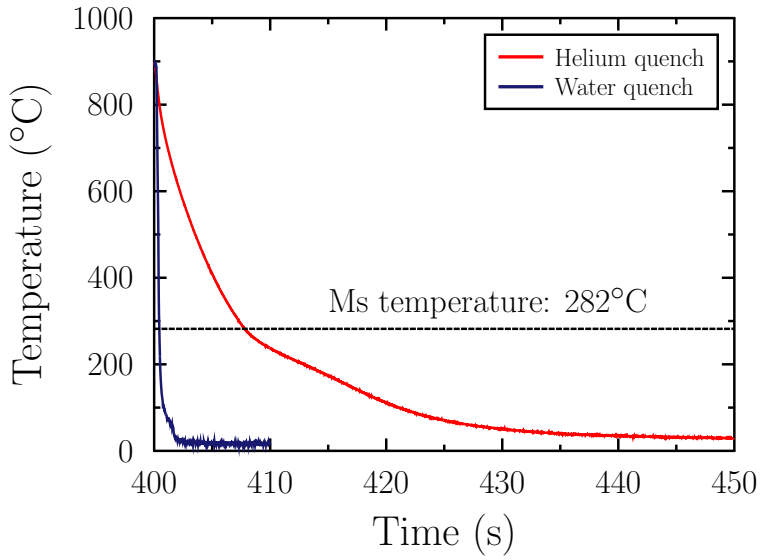

(a)

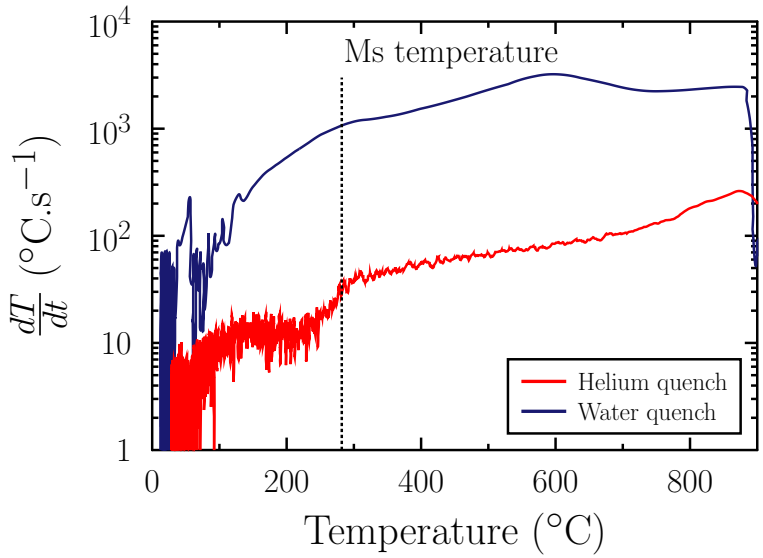

(b)

Figure 4.8: Comparison of the cooling rates obtained with water and helium gas. a) temperature versus time curve, and b) cooling rate versus temperature curve. Note the logarithmic scale in b).

(see figure 4.8(b)). Figure 4.8(b) shows that the cooling rate obtained with helium gas was almost an order of magnitude lower than the cooling rate obtained with water. At the Ms temperature, the cooling rate was 1100°C/s for the water quench and 30°C/s for the helium quench. The average cooling rate between the Ms temperature and room temperature was 150°C/s for the water quench and 9°C/s for the helium quench.

4.3.2 Aging and tempering of martensite

In many cases the as-quenched samples were subsequently aged or tempered at elevated temperature to vary the microstructure. Tempering between room temperature and 200°C was done in a stirred oil bath. The temperature was controlled by a type-K thermocouple, and an extra thermocouple was put into the bath to check the bath temperature homogeneity. The temperature in the bath varied by no more than two degrees centigrade compared to the set temperature.

For tempering at higher temperatures, the specimens were inserted in an atmosphere-controlled tube furnace, where they were tempered under a constant flow of Argon gas to avoid oxidation.

After completion of the heat treatment, in the oil bath or in the tube furnace, the samples were brought back to room temperature by quenching them in water.

4.4 Microstructure characterization tools

In this section the tools that were used to investigate the microstructure are presented, and sample preparation is described. Standard techniques such as electron microscopy (transmission electron microscopy and scanning electron microscopy) and calorimetry were used. Those techniques are common for analyzing metals, and are thus only briefly presented. Three dimensional atom probe tomography has also been used, with the objective of observing microstructure evolution at the atomic scale. Since this technique is less common, the methodology is described in more detail.

4.4.1 Sample preparation

Because it was generally not possible to extract samples for electron microscopy observation directly from the tubular samples, flat samples were prepared from the as-received material. Sheets having dimensions of $100 \times 20 \times 1$ mm^3 were obtained by cold rolling samples of the steel. The strips were annealed in the Gleeble for 5 minutes at 900°C followed by water quenching. The area of the sample where the temperature and cooling rate were homogeneous consisted of a square having dimensions of 15×15 mm^2, located on the center of the strip (see schematic in figure 4.9).

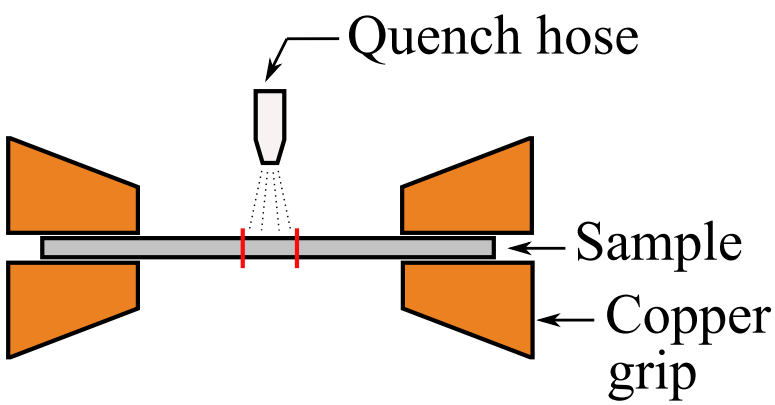

Figure 4.9: Schematic of the set-up used in the Gleeble to anneal the strips. Samples were clamped into copper grips and a quenching system was installed and the hose was fixed so that the quenchant (water or helium gas) hit the sample in the centre during the quench. The area where temperature and cooling rate were homogeneous is delimited schematically by the two red vertical bars.

The cooling rate obtained in this procedure was similar to the cooling rate obtained on the thin-walled torsion samples (see figure 4.10). Figure 4.10(b) shows that the cooling rate at the Ms temperature was lower for the sheet specimen compared to the thin-walled tube (575°C/s compared to 1100°C/s). Below the Ms temperature, the difference in cooling rates decreased until it was approximately zero. This ensured that the mechanical properties could be linked to microstructure observations.

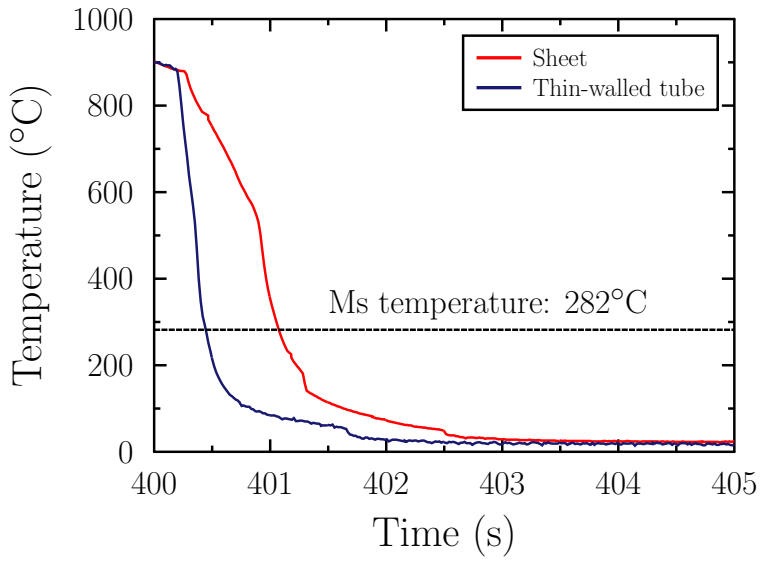

(a)

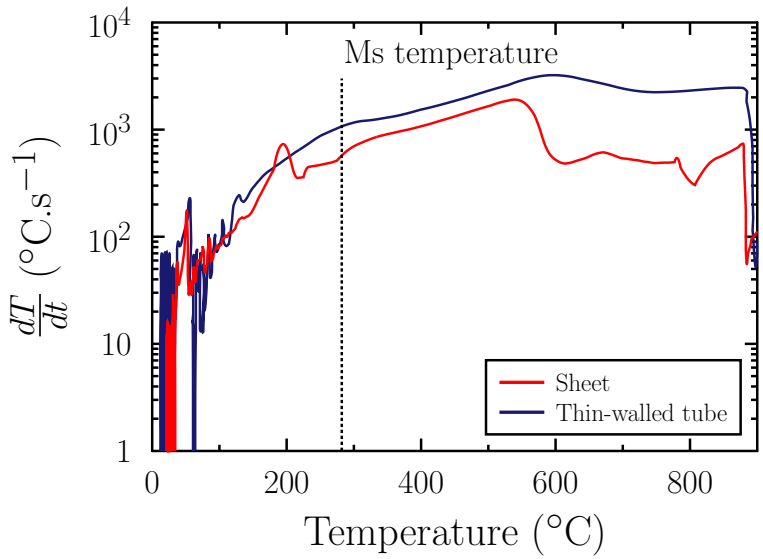

(b)

Figure 4.10: Comparison of the cooling rates obtained on the thin-walled torsion samples and on the sheet samples. a) Temperature versus time, and b) instantaneous cooling rate as a function of temperature.

Samples for calorimetry measurements were extracted from the homogeneous area of annealed sheet samples. Those samples were of dimensions $8 \times 8 \times 1$ mm^3. The time between the quench and insertion into the apparatus chamber was approximately two hours.

For electron back-scattered diffraction analysis, square samples of dimension 10×10 mm^2 were extracted from the homogeneous area of annealed sheet samples following quenching. Because it was not possible to index as-quenched martensite by the electron back-scattered diffraction technique, samples were tempered for four hours at 200°C. This tempering treatment was not expected to modify the microstructural features observable within the resolution limit of the technique (namely, the prior austenite grains, the packets and the laths). These samples were mounted in conductive epoxy and then mechanically polished. The final stage consisted of polishing with a cloth on which a 1 micron diamond solution was deposited. Samples were then further polished using an OPS solution for twenty minutes.

For transmission electron microscopy, specimens were prepared from square samples of dimensions 10×10 mm^2. These were extracted from the homogeneous area of Gleeble heat treated sheets. These were mechanically thinned to a thickness of 100 μm, from the side opposite to the water jet during the quench. This procedure ensured that the samples were taken as close as possible from the surface that saw the maximum quench rate. Discs of diameter 3 mm were then punched, and polished down to a thickness of 60 μm, with 1200 grade polishing paper. The final thinning was performed by jet-polishing using a 10% perchloric acid solution as described in [136]. Between 3 and 6 foils were observed for each condition.

Samples for three dimensional atom probe were also extracted from annealed strip samples, of which square samples of dimension 15×15 mm^2 were cut. Those samples were subsequently thinned down to 0.3 mm in thickness by mechanical polishing. Then, match-like samples of dimensions $0.3 \times 0.3 \times 15$ mm^3 were cut and electropolished to form a sharp needle, with a tip radius of approximately 50 nm, following a method described in [137].

4.4.2 Calorimetry measurements

Calorimetry measurements were made in a Setaram Calvet C80 scanning calorimeter, under atmospheric pressure. The apparatus design prevented the use of a protective atmosphere during the experiments. The sample was heated a first time from room temperature to 280°C at a rate of 2°C per minute, and subsequently cooled back to room temperature. The baseline was determined by reheating the specimen applying the same heating rate [55]. This technique was used to scan the phenomena occurring during tempering.

4.4.3 Electron microscopy

Electron back-scattered diffraction experiments were performed in collaboration with Dr. D. Barbier at ArcelorMittal Research Centre (France). The analysis was performed using HKL Channel 5 software.

Transmission electron microscopy was performed in collaboration with Dr. X. Wang at the Canadian Centre for Electron Microscopy in McMaster University. A Philips CM12 electron microscope, operated under a voltage of 120 kV was used. The samples were analysed by standard imaging procedures and diffraction pattern analysis.

4.4.4 Atom probe tomography

Atom probe tomography experiments were performed in collaboration with Mr. V. Bilyk, and Dr. X. Sauvage at the Université de Rouen (France) [138]. Two different apparatus were used: a regular electric atom probe (referred to as TAP) and a wide angle electric atom probe (referred to as ECOWATAP). The physics underlying the tomographic atom probe technique are described in detail in [139]. Essentially, this technique consists of applying a high difference of potential between a sharp tip and an electrode. The electric field at the tip is given by:

$$E = \frac{V}{\beta R} \tag{4.4}$$

Where E is the electic field, V is the difference of potential, R is the radius of the tip and β is a correction factor taking into account that the tip shape is not a perfect sphere. The voltage signal is pulsed at 2 kHz for the TAP and 30 kHz for the ECOWATAP. The maximum height of the voltage pulses is set so that the electric field is sufficient enough to ionize and evaporate atoms from the surface of the tip. The ionized atoms are accelerated in the electric field and collected on a position sensitive detector. The length between the tip and the detector is known. The nature of the atom hitting the detector is determined by its time of flight,

$$\frac{m}{n} = 2eV\frac{t_v^2}{L^2} \tag{4.5}$$

Where m is the mass of the ionized atom, n its charge, e is the elementary charge of an electron, V is the voltage, L is the tip-to-detector distance and t_v is the time of flight (difference between the pulse time and the time at which the atom arrives on the detector). Equation 4.5 shows that light atoms arrive quickly on the detector after the pulse whereas heavy atoms arrive later on the detector. From the time of flight measurements, a mass spectrum can be determined.

The atom probe experiments were run at 80K. The three dimensional volumes were reconstructed in the same way for all the data-sets, using the GPM 3d Software from the Université de Rouen. The product of the electric field E and β was fixed at 23 V/Å. The projection factor b (see reference [139]) was fixed at 1.6. Also, the atomic volume of iron was fixed at 11.89×10^{-3} nm^3.

A typical mass spectrum is plotted in figure 4.11. The mass spectrum was first analyzed for quantitative measurements of the chemical composition. In some cases, carbon atoms arrived on the detector under the form of clusters of ions [140]. Therefore, extra peaks were recorded. For instance, a carbon peak was detected at a mass over charge ratio of 18. This corresponded to clusters of three carbon 12 [2] with a charge 2+ [140]. Also, it was considered that half of the peak recorded at a mass over charge ratio of 24

[2] carbon 12 designates the carbon isotope having 6 protons and 6 neutrons in its nucleus.

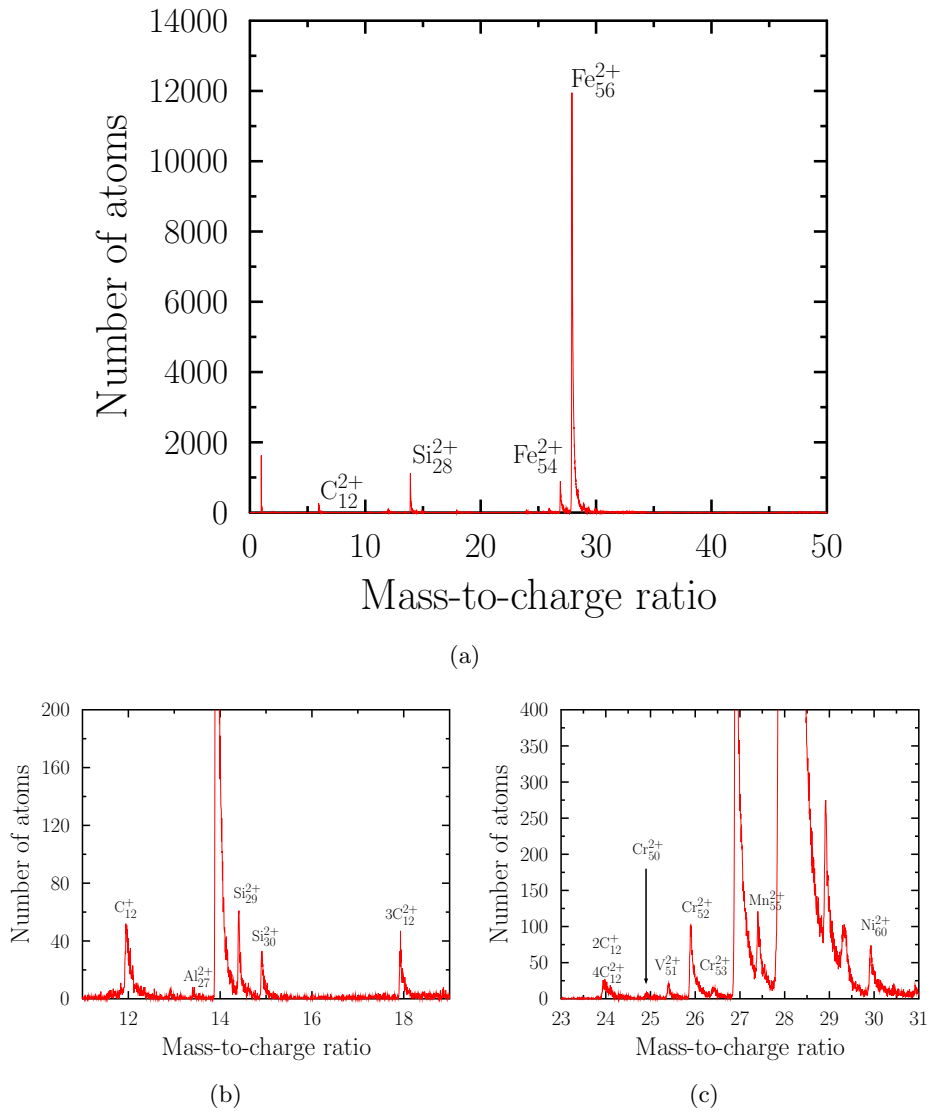

Figure 4.11: Typical mass spectrum recorded during atom probe tomography measurements. a) Global mass spectrum showing major peaks (indicated), b) and c) close-ups to reveal peaks corresponding to other chemical elements.

Isotope	Abundance (%)
Ni_{58}	68.1
Ni_{59}	trace
Ni_{60}	26.2
Ni_{61}	1.1
Ni_{62}	3.6
Ni_{64}	0.9

Table 4.2: Relative abundances of nickel isotopes. The values are used to estimate the contribution of Ni_58 to the Fe_58 peak in the mass spectrum.

was due to clusters of two carbon 12 charged 1+. The other half was due to clusters of four carbon 12 charged 2+ [140]. Therefore, in average, this peak corresponded to clusters of 3 carbon 12. Danoix *et al.* [141] pointed out that this assumption led to less than 10% relative error in carbon composition measurements.

In summary, the total number of carbon atoms detected from peak indexation was calculated as [140, 141]:

$$C_{total} = C_6 + C_{12} + 3C_{18} + 3C_{24} + 3C_{36} \tag{4.6}$$

Where C_{total} is the total number of carbon atoms, and C_x are the number of carbon atoms detected in carbon peaks at a mass over charge ratio of x.

Another difficulty arises from the fact that the peaks of some elements overlap. For instance, the peak for Fe_{58}^{2+} and the peak for Ni_{58}^{2+} are both located at a mass to charge ratio of 29. One can overcome this by considering the natural abundance of the different isotopes. All the peaks of nickel can be indexed, except the one at a mass to charge ratio of 29. The abundances of nickel are indicated in table 4.2. With those values, the number of atoms of nickel contributing to the peak at a mass to charge ratio can be estimated. Then, the nickel composition can be estimated.

4.5 Analysis of atom probe tomography data

The raw data obtained from three dimensional atom probe tomography measurements were specifically analyzed to determine the carbon composition remaining in solid solution, the distance between carbon segregation, the maximum composition in the regions of carbon segregation, and the thickness of carbon rich segregated regions. For early stages of aging (and in the as-quenched material), it was also desired to determine the degree of which carbon in solid solution was distributed randomly in the analyzed volume. In what follows, the methods for determining these parameters are described.

4.5.1 Carbon composition in the matrix

In specimens that showed substantial carbon segregation, it was desired to evaluate, among other parameters, the carbon composition remaining in solid solution. This was done following a careful method to correct the composition measurements by taking into account the noise contribution. According to Sauvage *et al.* [142], the noise contribution strongly affects low composition measurements. The method for removing the noise contribution from composition measurements is explained in this section.

During atom probe experiments, some atoms contained in the low pressure atmosphere were ionized and subsequently detected. Those atoms constituted the noise recorded on the mass spectrum. For instance, in figure 4.11(b), a certain number of atoms were measured to have a mass-to-charge ratio in between the mass-to-charge ratios of Si_{30}^{2+} and $3C_{12}^{2+}$. Those atoms did not belong to the peak corresponding to silicon nor to the peak corresponding to carbon, nor to the peak corresponding to any other element. Inevitably, some atoms belonging to the noise signal were detected in the peaks themselves, causing the composition of the considered element to be slightly over-estimated. This over-estimation was important in the case where the composition of the considered element was small [142], such as carbon. Therefore, it was necessary to remove the noise contribution when attempting to estimate the carbon composition remaining in solid solution.

The number of noise atoms contributing to a single peak could be estimated by counting the number of atoms detected in a similar mass-to-charge ratio interval on one side of the peak considered. This was done by integrating the mass-to-charge spectrum over the 'noise' interval (see figure 4.12). The total number of atoms (noise plus carbon) in the peak was measured by integrating the mass spectra over the interval for carbon (see figure 4.12). The true number of carbon atoms was calculated by subtracting the total number of noise atoms to the total number of atoms. This was done for the five peaks corresponding to carbon atoms. The corrected total number of carbon atoms, calculated with equation 4.6, allowed for a more accurate estimation of the carbon composition.

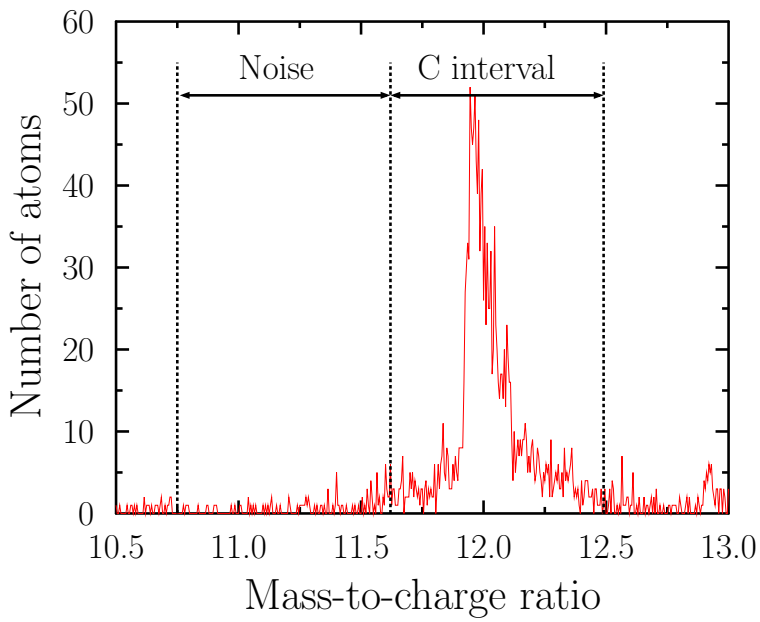

Figure 4.12: Focus on C_{12}^{2+} peak in the mass spectrum presented in figure 4.11(a). The interval over which the spectrum is integrated to estimate the number of noise atoms is indicated. It has the same length as the carbon interval.

Carbon depleted regions were selected visually from the volume analyzed by atom probe. Usually, those regions were located in between carbon rich

regions. The mass spectrum corresponding to the carbon depleted regions was plotted. The carbon composition was estimated after removal of the noise contribution, as discussed previously. A minimum of ten measurements were done for each condition. The carbon remaining in solid solution was determined by averaging all the carbon composition measurements done for a particular condition.

4.5.2 Mean distance between carbon segregated regions

In those samples where substantial segregation occurred, it was also sought to evaluate the mean distance between carbon enriched regions. This was done by isolating at least two enriched regions in the analyzed volume. Then, a linear composition profile was plotted along the isolated volume. This was done by the moving average technique [137]. The composition was measured in a volume 2 nm in length of cross section equal to the cross section of the isolated volume. The small probing volume 2 nm in length was moved by 1 Å and the composition measured again, until the whole isolated volume was scanned. A typical carbon composition profile is plotted in figure 4.13. In this figure, two distances between carbon segregated regions, λ_1 and λ_2, are shown.

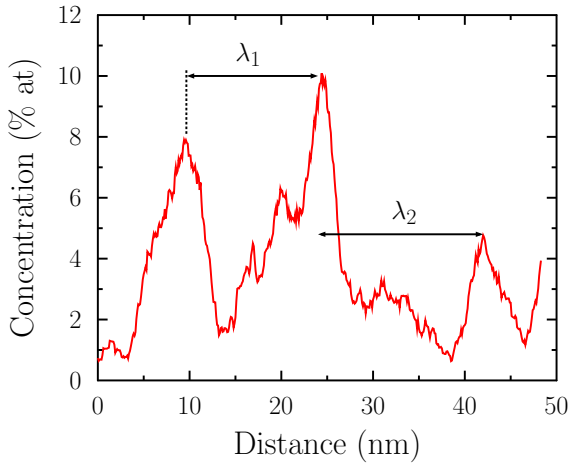

Figure 4.13: Carbon composition linear profile showing three carbon segregated regions.

For each condition where this method was applied, at least 10 measurements were made. The mean distance between carbon segregated regions was estimated by averaging the values determined this way, for a particular condition.

4.5.3 Maximum composition and thickness of carbon segregated regions

The maximum carbon composition in the carbon segregated regions was estimated. This consisted in isolating a single carbon segregated region from the volume analyzed and plotting the linear carbon composition profile, in the manner explained in section 4.5.2. Care was taken to isolate the carbon segregated region so as to be able to plot the linear profile perpendicular to the carbon segregated region. This ensured the evaluation of the maximum carbon concentration in the carbon segregated region. For a particular condition, measurements were done on all the carbon segregated regions that could be isolated. A typical linear carbon composition profile is presented in figure 4.14.

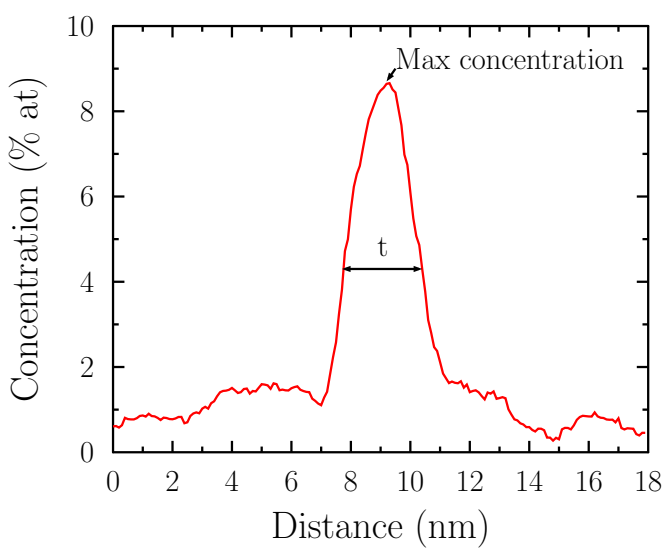

Figure 4.14: Example of a typical linear carbon composition profile obtained across a carbon segregated region.

4.5.4 Statistical analysis

In those conditions where carbon redistribution was difficult to judge, statistical analysis was used to check the homogeneity of the carbon distribution. Representative volumes were selected in a parallelipipedic box with a square section. The box was then sliced into smaller boxes having dimensions of approximately $2 \times 2 \times 2$ nm^3 and the carbon composition was measured in each of these boxes, allowing one to plot the carbon composition distribution in the bigger volume. The carbon composition distribution was compared to a Bernoulli distribution, which represents a perfectly random distribution. The same method was used in [35] to characterize the carbon composition distribution in as-quenched martensitic steels.

4.6 Summary

This chapter has described the tools that have been developed and used to undertake this thesis. A design for heat treatment and mechanical testing of thin-walled tubular samples was developed. The designed samples have been optimized for torsion testing as well as for performing controlled heat treatments to achieve samples having as uniform a thermal cycle as possible. This is a key feature of the experiments performed here. For microstructure observations tubular samples could not be used due to requirements on sample dimensions. In this case, flat samples were used. The cooling rates achieved with both geometries were similar, so that the link between microstructure and mechanical properties could be made.

Chapter 5

Microstructure Characterization of 300M Steel

5.1 Introduction

As revealed in chapter 2 there have been relatively few studies on martensitic steels performed with equal levels of attention to both microstructure characterization and mechanical characterization. In this chapter, the results of microstructure characterization are presented, these results being key to interpreting the mechanical properties in future chapters. Based on the information presented in chapter 2, the microstructural changes occurring during the low temperature aging and tempering focused on in this thesis include:

1. Carbon segregation and redistribution
2. Carbide precipitation
3. Limited dislocation recovery/rearrangements
4. Austenite decomposition

All of these processes occur at the nanometric scale. For this reason much of the characterization reported in this thesis focuses on tools capable of resolving features of this size. Transmission electron microscopy (TEM) has been used to study carbide precipitation and defect arrangement, while three dimensional atom probe tomography has been used to examine carbon distribution.

In order to choose the temperature/time combinations to explore in detail for the heat treatments, a first analysis was performed by calorimetry. Based on these results a set of times and temperatures for tempering were selected. The high resolution characterization of the microstructure commenced from the as-quenched state, where both TEM (see section 5.3.1) and atom probe tomography (APT) (see section 5.4.2) were used. With the as-quenched state characterized, high resolution characterization of selected tempered samples was made (see sections 5.3.3 and 5.4.4).

5.2 Calorimetry

As a first step in understanding the microstructure evolution of the 300M steel with tempering, calorimetry was used. The objective of this experiment was to provide guidance on the choice of tempering conditions for further detailed study. The results of a representative calorimetry experiment are presented in figure 5.1. As mentioned in section 4.4.2, the results presented in figure 5.1 were obtained as the difference in measured heat flows during two experiments. In the first experiment an as-quenched sample was heated at 2°C/min to 280°C and cooled back to room temperature. This same sample was then re-heated in the same way, this second run providing a baseline.

The results presented in figure 5.1 closely match those reported by Han *et al.* [47] on a 0.8 wt% C steel. Han *et al.* [47] correlated the peaks observed in calorimetry to the specific microstructural processes by combined calorimetry and TEM. It was shown that peak 1 (labeled on figure 5.1) corresponded to carbon segregation to lattice defects and spinodal decomposition. Peak 2 correspondded to the precipitation of transition carbides,

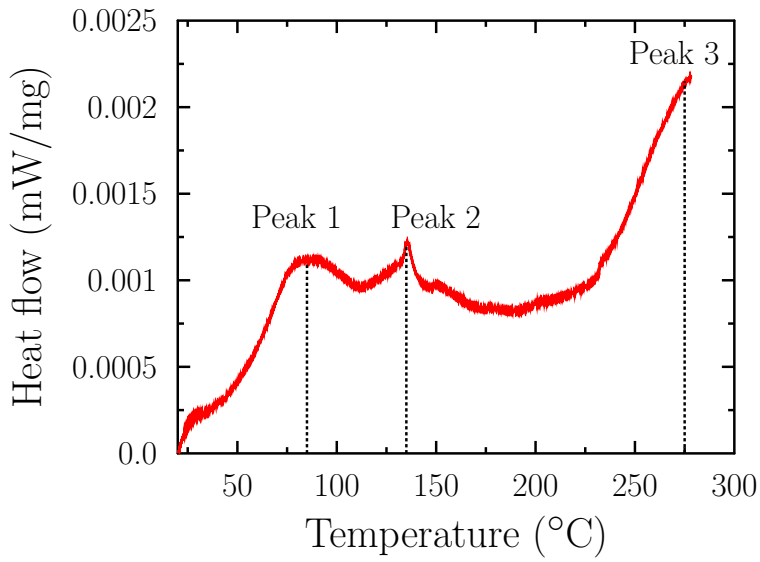

Figure 5.1: Heat flow recorded on heating an as-quenched 4340 sample from room temperature to 280°C at a speed of 2°C per minute. Each peak is reflecting the occurrence of a particular phenomenon (see text).

Temperature range	Phenomenon
50°C - 110°C	Carbon segregation
110°C - 220°C	η-carbide precipitation
220°C - ?	Decomposition of retained γ

Table 5.1: Phenomena occurring during tempering of martensite according to the calorimetry result, interpreted based on the work of Han *et al.* [47]. The question mark indicates that the upper limit for retained austenite decomposition could not be measured due to the limited temperature range of the apparatus.

and peak 3 to the decomposition of retained austenite and the precipitation of cementite. The approximate temperature range occurring for these peaks (as extracted from figure 5.1) are given in table 5.1.

Based on these calorimetry experiments, tempering conditions were chosen for further study (table 5.2), the focus being on low temperature tem-

T (°C)	Time (hours)	TEM	APT	Mon. Tors.	Bausch.
80	24	–	–	x	–
80	96	–	–	x	–
120	1	x	x	x	–
120	3	x	–	x	x
120	5	x	–	x	x
120	8	x	x	–	–
120	16	–	–	x	–
150	1	x	x	x	x
350	1	x	x	x	x

Table 5.2: Choice of tempering conditions of 300M steel based on calorimetry measurements and technique of invesigation. All conditions refer to material that was water quenched. The 'x' symbol signifies that the technique was used, and the '–' symbol means that the technique was not used. 'Mon. Tors.' means that a specimen of the condition was tested in monotonic torsion and 'Bausch.' means that a specimen of the condition was tested in strain reversal test. 'TEM' stands for 'transmission electron microscopy' and 'APT' for 'three dimensional atom probe tomography'.

pering where carbon segregation and transition carbide precipitation are expected to be dominant. One higher tempering temperature (e.g. 350°C) was also chosen. Unlike Han *et al.*, however, it will be shown that cementite precipitation was not observed in the higher temperature tempering condition used in this study.

5.3 Electron microscopy

5.3.1 As-quenched martensite

Electron back-scattered diffraction (EBSD) observations were made to give a low magnification overview of the microstructure of the martensitic material. Due to low indexation of the diffraction patterns in the as-quenched material, a low temperature tempering treatment had to be used to obtain reasonable

results. While this tempering treatment is expected to change the nanoscale structure of the material (see the following sections on TEM and APT), it is expected that its effect on the larger scale features (prior austenite grain boundaries, lath/block/packet boundaries) will be negligible [78].

EBSD observations revealed a structure typical of that observed in other lath martensite microstructures [35, 143]. Figure 5.2 shows a low magnification overview of the microstructure as an inverse pole figure map where the colours indicate the crystallographic directions parallel to the observation surface of the sample. A few prior austenite grains have been highlighted (in white) in this figure. Distinguishing prior austenite grains is difficult due to the fact that packets of laths within a single prior austenite grain are separated by high angle boundaries [35].

One can, however, unambiguously determine the extent of the prior austenite grains based on the fact that the martensite formed within a prior austenite grain exhibits a specific orientation relationship with the austenite. When viewed in pole figures, the martensite poles tend to cluster into patterns characteristic of the orientation relationship (e.g. see [143]). This is illustrated in figure 5.2 where the $\{001\}_{\alpha'}$ pole figure for the martensite within the highlighted prior austenite grain shows a pattern characteristic of Kurdjumov-Sachs ($\{110\}_{bcc} \parallel \{111\}_{fcc}$, $\langle 111\rangle_{bcc} \parallel \langle 101\rangle_{fcc}$) and Nishiyama-Wassermann ($\{110\}_{bcc} \parallel \{111\}_{fcc}$, $\langle 001\rangle_{bcc} \parallel \langle 101\rangle_{fcc}$) orientation relationships.

Figure 5.3 illustrates this more clearly. Unlike the map presented in figure 5.2 which was cleaned by grain dilation to remove unindexed points, the map in figure 5.3 has not been cleaned and shows that a large number of laths ($\sim 50\%$) are not indexed. A comparison between the size of features shown in this map and the TEM results presented later in this section, clearly reveals that EBSD fails to index the finest laths within the microstructure.

As mentioned above, the extent of prior austenite grains was determined by including all laths that exhibited the same type of orientation relationship with a single austenite orientation. When done correctly, it was possible to superimpose the $\{001\}_{\alpha'}$ pole figures for all of the prior austenite grains by plotting them with respect to the austenite lattice rather than the exter-

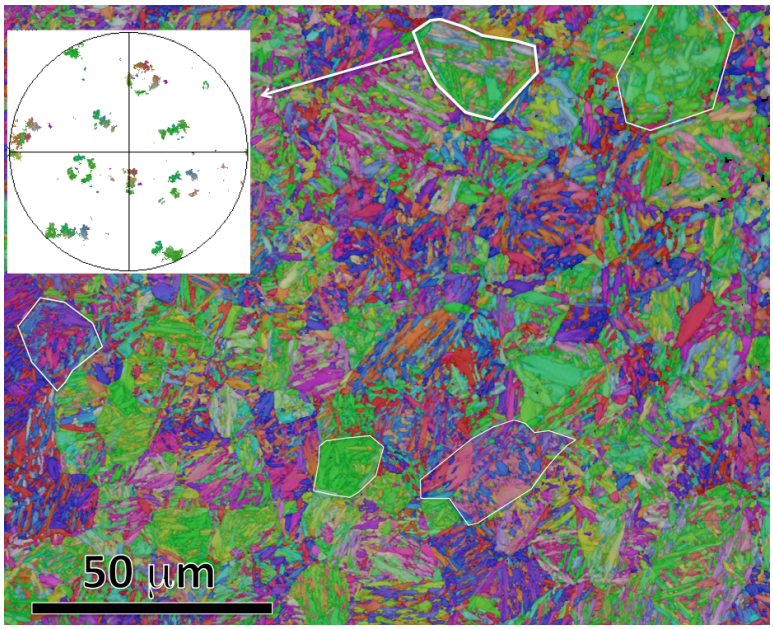

Figure 5.2: EBSD map following cleaning (using grain dilation) to remove non-indexed points, coloured based on the orientation of the grains parallel to the plane of observation. Several prior austenite grains are highlighted, the extent of the prior austenite grains having been determined based on the orientation relationship between austenite and the martensite formed within that prior austenite grain. If the prior austenite grain is enveloped properly then a specific pattern for the orientations of the martensite laths is revealed. This is illustrated for the highlighted grain where the inset $\{001\}_{\alpha'}$ pole figure shows the features characteristic of the orientation relationship between different martensite variants and the prior austenite grain.

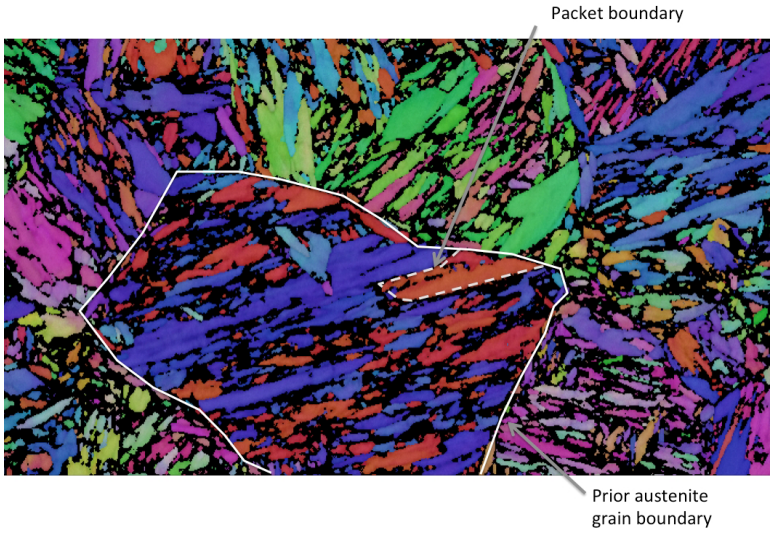

Figure 5.3: EBSD map using inverse pole figure colouring (as in figure 5.2) but presented without grain dilation to remove non-indexed points (non-indexed points are black). Comparison between feature size in this map with TEM observations reveals that the EBSD map misses measuring the finest features (laths) within the microstructure. Other aspects of the microstructure can also be revealed however. A packet boundary separating two packets of laths each sharing the same orientation relationship (red and blue) with the prior austenite is shown. Also highlighted is the extent of a prior austenite grain.

nal coordinate system. Figure 5.4 shows the experimental data from four grains shown in figure 5.3 superimposed and plotted in the austenite reference frame (projected on the $\{001\}_\gamma$ plane). Also plotted are the ideal positions of the martensite $\langle 001 \rangle$ directions assuming a Kurdjumov-Sachs orientation relationship (blue circles) and Nishiyama-Wassermann orientation relationship (red circles).

Using the method described above, the prior austenite grain size was estimated to be approximately 30 μm, consistent with previous studies that used similar processing conditions and steel chemistries compared to those used here.

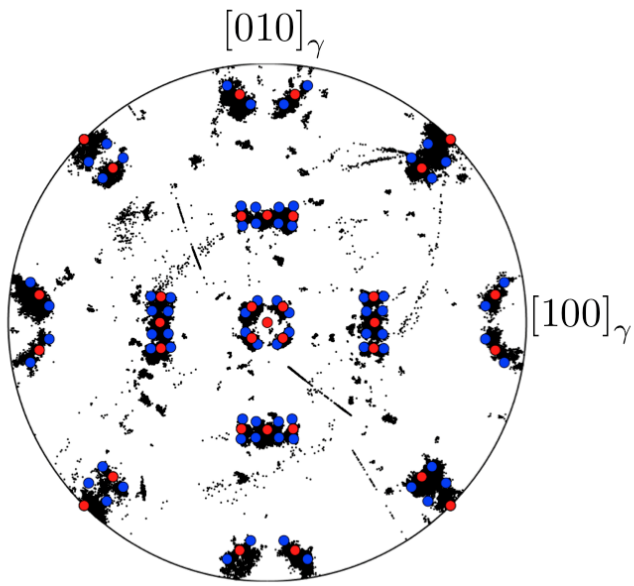

Figure 5.4: Experimental ⟨001⟩ martensite poles plotted in the austenite reference system. The orientations of the prior austenite grains were found by manually comparing the ideal positions of the ⟨001⟩ martensite poles assuming Kurdjumov-Sachs (blue circles) and Nishiyama-Wassermann (red circles) orientation relationships. The high degree of correspondence between the experimental data and the ideal orientations shows that the determination of the extent of the prior austenite grain boundaries is excellent.

To observe finer features of the microstructure not visible using the EBSD technique transmission electron microscopy (TEM) was used. Viewed at low magnification in the TEM (figure 5.5) the microstructure was found to consist of fine parallel laths, with some twins. The fraction of twinned areas was estimated to be approximately 10%, which is typical of low alloyed medium carbon martensite [8]. Those features are presented in more detail in figure 5.6. Neither carbide precipitation nor the tweed structure were detected among the 3 TEM foils observed, suggesting that the quench was fast enough to prevent large scale redistribution of carbon.

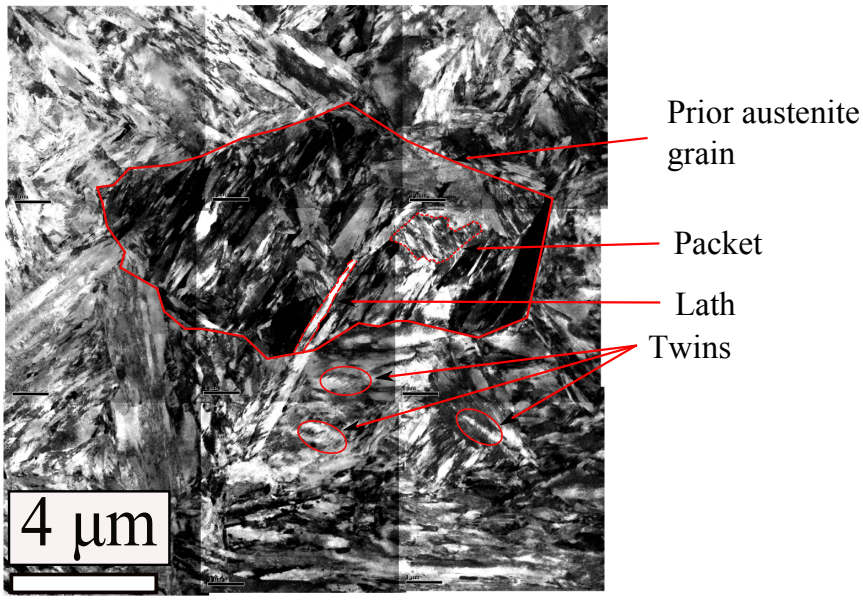

Figure 5.5: Montage of several low magnification TEM pictures showing an overview of the microstructure of the as-quenched material.

A lath size distribution was extracted from images such as the one presented on figure 5.6(a). Following previous studies [7, 26] (figure 5.7), the lath sizes were determined from the intersection of line segments drawn perpendicular to the lath boundaries on TEM images (figure 5.7(b)). Four hundred segments were measured this way alloying for the construction of the lath size distribution presented in figure 5.8. Low magnification images from samples after different tempering treatments did not show significant differences in this size distribution as will be discussed below.

The lath size distribution followed a lognormal distribution, consistent with data published in the literature [7, 26]. The mean lath size was found to be 0.19 μm, and the standard deviation was 0.22 μm. The most frequently observed lath thickness was between 0.17 and 0.18 μm, a result which is similar to that found by Apple *et al.* [26].

The twin thickness was evaluated to be between 10 and 100 nm based on

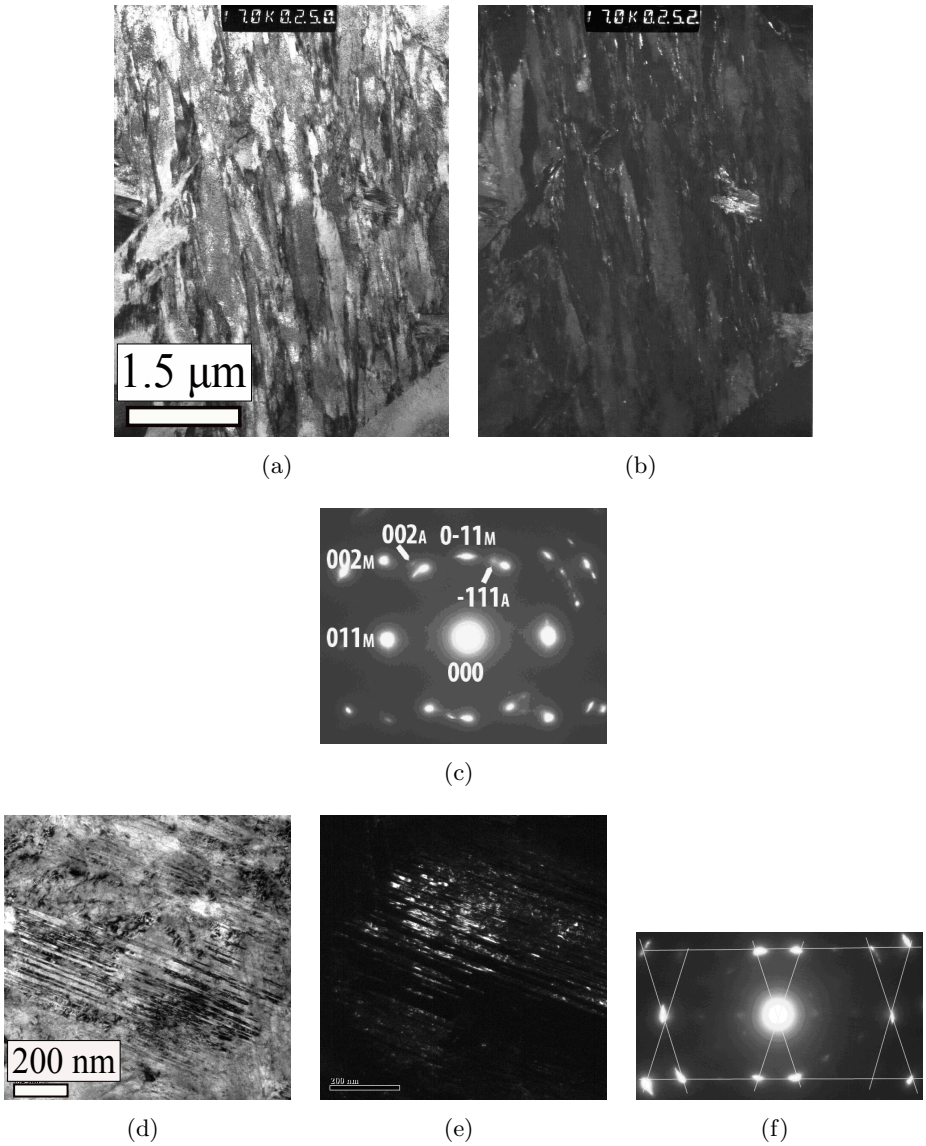

Figure 5.6: High magnification view of typical features in martensite a) Bright field image of a lath area, b) corresponding dark field image highlighting retained austenite, c) diffraction pattern showing extra spots due to retained austenite, d) bright field image of twinned area, e) corresponding dark field, and f) diffraction pattern.

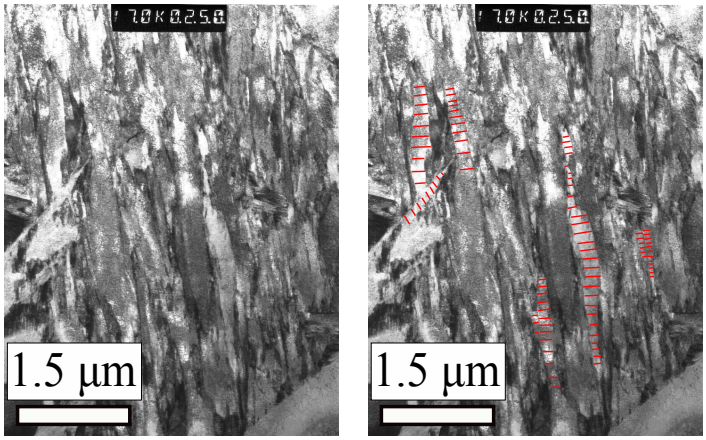

(a) (b)

Figure 5.7: Method for determining the lath size distribution a) raw bright field image of a lath area in the as-quenched specimen, and b) corresponding analyzed image. The length of each red segment was measured.

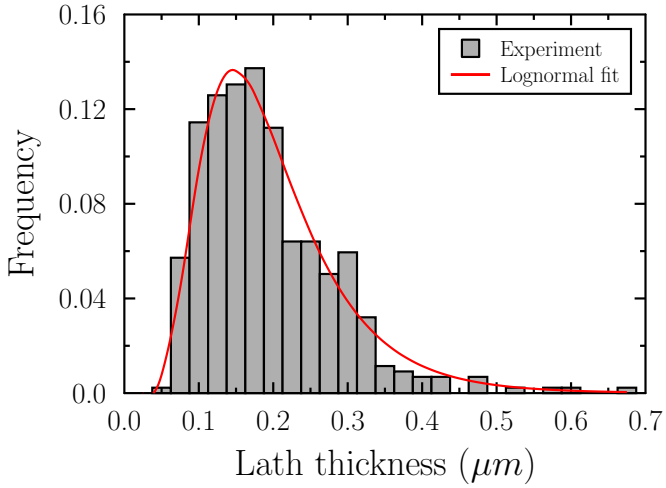

Figure 5.8: Distribution of lath sizes determined from the TEM picture of the as-quenched material, and log-normal fit. The mean value and standard deviation of the log-normal distribution was 0.19 μm and 0.22 μm, respectively.

figures 5.6(d) and 5.6(e), consistent with the findings of Richman and Cohen [144]. As expected, some retained austenite was found between the laths (see figure 5.6(b)). The volume fraction of retained austenite was difficult to assess, but based on images such as figure 5.6(b), it seems that it was much lower than the 5% typically measured in medium carbon steels [77]. Finally, careful examination by diffraction revealed no evidence of carbide precipitation in the as-water-quenched specimens.

5.3.2 Influence of cooling rate

In the literature review (chapter 2) it was shown that a strong dependence of microstructure on cooling rate has been previously described. To investigate this, strip samples were annealed for five minutes at 900°C and quenched using helium gas instead of water (see section 4.4.1). Samples were then extracted and prepared for TEM observation.

The microstructure in this condition was found to be similar to that observed in as-water-quenched samples, consisting of partially twinned lath martensite, containing a small fraction (below 5%) of retained inter-lath austenite. Unlike the as-water-quenched samples, however, carbide precipitation was observed at this slower cooling rate (see figure 5.10). The precipitates were identified as most likely being orthorhombic η-carbides based on selected area diffraction pattern analysis. Though, as mentioned in chapter 2, the differentiation between η and ϵ-carbides is very difficult, superlattice reflections (indicated by arrows in figure 5.9) arising from the orthorhombic Co_2N-type structure were observed in this condition. These superlattice reflections, corresponding to $\{110\}_\eta$ [65], have been previously used to argue for the identification of transition carbides as orthorhombic η-carbides rather than hexagonal ϵ-carbides [145].

Consistent with [68], the state of precipitation was observed to be heterogeneous through the microstructure, with some laths showing only very weak diffraction from precipitates (e.g. figure 5.10(a)) and others revealing much stronger diffraction spots arising from the precipitates (e.g. figure 5.10(d)).

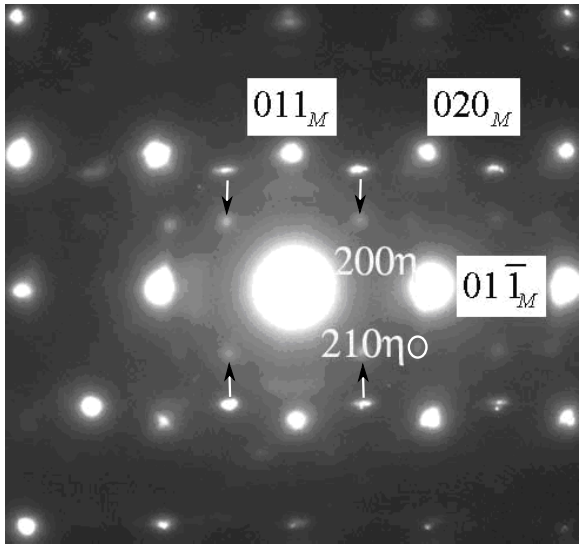

Figure 5.9: Typical selected area diffraction pattern obtained with the electron beam parallel to $[100]_{\alpha'}$. The superlattice reflections corresponding to a CoN_2-type structure are indicated by arrows. The white circle corresponds to $(210)_{\eta}$.

Temperature (°C)	Time (hours)
120	1
120	3
120	5
120	8
150	1
350	1

Table 5.3: Tempering conditions investigated by transmission electron microscopy.

5.3.3 Evolution of the microstructure with tempering

Microstructure observations were next made after tempering selected water-quenched samples. TEM observations were made on samples subjected to the tempering conditions presented in table 5.3.

The main microstructural difference between the as-water-quenched mi-

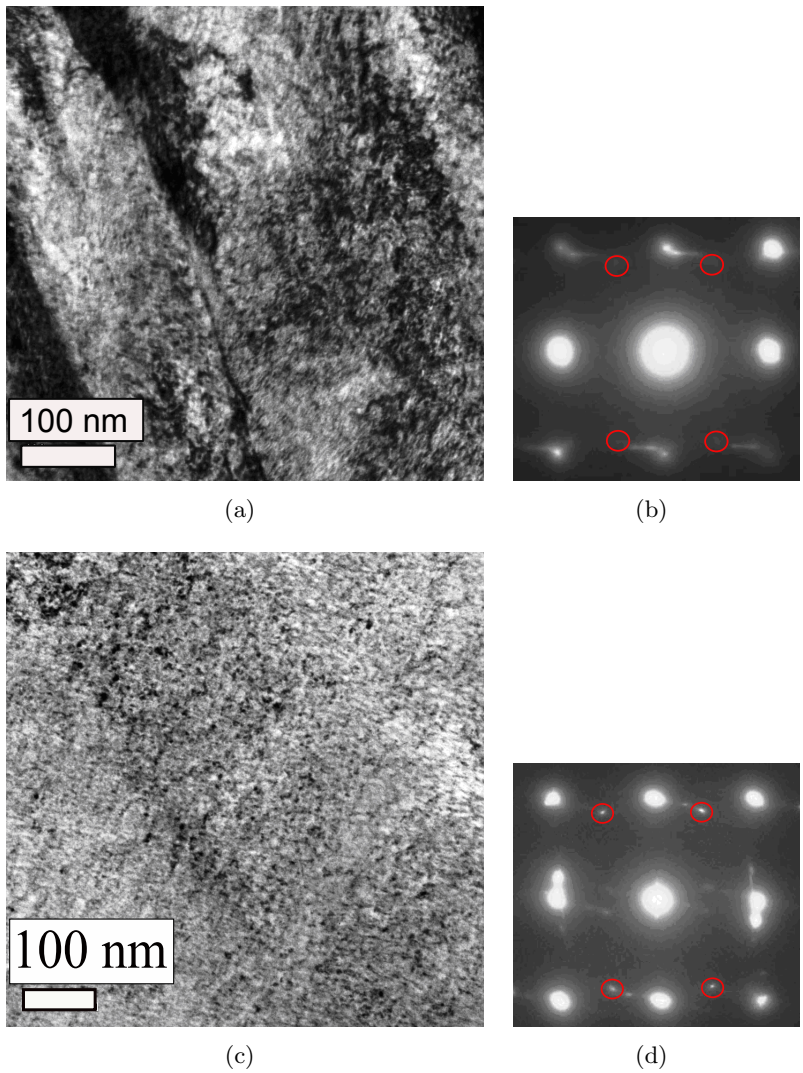

Figure 5.10: Carbide precipitation in the sample slowly quenched to room temperature. a) Bright field image of a small laths area showing small carbides (in black), b) diffraction pattern showing faint extra spots due to η-carbides, c) bright field image of a large laths area showing small carbides (in black), and d) diffraction pattern showing extra spots due to η-carbides. Note the difference in intensity of the spots.

crostructure (figure 5.6) and the microstructures observed after tempering was the appearance of transition carbides in the latter conditions. As in the case of the as helium-quenched state the carbides were identified as most likely being η-carbides consistent with the conclusions reached by Han *et al.* [47]. No clear evidence in the form of image contrast morphology or diffraction spot streaking corresponding to the tweed microstructure could be found in any samples observed.

Investigation of the specimen tempered one hour at 120°C revealed that the state of precipitation was not uniform throughout the microstructure (figure 5.11). Much like in the case of the as-helium-quenched material some areas of the microstructure appeared more well advanced in terms of precipitation (clear diffraction spots arising from the precipitates) while other regions appears to be at a much less advanced stage of precipitation with no or only weak diffraction spots being visible from the carbides.

Increasing the tempering temperature and/or time led to a more homogeneous distribution of precipitates. An example of this is presented in figure 5.12. After tempering for one hour at 150°C, extra spots corresponding to η-carbides were observed in all laths observed (see figure 5.12(c)). Also, some precipitates were observed on lath boundaries separating fine laths (see figure 5.12(b)).

The mean size of the carbides was estimated for each of the tempered states using image analysis from dark field images taken from within large lath that exhibited clear precipitate reflections (see figure 5.13). Assuming an ellipsoidal shape (see an example on figure 5.13(b)), the major and minor axes of carbides were recorded and the average of the two was recorded as the diameter. For each condition more than one hundred and fifty measurements were performed. From the dark field images used for image analysis, it was difficult to see the smaller precipitates, and thus the average precipitate size determined this way is probably underestimated.

From these measurements the number density of precipitates was also estimated based on the observation area and the number of precipitates measured. As stated before, some of the smallest precipitates were probably missed in the counting, therefore the number density determined by image

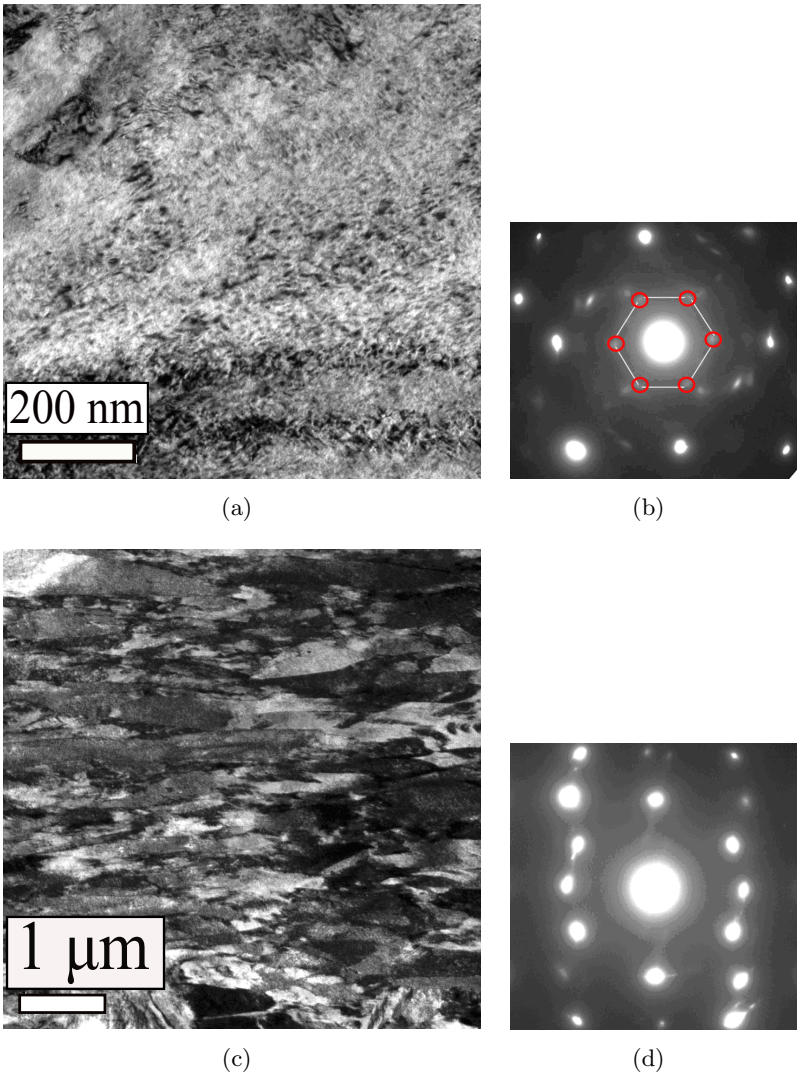

Figure 5.11: Typical microstructures observed by transmission electron microscopy on a specimen tempered one hour at 120°C. a) Bright field image of a large lath, b) corresponding diffraction pattern showing extra spots (highlighted in red) due to the presence of η-carbides, c) Bright field image of many small laths and d) corresponding diffraction pattern showing only spots due to bcc iron.

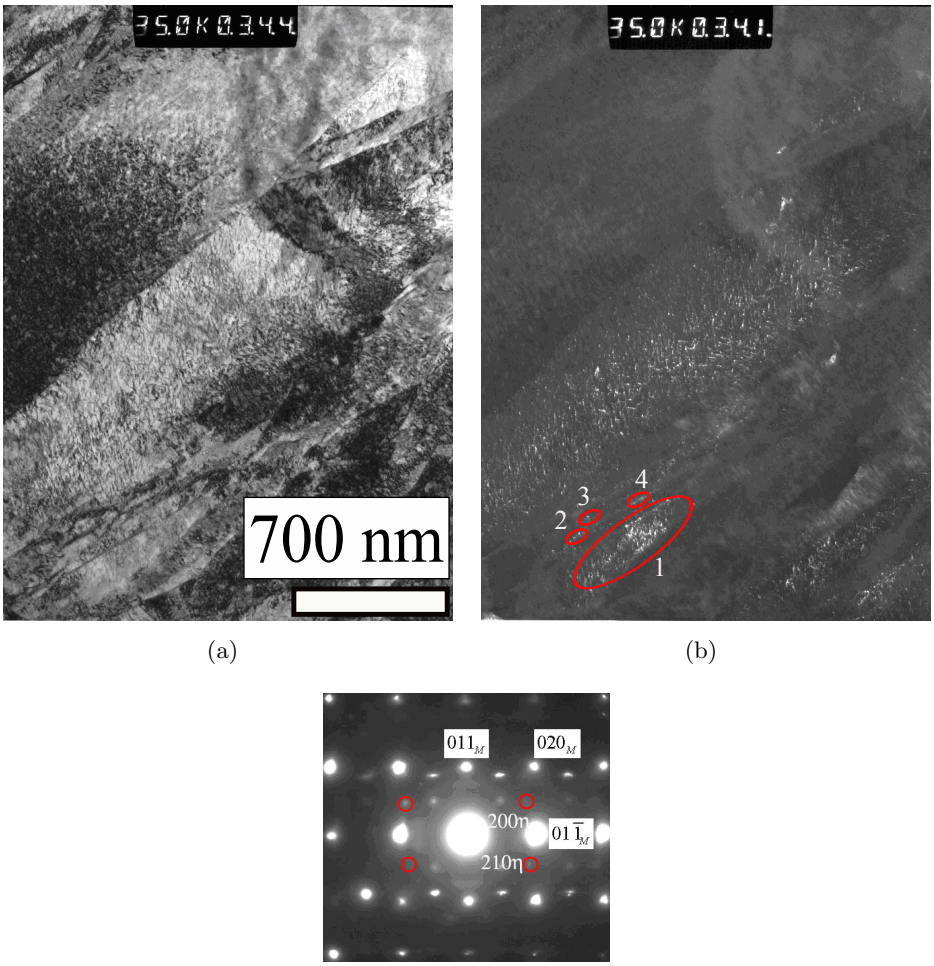

(a) (b)

(c)

Figure 5.12: Electron micrograph showing precipitation in fine laths of martensite. a) Bright field image, b) dark field image highlighting transition carbides, and c) corresponding diffraction pattern with η-carbides diffraction spots highlighted. In b), 1 indicates intra-lath precipitation, and 2,3 and 4 indicate precipitation along lath boundaries.

analysis was underestimated. In addition, it was not possible to obtain the foil thickness from these samples due to their highly dislocated state, thus the number density had to be estimated assuming different foil thicknesses (table 5.4). Since the foil thickness is usually of the order of 100 nm [146], it was decided in the following to use the estimation of the number density estimated assuming a foil thickness of 100nm (table 5.4). For the specimens

Tempering Temp. (°C)	Temp. Time (hr)	N (t = 50 nm) (m^{-3})	N (t =100 nm) (m^{-3})	N (t = 150 nm) (m^{-3})	
120	1	$\sim 2.5 \times 10^{22}$	$\sim 3.5 \times 10^{22}$	$\sim 6.9 \times 10^{22}$	
120	3	$\sim 1.8 \times 10^{22}$	$\sim 2.7 \times 10^{22}$	$\sim 5.4 \times 10^{22}$	
120	5	$\sim 2.7 \times 10^{22}$	$\sim 4.1 \times 10^{22}$	$\sim 8.2 \times 10^{22}$	
120	8	$\sim 0.9 \times 10^{22}$	$\sim 1.4 \times 10^{22}$	$\sim 2.8 \times 10^{22}$	
150	1	$\sim 3.7 \times 10^{22}$	$\sim 5.6 \times 10^{22}$	$\sim 11.2 \times 10^{22}$	
350	1	–	–	–	–

Table 5.4: Carbide number density N as a function of assumed foil thickness t.

tempered one hour at 350°C, the carbides precipitated in rows (see figure 5.15) and were so closely spaced that it was impossible to measure their size. In this case, the length and width of the rows were estimated. No attempt to measure a number density was made in this case.

Table 5.5 summarizes the obtained data, including the mean value and the standard deviation based on fitting a lognormal distribution to the data (see figure 5.14). The carbides in the specimen tempered one hour at 350°C were found to be approximately 15 nm in size with the width of the carbide rows being 18 nm and the length of the rows being 129 nm.

The carbide sizes reported here are in good agreement with the literature [65, 68, 81, 145, 147, 148]. Hirotsu and Nagakura estimated a carbide size of approximately 6.5 nm after tempering a plain 0.45 wt% C martensite 3 hours at 200°C, this value being slightly lower than the value obtained here on specimens tempered one hour at 150°C. Other studies performed on slightly different plain carbon steels showed carbide sizes ranging between 2 nm [147] and 10 nm [65] after low temperature tempering (between 120°C and 150°C). The observation of rows of precipitated carbides after higher temperature tempering (e.g. 350°C) is also consistent with the literature [145, 148, 149].

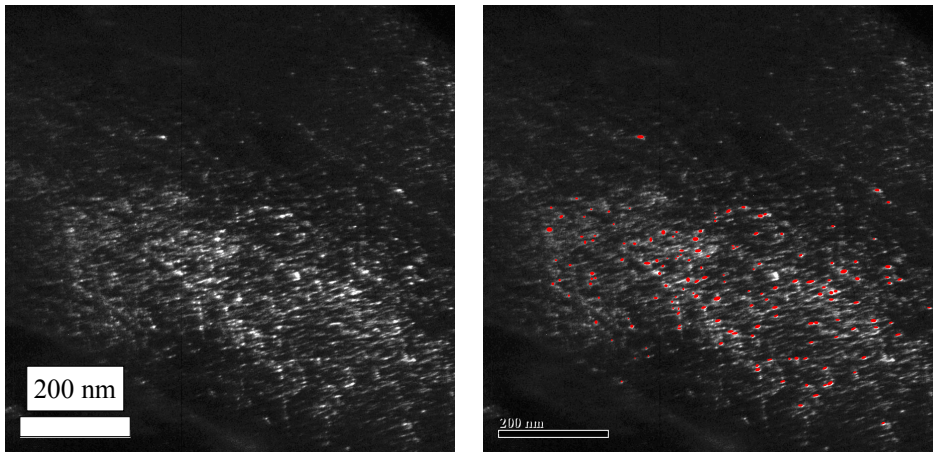

(a) (b)

Figure 5.13: Example of an image analysis performed on the microstructure tempered at 120°C for five hours a) raw image and b) image showing the method for determining the carbide size, which was estimated based on an the average of the long and short axis of the red ellipses.

Tempering Temp. (°C)	Temp. Time (hr)	Carbide Diam. (nm)	Std. dev. (nm)	Number Density (m^{-3})	Volume Fraction
120	1	3.2	1.3	$\sim 3.5 \times 10^{22}$	6×10^{-4}
120	3	4.5	1.3	$\sim 2.7 \times 10^{22}$	1.3×10^{-3}
120	5	5.6	2.0	$\sim 4.1 \times 10^{22}$	3.8×10^{-3}
120	8	7.6	2.0	$\sim 1.4 \times 10^{22}$	3.2×10^{-3}
150	1	9.3	2.4	$\sim 5.6 \times 10^{22}$	2.4×10^{-2}
350	1	~ 15	–	–	–

Table 5.5: Evolution of the average carbide diameter, number density and volume fraction with tempering. The number density is estimated assuming an average TEM sample thickness of 100 nm. The carbide size for the specimen tempered one hour at 350°C was only approximately estimated. The number density and volume fraction was not estimated in this case.

Padmanabhan *et al.* [149] studied the precipitation behaviour on tempering an identical 300M martensite at 280°C. In this case the rows of precipitated carbides were $\sim$ 100 nm long and $\sim$ 20 nm wide, in good agreement to the data presented above.

The amount of retained austenite remaining after tempering was estimated by dark field imaging. It was found that the retained austenite was stable up to high tempering temperatures with little observed change in its volume fraction. This is consistent with earlier work [20] and the well-known effect of silicon in delaying the decomposition of austenite [80].

Finally, the defect structure (dislocations and twins) also appeared relatively stable upon tempering. The lath structure did not show any sign of coarsening even after tempering one hour at 350°C. The changes in dislocation substructure were harder to assess, but no significant changes could be detected. This is consistent with the conclusions drawn by Malik and Lund's (based on X-ray diffraction measurements) that a small decrease of the dislocation density from 20.7×10^{14} m^{-2} to 13.2×10^{14} m^{-2} after tempering a 0.45 wt%C martensite one hour at 350 °C [97].

5.4 Measurement of carbon distribution by atom probe tomography

5.4.1 Introduction

Some conditions were selected for three dimensional atom probe tomography to measure the evolution of carbon distribution (see table 5.2). The difficulty of these experiments precluded the analysis of a large number of samples for each condition. Thus, while these experiments can not be considered to give a statistically representative overview of the entire microstructure, they will be shown to be consistent with the general observations presented in the previous section. At the same time they provide additional insight into the atomic scale arrangement of carbon on tempering.

As a first check on the reliability of the APT technique to obtain the chemistry of the studied alloy, the average composition of substitutional al-

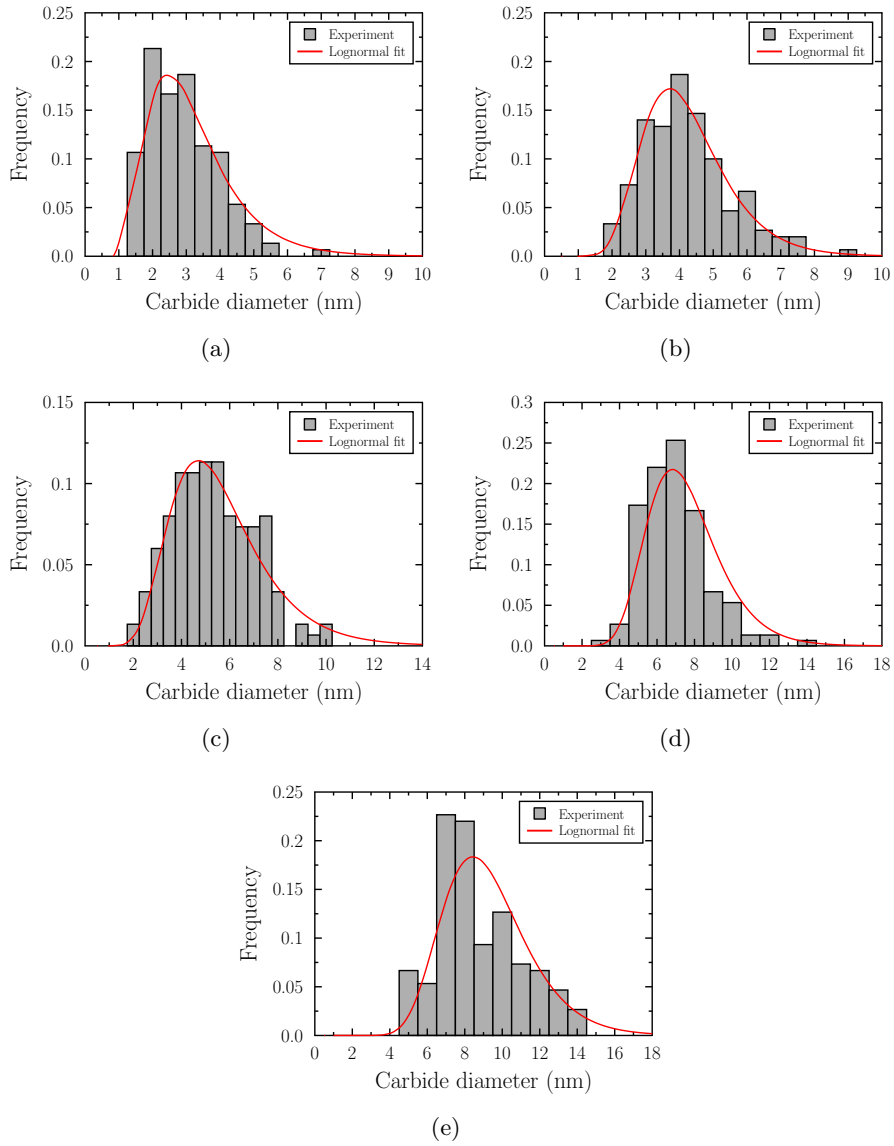

Figure 5.14: Carbides size distributions as a function of tempering conditions. a) 120°C one hour, b) 120°C three hours, c) 120°C five hours, d) 120°C 8 hours and e) 150°C one hour. Lognormal fits are represented in red.

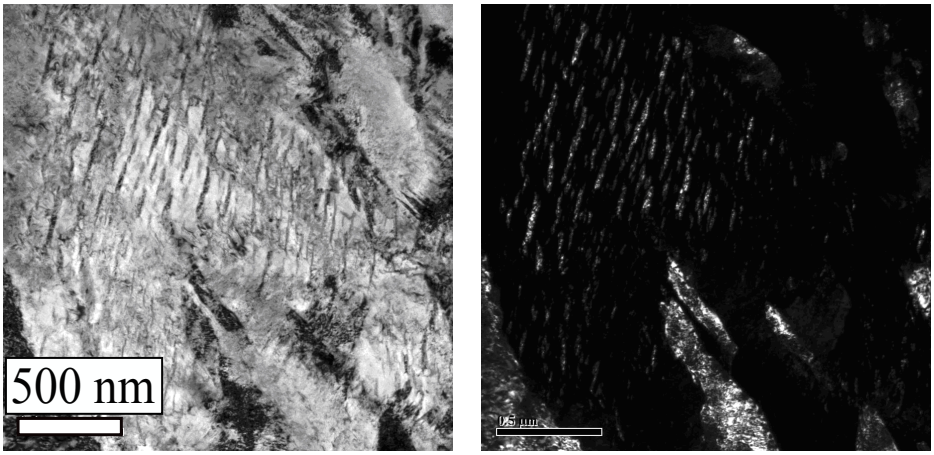

(a) (b)

Figure 5.15: Electron micrograph of the microstructure after tempering at 350°C for 1 hour a) bright field and b) corresponding dark field.

loying elements, i.e. nickel, silicon and chromium, was calculated in all of the examined volumes. As expected, the concentration of those major elements was found to be homogeneous at this scale [138] in all the samples studied by atom probe. Moreover, in each case, the absolute composition in alloying elements was comparable to the bulk composition (table 5.6). Based on these results, it was decided to not further evaluate the substitutional elements, rather the results presented below focus only on carbon distribution.

	Mn	**Mo**	**Cr**	**Ni**	**Si**
Bulk	0.64	0.19	0.75	1.75	3.22
Measured	0.83± 0.01	0.16± 0.003	0.9± 0.01	1.40 ± 0.02	3.46 ± 0.01

Table 5.6: Chemical composition obtained by APT, compared to the bulk composition. All the values are in at%.

Table 5.7 reports the average carbon composition obtained in the analyzed volumes. The carbon compositions measured by APT were found to be close to the nominal carbon composition of the alloy (1.76 at% C). It was

Tempering temp. (°C)	Tempering time	Vol. (nm^3)	at% C
WQ	–	8×8×300	1.34± 0.01
RT	1 month	8×8×260	1.73± 0.01
HeQ (Sample 1)*	–	48×48×74	1.76± 0.01
HeQ (Sample 2)	–	28×28×56	1.62± 0.03
120 *	1 hour	13×13×165	2.30± 0.01
120	8 hours	55×55×270	2.20± 0.01
150 (Sample 1) *	1 hour	15×15×310	2.18± 0.01
150 (Sample 2)	1 hour	12×12×63	2.03± 0.05

Table 5.7: Conditions selected for atom probe tomography. The volume analyzed and average carbon composition are indicated. The nominal carbon composition of the 300M steel was 1.76 at%C. 'WQ' designates the as-water-quenched sample and 'HeQ' designates as-helium-quenched samples. 'RT' means room temperature. * Samples also studied by Mr. Bilyk during his Master's thesis [138].

found that atom probe tomography gave higher carbon compositions for the more tempered samples. This may reflect the higher degree of decomposition in these samples and the fact that the small volumes analyzed tended to have large regions of carbon enrichment [34]. It may also, however, reflect local heterogeneities in chemical composition. It was found, for example, that a strong correlation between observed carbon content and silicon content was obtained in the observed volumes. Given the strong interaction between carbon and silicon in austenite [150] this might suggest a local concentration variation in carbon due to heterogeneities in the distribution of the substitutional alloying elements.

5.4.2 As-quenched martensite

The TEM observations made on the as-water-quenched martensite revealed no signs of carbide precipitation or tweed structure. To check if a finer scale redistribution of carbon had taken place during quenching, a sample was heat treated at Aperam Research center (France) following the same ex-

perimental conditions (using the same model of Gleeble thermomechanical simulator) as presented in section 4.4.1. Once the water-quench was completed, the sample was immediately quenched in liquid nitrogen to avoid carbon redistribution at room temperature. The sample was then transported in liquid nitrogen to the Université de Rouen (France), for three dimensional atom probe analysis. The sample was held approximately two hours at room temperature (due to specimen preparation) before entering the atom probe chamber, where the sample was cooled to 80K for analysis.

The results, presented in figure 5.16, show that the volume analyzed was close to having a homogeneous distribution of carbon. No particular features

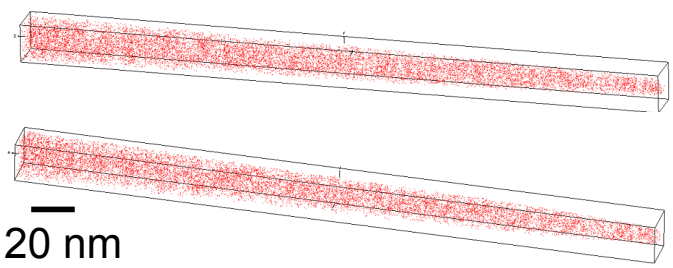

Figure 5.16: Three dimensional APT volume obtained on as-quenched specimens, $8 \times 8 \times 240$ nm^3, 7×10^5 atoms.

were observed in the reconstructed volume, suggesting that almost no carbon segregation had taken place during the quench. The linear profile along a sub-volume of dimensions $8{\times}8{\times}230$ nm^3 is presented in figure 5.17(b). It shows that the maximum concentration was $\sim 2.2 \pm 0.25$ at% C.

A statistical analysis of this volume (see section 4.5 for details of the method) revealed that the carbon distribution was not perfectly random, with some regions depleted and enriched (to approximately $3{\pm}0.3$ at % C) in carbon. Following aging of this material for one month at room temperature no significant changes in the carbon distribution were observed (figure 5.16).

This result is in contrast with the previously reported carbon distributions in as-quenched 4340 martensite [34] where a large volume ($30{\times}30{\times}300$ nm^3) was examined after quenching. Zhu *et al.* [34] found regions containing carbon segregation to 16 at% C, which is more than five times larger

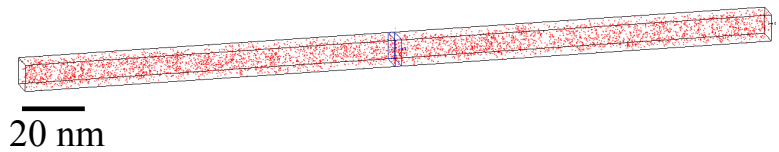

(a)

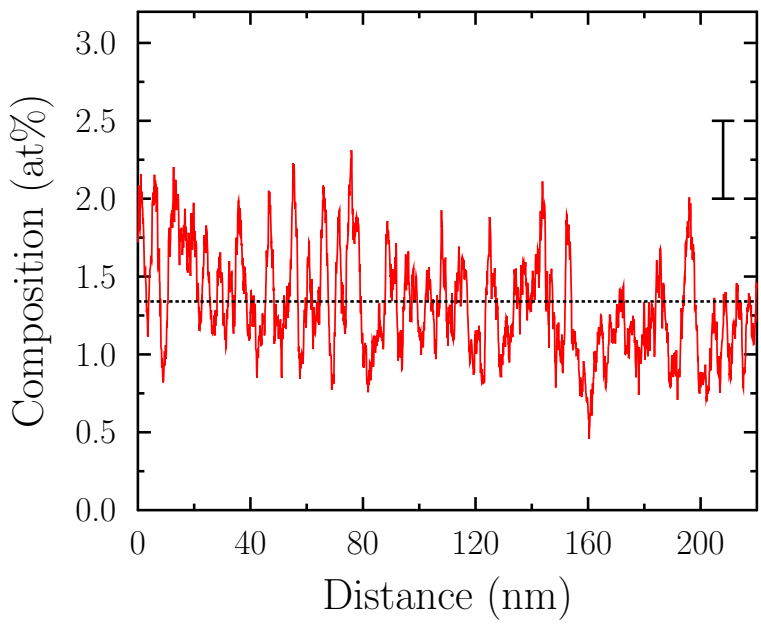

(b)

Figure 5.17: a) Image of a representative volume of dimensions $8 \times 8 \times 230$ nm^3 (only carbon atoms are represented), and b) linear profile of the carbon composition along the length of the volume in a). The composition was sampled using small volumes of $8 \times 8 \times 2$ nm^3 (represented in blue in a)) which were moved along the length with a step size of 1 Å. The error bar is indicated on the figure.

than the maximum concentration recorded here. It is notable that in this study no details were given regarding the method used to quench the sample. A slow cooling rate may be, therefore, responsible for the high degree of apparent carbon redistribution in their sample (see below). In support of this, Hutchinson *et al.* [35] have recently reported a very similar carbon concentration distribution as the one presented in figure 5.18. This was measured in a 0.5 wt%C martensitic steel having approximately the same Ms temperature as the 300M steel studied here after quenching at a similar rate to the fast water-quench used in the present study.

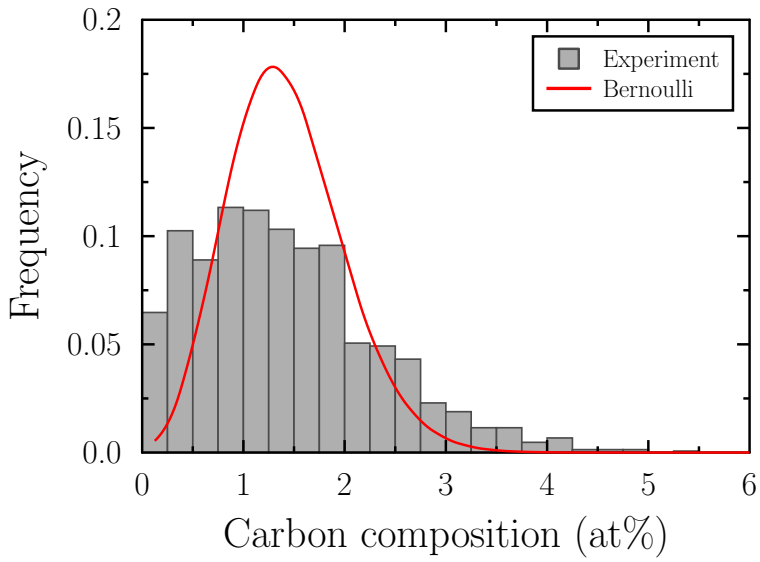

Figure 5.18: Carbon composition distribution obtained experimentally (gray rectangles) compared to a Bernoulli distribution (red line), for the as-quenched specimen. The total volume sampled is $8 \times 8 \times 230$ nm^3. A random spatial distribution of carbon should result in the measured histogram matching the Bernoulli distribution.

5.4.3 Effect of cooling rate

The condition of the material following helium quenching exhibited some significant differences from the results presented above for the water-quenched

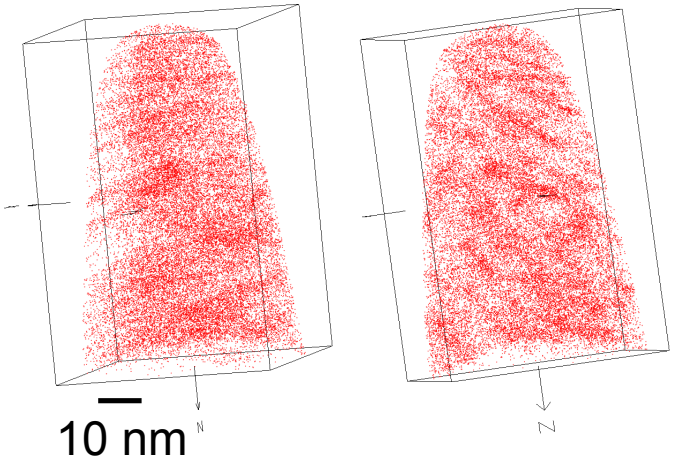

(a)

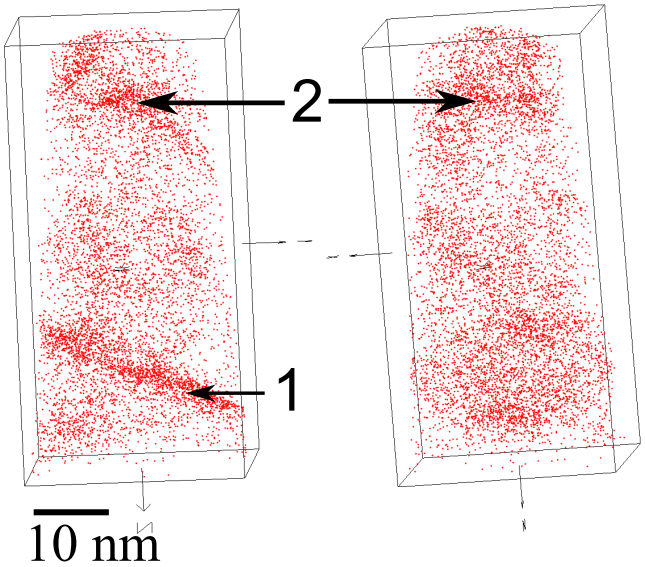

(b)

Figure 5.19: Three dimensional APT volumes obtained on as-helium-quenched specimens. a) Sample 1, 42×42×72 nm^3, 3.3 × 10^6 atoms, and b) Sample 2, 28×28×56 nm^3, 9.5 × 10^5 atoms.

state. An analysis of small volumes made in a helium-quenched sample by APT revealed that some carbon redistribution occurred during quenching (see figure 5.19) and that heterogeneity in the degree of carbon redistribution could be found. For example, figure 5.19(a) shows a measured volume exhibiting little carbon redistribution, while the volume shown in figure 5.19(b) appears to have more substantial carbon redistribution.

Linear composition profiles from these volumes are shown in figures 5.20(b) and 5.21(b). The maximum carbon composition in these profiles was found to be 5.4 ± 0.4 at% C and 5.2 ± 0.4 at% C, these values being more than twice the maximum carbon composition measured in the as-water-quenched sample.

The spacing between carbon-rich regions in the first volume was estimated as $\sim$ 10 nm while it was estimated to be $\sim$ 35 nm in the second volume.

The segregated regions in these two volumes were analyzed in more detail. In the first sample, only one clear feature could be identified (figure 5.22). This feature was found to be roughly equiaxed, having dimensions of approximately $5 \times 5 \times 4$ nm^3, and a maximum carbon composition of 7.8 ± 0.7 at% C. A variety of features were observed in the second volume (figure 5.23). The maximum carbon composition in this region was measured as 4 ± 0.1 at% C, based on the linear profile plotted in figure 5.23(b). The homogeneity of the carbon composition in this region was evaluated by plotting composition profiles along smaller volumes across the region, such as the one highlighted in figure 5.23(a). This allowed for a more local evaluation of the carbon composition. Nine carbon composition measurements were performed this way. This method showed that the carbon composition in this region varied between 3 ± 0.5 at% C to 6.8 ± 0.7 at% C.

The carbon-rich region labeled '2' in figure 5.19(b) appeared to be roughly equiaxed (figure 5.24). The carbon composition based on a linear profile (figures 5.24(a) and 5.24(b)) was approximately 9.8 ± 1 at% C and its volume was approximately $4 \times 4 \times 3$ nm^3. Similarly, other equiaxed carbon-rich regions were also observed in this volume, the maximum composition of these varying between 5.1 ± 0.7 at% C and 9.2 ± 1 at% C.

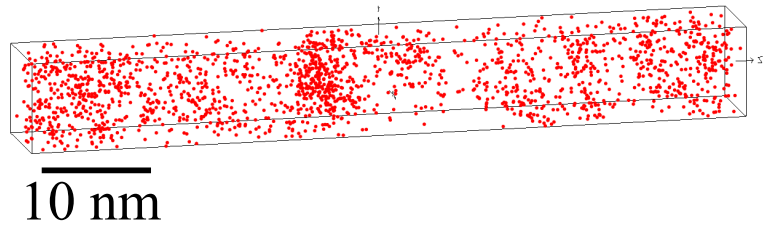

(a)

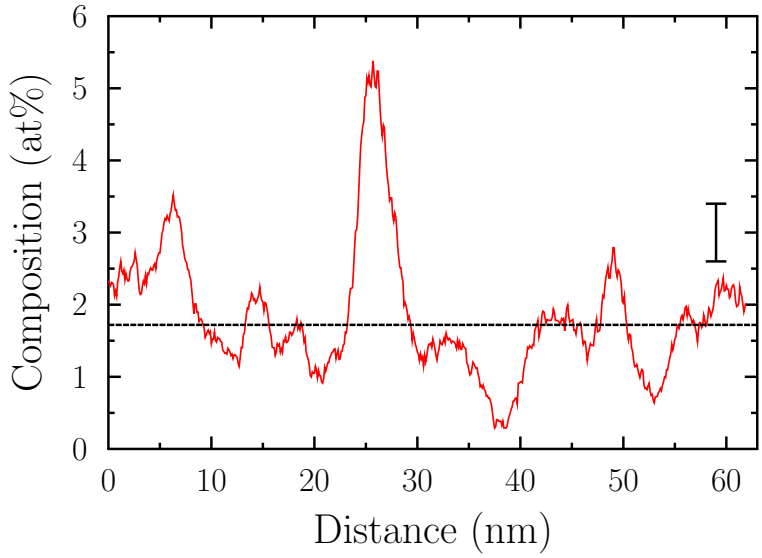

(b)

Figure 5.20: Three dimensional atom probe measurement of the carbon composition profile in the sample shown in figure 5.19(a). a) image of a representative volume of dimensions $8 \times 8 \times 64$ nm^3 (only carbon atoms are represented), and b) linear profile of the carbon composition along the length of the volume in a). The error bar is indicated in the figure.

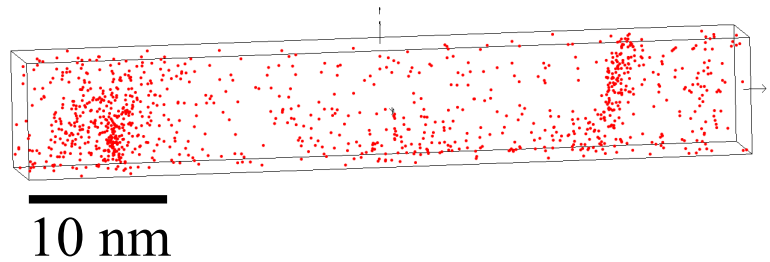

(a)

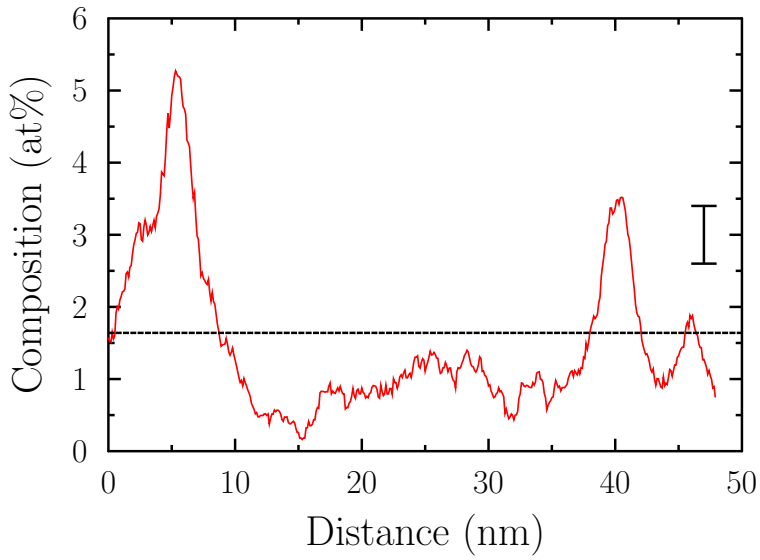

(b)

Figure 5.21: Three dimensional atom probe measurement of the carbon composition profile in the sample shown in figure 5.19(b). a) image of a representative volume of dimensions $8 \times 8 \times 50$ nm^3 (only carbon atoms are represented), and b) linear profile of the carbon composition along the length of the volume in a). The error bar is indicated in the figure.

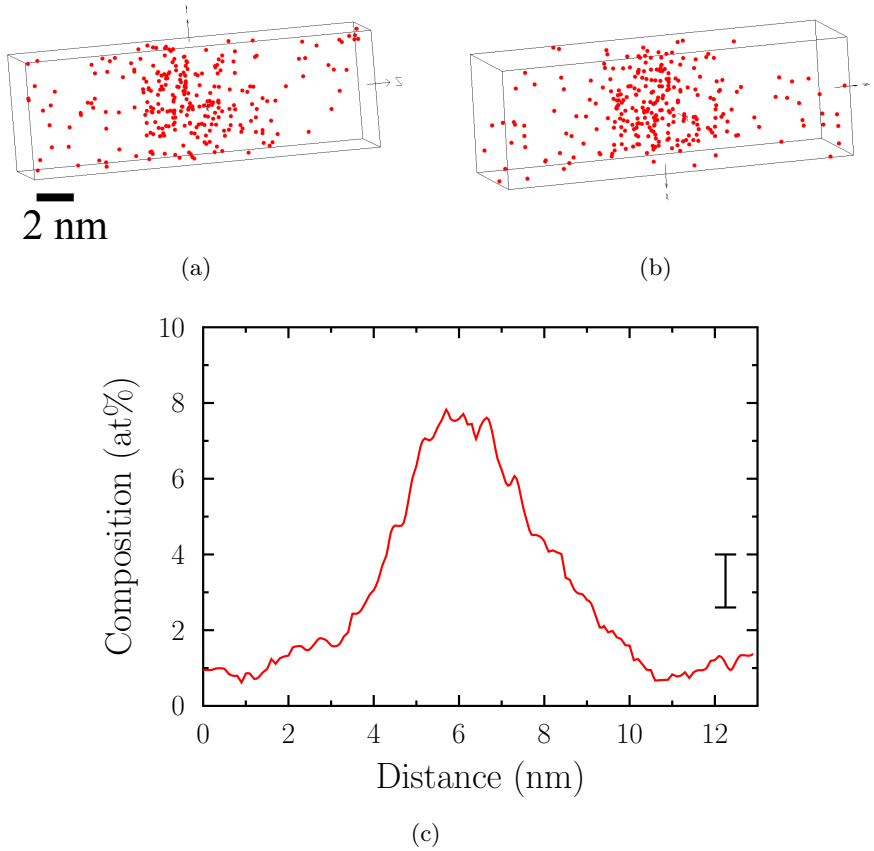

Figure 5.22: Equiaxed carbon-rich region observed in the as-helium-quenched sample. a) Three dimensional volume, $5 \times 5 \times 15$ nm^3 showing the equiaxed carbon-rich region, b) same as in a) but tilted 90° with respect to the length axis, and c) linear carbon composition profile obtained along the length of the box.

The carbon composition remaining outside of the segregated regions in the second volume was estimated. Fifteen measurements were made (section 4.5) giving an average solid solution carbon content of approximately 0.45 ± 0.04 at% C. In comparison, the average carbon level remaining in the first volume was found to be very close to the initial carbon content of the alloy.

This observed inhomogeneity in carbon distribution within the slow helium-quenched samples compared to the relative homogeneity of the car-

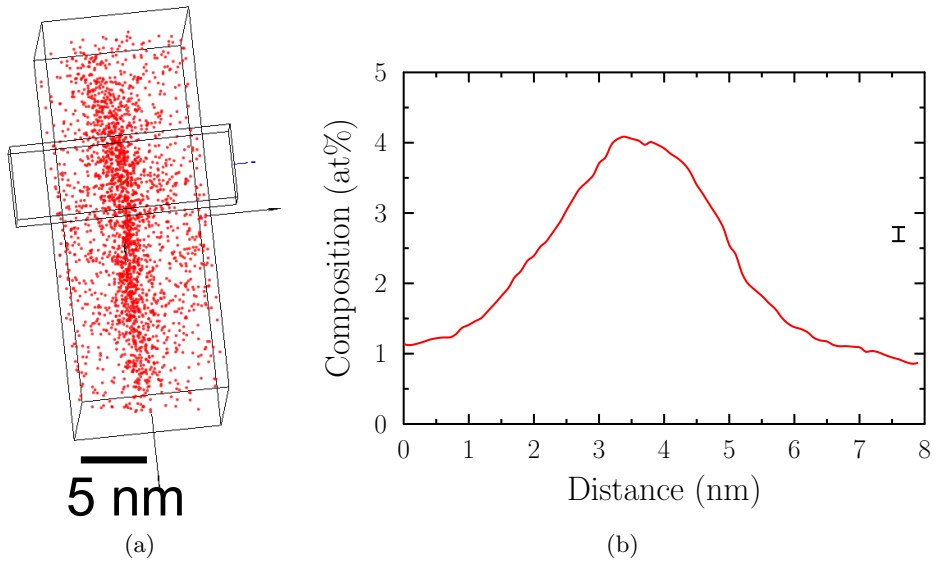

Figure 5.23: Close view of region '1' indicated in figure 5.19(b), and b) linear profile of the carbon composition along the length of the volume in a). The error bar is indicated in the figure.

bon distribution in the fast water-quenched samples mirrors the results obtained in an earlier study on a similar 4330 martensitic steel [18].

5.4.4 Evolution of the microstructure with tempering

To follow the evolution of the carbon distribution upon tempering, samples quenched and tempered one hour at 120°C and one hour at 150°C were selected for APT experiments. An additional measurement was performed on a sample quenched and tempered eight hours at 120°C. In contrast to the as-water-quenched sample, clear evidence for carbon redistribution on tempering was found, this being generally consistent with other recent observations by APT on other low alloyed martensitic steels [18, 34, 36, 57, 60].

Figure 5.26 presents an APT volume obtained from a sample tempered one hour at 120°C. Carbon segregation appeared as planar features (labeled '1' and '3') as well as more equiaxed features (labeled '2' and '4'). The maximum carbon composition within these segregated regions was obtained

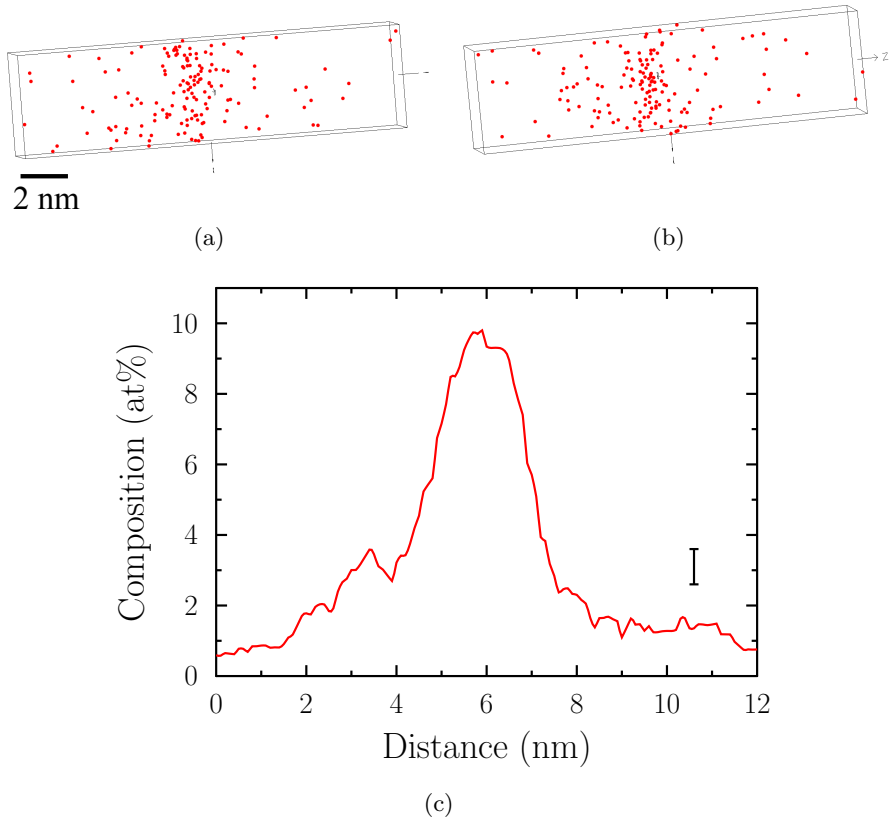

Figure 5.24: Equiaxed carbon-rich region '2' observed in sample 2 of the as-helium-quenched condition. a) Three dimensional volume, $4\times4\times15$ nm^3 showing the equiaxed carbon-rich region, b) same as in a) but tilted 90° with respect to the length axis, and c) linear carbon composition profile obtained along the length of the box.

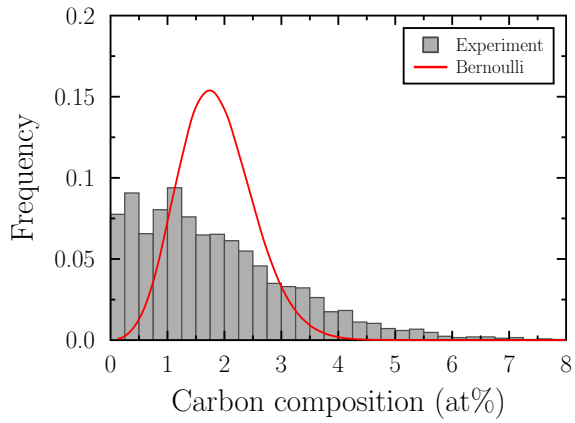

(a)

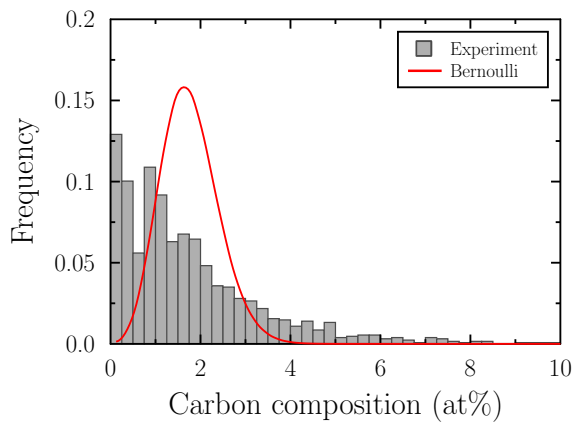

(b)

Figure 5.25: a) Carbon composition distribution obtained in sample 1 (the sampled volume had dimensions $24 \times 24 \times 60$ nm^3), and b) same as in a) for sample 2 (the sampled volume had dimensions $18 \times 18 \times 50$ nm^3).

by selecting a small box around the segregated region and drawing a linear profile across it. In regions '1' and '3' the maximum carbon composition was found to be $\sim 8 \pm 0.45$ at% C whereas in the equiaxed regions '2' and '4', it was $\sim 11 \pm 0.7$ at% C.

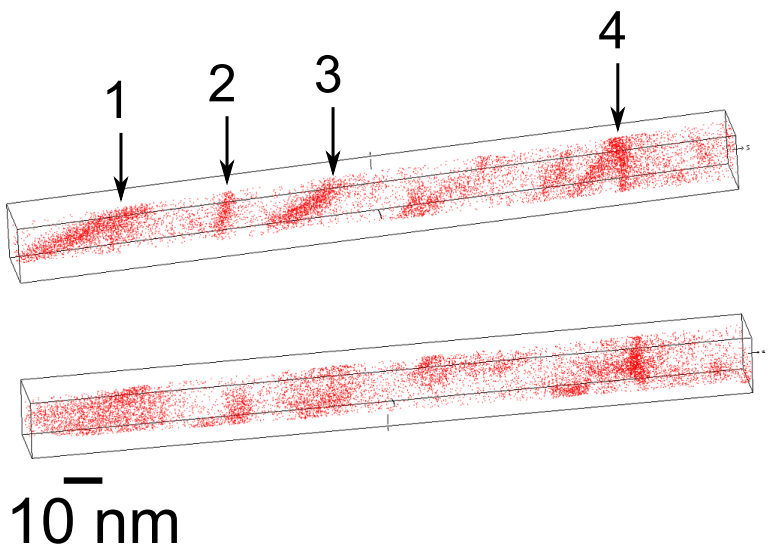

Figure 5.26: Reconstructed volume obtained on the specimen tempered one hour at 120°C. The total number of atoms detected was 8.5×10^5.

The mean distance between carbon-rich segregated regions was determined to be approximately 20 nm while the carbon level remaining in solid solution was estimated to be 0.64 ± 0.09 at% C (0.14 ± 0.02 wt% C).

A sample tempered for 8 hours at 120°C was also analyzed, the measured volume being shown in figure 5.27. The volume analyzed in this case was much larger than the volume analyzed after tempering for 1 hour at 120°C (figure 5.26) making it difficult to compare the two datasets purely based on visual inspection of the volumes themselves. Also, because of the relatively large thickness of the volume presented in figure 5.27, the morphologies of the carbon-rich regions were not obvious, except for one planar feature (labeled '1') that appeared to cross the entire measured volume at approximately 45° to the volume length.

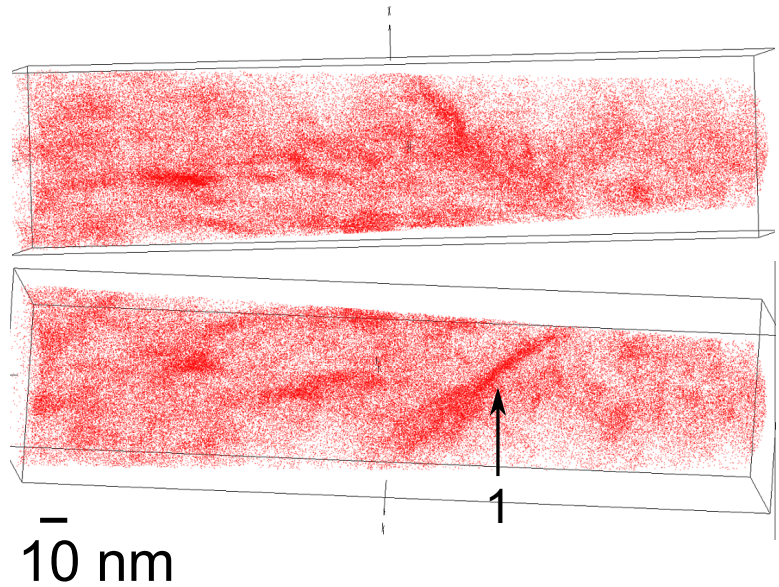

Figure 5.27: Reconstructed volume obtained on the specimen tempered 8 hours at 120°C. The total number of atoms detected was 21.8×10^6.

The carbon composition of this carbon-rich region (labeled '1' in figure 5.27) was determined as previously, by plotting a linear carbon composition profile across it (figure 5.28). The linear profile plotted in figure 5.28(b) shows that the maximum carbon composition in this carbon-rich region was 4.4 ± 0.02 at% C.

Close investigation of this carbon-rich region revealed that the carbon composition was not homogeneous everywhere in the region. Selecting cubic boxes with a smaller cross section allowed for more local carbon composition measurements. Four linear profiles across this flat carbon-rich region were obtained using boxes having dimensions $5 \times 5 \times 20$ nm^3. The minimum and maximum carbon compositions measured were 3.4 ± 0.5 at% C and 5.8 ± 0.6 at% C, respectively. The average of these two extreme values (e.g. 4.6 at% C) corresponded well to the maximum carbon composition of the whole flat carbon-rich region determined in figure 5.28(b).

Upon further investigation it was found that approximately equiaxed

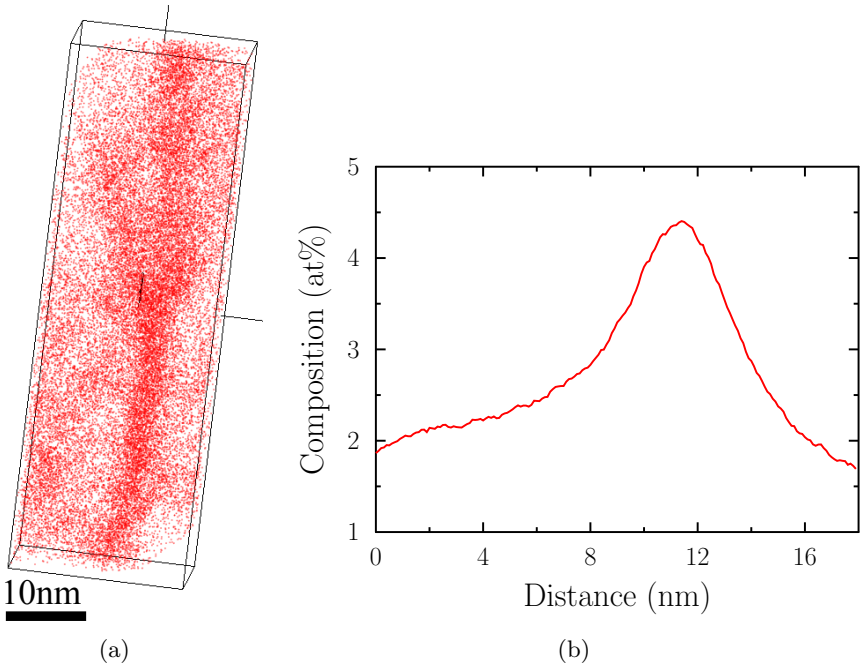

Figure 5.28: a) Carbon-rich region '1' singled out in a box having dimensions $60 \times 60 \times 20$ nm^3, and b) linear carbon composition profile along the length of the box shown in a).

carbon-rich features could be found within the planar carbon-rich region. One of these equiaxed carbon-rich region is highlighted in figure 5.29. The carbon composition of this equiaxed carbon-rich region was estimated by plotting the linear profile along the smaller box (having dimensions $5 \times 5 \times 20$ nm^3) shown in figure 5.29 (see figure 5.30). As shown in figure 5.30(c), the maximum carbon composition in this carbon-rich region was 12.6 ± 0.9 at% C. Two similar carbon-rich regions were detected as well within the planar carbon-rich feature. The maximum carbon compositions of those two regions were found to be 8.5 ± 0.7 at% C and 8.1 ± 0.7 at% C, respectively.

Equiaxed carbon-rich regions such as those observed in the flat carbon-rich region were observed through the entire measured volume. The maximum carbon composition of nineteen of those equiaxed regions was measured by plotting linear composition profiles across them. The maximum carbon

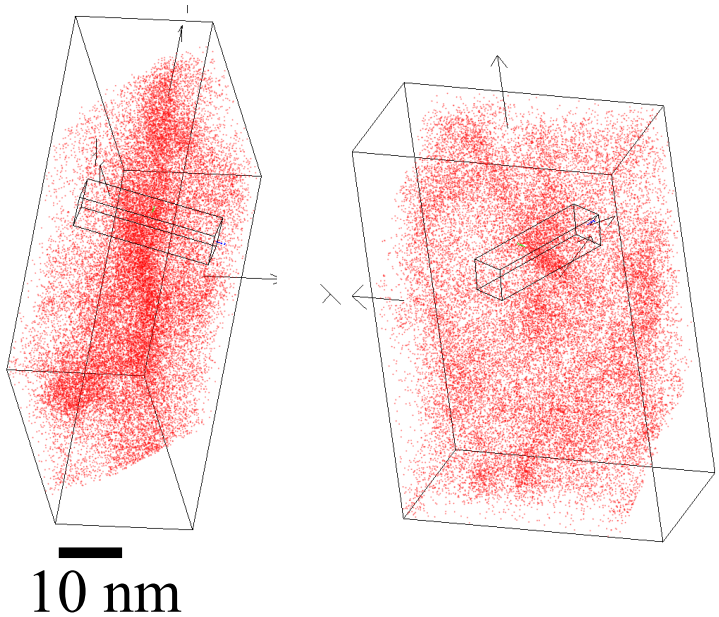

Figure 5.29: Two views of region '1' showing a roughly equiaxed particle.

compositions of the linear composition profiles varied between 6.9 ± 0.7 and 12.1 ± 0.9 at% C. The volumes of these carbon-rich regions were estimated to be roughly similar, i.e. approximately $5 \times 5 \times 5$ nm^3.

Another type of geometry was observed in this volume. An example of a linear feature having a high level of segregated carbon is shown in figure 5.31. This linear carbon-rich region was approximately 26 nm long. The carbon composition along the carbon-rich feature was followed by plotting linear carbon composition profiles across it. Five measurements were performed this way. The minimum and maximum carbon composition measured were 5 ± 0.5 at% C and 6 ± 0.6 at% C, respectively.

The mean distance between carbon-rich regions, estimated as described in section 4.5, was approximately 17 nm. This value was comparable to the value obtained in specimens tempered one hour at 120°C. The mean carbon composition remaining in solid solution was 0.76 ± 0.15 at% C. This value was found to be slightly higher than the value found for specimens

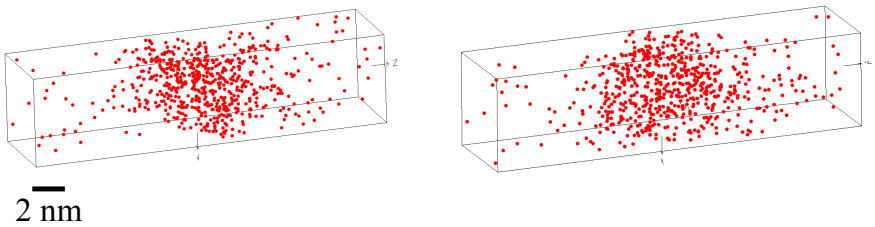

(a) (b)

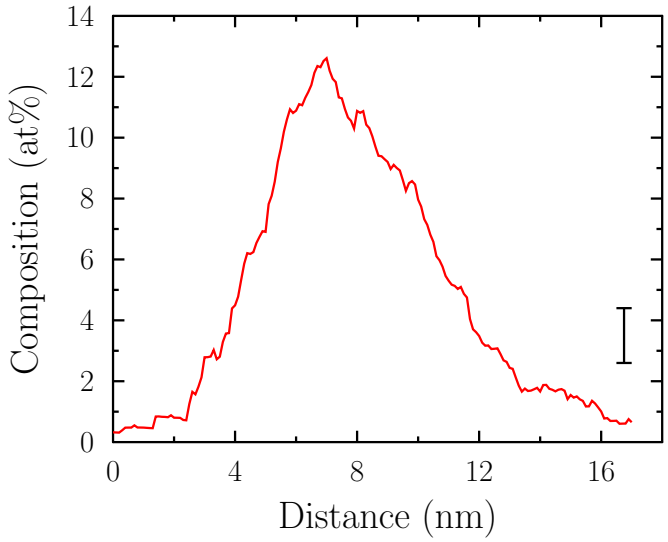

(c)

Figure 5.30: Example of an equiaxed carbon-rich region observed in a specimen water-quenched and tempered 8 hours at 120°C. a) Three dimensional volume, $5\times5\times15$ nm^3 showing the equiaxed carbon-rich region, b) same as in a) but tilted 180°with respect to the length axis, and c) linear carbon composition profile obtained along the length of the box.

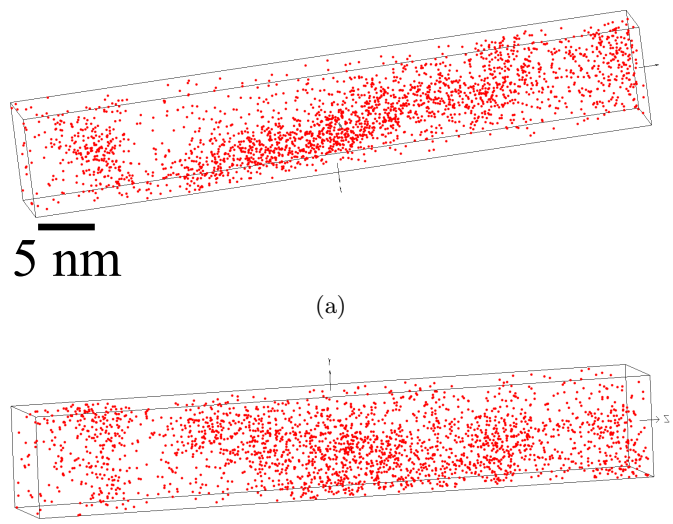

(a)

(b)

Figure 5.31: Linear carbon-rich region observed in a specimen water-quenched and tempered 8 hours at 120°C. a) Three dimensional volume, $8 \times 8 \times 30$ nm^3 showing the linear carbon-rich region, and b) same as in a) but tilted 180°with respect to the length axis.

tempered one hour at 120°C. However, the larger volume analyzed in this case, compared to the volume analyzed in the condition tempered one hour at 120°C, allowed for a larger number of measurements. Therefore, better statistics could explain this discrepancy.

Finally, specimens tempered for one hour at 150°C were also observed by APT. A reconstructed three dimensional volume from this condition is shown in figure 5.32. As for the sample annealed for 1 hour at 120°C, distinct carbon-rich areas having planar, equiaxed and linear geometries were observed. For example, the region labeled '1' in figure 5.32 was roughly equiaxed. This is best seen on a closer view presented in figures 5.33(a) and 5.33(b). The linear profile, plotted in figure 5.33(c), shows that the maximum carbon composition in this carbon-rich region was 15.8 ± 1 at% C.

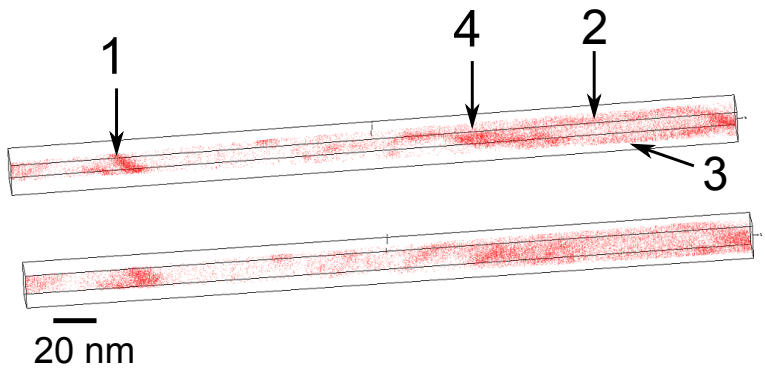

Figure 5.32: Reconstructed volume obtained on the specimen tempered one hour at 150°C. The total number of atoms detected was 1.7×10^6.

Another equiaxed carbon-rich region was detected, the composition of which was measured as approximately 9.2±0.8 at% C. Similar carbon compositions have been observed in APT experiments performed on as-quenched 0.4 wt% C martensitic steels similar to the steel under investigation here [34, 36].

Carbon-rich regions labeled '2' and '3' in figure 5.32 appeared to be more linear than planar. These two regions were found to extend over a length of approximately 80 nm and their carbon composition was found to vary between 2.9 ± 0.45 at% C and 5.6 ± 0.62 at% C.

The limited thickness of the volume sampled in this experiment prevented the exact determination of the shape of the carbon-rich region labeled '4' in figure 5.32. The composition of this region, measured by plotting a linear profile across it, was found to be approximately 9 ± 0.8 at% C.

In this case, the mean distance between carbon rich regions was approximately 31 nm and the carbon remaining in solid solution was 0.48 ± 0.1 at% C (0.1 ± 0.02 wt% C). This result indicates that the carbon remaining in solid solution in the matrix decreased as tempering increased. Similar observations have been made by APT experiments on a similar 0.78 wt% C plain carbon martensite [57].

A second, smaller APT volume was also measured on a sample obtained after tempering one hour at 150°C (figure 5.34). This small volume was

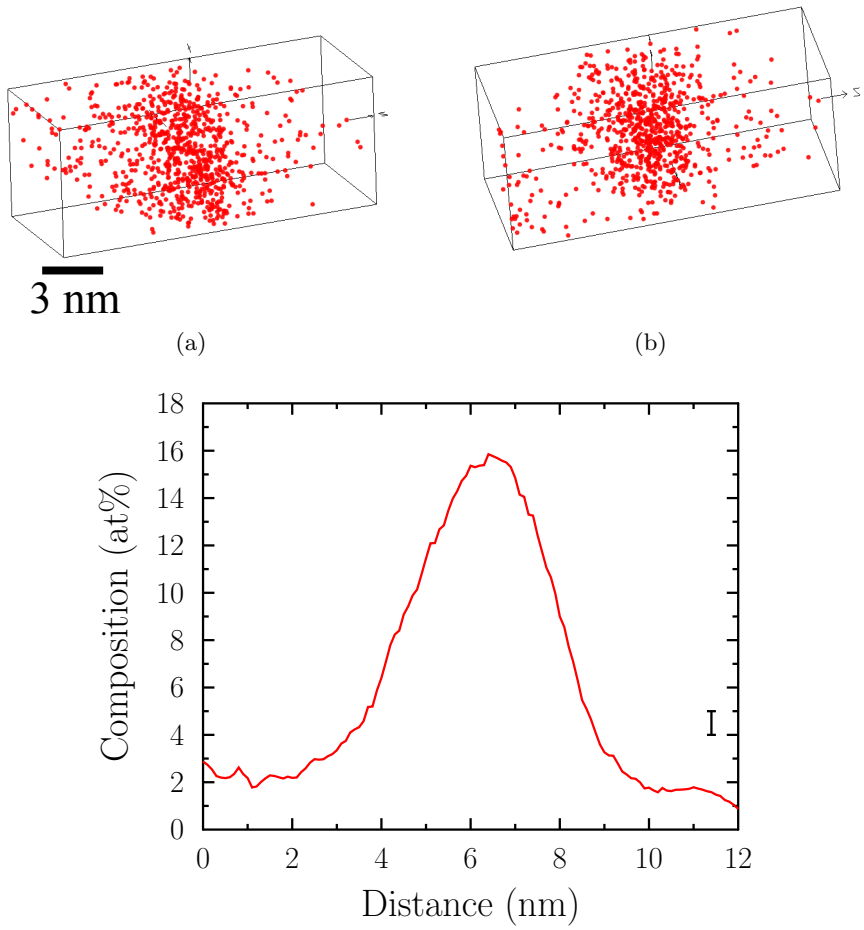

Figure 5.33: Equiaxed carbon-rich region labeled '1' in figure 5.32. a) Three dimensional volume, $5\times5\times12$ nm^3 showing the equiaxed carbon-rich region, b) same as in a) but tilted 180°with respect to the length axis, and c) linear carbon composition profile obtained along the length of the box.

found interesting since it contained what appeared to be a planar carbon-rich region, a feature which was not observed in the other volume described above. The carbon rich feature in this volume was isolated from the rest of the dataset and the carbon composition was estimated by plotting a linear profile across it. The carbon composition measured this way was approximately 6.9 ± 0.3 at% C, corresponding well to level of carbon segregation to planar features in another recent study [36].

Like the sample tempered 8 hours at 120°C, the carbon composition within the planar carbon-rich region labeled '1' in figure 5.34 was found to vary. The minimum carbon composition was approximately 5.1 ± 0.7 at% C, and the maximum carbon composition was approximately 11.4 ± 1.1 at% C. This high carbon composition area of region '1' seemed to correspond to a roughly equiaxed region, as observed for the specimen tempered 8 hours at 120°C (see figure 5.35).

The main results obtained by APT on as-water-quenched, as-helium-quenched and water-quenched and tempered conditions are summarized in table 5.8. This table shows that the carbon composition remaining in solid solution decreased roughly continuously with tempering. Also, the maximum carbon composition of the carbon-rich regions increased from ~ 8 at% C in the as-helium-quenched specimen, to ~ 16 at% C in the specimen tempered one hour at 150°C. Also, in the conditions studied here, the carbon-rich regions containing the highest carbon composition corresponded to regions roughly equiaxed in shape. Linear and planar carbon-rich regions were observed to have a lower carbon composition (between ~ 3 at% C and ~ 8 at% C, depending on the condition).

5.5 Discussion

5.5.1 Microstructures of as-quenched martensites

TEM observations of the as-water quenched martensite revealed a microstructure similar to what has been previously reported with regard to twin fraction, fraction and location of retained austenite and lath size distribu-

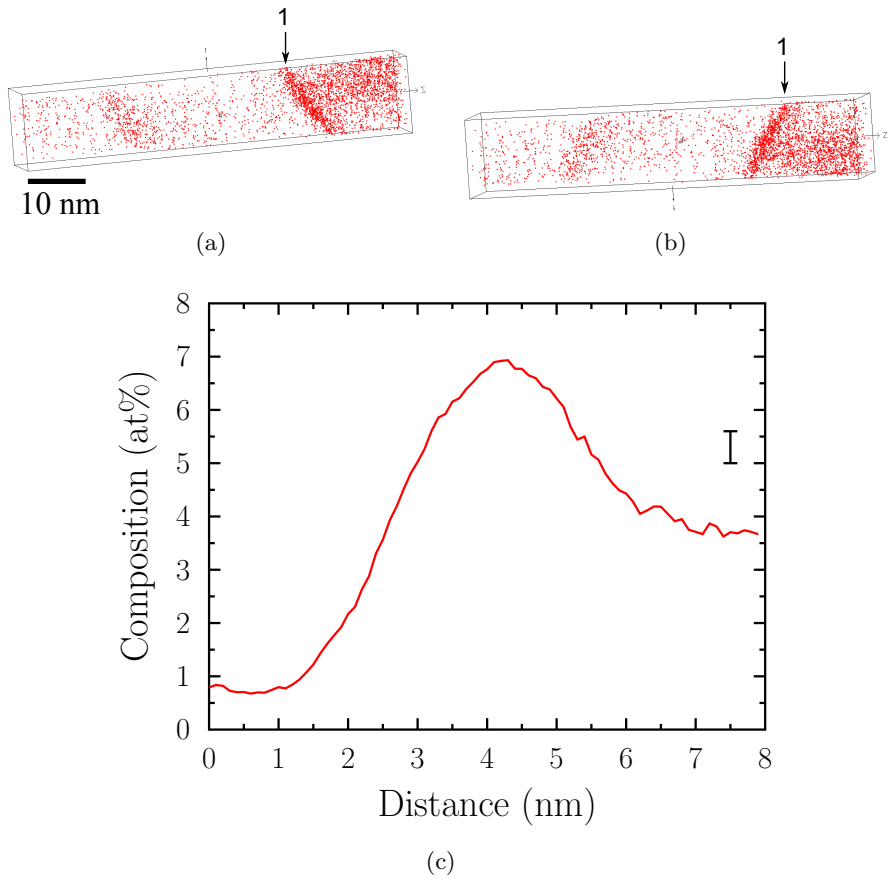

Figure 5.34: Reconstructed volume obtained in a specimen tempered one hour at 150°C. a) Three dimensional volume, $12 \times 12 \times 63$ nm^3 showing the flat carbon-rich region (3×10^5 atoms were detected), b) same as in a) but tilted 180° with respect to the length axis, and c) linear carbon composition profile obtained across region '1'.

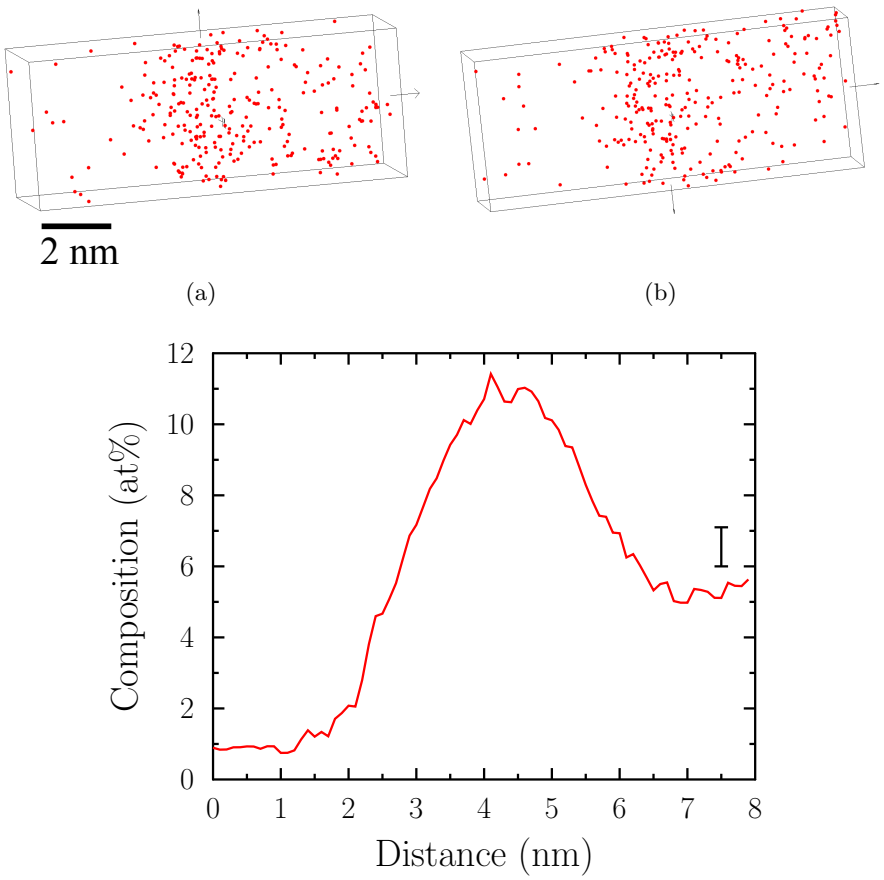

Figure 5.35: Reconstructed volume obtained in a specimen tempered one hour at 150°C. a) Three dimensional volume, $4 \times 4 \times 15$ nm^3 showing the equiaxed carbon-rich region, b) same as in a) but tilted 180°with respect to the length axis, and c) linear carbon composition profile obtained along the length of the box shown in a) and b).

Condition	at%C in seg.	t (nm)	λ (nm)	at%C in matrix
AQ	–	–	–	1.76
HeQ (sample 1)	3 ±1 - 8 ±1	3	–	∼1.76
HeQ (sample 2)	3 ±1 - 10 ±1	3.5	–	0.45
Q&T 120°C 1 hr	3 ±1 - 13 ±1	3	20	0.64
Q&T 120°C 8 hrs	3 ±1 - 12 ±1	4.5	17	0.76
Q&T 150°C 1 hr	3 ±1 - 16 ±1	5.1	31	0.48

Table 5.8: Summary of the three dimensional atom probe results. The thickness t of the segregations and the mean distance λ between two nearest segregations are presented. The carbon composition of the matrix and the carbon-rich regions are also indicated.

tion [7, 25]. More surprising, however, was the lack of carbide precipitation in TEM observations and the apparent homogeneity of carbon as observed in the APT volumes observed. Speich [12] has argued that all defects (lath boundaries, twin boundaries and dislocations) should be saturated in carbon after quenching a 1.5 mm thick sample having an Ms temperature of ~ 280°C (i.e. similar to that of the steel studied here) in ice brine (a cooling rate of $\sim 10^3$°C/s), this conclusion being raised on the basis of indirect electrical resistivity and internal friction measurements. According to calculations performed by Kalish and Cohen [71], a dislocation density of 10^{16} m^{-2} would lead to approximately 25% of the carbon being trapped by dislocations in a 0.4 wt% C martensite. The carbon level in the segregated regions around dislocations has been estimated to be approximately 8 at% C [60, 84], such a high degree of carbon redistribution should have been apparent in the observed APT volumes. It is possible that the observed volumes were too small to contain a defect. The volume presented in figure 5.17 (as well as the second volume observed after holding at room temperature for one month) were approximately 300 nm in length. This is significantly larger than the average lath size (0.19 μm, see figure 5.8) and twin spacing (between approximately 10 nm and and 100 nm). Moreover, though the dislocation density was not measured here, it is typically reported to be between $\rho = 10^{15}$ m^{-2} and 10^{16} m^{-2} in similar steels [12, 30, 97]. Based on these densities the

mean distance between dislocations should be between $\sim$ 32 nm and $\sim$ 10 nm. Therefore, the probability of having 1 or more dislocations within a sample volume 300 nm in length should be $1 - \exp(-300/32) \approx 1$. This observation appears to corroborate similar observations made recently by Hutchinson and co-workers in a low alloy 0.5 wt% C martensitic steel that had been brine quenched [35]. In this study APT measurements showed a close correspondence between the statistical distribution of carbon and the Bernoulli distribution (much closer than even that shown in figure 5.18) indicating a nearly random carbon distribution on quenching.

While the as-water-quenched condition studied here did not seem to have segregation at the amplitude expected based on the classic work of Speich and co-workers, some fluctuation around the mean composition (maximum amplitude being $\sim$ 3 at% C) was observed leading to a deviation between the measured carbon distribution and a Bernoulli distribution as shown in figure 5.18. This figure reveals that the carbon composition fluctuates around the mean composition with a wavelength of approximately 8 nm. Carbon fluctuations having a wavelength of this order of magnitude have been previously observed in Fe-Ni-C martensites [44] and have been linked to the appearance of the tweed microstructure in TEM observations. The observed carbon fluctuations here, however, seem to have a much lower amplitude than those observed in the Fe-Ni-C martensites ($\sim$ 3 at% C rather than $\sim$10 at% C). Moreover, none of the three TEM foils observed in the as-water-quenched condition revealed the morphological or diffraction features characteristic of the tweed microstructure.

While little evidence for extensive carbon redistribution was found in the case of the as-water-quenched martensite, the opposite was true of the as-helium-quenched martensite. TEM observations revealed substantial carbide precipitation (see figure 5.10) and APT revealed correspondingly significant carbon redistribution at the atomic scale (figure 5.19). An important observation was the heterogeneity of the precipitation/carbon distribution through the microstructure of materials prepared in this way, this having been previously reported in other slowly quenched martensitic steels (e.g. [68]). Carbide precipitation appeared absent in some portions of the micro-

structure (c.f. figure 5.10) and the two APT volumes observed in this state exhibited very different levels of carbon redistribution (figure 5.19).

One could understand this heterogeneity based on the fact that some laths are formed at, or close to, the Ms temperature while others will form at temperatures closer to room temperature. Equation 2.2 [14] allows for a prediction of the volume fraction of martensite formed as a function of the temperature below the Ms temperature. Linking this to a simple estimate of the effective carbon diffusion distance can give an idea of the extent of microstructure evolution, and its heterogeneity within a sample, as a function of the quench rate.

Estimating an effective average carbon diffusion distance as $\left\langle \sqrt{Dt} \right\rangle$ within a lath formed at a temperature T_0 below Ms one obtains,

$$\left\langle \sqrt{Dt} \right\rangle = \frac{1}{t_f - t_0} \int_{t_0}^{t_f} \sqrt{D\,(t - t_0)}\, dt \tag{5.1}$$

Where $D = 2 \times 10^{-6} \times \exp\left(-1.08 \times 10^5 / \left(8.314T\right)\right)$ [40, 151, 152] is the diffusion coefficient of carbon in martensite [1], t_0 is the time at which the lath formed, t_f is the time at which the temperature reaches room temperature, and t is the current time. If the cooling rate α is assumed to be constant between the Ms temperature and room temperature, then the temperature T and time t are related as,

$$T = \alpha(t - t_f) + T_f \tag{5.2}$$

Where T_f is the final temperature reached during cooling (e.g. room temperature) and t_f the corresponding time. Using equation 5.2, equation 5.1 can be expressed only as a function of temperature,

$$\left\langle \sqrt{Dt} \right\rangle = \frac{1}{T_f - T_0} \int_{T_0}^{T_f} \sqrt{D(\frac{T - T_f}{\alpha} + t_f)}\, dT \tag{5.3}$$

Varying T_0 between the Ms temperature (e.g. 282°C) and room tempe-

[1] As noted by Zener and Hillert [40, 151], the diffusion coefficient of carbon in martensite is typically lower than that for carbon in ferrite. Here we use the estimate made by Wang *et al.* [152].

rature (e.g. 20°C) allows for the distribution of carbon diffusion distances within a sample to be calculated as a function of quench rate. Assuming a constant quench rate of 190°C/s (water-quenching) and of $\sim$ 50°C/s (helium-quenching) (see section 4.3) gives the distribution of diffusion distances shown in figure 5.36. The maximum diffusion distance obtained after water quenching is only $\sim$ 3 nm and that after helium quenching is nearly twice that value. The absolute values of these estimated diffusion distances have to be viewed in light of the simple method used to obtain them, but the method does show a much more significant heterogeneity in the diffusion distance when helium quenching is considered compared to water quenching.

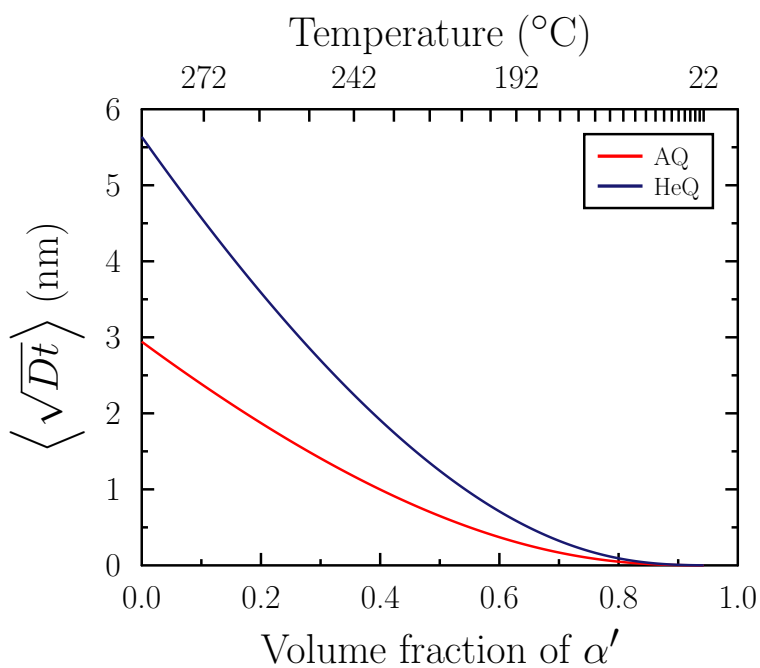

Figure 5.36: Diffusion distance as a function of total martensite fraction. AQ designates the as-water-quenched specimen and HeQ the as-helium-quenched specimen.

Focusing on the nature of the regions of carbon enrichment observed in the as-helium-quenched sample (figure 5.19), different morphologies and levels of enrichment were observed. Several roughly equiaxed features were

Condition	Atom probe	TEM
WQ	Slightly decomposed	No carbides detected
WQ + 1 month at RT	Slightly decomposed	–
HeQ	Largely decomposed	Carbides detected

Table 5.9: Summary of the microstructural observations revealing the effect of cooling rate.

observed in this volume. The size of these features as observed in the APT volume ($\sim$ 3nm) corresponds well to the size of carbides measured in the TEM (c.f. Table 5.5). Moreover, based on the estimated number density of precipitates ($\sim 10^{22}$ m^{-3}) in these samples it is anticipated that the APT volumes analyzed here should have a high probability of having 1 or more precipitates within them. If these equiaxed features were carbides, however, their measured compositions ($\sim$ 9.8 at% C) are much lower than those expected for stoichiometric η-carbides or ϵ-carbides [65]. This apparent discrepancy has been previously pointed out by Olson and Cohen [41] who noted that the expected carbon composition for η-carbides has never been observed in APT experiments. Instead, the carbon content of the carbides measured by APT appears to continuously increase during tempering from the bulk carbon content of the steel to 25 at% C corresponding to Fe_3C cementite [41].

Other regions of carbon enrichment were also observed in the as-helium quenched sample. Notably, one planar feature having a maximum carbon composition of $\sim$ 4 at% C was observed in the second volume shown in figure 5.19. It is impossible to be definitive about the nature of this feature. It is possible that it corresponded to segregation to a lath or twin boundary, or it could be a very thin layer of retained austenite between two lath boundaries. It is notable, however, that the level of carbon enrichment on this planar feature is similar to carbon segregation on lath boundaries in previous APT studies [18, 36, 57].

5.5.2 Effect of tempering on the microstructure of water-quenched specimens

As described above, the as-water-quenched samples appeared to be free of carbides and relatively (though not completely) homogeneous in carbon distribution. Upon tempering, however, significant changes in the precipitation state and carbon distribution were observed.

TEM observations of samples tempered for one hour at 120°C (see figure 5.11) revealed clear evidence of precipitation in some laths, though only weak or no evidence for precipitation in some other laths. As tempering time and/or temperature increased, this heterogeneity between the precipitation state in different laths diminished, while the measured average size and estimated volume fraction of precipitates were observed to increase. It is notable that the estimated number density of precipitates did not evolve strongly over the range of the tempering conditions (table 5.5) suggesting that precipitate growth (rather than nucleation or coarsening) was the dominant process occurring over the observed conditions.

It appears that the carbides were also inhomogeneously distributed within individual laths. As illustrated by figure 5.37 the carbides tended to be oriented along linear features within the microstructure. There has been some discussion in the literature over whether η and ϵ-carbides form homogeneously or heterogeneously within the early stages of tempering [41]. Early studies suggested that precipitation occurred homogeneously but more recent studies have strongly suggested at nucleation on dislocations (or other defects) or a nucleation from the initial tweed microstructure (when it exists) [41]. In the work of Hirotsu and Nagakura [65, 68] detailed transmission electron microscopy was used to clearly show that the precipitation of η-carbides occurred on dislocations, forming a pattern similar to that shown here in figure 5.37. Due to the high dislocation density in the current steels definite determination of carbide precipitation onto quenched-in dislocations was difficult. However, evidence of carbide precipitation onto lath boundaries was observed in samples tempered at 150°C for 1 hour via TEM (figure 5.12). APT observations on samples tempered for 8 hours at 120°C and 1 hour at 150°C also appeared to show equiaxed features having carbon compositions

of $\sim$ 12 at% C within planar features having lower levels of carbon enrichment (see figures 5.30 and 5.35), this also being suggestive of heterogeneous precipitation onto lath or twin boundaries. This view that the precipitation is heterogeneous and related to defects in the microstructure would be consistent with the view that the precipitation of the carbides is associated with a large volume change and that precipitation in the vicinity of defects (dislocations, lath or twin boundaries) may allow for a reduction in total strain energy associated with their formation.

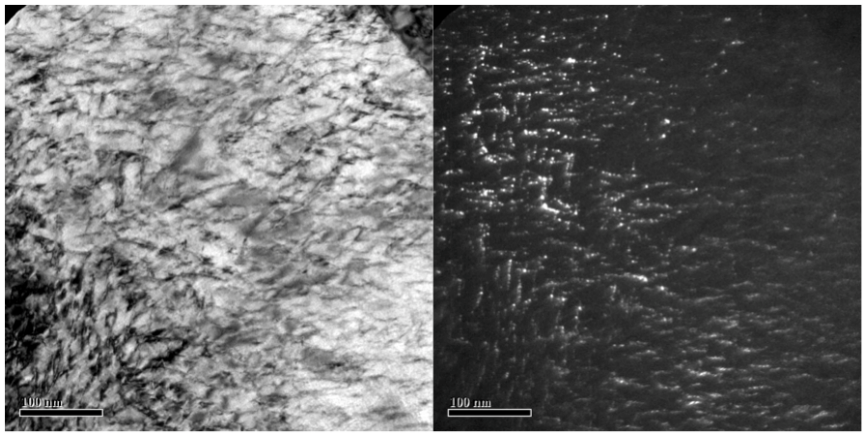

Figure 5.37: a) Bright field, and b) dark field TEM images revealing the non-homogeneous distribution of carbides within a single lath after tempering for 1 hour at 150°C.

At the atomic scale, the microstructure revealed by APT measurements in the tempered conditions shared many similarities with the decomposed microstructure of the as-helium quenched sample. In the tempered samples significant carbon redistribution was observed with linear, planar and equiaxed regions of carbon enrichment observed. The level of carbon enrichment measured by APT seemed to correlate to the morphology of the feature with the equiaxed features having higher carbon compositions than the planar and linear features (table 5.10).

The reconstructed volume shown in figure 5.26 contained two planar carbon-rich regions separated by a distance of $\sim$ 46 nm. This distance would

Shape	Composition range (at% C)
flat	$\sim$ 4 - 7
linear	$\sim$ 3 - 7.5
equiaxed	$\sim$ 5 - 16

Table 5.10: Summary of the microstructural observations revealing the effect of cooling rate.

be comparable to the spacing between fine laths or between twin boundaries (see figure 5.6). The carbon composition in these two carbon rich regions were similar, e.g. approximately 8 at% C. It has been reported that the carbon enrichment due to segregation to twin boundaries during tempering could be as high as 8.7 at% [57]. On the other hand, the maximum carbon composition segregated to inter-lath austenite films, or lath boundaries themselves, has been reported to be similar (e.g. $\sim$ 8 at% C) [18, 36].

Aside from planar (two-dimensional) features, there was also evidence of carbon enrichment along linear features as illustrated in figure 5.31 and 5.32. The level of carbon enrichment on these features was in the range expected for Cottrell atmospheres formed around dislocations [60, 153]. The maximum enrichment near these features also appeared to slighlty decrease when tempering was performed at 150°C compared to 120°C. This would be consistent with the expected dependence of segregation on temperature [153].

Finally, equiaxed carbon enriched clusters were also observed in the majority of the observed volumes from tempered samples. As in the case of the helium-quenched volumes, the spacing and size of these features were similar to that expected of carbides based on the TEM measurements. Also, as mentioned above, cases were observed where these equiaxed regions appeared to exist on planar regions of lower carbon enrichment, this being interpreted here as an example of heterogeneous precipitation on lath or twin boundaries. As illustrated in table 5.10, the composition of these regions fell well short of that expected based on the stoichiometric composition of η-carbides (Fe_2C [65]). As mentioned above, this carbon deficiency in carbides appears

to be characteristic of APT measurements on a wide range of steels [41].

Attempting to predict the above features of the carbon redistribution upon tempering is difficult owing to a poor knowledge of the metastable equilibrium between the transition carbides and carbon in solid solution within the martensitic materials. Moreover, as illustrated here, there appears to be significant discrepancy between the expected stoichiometry of the carbides and what is measured in APT. Despite this poor knowledge, it was attempted to capture the basic features of the observed behaviour based on pre-existing models for carbon segregation and precipitation.

In order to predict the evolution of the precipitation state, one needs to know the level of carbon in solid solution as well as the equilibrium solubility of carbon in the matrix phase with respect to the precipitate phase. It is expected, as described above, that carbon segregation to defects (most importantly dislocations owing to their high density in this material) will occur very rapidly upon tempering, the process being much faster than precipitation [154]. Above it was noted that for an upper bound dislocation density of 10^{16} m^{-2}, Kalish and Cohen [38] predict a total segregation of up to 0.1wt%C to these defects. This reduces the level of carbon remaining in solid solution from 0.4wt%C (1.8 at%C) to 0.3 wt%C (1.3 at%C), meaning that there would be a large amount of carbon remaining in solid solution. It is expected that such a high dislocation density would not be present uniformly throughout the material. Thus, it is likely that even after saturation of all defects that more than 0.3wt%C carbon remains in solid solution to facilitate precipitation.

The solubility of η-carbides (or ϵ-carbides) in martensite appears to remain an open question. In the recent work of Wang *et al.* [152] the experimental data presented by Chipman [155] was used to propose a solubility of $C_{eq} = 1.15\kappa \exp\left(-6100/\left(8.314T\right)\right)$ for ϵ-carbides (assumed as Fe_2C) in martensite. Here, this evaluation was also used as a starting point along with the assumption that the carbides are formed with the expected stoichiometry of Fe_2C. Clearly this does not match well with APT measurements made above but given the uncertainty in both the solubility and stoichiometry of the precipitates it was decided to use the above assumptions rather than

leave these parameters as variables. Despite these assumptions, this leads to a predicted equilibrium volume fraction of $\sim 3\%$ carbides at 350°C, this being similar to the volume fraction estimated experimentally in this study (table 5.5).

One of the features of the microstructure that appears characteristic of the low temperature tempered states is heterogeneity in the degree of precipitation from one lath to another. A possible source of this heterogeneity could be heterogeneity in local carbon composition due to, for example, carbon segregation to defects. Also, if as suggested above, the precipitation is heterogeneous this spatial variation in precipitation state could reflect variations in the defect density within different laths. It has previously been suggested that fine laths may posses a higher dislocation density than coarse laths [156]. Such a lath to lath variation may reflect the plastic accommodation processes that must occur during the formation of the martensite during quenching due to the volume expansion and shear accompanying the FCC $\rightarrow$ BCT transformation [30]. A simple model based on the idea of geometrically necessary dislocations [157] would suggest that the density of dislocations formed in a lath of thickness λ would be $\Delta\rho \approx K/(b\lambda)$, with K being a geometric constant and b being the Burgers vector.

To examine these possible effects a simple model has been developed to predict the kinetics of precipitation as a function of the dislocation density. This model builds on the original model of Deschamps and Bréchet [158], including some of the modifications suggested by Zurob *et al.* [159] to include site saturation on the rate of heterogeneous nucleation (the model is described in detail in appendix C). This model considers separately nucleation, growth and coarsening of precipitates (with an empirical transition between growth and coarsening regimes) and allows for the average precipitate size and number density to be tracked as a function of temperature and time. Using the equilibrium carbon solubility (C_{eq}) and carbide stoichiometry mentioned above, the volumetric free energy driving precipitation was

taken following Wang *et al.* [152] as,

$$\Delta G_v = \frac{kT}{\nu_{at}} \left[C_p \ln\left(\frac{C_{eq}}{C}\right) + (1 - C_p) \ln\left(\frac{1 - C_{eq}}{1 - C}\right) \right] \tag{5.4}$$

where ν_{at} is the atomic volume of iron, C_p is the atomic fraction of carbon in the carbides and C is the current average carbon atomic fraction dissolved in martensite. The effect of dislocations on nucleation was included in three separate ways in the model. First, the total number of nucleation sites was taken to be $N_{tot} = \rho/b$ where ρ is the dislocation density and $b \approx 0.25$ nm [159]. The possible saturation of these nucleation sites was accounted for by adding an Avrami-like term $(1 - N/N_{tot})$ to the classical nucleation equation following [159]. The effect of nucleation on dislocations in lowering the energy barrier for nucleation (ΔG^*) was simply captured by multiplying the barrier for homogeneous nucleation by a fitting parameter, ζ, where $0 < \zeta < 1$ [152]. The effect of dislocations was also considered based on the possible reduction in carbon in solid solution due to the segregation of carbon to defects dislocations [71]. Here we have assumed that segregation to dislocations occurs much more quickly than precipitation such that the defects are saturated in carbon prior to the onset of precipitation. Following Kalish and Cohen [71] the atomic fraction of carbon that can be segregated to dislocations is given by,

$$C_{sat} = \frac{\rho}{a_{seg}} \nu_{at} \tag{5.5}$$

where $a_{seg} \approx 2.5$ nm. Depending on the local dislocation density (ρ) the amount of carbon available for feeding precipitation is therefore given by $C_0 - C_{sat}$ where C_0 is the bulk carbon content of the alloy. This approach is clearly oversimplified as it does not consider the possible desegregation of carbon to feed the growth of precipitates nor does it consider the details of how segregation and precipitation may interact with one another.

Table 5.11 lists all of the parameters used in the model. Of these three were adjusted in order to get good agreement between the model and the experimentally measured volume fraction and size of precipitates for the

Parameter	Value (units)	Physical Meaning
a_{set}	2.5 nm	average distance between carbon atoms segregated to a dislocation
ν_{at}	1.1806×10^{-29} m^{-3}	Atomic volume of iron
D_0	2×10^6 m^2/s	Pre-exponential for diffusion [152]
Q	108 KJ/mol	Activation energy for carbon diffusion [152]
C_p	0.333	Atomic fraction of carbon in the carbides (assumed Fe_2C)
Adjustable parameters		
κ	0.95	*Adjustable* parameter for solubility of carbon in martensite in equilibrium with carbide
γ	85 mJ/m^2	Precipitate/matrix surface energy (*adjustable*)
ζ	0.2	*Adjustable* pre-factor for free energy barrier due to heterogeneous nucleation

Table 5.11: Summary of the inputs used for the modelling of precipitation and segregation.

measurements at 120°C and 150°C described in table 5.5. The interfacial energy between the precipitates and matrix (γ) was found to be most crucial for predicting the evolution of the size of the precipitates, while the pre-factor ζ for free energy barrier was crucial for obtaining the correct rate of precipitate evolution. Finally, it was found necessary to slightly adjust the solubility data proposed by [152] based on the experimental data of Chipman [155] by decreasing the solubility by 5% to obtain reasonable agreement with the estimated volume fraction of precipitates, i.e. $\kappa = 0.95$.

Despite the simplifications made in applying the above model, figure 5.38 illustrates that it captures reasonably well both the magnitude and evolution of the precipitate size and volume fraction upon aging at 120°C and 150°C. In order to make this comparison it was necessary to select a single dislocation density. Based on previous studies (as well as on the conclusions presented in chapter 7) that have reported dislocations densities of between 10^{14} m^{-2} and 10^{16} m^{-2}, a dislocation density of 3×10^{15} m^{-2} was used for these calculations.

Figure 5.39 illustrates the effect of changing the dislocation density between the absolute upper and lower limits expected within martensite [30] on the precipitation kinetics. As one can see, the rate of precipitation is

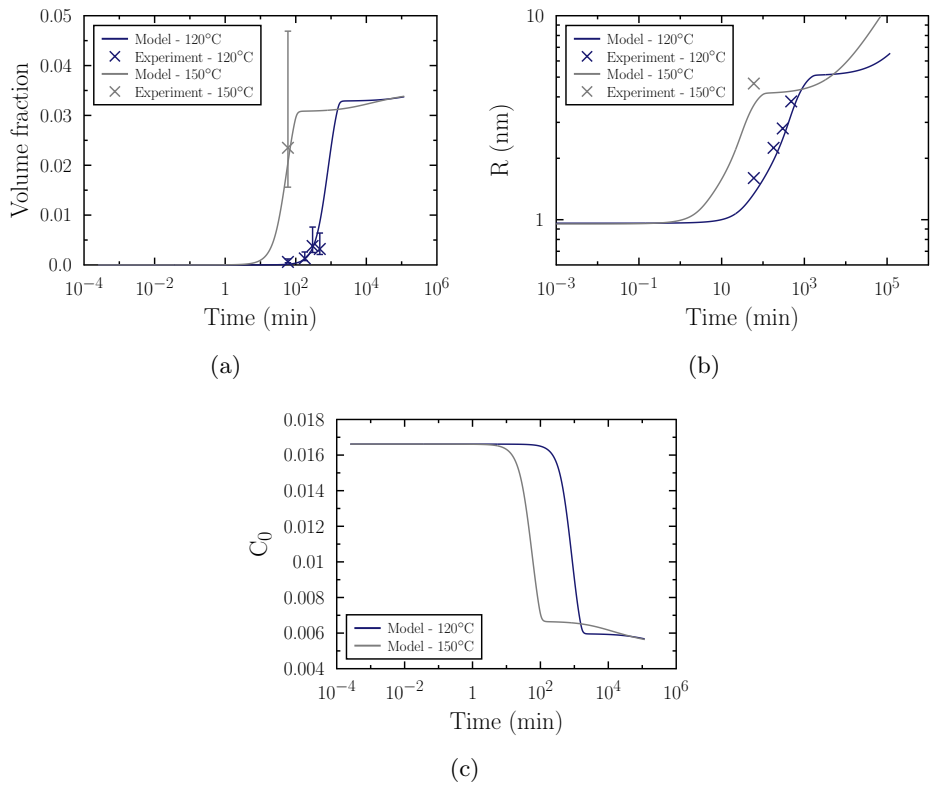

Figure 5.38: A comparison between model prediction (lines) and experimentally measured, a) precipitate radii, and b) precipitate volume fraction at 120°C and 150°C. Also presented (c) is the predicted evolution of the carbon in solid solution as a function of aging time. The calculations were performed using the parameters listed in table 5.11 and a dislocation density of $\rho = 3 \times 10^{15}$ m^{-2}. The error bars in a) represent the incertitude on the foil thickness.

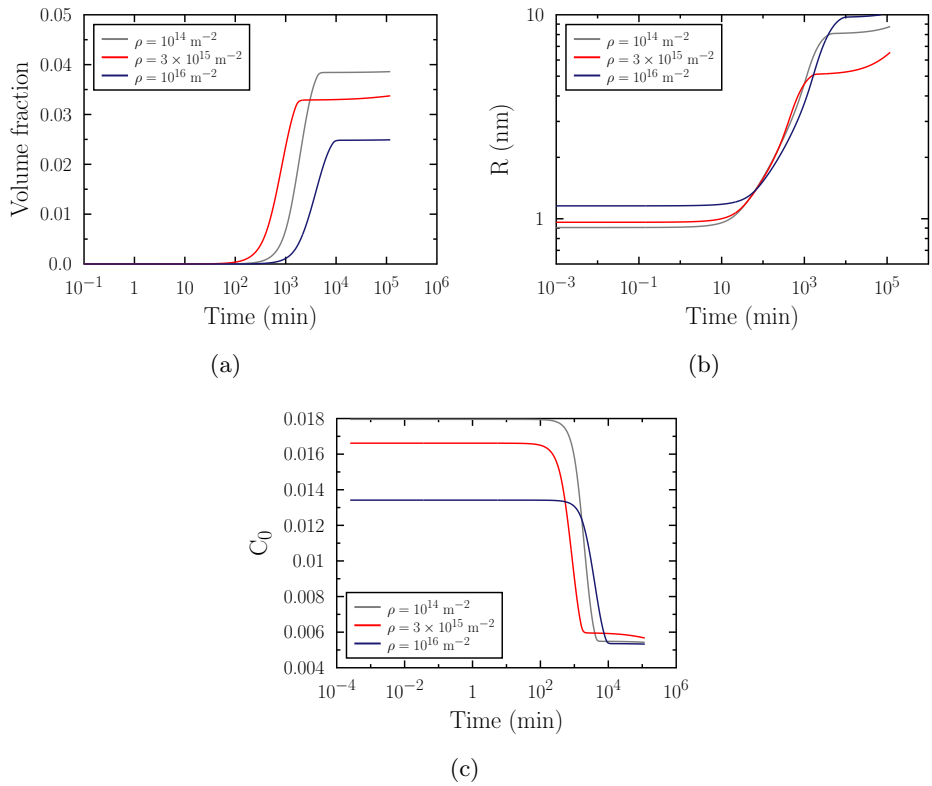

Figure 5.39: Effect of dislocation density on precipitation predicted by the model on tempering at 120°C. a) Volume fraction of precipitates as a function of tempering time, b) precipitate radii, and c) carbon in solid solution.

expected to be very low for dislocation densities below 10^{14} m^{-2}. While the evolution of the mean precipitate size with time does not appear to vary strongly with starting dislocation content, the evolution of the volume fraction does change significantly. With increasing density above 10^{15} m^{-2} the effect of increased nucleation sites causes a rapid increase in precipitation. This is also facilitated by the fact that the Kalish and Cohen model predicts only a slight decrease in carbon in solid solution for dislocation densities up to 3×10^{15} m^{-2} (e.g. at $\rho = 10^{15}$ m^{-2} 1.75 at% carbon is predicted to remain in solid solution). Increasing the dislocation density further leads to

a rapid decrease in the precipitation kinetics owing to a strong reduction in the amount of carbon predicted to remain in solid solution. At a dislocation density of 10^{16} m^{-2}, for example, the amount of carbon in solid solution after segregation is predicted to drop to 1.34 at% C.

This effect is further illustrated in figure 5.40 where the precipitate volume fraction and the amount of carbon remaining in solid solution is predicted as a function of dislocation density based on tempering at 120°C for 8 hours. Thus, if one were to envision a material which exhibited lath-to-

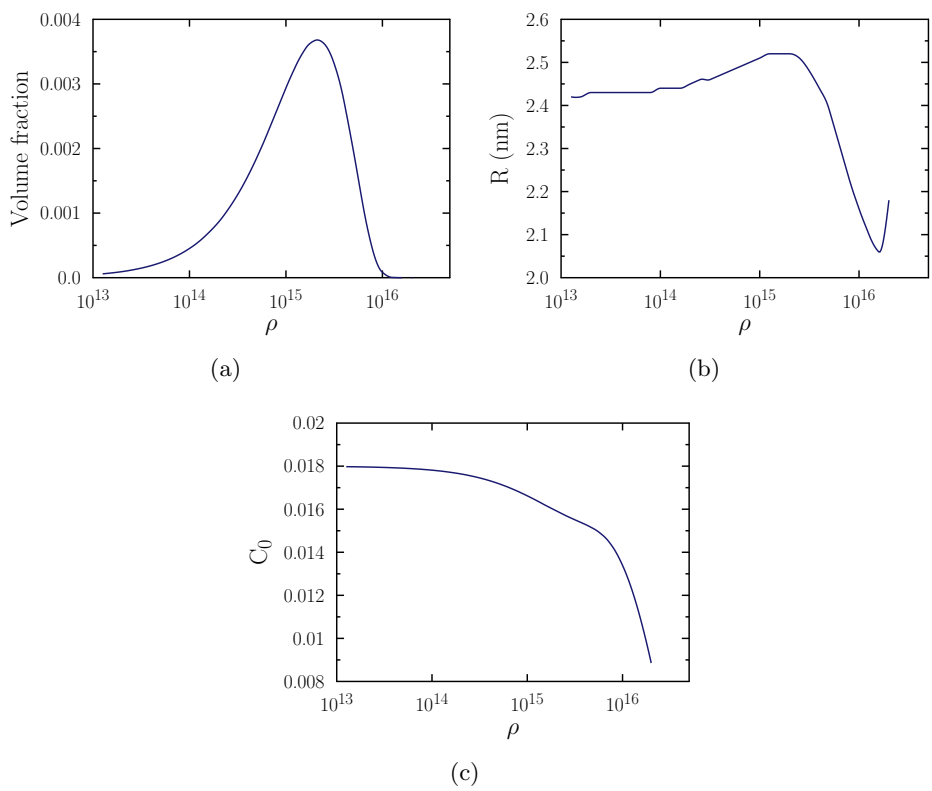

Figure 5.40: Effect of dislocation density on precipitation predicted by the model on tempering 5 hours at 120°C. a) Volume fraction of precipitates as a function of dislocation density, b) precipitate radii, and c) carbon in solid solution.

lath variations in the stored dislocation content within the range presented

here, one would expect to see strong heterogeneities in the lath-to-lath precipitation state (i.e. volume fraction) with some laths having nearly no precipitates and others having a well developed precipitate state.

Finally, it is interesting to observe what is predicted for higher tempering temperatures. Figure 5.41 shows the predicted evolution of the precipitate size and volume fraction on tempering at 350°C. While the ability to be

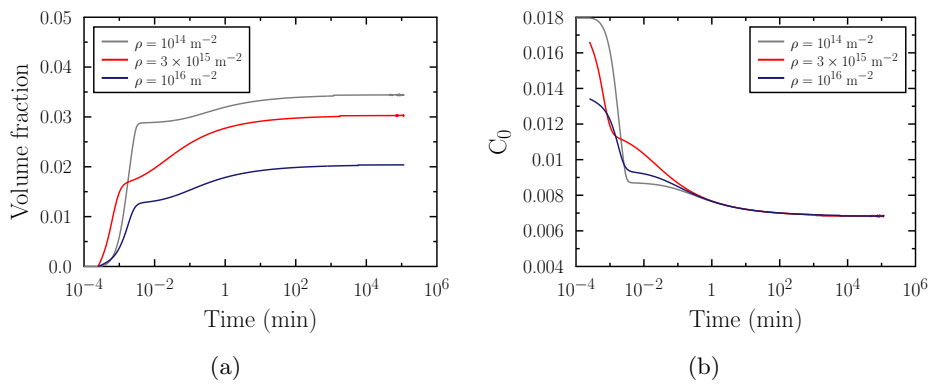

Figure 5.41: Model predictions for the a) volume fraction of precipitates and b) carbon remaining in solid solution for three different values of the dislocation density, after tempering at 350°C.

predictive in this condition is suspect due to uncertainty in (among other things) the carbon solubility at this temperature, the model clearly shows that at this temperature the precipitates are well into the coarsening regime and that the variation of the precipitate size and volume fraction becomes nearly independent of the dislocation density in this condition. This qualitatively matches with the experimental observations from the TEM observations described above.

5.6 Summary

A detailed microstructural study has been undertaken on the 300M alloy in both the as-quenched and quenched and low temperature tempered states. It has been shown that changing the cooling rate drastically changes the microstructure, particularly its heterogeneity at the microscopic and atomic

scale. In the as-water-quenched state only relatively small scale fluctuations of carbon were observed due to APT. Upon tempering this material, however, both carbon segregation to defects and carbide precipitation were observed. The carbides were identified based on diffraction as η-carbides, though (as in previous studies) the precipitates appeared to be substantially sub-stoichiometric based on APT measurements. The precipitation during tempering at 120°C was observed to be heterogeneous both within laths as well as from lath to lath. The heterogeneity within individual laths was attributed to heterogeneous precipitation of carbides onto defects, evidence of carbide precipitation on lath boundaries being found in both in TEM and APT observations. The lath to lath variation in precipitation kinetics was hypothesized as being due to differences in the dislocation density within laths. A model was developed and calibrated to the TEM measured precipitate size and volume fraction evolution at 120°C and 150°C. While the model predictions are hampered by a lack of knowledge about the equilibrium solubility of the carbides and the uncertainty in their composition, it was shown that the strong variations of the precipitation state after low temperature tempering could be qualitatively explained. Moreover, as observed experimentally, an increasing homogeneity of the precipitate state from one lath to another is predicted for higher tempering temperatures and/or longer tempering times.

Chapter 6

Mechanical Properties: Monotonic Loading

6.1 Introduction

The previous chapter provided a detailed characterization of the microstructure of the 300M steel following quenching and tempering. In this chapter, the material's monotonic mechanical response is reported and briefly discussed in relation to previous literature and the observed microstructure. A fully quantitative description is, however, reserved for chapter 7.

6.2 Monotonic torsion testing of the as-quenched and tempered steel

Torsion samples were austenitized and water-quenched following the procedure outlined in section 4.3. As shown in chapter 5, this processing is expected to minimize the auto-tempering on quenching, thus allowing us to study the evolution of the mechanical response starting from as close to a 'virgin' martensite as possible (in this type of steel) to conditions where significant carbon redistribution was observed. The resulting stress-strain responses, illustrated in figure 6.1 reveal a range of behaviours.

The mechanical behaviour shown in figure 6.1 can be separated into three

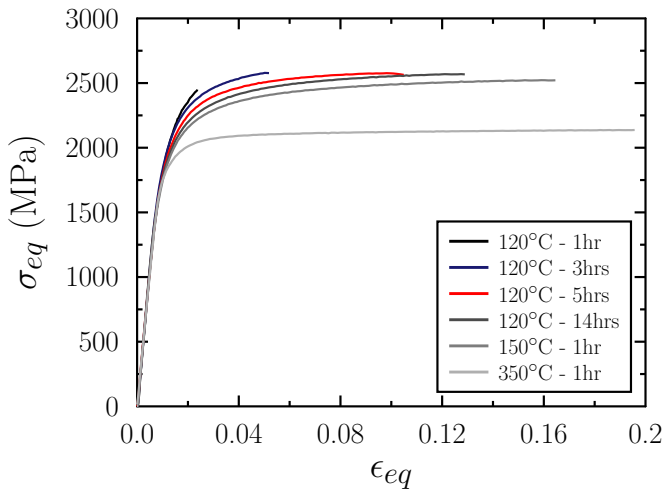

(a)

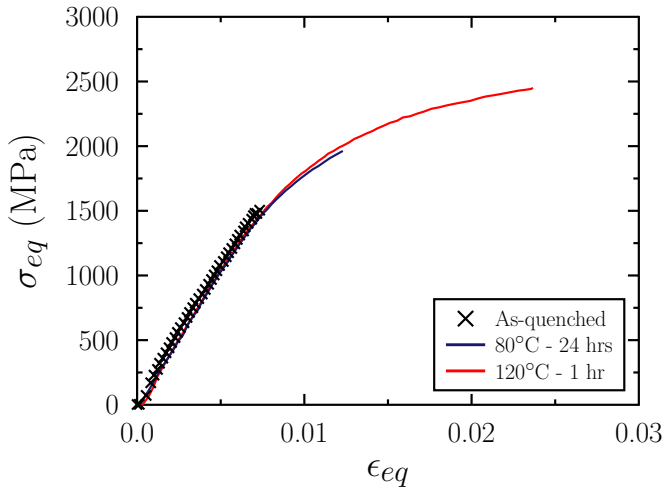

(b)

Figure 6.1: Equivalent stress-strain curves, up to fracture of a) all the conditions where ductility was observed, and b) a selection of conditions that exhibited brittle intergranular fracture.

types based on how the samples fractured (figure 6.2, table 6.1). When tem-

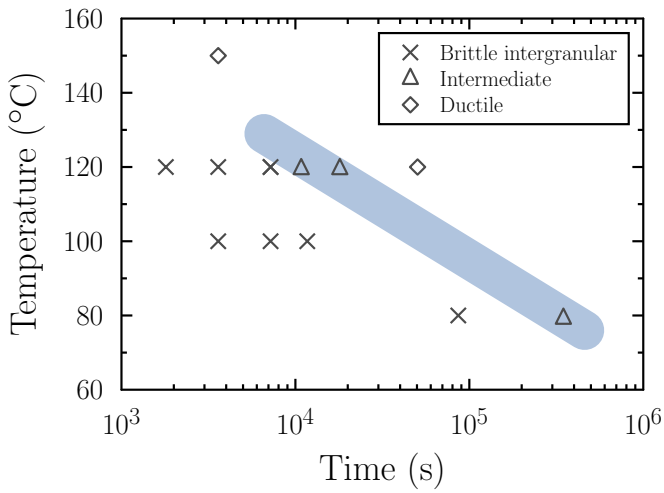

Figure 6.2: Summary of fracture behaviour as determined by observation of the fracture surface of samples as a function of tempering condition (cf. figure 6.3), particularly highlighting conditions at the transition between brittle and ductile behaviour. The blue line roughly separates intergranular brittle fracture from ductile fracture and passes through those conditions leading to an intermediate fracture condition.

pering was performed at too low a temperature and/or for too short a time it was found that the fracture was brittle as evidenced by a macroscopically flat fracture surface oriented at 45° to the torsion axis (i.e. perpendicular to the principal tensile stress). On the other hand, for tempering conducted at high temperatures and/or long time, the fracture surface appearance became rough and was oriented perpendicular to the torsion axis (i.e. in the plane of maximum shear stress). Finally, for some intermediate conditions, the fracture surface was found to have a macroscopic appearance that was very rough but not clearly oriented at either 45° or 90° to the torsion axis.

Observation of the fracture surfaces of these samples in the scanning electron microscope (SEM) revealed these differences to coincide with differences in the microscopic fracture behaviour. In the as-water-quenched and low temperature tempered conditions a brittle intergranular fracture

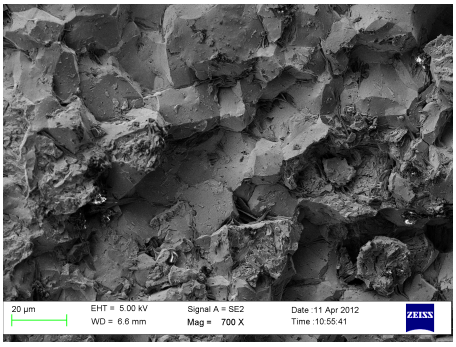

(a)

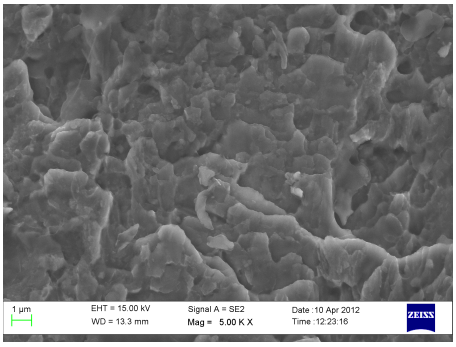

(b)

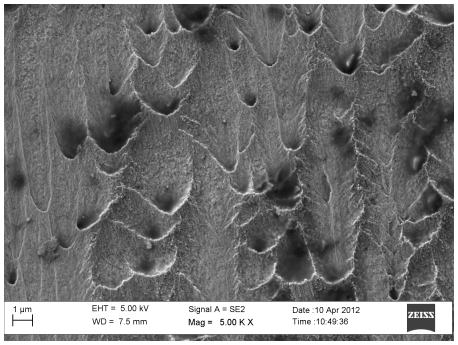

(c)

Figure 6.3: Typical fracture surfaces observed in the SEM for samples in the a) as-water quenched and b),c) tempered conditions. The fracture surface appears intergranular with facet sizes consistent with the prior austenite grain size. b) Fracture surface obtained for intermediate tempering conditions. The features on the fracture surface are difficult to identify but roughly correspond to the expected dimensions of laths [160]. c) Fully ductile shear fracture obtained from samples temperature at high temperatures and/or long times.

surface was observed, the facet sizes corresponding well to the prior austenite grain size (figure 6.3(a)). The high temperature/long time tempered samples, on the other hand, exhibited a fracture surface exhibiting ductile shear dimples (figure 6.3(c)). The fracture surface of the samples tempered under intermediate conditions revealed a more complex fracture surface with features having dimensions on the order of $\sim 1\ \mu m$.

Focusing first on the stress-strain response of those samples that exhibited purely intergranular brittle fracture (figure 6.1(b)) it was found that the fracture stress monotonically increased with tempering (figure 6.4 and table 6.1). In the as-water-quenched state, the material was observed to be macro-

Tempering temp. (°C)	**Tempering time**	σ_f **(MPa)**
AQ	–	1500
80	24 hours	1960
100	1 hour	1780
100	2 hours	2280
100	3.25 hours	2190
120	16 min.	1730
120	30 min.	2380
120	1 hour	2450
120	2 hours	2500

Table 6.1: Fracture stress (σ_f) as a function of tempering temperature and time. All the specimens failed in a brittle intergranular manner along the prior austenite grain boundaries.

scopically linear-elastic up to the point of fracture. No macroscopic evidence of plasticity was observed prior to fracture. Upon tempering at temperatures as low as 80°C, the fracture stress was observed to increase and evidence of bulk plastic flow became apparent prior to fracture. The tempering condition of 120°C for 1 hour (figure 6.1(b)) shows substantial evidence of non-linear plastic deformation, though the fracture surface appeared nearly identical to that of the as-water-quenched sample (figure 6.3(a)).

Figure 6.4 presents this evolution in fracture stress graphically, illustrating that by tempering at 100°C and 120°C the fracture stress of the material

could be increased by approximately 67% within a matter of a 1 - 5 hours.

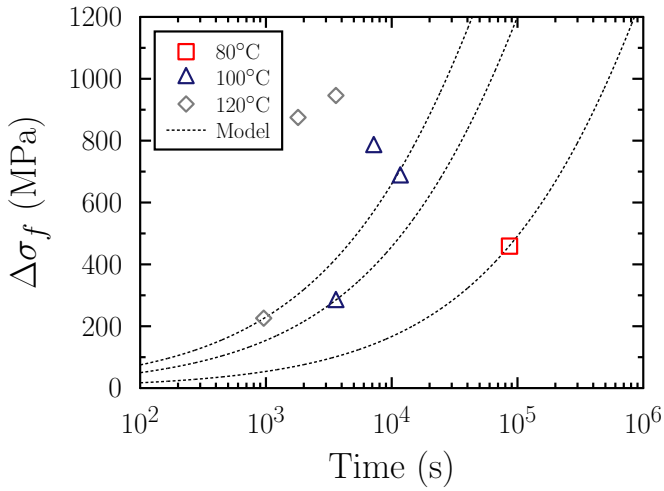

Figure 6.4: Measured evolution of in intergranular fracture stress with tempering at 80°C, 100°C and 120°C. Also plotted are the predicted kinetics of fracture strength evolution based on the assumption that the fracture strength evolves linearly with the degree of segregation to the grain boundary as predicted by the McLean equation (equation 6.1). Each curve corresponds to a different tempering time where the curves have been made to pass through the first data point in the case of each tempering condition. It can be seen that the rate of fracture stress evolution changes much more rapidly than this simple model would predict.

Tempering the material for longer times or at higher temperatures eventually led to increased plastic flow and to ductile fracture. Even in the case of the samples exhibiting the 'intermediate' fracture behaviour (figure 6.3(b)) elongations to fracture of $\sim$ 10% were obtained. In these ductile samples the yielding and work hardening behaviour were the focus of investigation. To compare the mechanical properties obtained in this work with mechanical properties obtained on similar martensitic steels, the ultimate tensile strength (UTS), the 0.2% offset yield strength and the uniform elongation

Temperature (°C)	Time (hours)	$\sigma_{0.2\%}$ (MPa)	ϵ_u (%)	UTS (MPa)
120	3	1820	–	–
120	5	1805	5.2	2360
120	14	1780	5.5	2350
150	1	1740	5.4	2290
350	1	1750	3.0	2010

Table 6.2: Mechanical properties of 300M martensite as a function of tempering.

have been obtained [1] and tabulated in table 6.2 and figure 6.5.

It has been reported on several occasions [79, 103, 108] that the offset yield stress of 0.4 wt% C martensitic steels increases after low temperature tempering, reaching a plateau after tempering for one hour at $\sim$ 200°C. Tempering for longer times or at higher temperatures results in a decrease in the 0.2% offset yield stress. For example, Shih *et al.* [79] have reported that the maximum increase in 0.2% yield stress upon low temperature tempering (at or below $\sim$ 200°C) of a 300M martensitic steel was $\sim$ 410 MPa. The results reported in table 6.2 and figure 6.5, however, show a continuous decrease of the 0.2% yield stress with tempering. These results, however, converge towards the behaviour reported in the literature with higher degrees of tempering [77, 79]. For example, Horn and Ritchie [77] reported a 0.2% offset yield strength of $\sim$ 1730 MPa for a 300M steel after tempering one hour at 350°C. This is within $\pm$10 MPa of the value reported here.

While the results for the offset yield stress presented above appear to deviate from the trends reported in the literature for short tempering times, the monotonic decrease of the UTS with tempering appears to agree well with literature [79, 108]. As for the 0.2% offset yield stress, the agreement between the results obtained here and those found in the literature is particularly good for higher tempering temperatures. The results obtained here

[1] The true uniform elongation was obtained based on the intersection between the Von Mises Equivalent stress-strain curve at its derivative plotted as a function of strain assuming the Considére Criterion. Based on this UTS was determined from the σ_{eq}, ϵ_{eq} curves based on the maximum equivalent stress and the true uniform elongation as, $UTS = \sigma_{ts} \times \exp(-\epsilon_u)$.

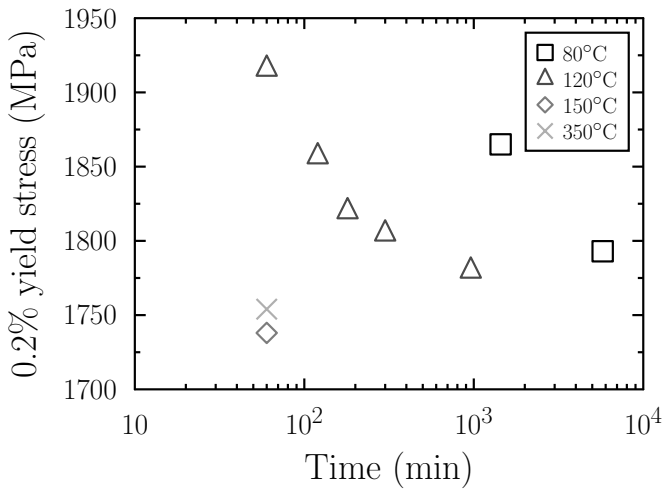

Figure 6.5: Evolution of the 0.2% yield stress with time, at different temperatures.

for samples tempered at 350°C corresponded closely to those of Shih *et al.* [79] and Horn and Ritchie [77] who also studied 300M steels. Shih *et al.* [79] obtained a UTS of ∼ 1930 MPa after tempering one hour at 700°F (∼ 370°C) and ∼ 2070 MPa after tempering one hour at 600°F (∼ 316°C). Horn and Ritchie [77] reported similar values of ∼ 2000 MPa after tempering one hour at 350°C.

For all samples exhibiting brittle intergranular fracture it was found that the samples failed prior to satisfying the Considère criterion. In all cases exhibiting intermediate or ductile shear fracture, it was found that the uniform elongation predicted based on the Considère criterion was nearly constant, and very low, at ∼ 5%. The only deviation from this was found for the sample tempered at 350°C where the uniform elongation was observed to drop to ∼ 3%. These results are consistent with other work [79, 102] where a similar drop in uniform elongation for higher temperature tempering has been reported, e.g. [79].

The apparent discrepancy between the evolution of the 0.2% offset yield strength measured here and that reported in the literature may have its origins in the initial work hardening response since the 0.2% offset yield

strength is sensitive to the shape of the stress-strain curve (figure 6.6) [102]. Significant differences in this aspect of the stress-strain response are found when the curves shown in figure 6.1 are compared to those found in the literature.

To study this further, the equivalent stress-strain curves were numerically differentiated and plotted as work hardening rate ($\theta_{eq} = d\sigma_{eq}/d\epsilon_{eq}$) versus equivalent stress (i.e. a Kocks-Mecking plot [161]). In these plots the work hardening rate was normalized by the Young's modulus measured on each stress-strain curve to remove small variations from test to test and to allow for the deviation from elastic behaviour to be clearly identified.

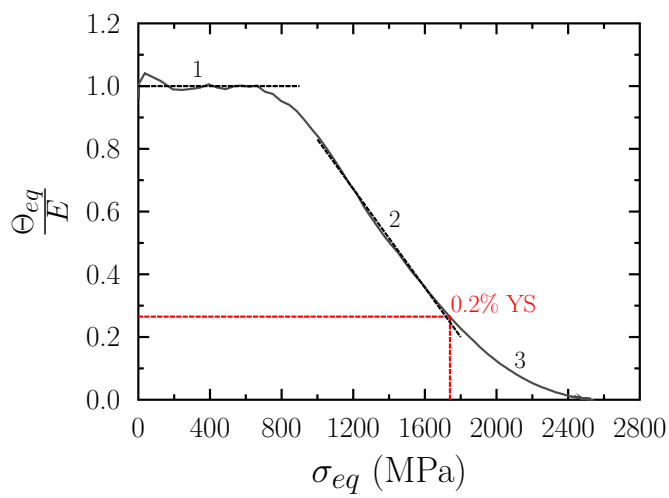

Figure 6.6: Typical normalized work hardening rate obtained on a specimen tempered one hour at 150°C, showing the three different regimes (see text).

The Kocks-Mecking plots obtained on all conditions exhibiting ductile behaviour are compared in figure 6.7. The work hardening response of these samples can be described as consisting of three parts (figure 6.6); an initial elastic regime (regime 1) followed by an approximately linear decrease of hardening rate with applied stress (regime 2), and a final exponential decay (regime 3). As previously pointed out by Saeglitz and Krauss [102] the initial rate of work hardening is extremely high. In simple cubic metals (such as

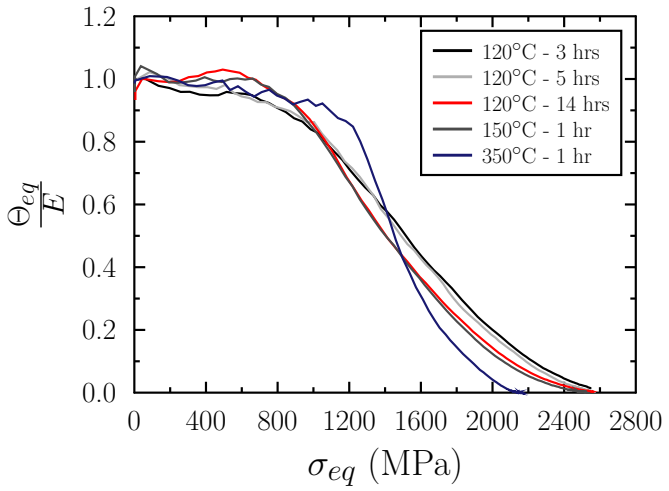

(a)

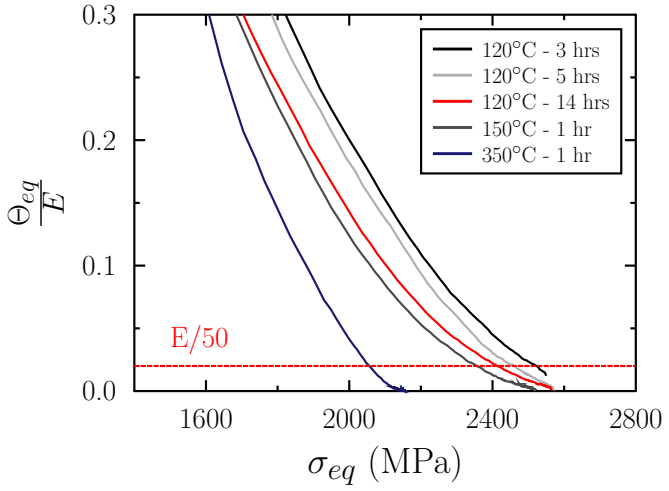

(b)

Figure 6.7: Normalized work hardening as a function of applied stress a) full curves and b) zoom-in to show the monotonic decrease of work hardening with tempering temperature and/or time. Note that, for clarity, not all the conditions are presented on the graphs.

pure iron) whose hardening is dominated by dislocation accumulation, the maximum rate of work hardening is typically found to be $\theta \approx \mu/20 \approx 0.02E$. In the case of the curves shown in figure 6.7(a) this hardening rate is achieved only well into regime 3.

Careful examination of figure 6.7(a) also reveals that the proportional limit [2] was between 600 MPa and 800 MPa, for samples tempered at 120°C and 150°C, the promotional limit appearing to increase with increased tempering. At 350°C the proportional limit was found to correspond to approximately 1000 MPa.

These proportional limits are similar to the few reported elastic limits [3] reported for similar steels in the literature ($\sim$ 550 MPa to $\sim$ 800 MPa) [79, 103, 162].

While the the transition between regime 1 and regime 2 in figure 6.6 appeared to be only weakly sensitive to tempering at temperatures below 350°C, the work hardening rate (at a given stress) in regime 2 decreased monotonically with tempering (figure 6.7(a)). This is associated with a change in the shape of the stress-strain response, the behaviour in regime 2 becoming less linear with increased tempering, similar to the observations made by Saeglitz and Krauss [102].

6.3 Effect of cooling rate on work hardening and yielding of the 300M martensite

As reported in chapter 5, the starting microstructure of the material depends on the rate of quenching, with the more slowly cooled helium quenched samples exhibiting significant decomposition (precipitation) following quenching. The resulting effect of this microstructural difference on the mechanical properties of the steel are illustrated in figure 6.8.

The most obvious effect of the quench rate was the fracture behaviour

[2] The stress at which first departure from a constant value of θ_{eq}, corresponding to linear elastic behaviour, was observed

[3] The elastic limits in [103] were measured by incremental loading-unloading of tensile specimens. The elastic limit was determined as the stress at which the first permanent deformation was observed after unloading. This should be comparable to proportional limit measurements performed here.

of the materials. The as-helium-quenched samples were found to be ductile, exhibiting a fracture surface with dimples identical to that shown in figure 6.3(c). In this condition the material exhibited significant ductility (the total elongation being $\sim 6.3\%$), and a UTS of 2510 MPa, this being slightly higher than the maximum UTS recorded in water-quenched and tempered specimen (2440 MPa).

Despite this higher UTS, the 0.2% offset yield stress was found to be 1610 MPa, approximately 200 MPa lower than the 0.2% offset yield stress measured for the water-quenched and low temperature tempered martensite materials (see table 6.2). The 0.2% yield stress measured in the helium-quenched samples was, however, in better agreement with the 0.2% yield stresses measured in the literature. Horn and Ritchie [77] found a value of $\sim$ 1660 MPa for the 0.2% yield stress of an as-quenched (in oil) specimen. This value is only 40 MPa higher than the value measured here.

The lower value of the 0.2% yield stress measured for the as-helium-quenched samples can be traced to significant differences between the work hardening behaviour of the helium-quenched and water-quenched and tempered samples as shown in figures 6.8(a) and 6.8(b). It was observed that the as-helium-quenched material yielded at stresses much lower than the $\sim$ 600 MPa to $\sim$ 800 MPa measured for the water-quenched and low temperature tempered specimens.

To investigate the effect of tempering on the behaviour of a helium-quenched sample, a sample was tempered one hour at 150°C (figure 6.8). Figures 6.8(a) and 6.8(b) show that the tempering treatment restored a clear linear elastic behaviour to the as-helium-quenched material. Moreover, the resulting mechanical response of this tempered state was nearly identical to the mechanical response obtained from the water-quenched material tempered under the same conditions (figures 6.8(a) and 6.8(b)).

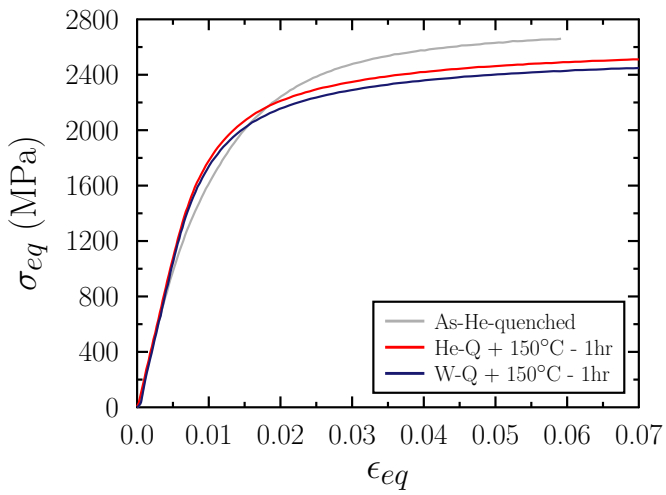

(a)

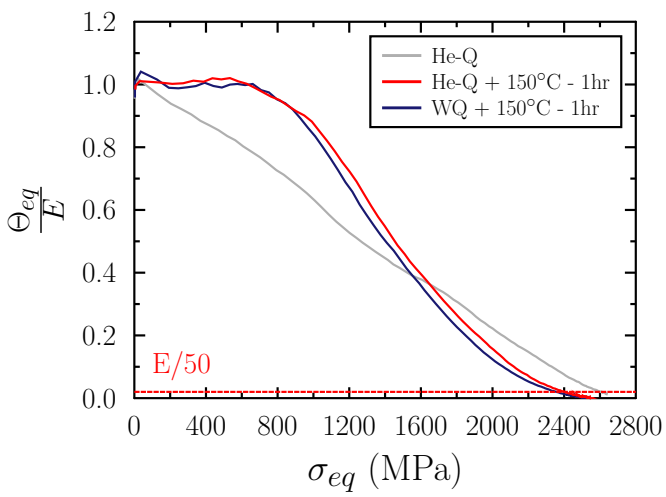

(b)

Figure 6.8: Influence of the cooling rate on the mechanical properties of martensite. a) equivalent stress strain curves up to fracture, and b) corresponding work hardening rate as a function of applied stress.

6.4 Discussion

6.4.1 Evolution of fracture behaviour on tempering

Intergranular fracture of as-quenched martensitic specimens tested at room temperature have been reported many times in the literature [10]. This phenomenon has been called 'quench embrittlement' as opposed to 'temper martensite embrittlement' [10]. However, quench embrittlement leading to brittle intergranular fracture was usually observed on martensitic steels containing more than 0.4 wt% C [10]. Here it was observed on a martensitic steel containing 0.4 wt% C. This is, however, not necessarily inconsistent with the literature. Shih *et al.* [79] reported a decrease in ductility in as-quenched 300M martensitic steels, compared to an as-quenched 4340 steel. Unfortunately, neither the fracture stress nor the fracture surface was reported for the as-quenched 300M steel in this work.

As noted in the chapter 2, quench embrittlement has been attributed to the segregation of impurities during austenitization [10]. Elements such as nickel, manganese and silicon are known to be grain boundary embrittlers [163–165]. Thus, in the present case, it is possible that quench embrittlement was due to prior austenite grain boundary segregation during austenitization.

As was shown in tables 6.1 and 6.2, the 0.2% yield stress was observed to vary weakly compared to the fracture stress with tempering. It would appear, then, that the evolution of the fracture behaviour upon tempering can be attributed to an increase of the fracture stress of the material rather than due to a change in the plastic response. More specifically, tempering appears to lead to an increased resistance of the prior austenite grain boundaries to brittle intergranular fracture.

In chapter 5, it was shown that the as-water-quenched microstructure had a relatively homogeneous carbon distribution, there being no evidence of precipitation in the TEM observations and no observations of large scale carbon enrichment/depletion in the, albeit limited, APT volumes observed. Upon tempering, the main changes to the microstructure involved the redis-

tribution of carbon to form regions of local enrichment due to segregation on defects and carbide precipitation. This observation would appear to be consistent with results obtained on the low temperature fracture of ferrite [166, 167] where it was observed that decarburizing ferrite to low carbon levels changed the fracture mode at 77K (in tensile tests) from intragranular cleavage to intergranular grain boundary fracture [166]. Recarburizing the material after a first decarburization restored the fracture mode to intragranular cleavage. This effect was ascribed to the increase of the cohesive strength of the grain boundaries by carbon segregation. The same qualitative conclusions were drawn by McMahon [167] whose experiments suggested that carbon strengthened grain boundaries as well as from recent theoretical calculations [163, 168, 169]. This interpretation would be consistent with the observation that as-helium-quenched samples were ductile (see figure 6.8), given that it was shown that in this state the material was strongly auto-tempered.

If the fracture strength of the material is controlled by carbon segregation to the grain boundaries on tempering then one would expect a correlation between the predicted segregation kinetics and the rate of evolution of the fracture strength (see e.g. figure 6.4). The McLean model for grain boundary segregation [170] is often used to describe the kinetics of grain boundary segregation,

$$\frac{C_b(t) - C_b(0)}{C_b(\infty) - C_b(0)} = \exp(s^2) erfc(s) \tag{6.1}$$

With $s = 2\sqrt{Dt}/\beta d$, where $C_b(t)$ is the instantaneous solute composition segregated on the boundary, D is the solute bulk diffusion coefficient, β is the equilibrium boundary enrichment ratio ($= C_b(\infty)/C_m$, where C_m is the bulk composition), and d is the boundary thickness.

Equation 6.1 suggests that for small times the grain boundary segregation kinetics exhibit a parabolic dependence with time [165]. Here, the evolution of the fracture stress with time was found to be much more rapid than what would be expected based on the McLean equation. This is particularly surprising given that the competition arising from segregation of carbon to other defects (e.g. dislocations, lath boundaries) should slow the

kinetics of grain boundary segregation [154]. Instead, this result would suggest that the fracture stress depends very strongly on the level of carbon segregation (i.e. the dependence is not linear between the two phenomena). It would appear that the functional dependence of carbon composition and grain boundary fracture strength is not known, and thus the results presented are not sufficient to confirm or deny this hypothesis. It is known, however, that very small carbon levels in ferrite are known to be effective in strongly increasing the fracture strength of ultra low carbon steels [166, 167].

As a final comment on the observed fracture response of these steels an intermediate fracture behaviour was also observed (see figure 6.3) that could not be clearly identified as brittle or ductile. The typical scale of the features observed on this fracture surface was approximately 1 μm or lower. This length-scale is similar to the lath size and packet size (see chapter 5). Ohtani and McMahon [160] have observed an identical type of fracture surface in bainitic steels. Here they attributed the fracture to be due to the propagation of cracks along the packets and/or lath boundaries. This was demonstrated by careful metallographic investigation involving electron microscopy observation of cracks on polished and etched specimens to reveal the microstructure.

6.4.2 Plastic deformation: yielding and work hardening behaviour

When the 300M martensite was sufficiently ductile, yielding was observed to be continuous (see figure 6.1) with no yield point. This observation is perhaps surprising since, as shown in chapter 5, carbon is expected to form Cottrell atmospheres around dislocations. In low carbon ferrite ($\sim$ 10 ppm by weight), the stress strain response exhibits a clear upper yield point, followed by a small yield drop and Lüders elongation under conditions where the material is strain-aged [171]. The upper yield point is considered to be characteristic of the stress needed to unpin dislocations from these atmospheres [61] and the length of the Lüders plateau is observed to be inversely proportional to the grain size [172]. As shown in chapter 5, the lath spacing of the 300M is fine ($\sim$ 200 nm). Therefore, all the conditions

were favourable for the observation of a yield point phenomenon and Lüders bands during mechanical testing of the 300M martensite.

The lack of yield point has previously been attributed to the possible existence of large residual stresses in as-quenched samples [90, 102]. An alternative explanation, however, would be that it is not the locked dislocations arising from the martensitic transformation that carry plastic deformation. In this case the plastic deformation of the martensite would be facilitated by the generation of new dislocations free of carbon atmospheres.

To test these hypotheses a simple experiment was performed where two tempered samples (5 hours at 120°C) were deformed to 0.45% and to 3.6% strain. Following this the samples were re-tempered for 3 hours at 120°C. One can clearly see the increase of yield strength following the second tempering treatment (figure 6.9). The sample pre-strained 0.45% did not exhibit

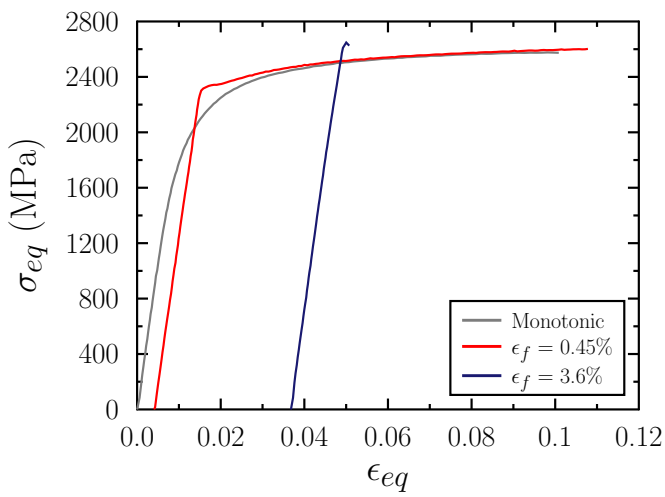

Figure 6.9: Mechanical properties of strain-aged specimens after two different pre-deformations. The material was tempered 5 hours at 120°C, plastically deformed, re-tempered 3 hours at 120°C and subsequently redeformed.

a clear yield point but this may be due to the relatively low image acquisition frequency for the DIC system compared to the sharp yield point behaviour expected. More interestingly, it was found that the sample pre-strained

3.6% exhibited a large increase in yield strength following tempering but that the sample failed immediately following the onset of yielding. Such a strain-aging effect has been previously observed in martensite [83, 85, 173].

The fact that the material subjected to the initial tempering treatment (5 hours at 120°C) exhibited the rounded yielding behaviour but that the samples strain aged for 3 hours at 120°C exhibited a sharp yield point would seem to preclude residual stresses as the origin of the rounded stress-strain response since there is no reason to believe that the second thermal treatment would be able to remove these residual stresses when the first treatment could not. As will be seen in chapter 7, the lack of large residual stresses in the tempered conditions is also fully consistent with the results of Bauschinger testing.

Saeglitz and Krauss [102] interpreted the high work hardening of quenched and tempered medium carbon martensites (similar to the material studied here), as being due to solute drag between carbon atoms in solid solution and moving dislocations. They claimed that this would be supported by the fact that negative strain rate sensitivity (at room temperature) was measured in similar martensitic steels [90]. To further investigate this, the room temperature strain rate sensitivity of a specimen tempered one hour a 150°C was tested monotonically at a lower strain rate ($\sim 10^{-4}$ s^{-1}) than that used in the experiments reported above ($\sim 10^{-3}$ s^{-1}) and in strain rate jump experiments. The strain rate jump experiments were performed by changing the displacement rate of the machine to give strain rates of $\sim 10^{-4}$ s^{-1} and $\sim 10^{-3}$ s^{-1}. Due to the relatively low frequency of DIC image acquisition it was not possible to measure accurately the flow stress jump associated with the fast jump in strain rate. Thus, in these cases the strain was monitored by the rotational displacement of the actuator.

Figure 6.10(a) shows the monotonic stress-strain response performed at $\sim 10^{-3}$ s^{-1} and $\sim 10^{-4}$ s^{-1}. Indeed, it is observed that the test performed at $\sim 10^{-4}$ s^{-1} results in a slightly higher rate of work hardening than that performed at $\sim 10^{-3}$ s^{-1} suggesting a negative rate sensitivity. It is notable, however, that the two curves only start to diverge above ~ 2000 MPa and that the separation between the curves is not very large ($\leq 10\%$). The

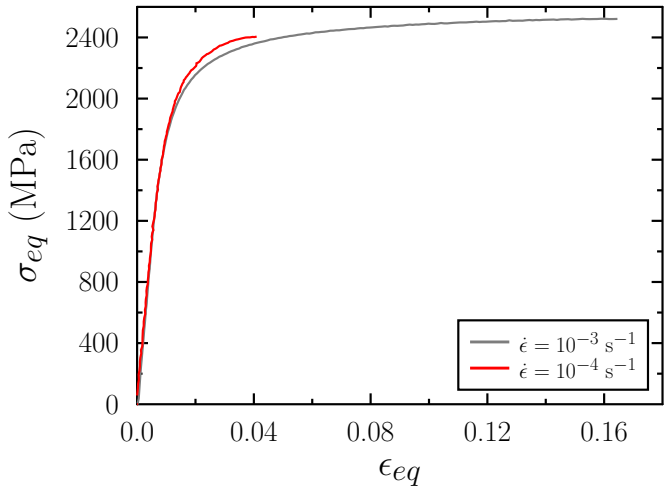

(a)

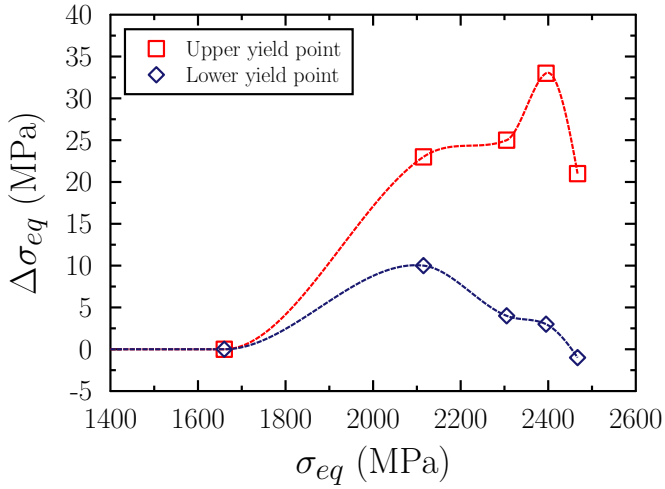

(b)

Figure 6.10: Rate sensitivity tests performed in the 300M martensite tempered one hour at 150°C. a) Comparison of monotonic stress-strain curves performed at $\sim 10^{-3}$ s^{-1} and $\sim 10^{-4}$ s^{-1}. b) The change in flow stress following a jump from $\sim 10^{-4}$ s^{-1} to $\sim 10^{-3}$ s^{-1}.

difficulty with the determination of rate sensitivity from monotonic tests is that the two materials may develop very different microstructures. In the present situation, the segregation of carbon to dislocations may produce a cumulative effect on the shape of the stress strain curves in figure 6.10(a). By measuring the change in flow stress by performing rate jumps one can attempt to overcome this since the flow stress of the same (or nearly the same) microstructure can be tested. The change in the flow stress following upward rate jumps (i.e. from the slower to the faster strain rate) is illustrated in figure 6.11. In these tests, the material was deformed alternatively

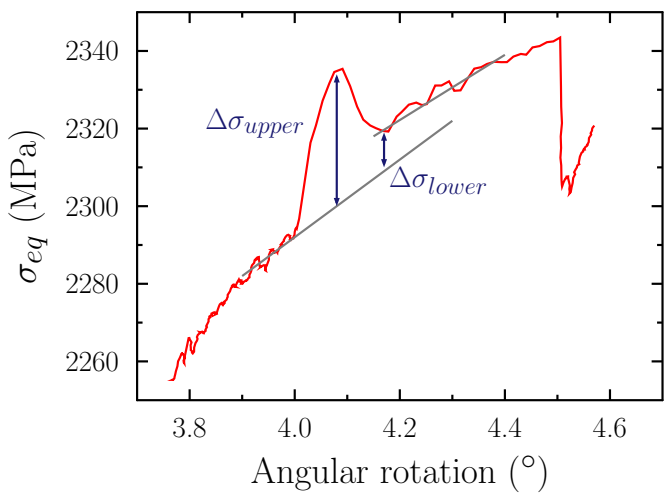

Figure 6.11: Stress-angular rotation graph showing the typical response of the material to a sudden increase in strain rate. The upper and lower increases in flow stress corresponding to figure 6.10(b) are indicated.

at two different strain rates (e.g. $\sim 10^{-4}$ s^{-1} and $\sim 10^{-3}$ s^{-1}), the transition between the low strain rate regime and the high strain rate regime being almost instantaneous. The angular rotation during each regime was fixed at $\sim 0.5°$.

As shown in figure 6.11 the flow stress showed a transient behaviour upon a rate jump, a distinct transient yield point being observed at the point of the jump. Following this, the flow stress decreased and approached a smooth

evolution. This does suggest that there is a dynamic interaction between the mobile dislocations and solute atoms. Upon an increase in strain rate, dislocations are forced to pull away from their solute clouds leading to a small yield point, the magnitude, however, being very small as shown in figure 6.10(b). Also plotted in this figure is the change in flow stress when the flow stress following the jump is taken following the yield point. These results show that the rate sensitivity increases from approximately zero at the point of the first rate jump (at 1600 MPa, well beyond the first point of yielding) coming to a maximum at $\sim$ 2100 MPa. Above this level of stress, the rate sensitivity appeared to decrease again towards zero. Indeed it was observed to be slightly negative as shown in figure 6.10(b). These results would suggest that the strain rate sensitivity is negative only once the material has undergone significant plastic deformation, i.e. after the elasto-plastic transition where the largest rate of work hardening is observed. Thus, while it is quite likely that dynamic strain-aging contributes to the work hardening at larger strains, it can be seen that this work hardening rate is very small relative to the behaviour within the initial yielding regime.

As noted above, the extremely high work hardening rate upon yielding is also incompatible with typical dislocation based forest hardening mechanism observed in single phase cubic materials ($d\sigma/d\epsilon \sim \mu/20$). Saeglitz and Krauss [102] proposed that transition carbides could modify the hardening rate but their interpretation was based on the assumption that the precipitates are non-sharable and that relaxation processes do not significantly reduce the load-transfer to the precipitates. Given the small size and roughly equiaxed morphology of the precipitates (at least for tempering below 350 °C) presented in chapter 5, these assumptions do not appear to be easy to justify.

It is important, however, to reflect upon the observations presented in chapter 5 regarding the heterogeneity of the microstructure. A distribution of lath size, dislocation density, precipitation state and carbon in solid solution was argued for in the cases of the low temperature tempered samples. This observation presents the possibility that very different stresses are required to initiate plastic flow in different laths. Considering the fact

that the state of precipitation was hypothesized to be directly linked to the dislocation density and the lath size distribution (with an increasing rate of precipitation within finer laths containing a higher density of dislocations) one might expect a direct or indirect correlation between mechanical response and lath size/lath size distribution. As mentioned earlier, the 0.2% offset yield strength has often been linked to the lath size distribution in martensitic steels and, empirically, strengthening laws for martensite often incorporate a Hall-Petch like expression including the effect of the average lath and/or packet size [108].

This interpretation would point to the initial yielding response of martensite being like that of a composite material containing a large number of elements each having a different yield stress and (possibly) work hardening rate. This would be consistent with the large work hardening rate observed between the proportional limit and the UTS of the material. In this case, the work hardening would reflect an extended elasto-plastic transition. Such an interpretation would be consistent as well with the strain rate change experiments illustrated in figure 6.10(b). Since the rate sensitivity of elastically loaded 'elements' of the microstructure would be zero, it would be expected that the rate sensitivity should monotonically increase with the fraction of material that has yielded, as observed here.

Another factor that may play an important role, however, are residual stresses generated during the quenching. While it was argued above that these could not completely explain the observed elasto-plastic transition, they could significantly affect the shape of the loading behaviour and, thus, measurements of parameters such as the 0.2% offset yield strength. It was pointed out that the elasto-plastic transition was very different for the helium-quenched materials when compared to samples that had been subjected to low temperature tempering (see figure 6.8). Part of this difference may come from the larger degree of heterogeneity in the as-helium-quenched samples as illustrated by the comparison of the diffusion distances in figure 5.36. However, this explanation alone seems unable to explain the very low proportional limit measured for the as-helium-quenched material. Low elastic limits have been observed in as-quenched and quenched and

low temperature tempered martensitic steels with various carbon contents [79, 103]. Muir *et al.* [103] reported elastic limits for as-quenched martensitic steels between $\sim$ 140 MPa (for a 0.2 wt% C martensitic steel) and $\sim$ 165 MPa (for a 0.4 wt% C martensitic steel). These values were reported to markedly increase (by $\sim$ 275 MPa for the 0.2 wt% C martensite and by $\sim$ 415 MPa for the 0.4 wt% C martensite) after tempering one hour at or above 150°C. This increase was attributed to the relaxation of quenched-in residual stresses. Although the physical origin of those quenched-in residual stresses was not discussed by these authors, one could assume that they came from the use of both low quench rates (oil quench is less efficient than water quench [32]) and large tensile testing samples (round bars 6.4 mm in diameter) [103]. The low quench rate would favour carbon redistribution [12] during the quench and large samples would favour heterogeneities of carbon redistribution across the specimen's cross section [33]. Waterschoot *et al.* [63] performed dilatometric measurements that showed that carbon redistribution during tempering at low temperature induced volume compression. Therefore, heterogeneous carbon redistribution would cause heterogeneous local variations of volume. Those variations of volume could induce the observed quenched-in residual stresses in as-quenched and quenched and low temperature tempered martensite [103]. Tempering would tend to even out the heterogeneities in carbon redistribution, thereby evening out the local volume changes associated with carbon redistribution. This would explain why quenched-in residual stresses are relaxed on low temperature tempering. Monotonic mechanical testing alone is not well suited for assessing the presence of such internal residual stresses. Thus, in order to go further with the interpretation of this material it was necessary to undertake a set of experiments that would give us further insights into the mechanical response. These tests are described in the next chapter.

6.5 Conclusion

The monotonic torsion response of the 300M steel in the as-quenched and tempered states has been summarized here. The results generally follow

the trends observed in the literature, though it has been argued that slight differences in the sample size and/or cooling rate can have a significant effect on parameters such as the 0.2% offset yield strength. In fact, it has been argued that parameters such as the 0.2% offset yield strength, which is often given in the literature as a measure of the material's yield strength, is actually very sensitive to a number of factors as it is strongly influenced by the shape of the initial portion of the stress-strain response. This initial work hardening rate has been analyzed and some comparisons with previous suggestions about the origins of the high initial work hardening rate have been made. It is argued here that the initial yielding response is indicative of a material undergoing an elasto-plastic transition where the material yields progressively over a wide range of imposed stresses. The origins of this extended yielding response have been argued as being related to the heterogeneity of the microstructure of the material as revealed in chapter 5. In the next chapter the consequences of this heterogeneity on the mechanical response are explored in more detail.

Chapter 7

A Composite Model for the Room Temperature Mechanical Response of Martensite

7.1 Introduction

It was noted that the initial work hardening rate observed in tempered 300M steel samples is much higher than the maximum hardening expected from dislocation-based hardening alone. To try to better understand the origins of this hardening behaviour as well as to provide more information on the possible strengthening mechanisms Bauschinger experiments were performed.

The accumulation of internal stresses during plastic deformation of metals give rise to an asymmetry in the yield strength upon a strain path change, this being referred to as the Bauschinger effect [174]. Thus, measuring this can allow for the determination of the magnitude of internal stresses contributing to the total hardening of the material. The Bauschinger effect has proven to be useful in understanding of the work hardening process in,

for example, precipitation hardened alloys [175–177], single phase materials [178–181] and metal matrix composite materials [182].

Samples tempered 3 hours and 5 hours at 120°C, one hour at 150°C, one hour at 350°C, and as-helium quenched have been studied. As shown in chapter 5, these conditions led to a wide range of microstructures. In this chapter, the Bauschinger effect of the 300M material treated as described above is analyzed. This starts with a short description of the experimental results, and continues on with a more sophisticated approach building on Masing's original idea [183]. It is hypothesized here that the mechanical behaviour of martensite must consider the heterogeneity of the microstructure as characterized in chapter 5. Thus, rather than describing the material as being composed of one hard phase (precipitate) and one soft phase (matrix) it would be much more appropriate to describe the material as being made up of a distribution of yield strengths attributable to different 'elements' of the microstructure. In this case, these 'elements' are considered to be the individual laths since it was shown that the dislocation density and precipitation state seem to vary strongly from one lath to another.

The method originally developed by Masing [183] provides a basic framework for considering the scalar behaviour of materials having a distribution of yield strengths in the limit of elastic-perfectly plastic behaviour of the individual elements, elastic and plastic isotropy and conditions of uniform strain. While the original Masing model was built from a finite number of microstructural 'elements', it has been extended more recently to use a continuous distribution of yield strengths as suggested by [184–187]. This approach has been used to explain the effect of grain size distribution on the yielding of polycrystals [188] as well to the evolution of internal stresses (determined by X-ray diffraction) during straining of high and low carbon spheroidized steels [184]. Most importantly, the model has been applied with some success in a very recent study to the elasto-plastic transition in martensite [189].

The Masing model is applied in this thesis to capture both the monotonic and strain reversal experiments described in the past two chapters. As a starting point, it is hypothesized (based on the work in [189]) that the

continuous distribution of yield strengths of the microstructural 'elements' in the material can be reasonably captured by a log-normal distribution. This choice is motivated by the above results which suggest a relationship between the microstructural heterogeneity (dislocation density, precipitation state and carbon in solid solution) and the lath size distribution. Having empirically fit these distributions to the experimentally measured stress-strain curves, a simple physical model will be developed to explain the shape of these distributions and its evolution on tempering. Finally, the model will be applied to two other steels in order to evaluate its ability to capture the response for martensite having other carbon contents.

7.2 Measuring the Bauschinger effect in martensite

Bauschinger tests were performed according to the methodolgy outlined in chapter 4, and the results are summarized in figure 7.1. All the curves exhibited a transient regime after strain reversal, before approaching a similar flow stress to that measured in the forward portion of the test. In none of the conditions investigated was permanent softening observed.

A common way to quantify the Bauschinger effect is to measure the back-stress σ_b [107], which is a measure of the internal stress in the softest phase of the material [184, 190, 191] (see appendix D). However, the back-stress determined this way necessitates the use of an offset to calculate the reverse yield stress, making the final results strongly dependent upon the choice of the offset [107, 175]. In addition, unlike in precipitation hardened alloys where the soft phase (matrix) can be easily differentiated from the hard phase (precipitates), as shown in chapter 5 describing martensite as a two-phase composite is inadequate. For these reasons, it was felt that another technique would be needed to interpret the overall stress-strain response.

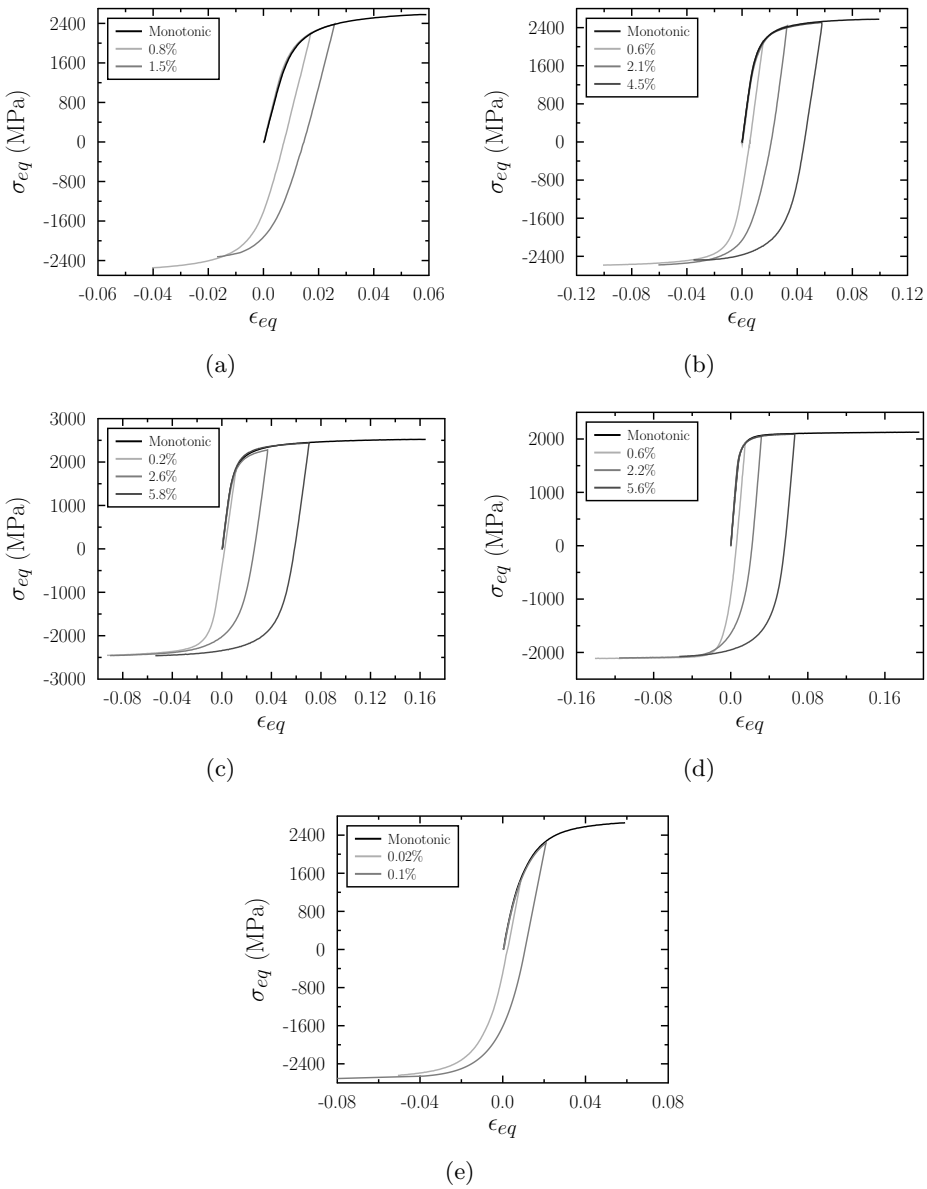

Figure 7.1: Equivalent stress-strain curves obtained during Bauschinger trials on the 300M martensite a) tempered three hours at 120°C, b) tempered five hours at 120°C, c) tempered one hour at 150°C, d) tempered one hour at 350°C, and e) helium gas-quenched. The level of forward pre-strain is indicated.

7.3 Interpreting the Bauschinger effect via a continuous Masing model

7.3.1 Continuous distribution of yield stress and the macroscopic monotonic stress-strain response

As mentioned above, the classic Masing model considers a finite number of microstructural 'elements' having a definite volume fraction and yield strength. The stress-strain response of such a composite material (in both monotonic and strain reversal loading experiments) can then be easily obtained if one considers that:

- The individual elements are elastic, perfectly plastic – i.e. the individual elements exhibit no intrinsic work hardening
- The elements are both elastically and plastically isotropic
- The strains are everywhere uniform within the material

It is unlikely that the first assumption listed above is strictly true. Recalling the discussion in chapter 6, however, the macroscopic work hardening rate of the martensite during the elasto-plastic transition is much higher than what would be anticipated based on isotropic hardening of the individual elements alone. This is seen in the stress-strain response itself where the apparent work hardening rate at higher strains is very small compared to the flow stress of the material. Based on these arguments, it is felt that neglecting the work hardening response of the individual microstructural 'elements' within the martensite is unlikely to have a significant effect on the overall predicted behaviour. Similarly, the second assumption is not strictly true, though it is believed that this effect should not be much different from the behaviour of other polycrystalline metals and therefore second order in importance. The third assumption is clearly not true and is very important in predicting the overall mechanical response. This assumption will be re-visited and modified below.

The other key difference between the approach taken here and that originally proposed by Masing is that a continuous, rather than discrete, distribution of yield strengths is envisioned. In this case the volume fraction of material (dF) having a yield strength in the range $d\sigma$ is related by the continuous probability density function f, where,

$$\int_0^{\sigma} dF = \int_0^{\infty} f(\sigma)\, d\sigma = 1 \tag{7.1}$$

The volume fraction of material having a yield strength equal to, or less than, σ is then given by,

$$F(\sigma) = \int_0^{\sigma} f(x)\, dx \tag{7.2}$$

Allain *et al.* [189] considered that the continuous distribution function f as a Weibull distribution, with no physical justification for the choice of this distribution shape. Here, a similar approach is taken except that, motivated by the results in the previous chapters, a log-normal distribution is selected for f. The approach developed below follows directly from the methodology described in [189].

Upon loading of this hypothetical material to a macroscopic strain $\overline{\epsilon}$ (assumed uniform throughout the material), the local stress in each of the elements of the composite depends on whether or not they have yielded. If E is the Young's modulus of the material, an individual element in the composite has yielded if its yield stress σ is inferior to $\sigma_l = E\overline{\epsilon}$, where σ_l is the stress carried by all elements that have not yet yielded. Once yielded, the stress carried by an element remains at its yield/flow stress (σ) as long as the deformation continues in the same sense. The macroscopic stress $\overline{\sigma}$ is then [185, 192],

$$\overline{\sigma} = \int_0^{\sigma_l} \sigma f(\sigma)\, d\sigma + \sigma_l \int_{\sigma_l}^{\infty} f(\sigma)\, d\sigma \tag{7.3}$$

In equation 7.3, the first term of the right-hand side of the equation represents the contribution of the elements that have yielded, whereas the

second term on the right-hand side represents the contribution of the elements that have not yielded (figure 7.2).

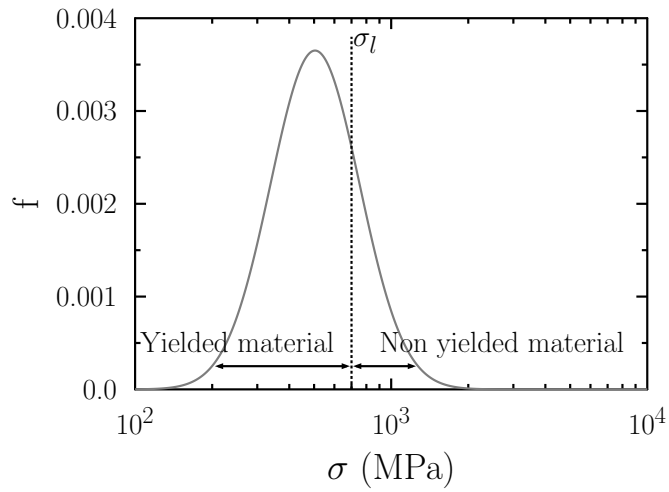

Figure 7.2: Schematic of a stress-distribution function showing the amount of material that has yielded after straining to a strain $\bar{\epsilon} = \frac{\sigma_l}{E}$.

For a general distribution function f it may not be possible to obtain an analytical solution to equation 7.3. However, the macroscopic work hardening rate ($d\bar{\sigma}/d\bar{\epsilon}$) obtained from this expression is a simple function of the Young's modulus E and the cumulative volume fraction of yielded elements, F [184, 189],

$$\frac{d\overline{\sigma}}{d\overline{\epsilon}} = E(1 - F(\sigma_l)) \tag{7.4}$$

Where σ_l has the same definition as before. Thus, from equation 7.4 one can numerically integrate the work hardening behaviour to obtain the macroscopic stress-strain response.

7.3.2 Internal stresses and prediction of the Bauschinger effect

Internal stresses are predicted to develop within the individual elements of the maxing model once yielding commences due to the heterogeneous

distribution of yield stresses within the material. By definition, the internal stress ($\overline{\epsilon}_f$) in an element is the difference between its yield stress σ and the macroscopic stress $\overline{\sigma}_f$,

$$\sigma_{int} = \overline{\sigma}_f - \sigma \tag{7.5}$$

In the elements that have not yielded, the internal stress is:

$$\sigma_{int} = \overline{\sigma}_f - \sigma_l^f \tag{7.6}$$

These internal stresses are expected to be the dominant source of the Bauschinger effect. It should be noted, however, that other sources of the Bauschinger effect can exist. Notably there maybe an intrinsic difference in the strength of obstacles to different loading directions as described by Orowan [193]. These are not considered in the present approach. Initial residual stresses may also alter the observed Bauschinger effect. While these initial residual stresses are not dealt with explicitly here, it will be shown that their existence can be inferred from the present approach. The description below builds from the methodology described by Allain *et al.* [189] for the prediction of the forward flow behaviour and extends it to consider the behaviour during the Bauschinger test.

If, after deforming to a macroscopic strain $\overline{\epsilon}_f$ the strain path is reversed, the distribution of internal stresses stored in the material will act to modify the macroscopic yielding behaviour in the opposite direction. If an element has a positive internal stress (i.e. its yield stress is below the macroscopic stress), then its yield stress in the reverse direction will be decreased by the value of internal stress. The opposite is true for an element having a negative internal stress (i.e. an element which carried a stress higher than the macroscopic stress prior to unloading). With the notation introduced above, the yield stress σ', in the reverse direction, of an element that has yielded is given by [194],

$$\sigma' = 2\sigma - \overline{\sigma}_f \tag{7.7}$$

Whereas the yield stress of an element that has not yielded during the

forward deformation is:

$$\sigma' = \sigma + \sigma_l^f - \overline{\sigma}_f \tag{7.8}$$

A result of this is that the *apparent* yield stress distribution is different compared to that obtained in the forward direction. To construct the reverse flow curve, one can shift the origin of the coordinate system to the point ($\overline{\epsilon}_f$,$\overline{\sigma}_f$) where the strain reversal initiated. In this new coordinate system the yield stress of an element that has yielded is 2σ, whereas, according to equation 7.8, the yield stress of an element that has not yielded is $\sigma + \sigma_l^f$. For this reason, the calculation of the macroscopic stress $\overline{\sigma}_r$ in the reverse direction requires the contributions arising from previously yielded and unyielded elements to be treated separately.

The volume fraction of elements having the yield stress 2σ in the reverse direction can be derived by making a change of variable in the log-normal distribution,

$$g : \sigma \mapsto 2\sigma \tag{7.9}$$

Then, the probability density function associated with 2σ is given as,

$$h(\sigma) = \left| \frac{1}{g'(g^{-1}(\sigma))} \right| f(g^{-1}(\sigma)) \tag{7.10}$$

Where h is the new probability function, g is the function defined in equation 7.9 and g' is the first derivative of the function g. With g defined in equation 7.9, equation 7.10 yields,

$$h(\sigma) = \frac{1}{2} f(\frac{\sigma}{2}) \tag{7.11}$$

When the material is strained to a macroscopic strain $\overline{\epsilon}_r$ in the reverse direction, the macroscopic stress is given by equation 7.3 replacing f by h and σ by 2σ,

$$\overline{\sigma}_r = \int_0^{\sigma_{lr}} 2\sigma h(\sigma)\, d\sigma + 2\sigma_{lr} \int_{\sigma_{lr}}^{\infty} h(\sigma)\, d\sigma \tag{7.12}$$

Where σ_{lr} is equal to $E\overline{\epsilon}_r$. Using equation 7.11, equation 7.12 can be rewrit-

ten as,

$$\overline{\sigma}_r = \int_0^{\sigma_{lr}} \sigma f(\frac{\sigma}{2})\, d\sigma + \sigma_{lr} \int_{\sigma_{lr}}^{\infty} f(\frac{\sigma}{2})\, d\sigma \tag{7.13}$$

As in equation 7.3, the first term on the right hand side corresponds to the contribution of the elements that yielded at the applied reverse strain $\overline{\epsilon}_r$, whereas the second term on the right hand side corresponds to the contribution of the elements that did not yield at the same applied reverse strain. The macroscopic work hardening rate is obtained as before by deriving equation 7.13,

$$\frac{d\overline{\sigma}_r}{d\overline{\epsilon}_r} = E(1 - F(\frac{\sigma_{lr}}{2})) \tag{7.14}$$

Again, equation 7.14 is valid only for those elements that yielded during the forward deformation, i.e. for $\sigma_l \leq \sigma_l^f$ or, with the change of variable described above, for $\sigma_{lr} \leq 2\sigma_l^f$.

For the elements that did not yield during the forward deformation ($\sigma_{lr} \geq 2\sigma_l^f$), the change of variable is given as,

$$g : \sigma \mapsto \sigma + \sigma_l^f \tag{7.15}$$

And the new probability density function h calculated using equation 7.10 is,

$$h(\sigma) = f(\sigma - \sigma_l^f) \tag{7.16}$$

Replacing f by h (equation 7.16), and σ by $\sigma + \sigma_l^f$ (equation 7.15) in equation 7.3 yields,

$$\overline{\sigma}_r = \int_0^{\sigma_{lr}} (\sigma + \sigma_l^f) f(\sigma - \sigma_l^f)\, d\sigma + (\sigma_{lr} + \sigma_l^f) \int_{\sigma_{lr}}^{\infty} f(\sigma - \sigma_l^f)\, d\sigma \tag{7.17}$$

And in this case the macroscopic work hardening rate is:

$$\frac{d\overline{\sigma}_r}{d\overline{\epsilon}_r} = E(1 - F(\sigma_{lr} - \sigma_l^f)) \tag{7.18}$$

A consequence of this is that a correlation is expected between the work hardening rate in the forward and reverse directions. Setting σ_{lr} to $2\sigma_l^f$

in equation 7.14 and in equation 7.18, one finds the same value for the work hardening rate. Finally, as previously discussed by Asaro [194] the elasto-plastic transition in the reverse direction is predicted to be two times longer (in terms of strain) than the elasto-plastic transition in the forward direction.

As noted earlier, this description allows for the forward and reverse stress-strain response to be predicted in the absence of any initial residual stresses. Such initial residual stresses, which can arise due to thermal contraction differences or due to volume changes on phase transformations, will lead to an extra degree of asymmetry in the forward and reverse behaviour not captured by this model. These residual stresses most strongly influence the initial stress-strain response in the forward direction [195, 196]. As the material is loaded, however, and individual elements yield the plastic response of the material progressively removes these initial residual stresses. Once all elements of the material have yielded the initial residual stresses are completely removed and replaced with the set of internal stresses characteristic of the intrinsic distribution in flow stresses characteristic of the individual elements [197]. Thus, if a strain reversal is performed once all elements have yielded, then the flow curve in the reverse direction will reflect the intrinsic behaviour of the individual elements without any bias due to initial residual stresses. In an intermediate situation where only a fraction of the elements have yielded upon the first forward loading, then the initial portion of the reverse curve (corresponding to the yielding of the elements already yielded during the forward loading) will be characteristic of the intrinsic behaviour of the material but the response will be modified at larger strains. In this sense it is best to use Bauschinger tests performed at large forward strains to obtain, with as little interference from residual stresses as possible, the intrinsic distribution of yield stresses within the material.

From an empirical point of view, the effect of initial residual stresses can be quantified by independently fitting the forward part and the reverse part of the Bauschinger curves with different stress-distribution functions. The difference of these stress-distribution functions gives a measure of the sense and magnitude of any initial residual stresses present prior deformation.

7.3.3 Introduction of a localization parameter: effect of non-uniform strain

As noted above, the assumption of uniform strains in the classic Masing model is overly constraining. Here, an approach proposed by Allain *et al.* [189] to account for an intermediate stress/strain partitioning is evaluated. In this approach, a localization parameter β is introduced such that,

$$\beta = -\frac{\overline{\sigma} - \sigma_l}{\overline{\epsilon} - \epsilon_l} \tag{7.19}$$

Incorporating this into equation 7.4 gives the macroscopic work hardening rate predicted by the Masing model in the forward direction as,

$$\frac{d\overline{\sigma}}{d\overline{\epsilon}} = \frac{\beta(1 - F(\sigma_l))}{\frac{\beta}{E} + F(\sigma_l)} \tag{7.20}$$

While the behaviour in the reverse direction, equations 7.14 and 7.18 become,

$$\frac{d\overline{\sigma}_r}{d\overline{\epsilon}_r} = \frac{\beta(1 - F(\frac{\sigma_{lr}}{2}))}{\frac{\beta}{E} + F(\frac{\sigma_{lr}}{2})} \tag{7.21}$$

$$\frac{d\overline{\sigma}_r}{d\overline{\epsilon}_r} = \frac{\beta(1 - F(\sigma_{lr} - \sigma_l^f))}{\frac{\beta}{E} + F(\sigma_{lr} - \sigma_l^f)} \tag{7.22}$$

If one sets $\beta = \infty$ in equation 7.20, one obtains equation 7.4, i.e. $\beta = \infty$ corresponds to the iso-strain assumption. On the other hand, $\beta = 0$ corresponds to the iso-stress assumption. Fixing β at a finite, non zero value allows for intermediate levels of stress/strain homogenization.

7.4 Application: modelling the Bauschinger effect of martensite

As described in the introduction to this chapter, the first step in applying the above described continuous Masing model is to use it to extract the stress distribution function, $f(\sigma)$. As mentioned above, it has been assumed that

$f(\sigma)$ takes the form of a log-normal distribution,

$$f(\sigma) = \frac{1}{\sigma\sqrt{2\pi s^2}} \exp(-\frac{(\ln(\sigma) - m)^2}{2s^2}) \tag{7.23}$$

meaning that two parameters, m (scale parameter) and s (shape parameter) are allowed to vary to obtain a fit to the stress-strain responses.

The other ingredient needed in order to obtain $f(\sigma)$ is the localization parameter β. In the work of Allain *et al.* [189] a value of $E/4$ was chosen, E being the Young's modulus. This value falls within values obtained based on experimental observations of two-phase metals [198, 199]. In [199], β was found to decrease with applied macroscopic strain from E to $E/10$. To evaluate the sensitivity of the predicted $f(\sigma)$ on the choice of β the model was fit to the monotonic mechanical properties of a specimen tempered one hour at 150°C. The scale and shape parameters m and s required to obtain a best-fit to the forward stress-strain response are plotted as a function of β in figure 7.3. It is observed that for $\beta \geq 10E$ m and s are constant,

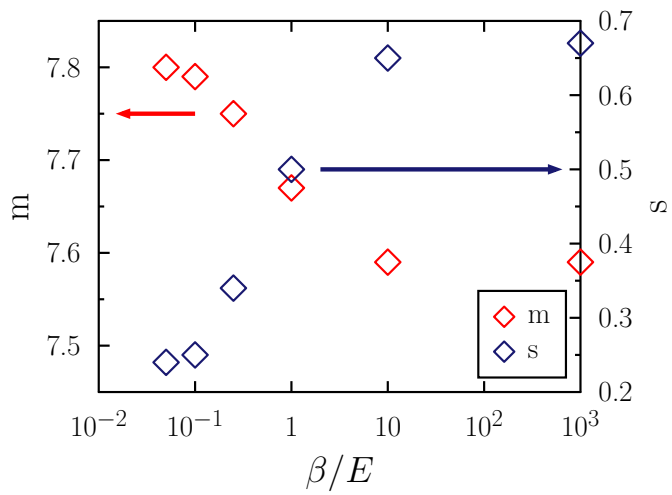

Figure 7.3: Optimal scale (m) and shape (s) parameters for different values of β obtained by fitting the Masing model to the forward stress-strain response of a sample tempered at 150°C for one hour.

consistent with reaching an iso-strain condition. For values of $\beta \leq 0.1E$,

m and s also saturated, though for $\beta \leq 0.1E$ the quality of the best-fit to the data was found to degrade substantially. While this analysis does not provide a definitive answer to the most physically realistic value of β it does suggest that it should be taken to be between $0.1E \leq \beta \leq 10E$. Based on the work of Allain *et al.* and the experimental work on two phase materials described above, it was decided here to use a fixed value of $\beta = E/4$.

Based on this selection of a log-normal distribution for f and the choice of $\beta = E/4$, optimal values for m and s were obtained to fit the forward stress-strain response for samples in a range of different conditions. Figure 7.4 shows the resulting fits to the experimental stress-strain behaviour, including the reverse portion of the curves obtained from Bauschinger tests.

Two main observations can be made at this point. First, the forward portions of the stress-strain curves are very well fit for all conditions based on the assumed log-normal distribution for f. Second, though not fit to the reverse portions of the curves, the f obtained from the forward portion of the curves does a reasonably good job of also capturing the flow curve in the reverse direction. It is observed that the predicted reverse part of the Bauschinger stress-strain curves for specimens tempered 3 and 5 hours at 120°C (see figures 7.4(a) and 7.4(b)) exhibits a slightly larger Bauschinger effect compared to the experiments (a slightly more gradual yielding in the reverse direction). In specimens tempered 5 hours at 120°C, this seems to decrease with forward pre-strain. In the case of the samples tempered for one hour at 150°C for one hour, the fit is extremely good independent of the level of forward pre-strain (see figure 7.4(c)).

In the case of the sample tempered for one hour at 350°C (figure 7.4(d)) the Bauschinger effect was actually under-predicted (i.e. the experimental curve was more rounded in the reverse direction than predicted), this under-prediction increasing with forward pre-strain. Similarly, the fit of the as-helium-quenched specimens was found to be increasingly poor in the reverse direction as the level of forward strain was increased. Overall, it was found that this condition showed the poorest agreement between the model and the reverse stress-strain behaviour.

The stress-distribution functions used for the Masing fits are plotted in

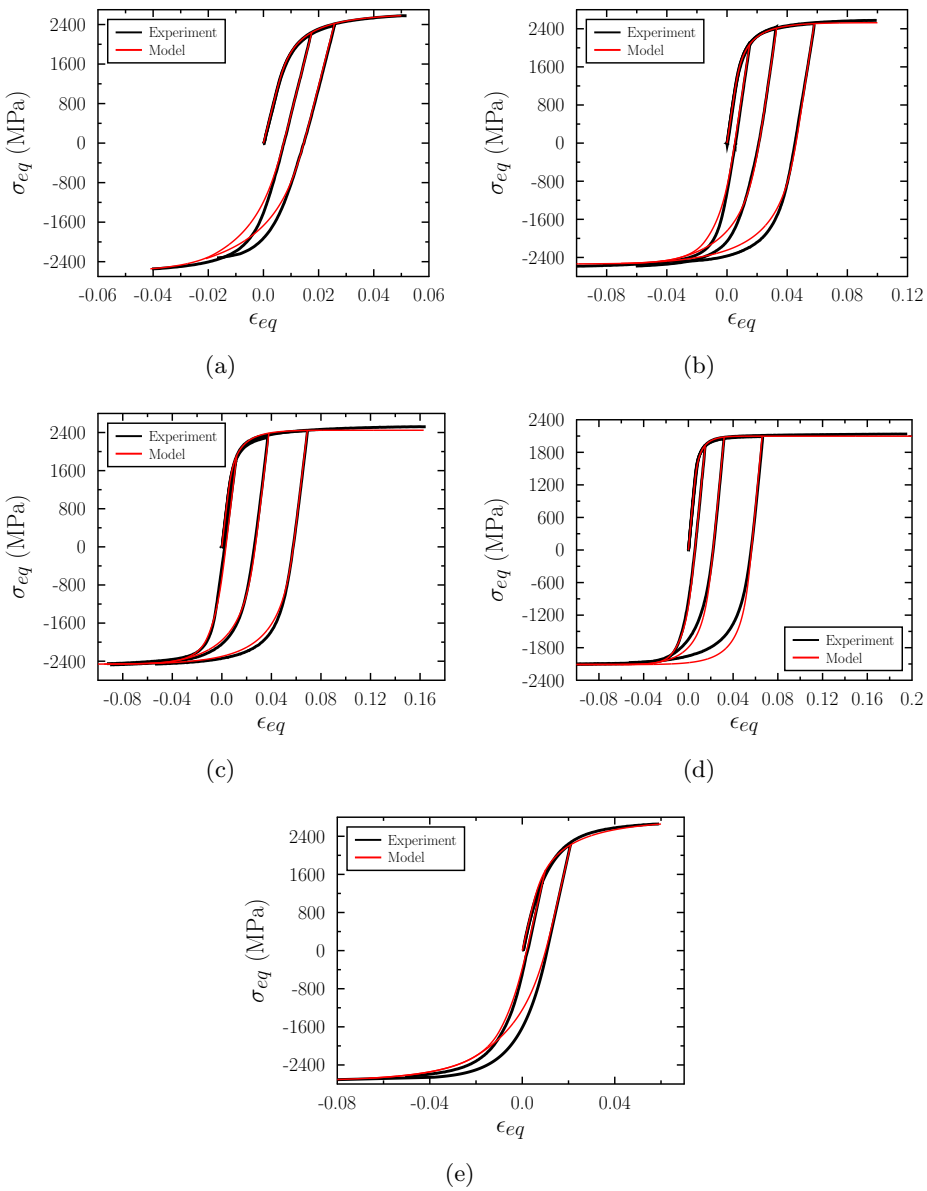

Figure 7.4: Masing fits of the Bauschinger response of martensite after tempering a) 3 hours at 120°C, b) 5 hours at 120°C, c) 1 hour at 150°C, and d) 1 hour at 350°C. e) As-helium-quenched.

figure 7.5 and the parameters s and μ used in the lognormal distributions are presented in table 7.1. Based on these observations it would appear that the

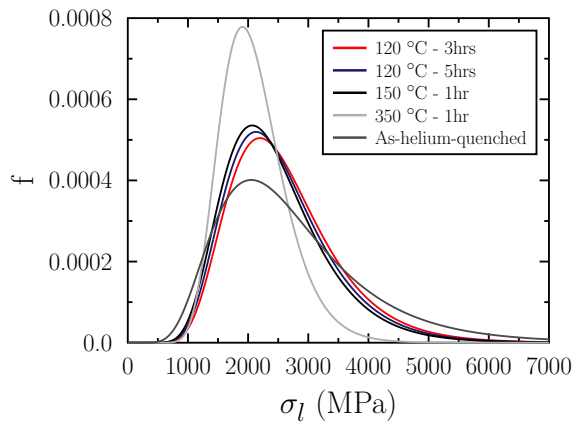

(a)

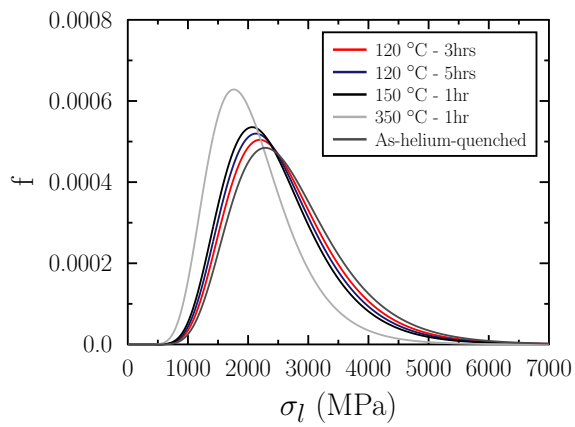

(b)

Figure 7.5: a) Stress-distribution functions used for fitting the stress-strain curves in the forward direction, and b) same as in a) for the reverse direction.

stress-distribution functions do not drastically evolve with low temperature tempering (e.g. up to one hour at 150°C). Indeed, the overall decrease in the UTS observed in chapter 6 appears on the basis of these results to be a consequence of a decrease in the mean of the distribution (i.e. changes in

Tempering temp. (°C)	**Tempering time**	s_f	m_f	s_r	m_r
120	3 hours	0.34	7.81	0.34	7.81
120	5 hours	0.34	7.78	0.34	7.78
150	1 hour	0.34	7.75	0.34	7.75
350	1 hour	0.26	7.62	0.34	7.59
HeQ	–	0.44	7.82	0.34	7.85

Table 7.1: Parameters used in the log-normal distributions. The subscript 'f' refers to the forward direction whereas the subscript 'r' refers to the reverse direction.

m) rather than a change in the shape of the distribution (via s). Conversely, the shapes of the distributions for the samples that were as-helium-quenched and water-quenched and tempering one hour at 350°C exhibit distributions quite different from the rest. In the case of the as-helium-quenched material, the distribution was found to be much wider than the lower temperature quenched material whereas the 350°C tempered sample was found to be much more narrow than the low temperature tempered cases.

The above analysis was performed by fitting the forward flow stress of the sample. However, as stated earlier, if a material carries initial residual stresses then the intrinsic behaviour of the material may be better represented in the reverse portion of the Bauschinger curves. Thus, to examine this the same fitting procedure was performed but on the reverse portion of Bauchinger experiments, the reverse curve after the largest forward prestrain being selected in each case. Also the specimens tempered at low temperature (e.g. up to 1 hour at 150°C) were not re-analyzed given the good agreement of the data in figure 7.4.

Focusing on the obtained fits to the reverse loading behaviours of the specimen tempered one hour at 350°C and the as-helium-quenched specimen, one can see the difference in predicted stress-distribution considering the forward and reverse loading directions (figure 7.6). Examining these results more carefully illustrates that, when comparing the stress-distributions f obtained from the reverse portion of the Bauschinger tests, the behaviour

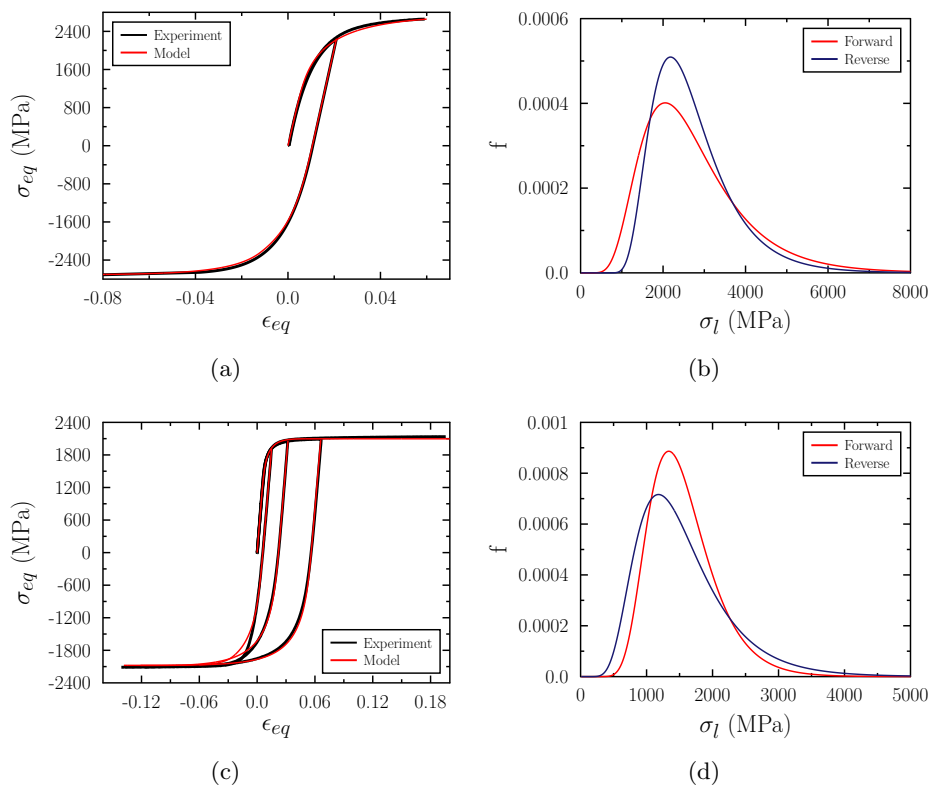

Figure 7.6: a) Masing fit of the Bauschinger stress-strain behaviour of as-helium-quenched specimens obtained after modifying the stress-distribution function to fit the reverse stress-strain curve. b) Forward and reverse stress-distributions. c) and d) Same as in a) and b) for specimens tempered one hour at 350°C.

of all of the samples was very similar (see figure 7.5 and table 7.1). Indeed, it is found that an excellent matching between the reverse portion of the experimental Bauschinger curves and the model can be obtained when s is kept fixed and only m (a measure of the mean value of the log-normal distribution) is varied (cf. table 7.1). This fact strongly suggests that the behaviour of the tempered 350°C and the as-helium-quenched specimens as being strongly influenced by residual stresses and that these residual stresses modify the forward loading curve away from what would be expected in the

simple Masing model described above. Possible sources of these internal residual stresses are discussed below.

7.5 Discussion

As it was shown in figure 7.4, the Bauschinger response of the quenched and tempered 300M martensitic steel can be successfully captured using a Masing 'composite' model. This would suggest that the work hardening in the conditions investigated here, was approximately due to a distribution of elements having different yield stresses. This was probably due to a heterogeneous microstructure, as described in chapter 5.

Apart from the heterogeneous microstructure contributing to the overall strength of the material, it is expected that a smaller, but non negligible, portion of the strength comes from a friction stress due to solid solution strengthening [189]. This friction stress is assumed to be a linear sum of the friction stress due to substitutional elements, interstitial carbon and the friction stress of the pure iron lattice.

The friction stress due to substitutional elements is given as [189],

$$\sigma_{fr} = \sigma_0 + 33(Mn) + 81(Si) + 48(Cr) + 48(Mo) + 0(Ni) \tag{7.24}$$

Where σ_{fr} is expressed in MPa, (X) is the weight percentage of element 'X', and σ_0 is the lattice friction stress of pure iron ($\sim$ 60 MPa [189]). With the chemistry of the 300M material (table 4.1), equation 7.24 yields $\sigma_{fr} = 270$ MPa.

The additional friction stress due to carbon in solid solution can be estimated following Friedel's theory, the equivalent *tensile* stress σ_{fr}^C was estimated as [200],

$$\sigma_{fr}^C = M\frac{\mu}{30}(1 - \frac{T}{T_c})^{3/2}\sqrt{X_c} \tag{7.25}$$

Where M is the Taylor factor (=3), μ is the shear modulus of iron (80 GPa), T is the temperature in K, T_c is the temperature at which the solid solution hardening is zero (estimated as $\sim$ 620 K [200]), and X_c is the carbon atomic

fraction. At room temperature, σ_{fr}^{C} vary from 0 to 404 MPa when X_c varies from 0 to 0.0176 (the maximum carbon composition in solid solution in the 300M material).

It has been shown in chapter 5 that the lath thickness was distributed according to a log-normal distribution. Moreover, it has often been stated that part of the yield strength of martensite was related to the lath size [108]. This could be due to different effects.

For instance, it is possible that the dislocation density could vary substantially from lath to lath. This could be due to geometry necessary dislocations induced by the martensitic transformation, the amount of which being inversely proportional to the lath size, i.e. $\rho_{gnd} \sim \frac{1}{L}$ (where ρ_{gnd} is the density of geometrically necessary dislocations and L is the lath size [157]). This would be supported considering the mechanical behaviour of carbon free martensite. Since this material contains very little amount of carbon, strengthening would come from only the dislocation substructure inherited from the martensitic transformation and a friction stress.

The Masing model was used to fit the tensile stress-strain curve obtained on a very low carbon martensite (0.015 wt% C) [1] which can be approximated as a 'carbon-free' martensite. Given the chemistry of this material (see ref. [201] for details), the friction stress is expected to be 110 MPa. The results of the Masing fit are plotted in figure 7.7). Figure 7.7(b) presents the stress-distribution extracted (in blue) which takes into account the friction stress, and the stress-distribution where the contribution of the friction stress has been removed (in red), the latter being the stress-distribution due to the dislocation density distribution alone (the blue curve is shifted by σ_{fr} compared to the red curve).

If the local yield stress is assumed to be controlled by the local dislocation density, then the local dislocation density can be estimated as,

$$\rho = (\frac{\sigma_f}{\alpha M \mu b})^2 \tag{7.26}$$

Where σ_f is the local yield stress, M is the Taylor factor (~ 3), α is the

[1] The stress-strain data were obtained from ref. [201].

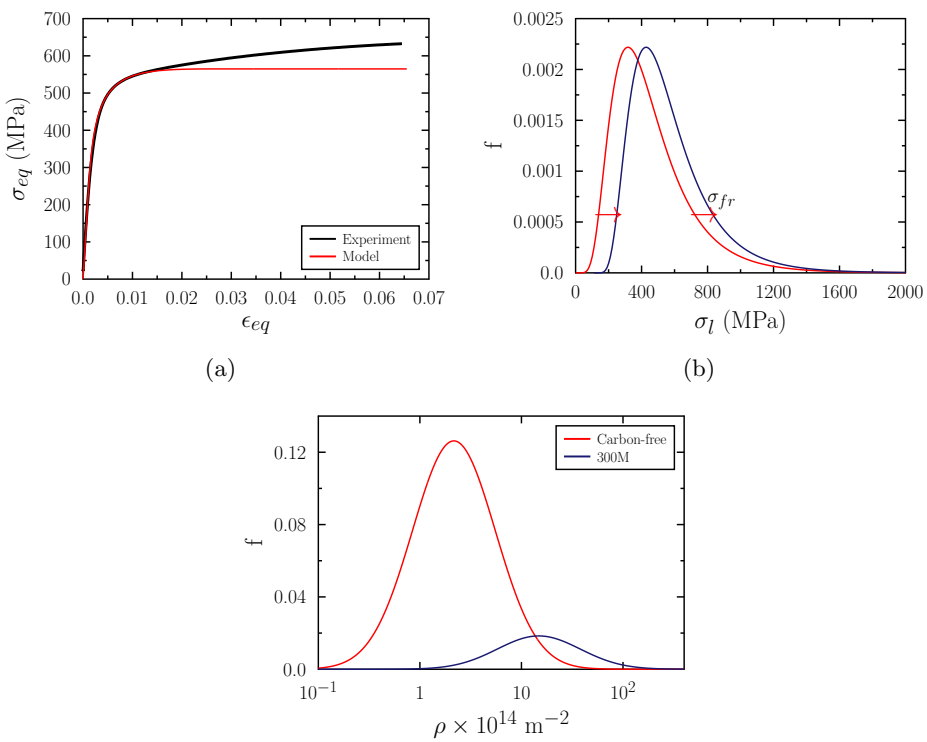

Figure 7.7: a) Masing fit of the tensile behaviour of as-quenched low carbon martensite, b) stress-distribution function used to fit the stress-strain curve in a), and c) dislocation density distribution estimated based on the stress-distribution plotted in b).

strength of the dislocations (~ 0.3), μ is the shear modulus of iron and b is the Burgers' vector of the dislocations. The stress-distribution presented in figure 7.7(b) (red curve) can be transformed into a dislocation density distribution via equation 7.26. This is done through the change of variable given by equation 7.9. If m is the scale parameter and s the shape parameter of the log-normal stress-distribution function, then the scale (m_ρ) and shape (s_ρ) parameters of the dislocation density distribution (which is also log-normal) are related to s and m as $m_\rho = 2(m - \ln(\alpha M \mu b))$ and $s_\rho = 2s$. This way, the stress-distribution presented in figure 7.7(b) is transformed

into the dislocation density distribution presented in figure 7.7(c), which ranges between $\sim 6\times10^{13}$ and $\sim 4\times10^{15}$, with an average value of 0.8×10^{15} m^{-2}. These values correspond well to typical values reported in similar low carbon martensitic steels [12, 30, 74, 108].

The dislocation density determined above may be too low to reflect the true dislocation density observed in the 300M martensite which contains significantly more carbon [30, 74]. Kehoe and Kelly [74] observed a linear increase with carbon content of the dislocation density in martensitic steels. The relationship, which was determined as $\rho \times 10^{15} = 0.43 + 12.83(wt\%C)$ would give an everage dislocation density of $\sim 5.6 \times 10^{15}$ m^{-2}, a value which is typical of medium carbon martensitic steels. Based on this simple estimate, the dislocation density determined for the carbon-free martensite was scaled to obtain a dislocation density with an average value of $\sim 5.6 \times 10^{15}$ m^{-2}. This was done by changing m_ρ from 33.87 to 35.82 and keeping s_ρ unchanged at 0.86.

Furthermore, it has been pointed out in chapter 5 that precipitation of transition carbides occurred during tempering, for the conditions investigated here. The precipitation model developed suggested that for tempering up to one hour at 150°C, the precipitation was in the 'precipitate growth' stage, which should lead to precipitation strengthening. This can be quantified by considering a simple precipitation strengthening model [96, 202],

$$\sigma_{ppt} = \begin{cases} M\frac{\mu b}{L}\beta_c^{3/2}(0.81 + \frac{1}{5\pi}\arccos(\beta_c)) & \text{if } \beta_c \leq 1 \\ M\frac{\mu b}{L}0.81 & \text{if } \beta_c \geq 1 \end{cases} \tag{7.27}$$

Where L is the average spacing between precipitates on a given slip plane ($= R\left(\frac{2\pi}{3V_f}\right)^{1/2}$) where R is the precipitates average radius and V_f their volume fraction), $\beta_c = R/r_c$ (r_c being the critical precipitate radius), the other parameters having the same definition as above. With $r_c = 10b$ [203] and using the parameters predicted by the precipitation model (chapter 5), equation 7.27 allows for the estimation of the extra strength given by the set of precipitates. The results for tempering at 120°C and 150°C, and obtained for three typical dislocation densities, are plotted in figure 7.8.

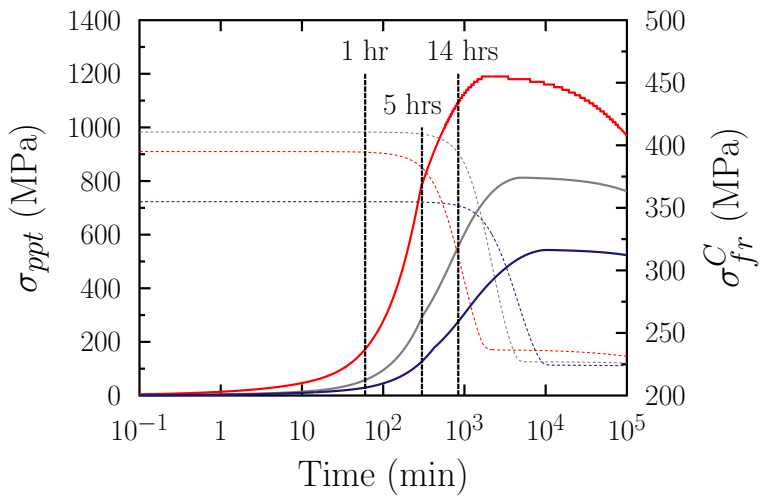

Figure 7.8: Precipitation (σ_{ppt}, solid line) and solid solution (σ_{fr}^{C}, dashed line) strengthening as a function of time and dislocation density, upon tempering at 120°C. The gray curves correspond to $\rho = 10^{14}$ m^{-2}, the red curves to $\rho = 3 \times 10^{15}$ m^{-2} and the dark blue curves to $\rho = 10^{16}$ m^{-2}.

Figure 7.8 shows that for the dislocation densities investigated, the strength should increase continuously with time upon tempering at 120°C, the increase being dependent on dislocation density. For instance, the maximum increase between tempering one hour and 14 hours is approximately 900 MPa (obtained for a dislocation density of 3×10^{15} m^{-2}) and the minimum increase is approximately 240 MPa (obtained for a dislocation density of 10^{16} m^{-2}).

Using the dislocation density distribution determined above (and plotted in figure 7.7(c)), stress-distribution functions can be estimated from the precipitation and carbon solid solution strengthening models described above, the different steps used for this calculation being illustrated in figure 7.9.

If f is the dislocation density distribution (determined above), then the volume fraction of material containing a dislocation density in the range $d\rho$ is equal to $df = f \times d\rho$. In each element of volume fraction df, the yield

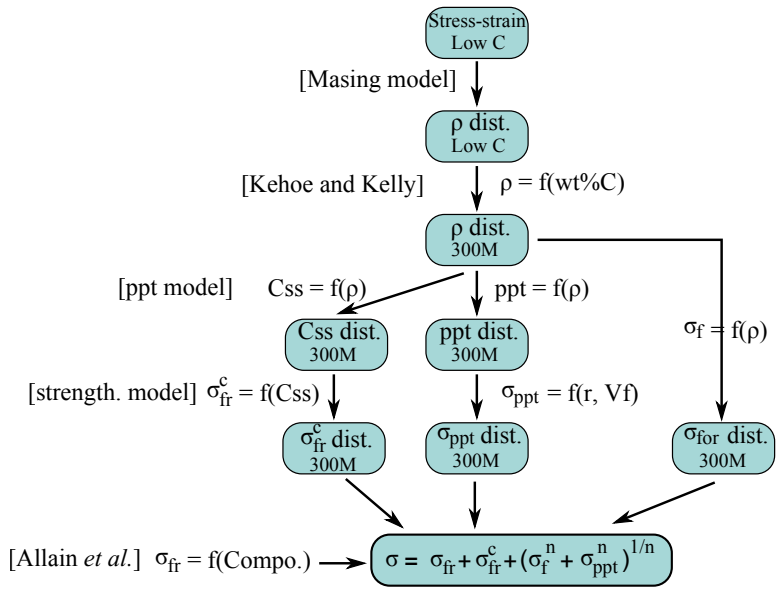

Figure 7.9: Diagram showing the different steps used for the determination of the stress-distribution functions plotted in figure 7.10.

strength is given as,

$$\sigma = \sigma_{fr} + \sigma_{fr}^{C} + (\sigma_f^n + \sigma_{ppt}^n)^{1/n} \tag{7.28}$$

Where σ_{fr}, σ_{fr}^{C} and σ_f have the same definition as before, σ_{ppt} is the stress due to precipitation strengthening. The addition law exponent n is expected to range between 1 and 2 depending on the relative strength of the precipitates compared to the strength of the forest dislocations [204]. When one of these contributions is much higher than the other it is expected that $n = 1$, whereas when the strengths of the two contributions are similar $n \approx 2$ [204].

The contributions of these distributed yield strengths are illustrated in figure 7.10(a) as is the predicted overall yield strength distribution assuming $n = 1$. An important point illustrated by this figure is that that σ_{fr}^{C} is distributed only over a very narrow range of stresses. This was found to be true in all of the conditions examined. Thus, to simplify further discussion, the contribution of carbon in solid solution has been assumed to act as a

Condition	σ_{fr}^{C} (MPa)
120°C - 1hr	400
120°C - 3hrs	400
120°C - 5hrs	390
120°C - 14hrs	300
150°C - 1hr	320
350°C - 1hr	260

Table 7.2: Solid solution strengthening predicted using equation 7.25 and based on the amount of carbon in solid solution predicted by the precipitation model.

uniform friction stress, its magnitude given by the average of the distribution due to the dislocation density. The resulting values used for σ_{fr}^{C} are shown in table 7.2.

The overall yield stress distribution functions predicted using equation 7.27 (assuming $n = 1$) after tempering for different times at 120°C are shown in figure 7.10(b). It is seen that the contribution of precipitation leads to the mean of the stress-distribution to be shifted (significantly) toward higher stresses with increasing time. This prediction is in contradiction to the experimental results (see figure 7.5) which showed that the mean stress decreased slightly with increased tempering at this temperature. This contradiction is clearly seen when one compares the strong predicted increase in proportional limit predicted by the model compared to the slight to no change observed experimentally (see figure 6.7).

The precipitation model predicts that precipitation strengthening is of a similar order of magnitude compared to forest dislocation strengthening after prolonged tempering at 120°C (for times equal or higher than 5 hours). In this case, one would expect that $n = 2$ is more appropriate for the addition law. As shown in figure 7.11, however, this does not significantly change the conclusions reached when $n = 1$.

These results clearly point to the fact that the predicted precipitation strengthening is i) too large and ii) tends to always predict strengthening upon tempering though softening is observed experimentally. One can mod-

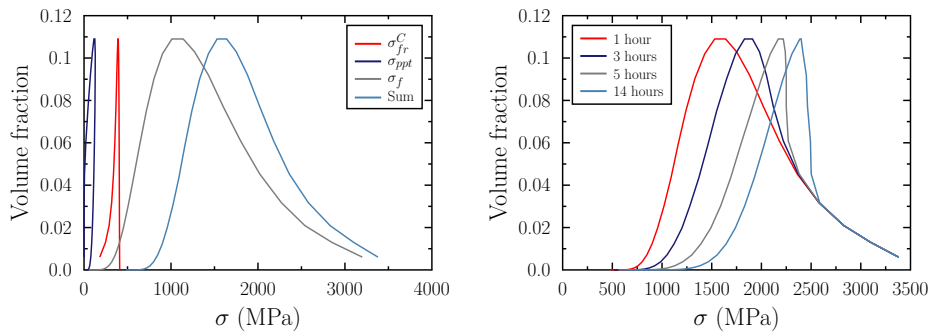

(a) (b)

Figure 7.10: a) Predicted stress-distributions corresponding to the different contributions after tempering one hour at 120°C. b) Evolution of the predicted overall stress-distributions with tempering at 120°C.

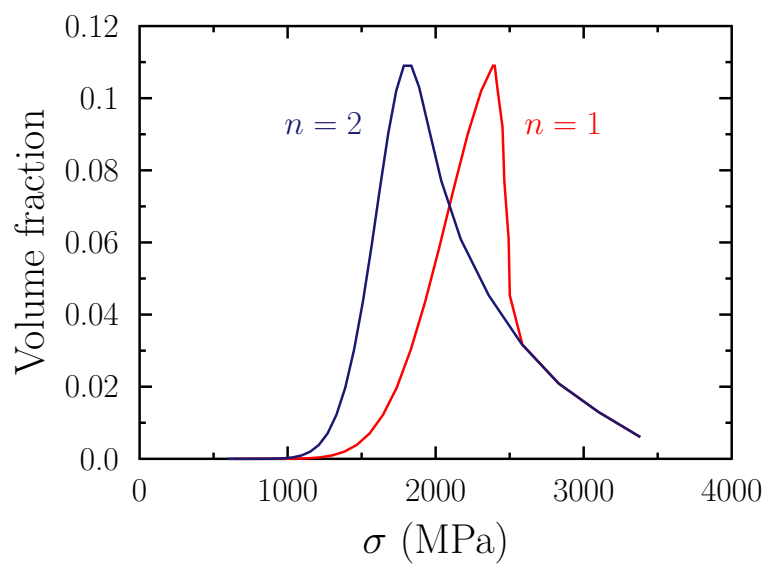

Figure 7.11: Predicted stress-distribution functions for $n = 1$ and $n = 2$ after tempering 14 hours at 120°C.

ify the strength of the precipitation hardening by adjusting the parameter r_c, but it is found that the results are not significantly changed unless unrealistically large values of r_c are chosen. Regardless of the magnitude of the predicted precipitation strengthening, the trend of strengthening due to precipitation hardening is in the wrong sense. For precipitation to give rise to softening, one would need to be in a regime of precipitate coarsening, this being inconsistent with the experiments presented in chapter 5.

One of the key assumptions in the above modelling is that precipitation occurs heterogeneously onto dislocations. A result of this is that the location of the precipitates and dislocations are correlated. In this case the concept of the addition law (equation 7.28) is questionable as it assumes that the two obstacles are randomly distributed in the glide plane [202]. If precipitation occurs onto the forest dislocations then one might better expect that the strength is controlled by whichever of the two obstacles is more prevalent (and perhaps stronger). Thus, one would anticipate that in the early stages of tempering (and in the as-quenched condition) the strength is controlled by the forest dislocations, whereas at longer aging times at higher temperatures, the precipitates become more important. The characteristic distance between dislocations and between precipitates in this case would, however, be given by the mean spacing between dislocations, $L = 1/\sqrt{\rho}$. In view of this, it is proposed that the yield stress be written as,

$$\sigma = \sigma_{fr} + \sigma_{fr}^{C} + \alpha' M \mu b \sqrt{\rho} \tag{7.29}$$

In this equation all the parameters have the same definition as before except for α' which must be considered to reflect the effective strength of the dislocation forest and the precipitates on these dislocations.

Using the dislocation density distribution determined above and equation 7.29, one can calculate the predicted stress-strain response under these conditions. Figure 7.12 shows the prediction for the case of a sample tempered at 150°C for one hour assuming $\alpha' = 0.3$ as originally used for extracting the dislocation density from the low carbon martensite described above.

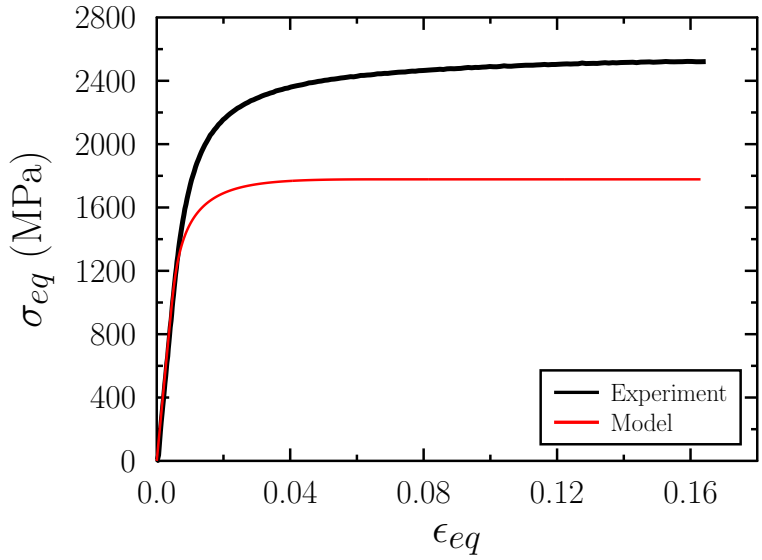

Figure 7.12: Predicted stress-strain curve (red line) compared to the experimental stress-strain curve obtained on specimens tempered one hour at 150°C.

It is seen that the Masing model significantly underestimates the strength of the material in this case. Based on the above discussion it is expected that the only parameter that may be free to adjust its value is α'. Figure 7.13 shows that the stress-strain curves could be well fit by allowing α' to vary as shown in figure 7.14 and table 7.3. Table 7.3 shows that α was found to decrease on tempering from $\alpha' = 0.52$ to $\alpha' = 0.39$.

This apparent decrease in α' is interpreted here to reflect the net change in strength coming from the combination of precipitation and the dislocation forest. It is notable, that the value predicted for α' is high for conditions where it is expected that there is little precipitation. One possible reason for this may be the segregated Cottrell atmospheres of carbon surrounding these dislocations. If up to 8 at% C is segregated around these dislocations as suggested in chapter 5, then their resistance to cutting by mobile dislocations might be significantly higher than expected in the case of forest dislocations free of a carbon atmosphere. In the case of aluminum copper alloys it has

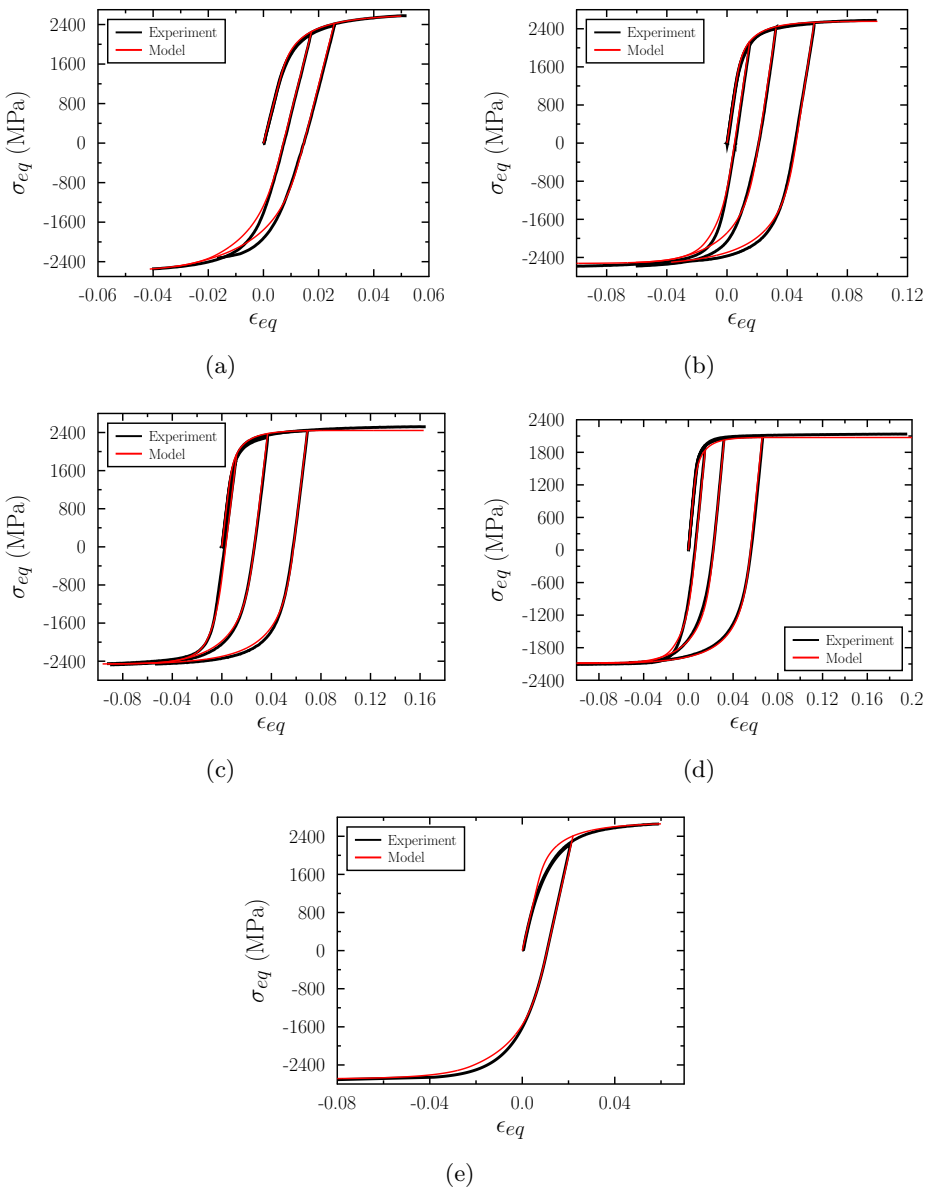

Figure 7.13: Masing fits of the Bauschinger response of martensite after tempering a) 3 hours at 120°C, b) 5 hours at 120°C, c) 1 hour at 150°C, and d) 1 hour at 350°C. e) As-helium-quenched.

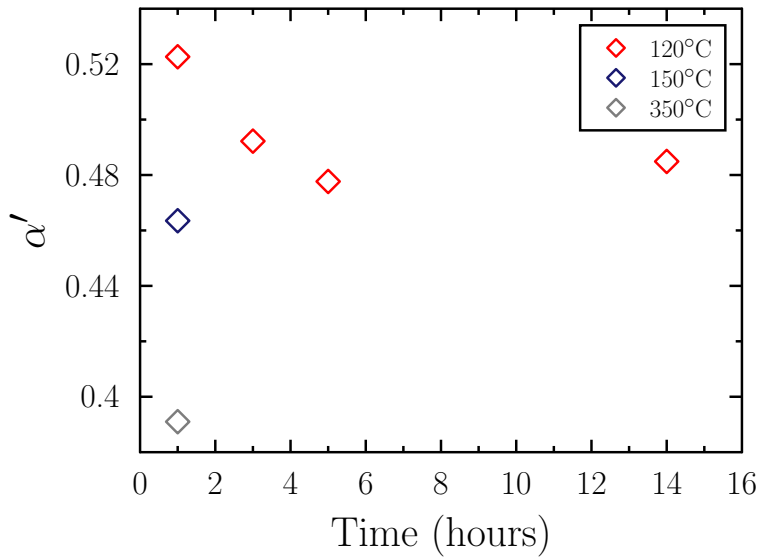

Figure 7.14: Typical stress-distribution function obtained for solid solution strengthening.

Specimen	m	s	$\alpha'(C)$
120°C - 1hr	7.54	0.43	0.523
120°C - 3hrs	7.48	0.43	0.492
120°C - 5hrs	7.45	0.43	0.478
120°C - 14hrs	7.465	0.43	0.484
150°C - 1hr	7.44	0.43	0.464
350°C - 1hr	7.25	0.43	0.391
HeQ	7.515	0.43	0.510

Table 7.3: Scale and shape parameters used in the log-normal distributions used to fit the mechanical behaviour of specimens tempered up to one hour at 150°C. The $\alpha'(C)$ parameter extracted is also indicated.

been reported that α' increases with solid solution from ~ 0.27 to ~ 0.48 [205].

The apparent decrease in α' with tempering may suggest a progressive removal of carbon from the atmospheres surrounding the dislocations. This may occur, for example, if precipitation consumes carbon from the atmospheres surrounding these dislocations. It is envisioned that a complex metastable equilibrium must be developed between the precipitates, carbon in the Cottrell atmospheres and carbon in solid solution. The strong decrease in α' required to fit the sample tempered at 350°C, where precipitation was well into the coarsening regime (see chapter 5) would be at least qualitatively consistent with this hypothesis (table 7.3). Moreover, the equilibrium carbon content in the Cottrell atmospheres is expected to decrease at higher temperatures [38].

The above analysis was made under the assumption that the dislocation density distribution did not evolve with tempering. This is supported by the work of Malik and Lund [97], who reported only a small decrease from $\sim 2\times10^{15}$ m^{-2} to $\sim 1.3\times10^{15}$ m^{-2} after increasing the tempering temperature from 250°C to 350°C (tempering time was one hour) in a similar 0.4 wt% C plain carbon martensite.

So far, the discussion has focused on the effect of the dislocation substructure on the mechanical properties of the 300M martensite. It was, however, pointed out in chapter 5 that a finite (though relatively small) volume fraction of twins and retained austenite exist within the material. The twin thickness was reported in chapter 5 to be between ~ 10 and ~ 100 nm. Based on similarly sized twins in twinning-induced plasticity steels, the yield stresses in these regions could range between ~ 600 MPa and ~ 6 GPa [206]. The highest value (6 GPa) corresponds approximately to the highest yield stress estimated in the stress-distribution functions presented in figure 7.5 after low temperature tempering. Thus, it is possible that the high stress tail of the stress-distribution function may have a contribution of these fine scale features within the microstructure. The strength of retained austenite is, on the other hand, difficult to assess because it depends on size and carbon content, which are themselves difficult to measure. APT

results shown in chapter 5 revealed that the retained austenite films were probably enriched in carbon, at $\sim$ 4 to $\sim$ 8 at% C. Such a high carbon content can cause the austenite to be very strong. Even though little is known about the hardness of retained austenite in martensite, it has been shown that carburizing austenitic stainless steels to cabron levels of $\sim$ 8 at% C led to hardnesses of $\sim$ 1000 Hv [207], which would in turn give a yield stress of $\sim 3GPa$. The volume fraction of retained austenite being very low (see chapter 5), however, it is expected that this phase will not influence drastically the mechanical behaviour of martensite.

A final point must be made regarding initial residual stresses. It was stated in section 7.4 that the observed differences between the forward and reverse stress-strain curves of specimens tempered one hour at 350°C and as-helium-quenched specimens could be interpreted as being due to the presence of initial residual stresses. The origin of the the residual stresses in the case of the as-helium-quenched specimens could possibly be explained by the heterogeneous microstructure observed in chapter 5. It is known that carbon redistribution can lead to significant local volume changes (measurable by dilatometry) [63]. In this case, such lath-to-lath variations in the degree of carbon redistribution may lead to a complex set of residual stresses within the material.

At the other extreme, the residual stresses found in specimens tempered one hour at 350°C may be a consequence of extensive carbide precipitation. In this case, it is known that carbide precipitation can lead to macroscopic changes in sample dimensions measurable by dilatometry experiments (e.g see [63]). This is due to the large misfit between the carbides and the surrounding matrix [66].

7.5.1 Application of model to other steel grades

The description developed above suggests that the tensile (or torsion) response of martensitic steels can be predicted if one knows:

- Friction stress due to substitutional alloying elements
- Friction stress due to carbon in solid solution

- The forest/precipitate strengthening due to a distribution of dislocation density
- The effective strength of the forest/precipitates via α'
- The residual stresses in the sample

As proposed above, the mean dislocation density can be predicted based on the carbon content of the steel, as discussed above and if the width of the dislocation density distribution is considered to be independent of the carbon content, then the value obtained from the low carbon martensite can be used for different steel grades (e.g. $s_\rho = 0.43$). Thus, under these conditions it should be possible to apply this model to the prediction of the forward and reverse stress-strain response of different martensite grades neglecting the contribution from residual stresses to the behaviour. As shown above, if the samples are rapidly quenched and the tempering times/temperatures are short the exclusion of these residual stresses should not strongly effect the predictions.

In this case it is only the value of α' that is unknown and expected to vary with the carbon content of the steel. To test this hypothesis, Bauschinger test data were obtained for two additional steels, an as-quenched 0.15 wt% C martensite and an as-quenched 0.24 wt% C martensite (figure 7.15). The former material was processed and tested at UBC following the same procedure as for the 300M steel while the latter was tested in uniaxial tension/compression, the data having been supplied by colleagues from McMaster University [208]. For these steels, the friction stress due to substitutional alloying was calculated based on equation 7.24 and found to be $\sigma_{fr} = 123$ MPa for the 0.15 wt% C steel and $\sigma_{fr} = 130$ MPa for the 0.24 wt% C steel . Due to the high Ms temperature of these steels it is assumed that the friction stress is the same in both cases and equal to $\sigma_{fr}^{C} = 220$ MPa, corresponding to 0.5 at% C in solid solution (cf. equation 7.25). Finally, the mean dislocation density was computed as a function of the carbon content according to the Kehoe and Kelly [74] relation described above.

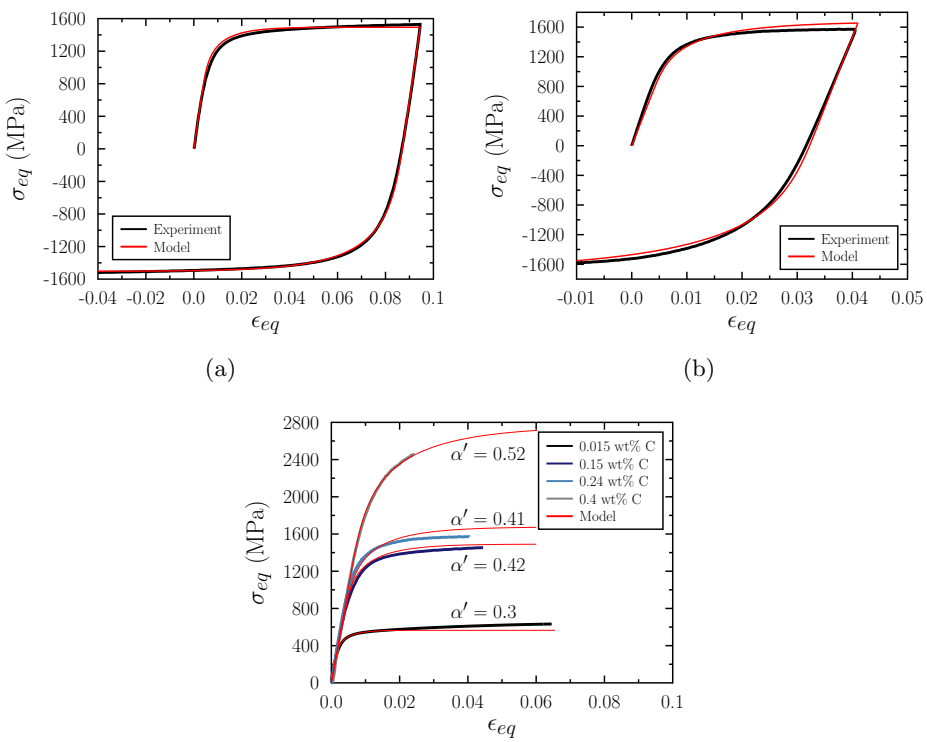

Figure 7.15: Masing model applied to the Bauschinger behaviour of a) an as-quenched 0.15 wt% C martensite, and b) an as-quenched 0.24 wt% C martensite. c) Masing model applied to as-quenched martensites containing various amount of carbon (the value of α' used is also indicated).

This approach was found to give excellent fits to the forward and reverse portions of the stress-strain curves in this case as illustrated in figure 7.15. In order to obtain these fits, a value of $\alpha' = 0.418$ was used for the 0.15 wt% C steel and $\alpha = 0.411$ for the 0.24 wt% C steel. Figure 7.15(c) summarizes the Masing fits to the monotonic stress-strain data for the low carbon martensite, the 0.15 wt% C martensite, the 0.24 wt% C martensite and the 300M steel, where the 300M behaviour has been fit based on the tensile response after tempering at 120°C for one hour (due to the brittle

fracture of the as-water-quenched material). One can see that for the as quenched/low temperatures tempered samples, the value of α' required to obtain a good match between experiments and the model depends on the bulk carbon content of the alloy. This is a valuable conclusion as it suggests that for a wide range of steels the model presented here can be adequately used to predict the forward (and reverse) stress strain response simply via a knowledge of the material's bulk carbon content.

7.6 Conclusion

In this chapter, the Bauschinger effect of the 300M martensitic steel was analyzed using a continuous composite Masing model. It was shown that all tempering conditions considered revealed a very similar distribution of yield strengths when the reverse portion of Bauschinger tests were considered, the mean of the distribution shifting with tempering but the shape remaining the same. The relatively high degree of asymmetry observed in some cases (e.g. the as-helium-quenched state) has been interpreted as being due to the presence of internal residual stresses. A model for precipitation strengthening and solid solution softening due to the removal of carbon from solution was implemented based on the precipitation model presented in chapter 5. The implementation of this model, however, showed that classical precipitation hardening leads to the opposite predictions of strength evolution on tempering compared with experimental observations. It has been hypothesized that the role of dislocation forest strengthening and precipitation strengthening cannot be treated separately owing to the fact that precipitation is considered to occur heterogeneously onto the dislocations in the microstructure. Instead, it was found that the stress-strain response could be adequately captured for a wide range of tempering conditions and alloys when a modified Taylor-like equation was used in conjunction with a dislocation density distribution and empirically varied strength parameter α'. To fit the different conditions α' had to be varied, the variation appearing to depend on the carbon content of the steel and the degree of carbon redistribution within the microstructure. The model was shown to adequately predict both for-

ward and reverse stress-strain responses in as-quenched martensites having 0.015 wt% C, 0.15wt % C, 0.24wt % C and 0.4 wt% C, the latter having been compared after a 1 hour temper at 120°C so as to avoid brittle fracture prior to plasticity.

Chapter 8

Conclusion

Little paradises take their time. Little parties end.
— Jack Kerouac

8.1 Summary and key results

The work presented is this thesis has advanced our basic understanding of the influence of microstructure, especially carbon re-arrangement during tempering, on the plastic behaviour of martensitic steels. While the literature on martensitic steels is long and detailed as highlighted by the literature review (chapter 2), it is believed that this work is the first to propose a physical, microstructurally based, explanation for the elasto-plastic transition and strength of martensite in the as-quenched and quenched and tempered states.

A detailed microstructural investigation was performed using TEM and APT to clarify the carbon distribution obtained on quenching and after tempering. The role of quench rate was highlighted as strong differences in the degree of auto-tempering were observed for the two quench rates studied here. Upon tempering, the precipitation of what were believed to be η-carbides was found, though the composition of these precipitates (from APT) did not appear to coincide with the expected stoichiometry. Importantly, lath-to-lath variations in precipitation state were observed and

interpreted based on i) lath-to-lath differences in dislocation density and ii) heterogeneous precipitation of carbides onto these dislocations. A mean-field precipitation model was applied to the experimentally obtained precipitate size and volume fraction measurements, the model being able to well reproduce the precipitation kinetics at 120°C and 150°C.

Based on the detailed monotonic and Bauschinger mechanical tests performed on these steels, it has been proposed that the high work hardening rate is due to the heterogeneous properties and structure of individual laths. It is believed that the local strength of a lath is controlled by the dislocation density contained within it. Consistent with the literature, it has been argued that the lath size is inversely related to the dislocation density formed on quenching of the steel. Based on the measured lath thickness distributed and experiments on a model 'carbon-free' martensitic steel, a dislocation density distribution was obtained for the martensite and shown to be consistent with the mean dislocation density reported in the literature.

Using a previously reported relation between dislocation density and carbon content [74], it was shown that the experimental Bauschinger experiments could be reproduced using a simple composite model similar to that originally proposed by Masing. The influence of the microstructure, and its modification on tempering or on quenching condition, was described based on the evolution of a single empirical parameter, α' (equation 7.29) with tempering. The parameter α' was found to vary between ~ 0.52 and ~ 0.39 for the 300M steel here, the value of α' decreasing with increasing tempering. Using the same approach it was shown that this parameter was well approximately by a linear relation to the bulk carbon content. It has been hypothesized that this relation may relate to changes in the level of carbon segregated to dislocations.

Though precipitation was observed to be significant in many of the conditions studied, the present work proposed that precipitation strengthening had little direct influence on the mechanical properties of the 300M martensitic steel. By combining the precipitation model described above to a precipitation strengthening model it was shown that the potential for precipitation hardening was very high upon tempering. However, this pre-

diction was found to be at odds with the experimentally observed decrease in strength on tempering. It has been hypothesized that the complex microstructure resulting from precipitation onto forest dislocations may make these two strengthening mechanisms not additive. Instead, the strength of the combined dislocations and precipitates must be considered as a single evolving obstacle. Given that precipitation strengthening in martensitic steels is far from being well-understood, this thesis provides an important insight that is absent from the existing literature.

In summary, based on this work, it is proposed that the stress-strain response of as-quenched and quenched and tempered martensitic steels can be estimated, based on the model developed here, knowing the nominal carbon content for martensitic grades containing between 0 wt% C and 0.4 wt% C, the only feature not covered by the model being initial residual stresses. These were shown to be present in both the as-quenched conditions (particularly high in slowly cooled samples) and to evolve on tempering. If residual stresses can be assumed to be small, or if subsequent models can be developed to predict them, the present work hardening model can be useful for different industrial applications where high strength steels are desirable [2], but where their poor predictability makes them difficult to design with.

8.2 Future work

This work reveals a number of topics that require further investigation. These are highlighted below:

1. The observation that precipitation behaviour depended on lath size was shown to be consistent with previous work, but further quantification of this behaviour is required by APT and/or TEM to clarify its origins

2. The carbon-rich areas interpreted as η-carbides in APT experiments had significantly different chemistries compared to that expected. A lack of knowledge regarding this carbide's chemistry and the solubility of carbon in ferrite in equilibrium with this phase strongly hinders any

attempt to predict the precipitation behaviour. Performing further APT experiments on 300M specimens tempered one hour at 350°C could help to assess the carbon solubility in the η-carbides, since, as revealed in chapter 5, the carbides found in these specimens were still η-carbides and not cementite. This microstructure would be certainly less complicated to analyze by APT since it can be reasonably expected that it would contain more carbides and less segregation to defects (dislocations and grain boundaries), and less carbon in solid solution, compared to the specimens studied here.

3. The model developed for predicting the work hardening and strength of the steels studied here relies on the empirical fitting of the parameter α'. The physical origins of this parameter, and particularly how it is that precipitation does not seem to provide a strong effect on strengthening the material in the classical way, needs a much deeper investigation. Perhaps atomistic simulations could be helpful in understanding how segregated carbon strengthens the forest dislocations. Alternatively, more thorough studies of the relationship between the microstructure and stress-strain response of as-quenched lower carbon (e.g. between 0 wt% C and 0.4 wt% C) martensites could provide useful experimental data to improve our understanding of the effect of carbon on α'.

4. It was suggested in this work that initial residual stresses were influencing the stress-strain behaviour, in the forward direction, of some of the specimens studied here. In the case of as-helium-quenched specimens, it was suggested that these initial residual stresses were partially relaxed after tempering at low temperature (e.g. one hour at 150°C). Initial residual stresses were suggested to influence the stress-strain behaviour of water-quenched and tempered at 350°C specimens. The origin of these initial residual stresses, as well as their evolution with tempering, should be further investigated in order to better understand their effect on the mechanical properties of martensitic steels.

Bibliography

[1] A. H. Cottrell, *Dislocations and plastic flow in crystals.* Clarendon Press, 1965.

[2] H. Fountain, "Many faces, and phases, of steel in cars," *The New York Times*, 2009.

[3] F. Lefevre-Schlick, O. Bouaziz, Y. Brechet, and J. Embury, "Compositionally graded steels: The effect of partial decarburization on the mechanical properties of spherodite and pearlite," *Materials Science and Engineering: A*, vol. 491, no. 1-2, pp. 80–87, 2008.

[4] G. B. Olson and W. S. Owen, *Martensite: a tribute to Morris Cohen.* ASM International, 1992.

[5] Z. Nishiyama, M. E. Fine, M. Meshii, and C. M. Wayman, *Martensitic transformation.* Academic Press, 1978.

[6] O. Johari and G. Thomas, "Factors determining twinning in martensite," *Acta Metallurgica*, vol. 13, no. 11, pp. 1211–1212, 1965.

[7] G. Krauss and A. Marder, "The morphology of martensite in iron alloys," *Metallurgical and Materials Transactions B*, vol. 2, no. 9, pp. 2343–2357, 1971.

[8] G. Speich and W. Leslie, "Tempering of steel," *Metallurgical and Materials Transactions B*, vol. 3, no. 5, pp. 1043–1054, 1972.

[9] C. Magee and R. Davies, "The structure, deformation and strength of ferrous martensites," *Acta Metallurgica*, vol. 19, no. 4, pp. 345–354, 1971.

[10] G. Krauss, "Deformation and fracture in martensitic carbon steels tempered at low temperatures," *Metallurgical and Materials Transactions B*, vol. 32, no. 2, pp. 205–221, 2001.

[11] E. Bain, "The nature of martensite," *American Institute of Mining and Metallurgical Engineers – Transactions*, no. 1299-S, p. 11, 1924.

[12] G. Speich, "Tempering of low carbon martensite," *Transactions of AIME*, vol. 245, no. 12, pp. 2553–2564, 1969.

[13] P. Winchell and M. Cohen, "The strength of martensite," *Transactions of the ASM*, vol. 55, pp. 347 – 361, 1962.

[14] D. Koistinen and R. Marburger, "A general equation prescribing the extent of the austenite-martensite transformation in pure iron-carbon alloys and plain carbon steels," *Acta Metallurgica*, vol. 7, no. 1, pp. 59–60, 1959.

[15] K. Ishida, "Calculation of the effect of alloying elements on the ms temperature in steels," *Journal of Alloys and Compounds*, vol. 220, no. 1-2, pp. 126–131, 1995.

[16] A. Greninger, "Martensite thermal – arrest in iron-carbon alloys and plain carbon steels," *American Society for Metals – Transactions*, vol. 30, no. 1, pp. 1–26, 1942.

[17] A. Marder and G. Krauss, "Morphology of martensite in iron-carbon alloys," *American Society of Metals – Trans*, vol. 60, no. 4, pp. 651–660, 1967.

[18] D. H. Sherman, S. M. Cross, S. Kim, F. Grandjean, G. J. Long, and M. K. Miller, "Characterization of the carbon and retained austenite distributions in martensitic medium carbon, high silicon steel," *Metallurgical and Materials Transactions A*, vol. 38, no. 8, pp. 1698–1711, 2007.

[19] S. Morito, K. Oh-ishi, K. Hono, and T. Ohba, "Carbon enrichment in retained austenite films in low carbon lath martensite steel," *ISIJ International*, vol. 51, no. 7, pp. 1200–1202, 2011.

[20] G. Thomas, "Retained austenite and tempered martensite embrittlement," *Metallurgical and Materials Transactions A*, vol. 9, no. 3, pp. 439–450, 1978.

[21] M. Sarikaya, A. Jhingan, and G. Thomas, "Retained austenite and tempered martensite embrittlement in medium carbon steels," *Metallurgical and Materials Transactions A*, vol. 14, no. 6, pp. 1121–1133, 1983.

[22] M. Carlson, B. Narasimha Rao, and G. Thomas, "The effect of austenitizing temperature upon the microstructure and mechanical properties of experimental Fe/Cr/C steels," *Metallurgical and Materials Transactions A*, vol. 10, no. 9, pp. 1273–1284, 1979.

[23] B. Sandvik and C. Wayman, "Characteristics of lath martensite: Part II. the martensite-austenite interface," *Metallurgical and Materials Transactions A*, vol. 14, no. 4, pp. 823–834, 1983.

[24] G. Speich and H. Warlimont, "Yield strength and transformation substructure of low-carbon martensite," *Iron and Steel Institute – Journal*, vol. 206, no. Part 4, pp. 385–392, 1968.

[25] A. Marder and G. Krauss, "Formation of low-carbon martensite in fe-c alloys," *Asm Transactions Quarterly*, vol. 62, no. 4, pp. 957–964, 1969.

[26] C. Apple, R. Caron, and G. Krauss, "Packet microstructure in fe-0.2 pct c martensite," *Metallurgical and Materials Transactions B*, vol. 5, no. 3, pp. 593–599, 1974.

[27] J. Christian, "The strength of martensite," in *Strengthening Methods in Crystals*, pp. 261 – 330, London: Apllied Science Publishers, 1971.

[28] R. Patterson and G. Wayman, "The crystallography and growth of partially-twinned martensite plates in fe-ni alloys," *Acta Metallurgica*, vol. 14, no. 3, pp. 347–369, 1966.

[29] K. Wakasa and C. Wayman, "The morphology and crystallography of ferrous lath martensite. studies of fe-20%Ni-5%Mn—II. transmission electron microscopy," *Acta Metallurgica*, vol. 29, no. 6, pp. 991–1011, 1981.

[30] S. Morito, J. Nishikawa, and T. Maki, "Dislocation density within lath martensite in fe-c and fe-ni alloys," *ISIJ International*, vol. 43, no. 9, pp. 1475–1477, 2003.

[31] J. Chilton and P. Kelly, "The strength of ferrous martensite," *Acta Metallurgica*, vol. 16, no. 5, pp. 637–656, 1968.

[32] D. Carney, "Another look at quenchants, cooling rates and hardenability," *Transactions of the ASM*, vol. 46, pp. 882–927, 1954.

[33] R. Aborn, "Low carbon martensites," *Transactions of the ASM*, vol. 48, pp. 51–85, 1956.

[34] C. Zhu, A. Cerezo, and G. D. Smith, "Carbide characterization in low-temperature tempered steels," *Ultramicroscopy*, vol. 109, no. 5, pp. 545–552, 2009.

[35] B. Hutchinson, J. Hagström, O. Karlsson, D. Lindell, M. Tornberg, F. Lindberg, and M. Thuvander, "Microstructures and hardness of as-quenched martensites (0.1–0.5%C)," *Acta Materialia*, vol. 59, no. 14, pp. 5845–5858, 2011.

[36] C. Lerchbacher, S. Zinner, and H. Leitner, "Atom probe study of the carbon distribution in a hardened martensitic hot-work tool steel X38CrMoV5-1," *Micron*, vol. 43, no. 7, pp. 818–826, 2012.

[37] H. Snyder, "Effect of quenching and tempering on residual stresses in manganese oil hardening tool steel," in *American Society for Metals – Meeting, Oct 20-24 1952*, American Society for Metals – Preprints, (Cleveland, OH, United States), p. 12, American Society for Metals, 1952.

[38] D. Kalish and E. Roberts, "On the distribution of carbon in martensite," *Metallurgical and Materials Transactions B*, vol. 2, no. 10, pp. 2783–2790, 1971.

[39] M. Miller, P. Beaven, S. Brenner, and G. Smith, "An atom probe study of the aging of iron-nickel-carbon martensite," *Metallurgical and Materials Transactions A*, vol. 14, no. 6, pp. 1021–1024, 1983.

[40] M. Hillert, "The kinetics of the first stage of tempering," *Acta Metallurgica*, vol. 7, no. 10, pp. 653–658, 1959.

[41] G. Olson and M. Cohen, "Early stages of aging and tempering of ferrous martensites," *Metallurgical and Materials Transactions A*, vol. 14, no. 5, pp. 1057–1065, 1983.

[42] A. Sherman, G. Eldis, and M. Cohen, "The aging and tempering of iron-nickel-carbon martensites," *Metallurgical and Materials Transactions A*, vol. 14, no. 5, pp. 995–1005, 1983.

[43] K. A. Taylor and M. Cohen, "Aging of ferrous martensites," *Progress in Materials Science*, vol. 36, pp. 151–272, 1992.

[44] K. Taylor, L. Chang, G. Olson, G. Smith, M. Cohen, and J. Sande, "Spinodal decomposition during aging of fe-ni-c martensites," *Metallurgical and Materials Transactions A*, vol. 20, no. 12, pp. 2717–2737, 1989.

[45] M. Kusunoki and S. Nagakura, "Modulated structure of iron–carbon martensite studied by electron microscopy and diffraction," *Journal of Applied Crystallography*, vol. 14, no. 5, pp. 329–336, 1981.

[46] S. Nagakura, Y. Hirotsu, M. Kusunoki, T. Suzuki, and Y. Nakamura, "Crystallographic study of the tempering of martensitic carbon steel by electron microscopy and diffraction," *Metallurgical and Materials Transactions A*, vol. 14, no. 6, pp. 1025–1031, 1983.

[47] K. Han, M. J. van Genderen, A. Böttger, H. W. Zandbergen, and E. J. Mittemeijer, "Initial stages of fe-c martensite decomposition," *Philosophical Magazine A*, vol. 81, no. 3, p. 741, 2001.

[48] L. Cheng, N. van der Pers, A. Böttger, T. de Keijser, and E. Mittemeijer, "Lattice changes of iron-carbon martensite on aging at room temperature," *Metallurgical and Materials Transactions A*, vol. 22, no. 9, pp. 1957–1967, 1991.

[49] M. Van Genderen, A. Böttger, R. Cernik, and E. Mittemeijer, "Early stages of decomposition in iron-carbon and iron-nitrogen martensites: Diffraction analysis using synchrotron radiation," *Metallurgical and Materials Transactions A*, vol. 24, no. 9, pp. 1965–1973, 1993.

[50] J.-M. Génin, "The clustering and coarsening of carbon multiplets during the aging of martensite from mössbauer spectroscopy: The preprecipitation stage of epsilon carbide," *Metallurgical and Materials Transactions A*, vol. 18, no. 8, pp. 1371–1388, 1987.

[51] H. Ino, T. Ito, S. Nasu, and U. Gonser, "A study of interstitial atom configuration in fresh and aged iron-carbon martensite by mossbauer spectroscopy," *Acta Metallurgica*, vol. 30, no. 1, pp. 9–20, 1982.

[52] W. Choo and R. Kaplow, "Mössbauer measurements on the aging of iron-carbon martensite," *Acta Metallurgica*, vol. 21, no. 6, pp. 725–732, 1973.

[53] N. DeCristofaro and R. Kaplow, "Interstitial atom configurations in stable and metastable fe-n and fe-c solid solutions," *Metallurgical and Materials Transactions A*, vol. 8, no. 1, pp. 35–44, 1977.

[54] N. DeCristofaro, R. Kaplow, and W. Owen, "The kinetics of carbon clustering in martensite," *Metallurgical and Materials Transactions A*, vol. 9, no. 6, pp. 821–825, 1978.

[55] M. Van Genderen, M. Isac, A. Böttger, and E. Mittemeijer, "Aging and tempering behavior of iron-nickel-carbon and iron-carbon martensite," *Metallurgical and Materials Transactions A*, vol. 28, no. 3, pp. 545–561, 1997.

[56] L. Cheng, C. M. Brakman, B. M. Korevaar, and E. J. Mittemeijer, "The tempering of iron- carbon martensite; dilatometric and calorimetric analysis," *Metallurgical Transactions A*, vol. 19, no. 10, pp. 2415–2426, 1988.

[57] M. Miller, P. Beaven, and G. Smith, "A study of the early stages of tempering of iron-carbon martensites by atom probe field ion microscopy," *Metallurgical and Materials Transactions A*, vol. 12, no. 7, pp. 1197–1204, 1981.

[58] O. N. C. Uwakweh, J. P. Bauer, and J. M. R. Génin, "Mössbauer study of the distribution of carbon interstitiels in iron alloys and the isochronal kinetics of the aging of martensite: The clustering-ordering synergy," *Metallurgical Transactions A*, vol. 21, no. 2, pp. 589–602, 1990.

[59] S. Ren and S. Wang (Wang Xiao Tian), "A theoretical analysis of the spinodal decomposition in fe- c martensite during aging stage of tempering," *Metallurgical and Materials Transactions A*, vol. 19, no. 10, pp. 2427–2432, 1988.

[60] J. Wilde, A. Cerezo, and G. D. W. Smith, "Three-dimensional atomic-scale mapping of a cottrell atmosphere around a dislocation in iron," *Scripta Materialia*, vol. 43, no. 1, pp. 39–48, 2000.

[61] A. H. Cottrell and B. A. Bilby, "Dislocation theory of yielding and strain ageing of iron," *Proceedings of the Physical Society. Section A*, vol. 62, no. 1, pp. 49–62, 1949.

[62] S. Harper, "Precipitation of carbon and nitrogen in cold-worked alpha-iron," *Physical Review*, vol. 83, no. 4, pp. 709–712, 1951.

[63] T. Waterschoot, K. Verbeken, and B. C. De Cooman, "Tempering kinetics of the martensitic phase in DP steel," *ISIJ International*, vol. 46, no. 1, pp. 138–146, 2006.

[64] K. H. Jack, "The iron-nitrogen system: The preparation and the crystal structures of nitrogen-austenite ($\gamma $) and nitrogen-martensite ($\alpha ^\prime$)," *Proceedings of the Royal Society of London. Series A. Mathematical and Physical Sciences*, vol. 208, no. 1093, pp. 200 –215, 1951.

[65] Y. Hirotsu and S. Nagakura, "Crystal structure and morphology of the carbide precipitated from martensitic high carbon steel during the first stage of tempering," *Acta Metallurgica*, vol. 20, no. 4, pp. 645–655, 1972.

[66] "Carbide precipitation during stage i tempering of fe-ni-c martensites," vol. 20.

[67] J.-M. R. Génin, "On the morphology of the modulated precipitation of extended multiplets and Fe9C4 epsilon or eta carbide obtained by aging and tempering in fe-c martensite," *Metallurgical Transactions A*, vol. 19, no. 12, pp. 2901–2909, 1988.

[68] Y. Hirotsu and S. Nagakura, "Electron-microscopy and diffraction study of carbide precipitated at first stage of tempering of martensitic medium carbon steel," *Transactions of the Japan Institute of Metals*, vol. 15, no. 2, pp. 129–134, 1974.

[69] C. Roberts, B. Averbach, and M. Cohen, "Mechanism and kinetics of first stage of tempering," American Society for Metals – Preprints, (Cleveland, OH, United States), p. 24, American Society for Metals, 1952.

[70] B. Lement, B. Averbach, and M. Cohen, "Microstructural changes on tempering iron-carbon alloys," in *American Society for Metals – Meeting, Oct 19-23 1953*, American Society for Metals – Preprints, (Cleveland, OH, United States), p. 27, American Society for Metals, 1953.

[71] D. Kalish and M. Cohen, "Structural changes and strengthening in the strain tempering of martensite," *Materials Science and Engineering*, vol. 6, no. 3, pp. 156–166, 1970.

[72] M. Maalekian and E. Kozeschnik, "A thermodynamic model for carbon trapping in lattice defects," *Calphad*, vol. 32, no. 4, pp. 650–654, 2008.

[73] C. Barton, "The tempering of a low-carbon internally twinned martensite," *Acta Metallurgica*, vol. 17, no. 8, pp. 1085–1093, 1969.

[74] M. Kehoe and P. M. Kelly, "The role of carbon in the strength of ferrous martensite," *Scripta Metallurgica*, vol. 4, no. 6, pp. 473–476, 1970.

[75] L. Norstrom, "On the yield strength of quenched low-carbon lath martensite," *Scandinavian Journal of Metallurgy*, vol. 5, no. 4, pp. 159–165, 1976.

[76] B. Lement and M. Cohen, "A dislocation-attraction model for the first stage of tempering," *Acta Metallurgica*, vol. 4, no. 5, pp. 469–476, 1956.

[77] R. Horn and R. Ritchie, "Mechanisms of tempered martensite embrittlement in low alloy steels," *Metallurgical and Materials Transactions A*, vol. 9, no. 8, pp. 1039–1053, 1978.

[78] R. Caron and G. Krauss, "The tempering of fe-c lath martensite," *Metallurgical and Materials Transactions B*, vol. 3, no. 9, pp. 2381–2389, 1972.

[79] C. Shih, B. Averbach, and M. Cohen, "Some effects of silicon on the mechanical properties of high strength steels," *Transactions of the ASM*, vol. 48, pp. 87–118, 1956.

[80] C. Altstetter, M. Cohen, and B. Averbach, "Effect of silicon on tempering of AISI 43XX steels," *ASM – Transactions*, vol. 55, no. 2, pp. 287–300, 1962.

[81] G. Miyamoto, J. Oh, K. Hono, T. Furuhara, and T. Maki, "Effect of partitioning of mn and si on the growth kinetics of cementite in tempered fe-0.6 mass% c martensite," *Acta Materialia*, vol. 55, no. 15, pp. 5027–5038, 2007.

[82] D. Wilson, "Effects of plastic deformation on carbide precipitation in steel," *Acta Metallurgica*, vol. 5, no. 6, pp. 293–302, 1957.

[83] N. Breyer and N. Polakowski, "Cold drawing of martensitic steels to 400,000 psi tensile strength," *ASM – Transactions*, vol. 55, no. 3, pp. 667–684, 1962.

[84] A. Cochardt, G. Schoek, and H. Wiedersich, "Interaction between dislocations and interstitial atoms in body-centered cubic metals," *Acta Metallurgica*, vol. 3, no. 6, pp. 533–537, 1955.

[85] E. Stephenson and M. Cohen, "Effect of prestraining and retempering on AISI type 4340," *Transactions of the ASM*, vol. 54, pp. 72 – 83, 1961.

[86] G. Krauss, "Heat treated martensitic steels: Microstructural systems for advanced manufacture," *ISIJ International*, vol. 35, no. 4, pp. 349–359, 1995.

[87] R. Grange, "Strengthening steel by austenite grain refinement," *ASM – Transactions*, vol. 59, no. 1, pp. 26–48, 1966.

[88] R. Vyhnal and S. Radcliffe, "Effects of pressure on the structure of iron-carbon martensites," *Acta Metallurgica*, vol. 15, no. 9, pp. 1475–1488, 1967.

[89] J.-Y. Kang, S. C. Kim, J.-O. Oh, H. N. Han, K. H. Oh, and H.-C. Lee, "Martensite in interstitial-free steel obtained by ultra-high pressure," *Scripta Materialia*, vol. 66, no. 1, pp. 45–48, 2012.

[90] W. Leslie and R. Sober, "Strength of ferrite and of martensite as functions of composition, temperature and strain rate," *ASM Transactions*, vol. 60, no. 3, pp. 459–484, 1967.

[91] G. Speich and P. Swann, "Yield strength and transformation substructure of quenched iron-nickel alloys," *Iron and Steel Institute – Journal*, vol. 203, no. Part 5, pp. 480–485, 1965.

[92] S. Radcliffe and M. Schatz, "Effects of high pressure on strength and structure of martensites," *Nature*, vol. 200, no. 490, pp. 161–&, 1963. WOS:A19638814B00522.

[93] R. L. Fleischer, "Substitutional solution hardening," *Acta Metallurgica*, vol. 11, no. 3, pp. 203–209, 1963.

[94] G. Eldis and M. Cohen, "Strength of initially virgin martensites at — 196 °C after aging and tempering," *Metallurgical and Materials Transactions A*, vol. 14, no. 5, pp. 1007–1012, 1983.

[95] J. W. Cahn, "Hardening by spinodal decomposition," *Acta Metallurgica*, vol. 11, no. 12, pp. 1275–1282, 1963.

[96] A. Ardell, "Precipitation hardening," *Metallurgical and Materials Transactions A*, vol. 16, no. 12, pp. 2131–2165, 1985.

[97] L. Malik and J. Lund, "A study of strengthening mechanisms in tempered martensite from a medium carbon steel," *Metallurgical and Materials Transactions B*, vol. 3, no. 6, pp. 1403–1406, 1972.

[98] R. Richman, "Plastic deformation modes in fe-ni-c martensites," *Metallurgical Society of American Institute of Mining, Metallurgical and Petroleum Engineers – Transactions*, vol. 227, no. 1, pp. 159–166, 1963.

[99] T. Swarr and G. Krauss, "The effect of structure on the deformation of as-quenched and tempered martensite in an fe-0.2 pct c alloy," *Metallurgical and Materials Transactions A*, vol. 7, no. 1, pp. 41–48, 1976.

[100] J. Embury, A. Keh, and R. Fisher, "Substructural strengthening in materials subject to large plastic deformation," *Transactions of the Metallurgical Society of Aime*, vol. 236, no. 9, pp. 1252–&, 1966. WOS:A19668283700003.

[101] J. Gil Sevillano, P. van Houtte, and E. Aernoudt, "Large strain work hardening and textures," *Progress in Materials Science*, vol. 25, no. 2–4, pp. 69–134, 1980.

[102] M. Saeglitz and G. Krauss, "Deformation, fracture, and mechanical properties of low-temperature-tempered martensite in SAE 43xx steels," *Metallurgical and Materials Transactions A*, vol. 28, no. 2, pp. 377–387, 1997.

[103] H. Muir, B. Averbach, and M. Cohen, "The elastic limit and yield behavior of hardened steels," vol. 47, pp. 380–407, 1955.

[104] M. Zaccone and G. Krauss, "Elastic limits and microplastic response in ultrahigh strength carbon steels," *Metallurgical and Materials Transactions A*, vol. 20, no. 1, pp. 188–191, 1989.

[105] T. Balliett and G. Krauss, "The effect of the first and second stages of tempering on microcracking in martensite of an fe-1.22 c alloy," *Metallurgical and Materials Transactions A*, vol. 7, no. 1, pp. 81–86, 1976.

[106] R. Brown, H. Rack, and M. Cohen, "Stress relaxation during the tempering of hardened steel," *Materials Science and Engineering*, vol. 21, pp. 25–34, 1975.

[107] A. Abel, "Historical perspectives and some of the main features of the bauschinger effect," *Materials Forum*, vol. 10, no. 1, pp. 11–26, 1987. Compendex.

[108] G. Krauss, "Martensite in steel: strength and structure," *Materials Science and Engineering A*, vol. 273-275, pp. 40–57, 1999.

[109] M. Vicente Alvarez, M. Bergant, and T. Perez, "Relaxation of the bauschinger effect by thermal treatment on tempered martensitic steels," *Materials Science and Engineering: A*, vol. 527, no. 21-22, pp. 5939–5946, 2010.

[110] M. Vicente Alvarez, M. Marchena, and T. Perez, "Recovery kinetics of cold-deformed cr-mo steels," *Metallurgical and Materials Transactions A*, vol. 39, no. 13, pp. 3283–3290, 2008.

[111] J. Yan, *Study of Bauschinger Effect in Various Spring Steels*. M.Sc thesis, University of Toronto, 1998.

[112] W. Owen and M. Roberts, "Dynamic aging effects in ferrous martensite," *Transactions of the Japan Institute of Metals*, vol. S 9, pp. 911–918, 1968.

[113] M. Roberts and W. Owen, "Unstable flow in martensite and ferrite," *Metallurgical and Materials Transactions B*, vol. 1, no. 11, pp. 3203–3213, 1970.

[114] F. Guiu, "The role of stress-induced ordering of interstitials in the deformation of fe-ni-c martensites," *Philosophical Magazine*, vol. 21, no. 170, pp. 365–374, 1970.

[115] L. Hyspecka, K. Mazanec, and R. Riman, "Contribution to the mechanism of unstable flow in martensite," *Energy Technology Review*, pp. 601–606, 1980.

[116] P. Wyslych, E. Mazancová, and K. Mazanec, "The instability of plastic deformation in as-quenched martensite," *Materials Science and Engineering: A*, vol. 234–236, no. 0, pp. 513–516, 1997.

[117] C. Prioul, "Snoek like relaxation in fe-ni-c martensite," *Journal De Physique*, vol. 46, no. C-10, pp. 665–668, 1985. WOS:A1985A685500148.

[118] M. Carrard, L. Hyspecka, J. Plusquellec, P. Azou, and P. Bastien, "Internal friction in martensite of a fe-ni-c alloy," *Kovove Materialy*, vol. 13, no. 1, pp. 52–65, 1975.

[119] M. Carrard, L. Hyspecka, J. Plusquellec, P. Azou, and P. Bastien, "Interactions between carbon and dislocations after martensitic transformation in fe-ni-c alloys," *Memoires Scientifiques de la Revue de Metallurgie*, vol. 71, no. 3, pp. 145–151, 1974.

[120] J. D. Eshelby, "Dislocations in visco-elastic materials," *Philosophical Magazine*, vol. 6, no. 68, pp. 953–963, 1961.

[121] G. Schoeck and A. Seeger, "The flow stress of iron and its dependence on impurities," *Acta Metallurgica*, vol. 7, no. 7, pp. 469–477, 1959.

[122] S. Okamoto, D. Matlock, and G. Krauss, "The transition from serrated to non-serrated flow in low-carbon martensite at 150°C," *Scripta Metallurgica et Materialia*, vol. 25, no. 1, pp. 39–44, 1991.

[123] J. Materkowski and G. Krauss, "Tempered martensite embrittlement in SAE 4340 steel," *Metallurgical and Materials Transactions A*, vol. 10, no. 11, pp. 1643–1651, 1979.

[124] H. Kwon, J. C. Cha, and C. H. Kim, "The effect of grain size on fracture behaviour in tempered martensite embrittlement for AISI 4340 steel," *Materials Science and Engineering*, vol. 100, pp. 121–128, 1988.

[125] F. Zia-Ebrahimi and G. Krauss, "The evaluation of tempered martensite embrittlement in 4130 steel by instrumented charpy v-notch testing," *Metallurgical and Materials Transactions A*, vol. 14, no. 5, pp. 1109–1119, 1983.

[126] N. Bandyopadhyay and C. McMahon, "The micro-mechanisms of tempered martensite embrittlement in 4340-type steels," *Metallurgical and Materials Transactions A*, vol. 14, no. 7, pp. 1313–1325, 1983.

[127] R. Ritchie, B. Francis, and W. Server, "Authors' reply," *Metallurgical and Materials Transactions A*, vol. 8, no. 7, pp. 1197–1199, 1977.

[128] U. S. Lindholm, A. Nagy, G. R. Johnson, and J. M. Hoegfeldt, "Large strain, high strain rate testing of copper," *Journal of Engineering Materials and Technology*, vol. 102, pp. 376–381, Oct. 1980.

[129] A. D. Rollett, *Strain Hardening at Large Strains in Aluminum Alloys.* Ph.D thesis, Drexel University, Philadelphia, 1988.

[130] "Davis StrainMaster," 2011.

[131] J.-J. Orteu, "3-d computer vision in experimental mechanics," *Optics and Lasers in Engineering*, vol. 47, no. 3–4, pp. 282–291, 2009.

[132] B. Pan, K. Qian, H. Xie, and A. Asundi, "Two-dimensional digital image correlation for in-plane displacement and strain measurement: a review," *Measurement Science and Technology*, vol. 20, no. 6, p. 062001, 2009.

[133] F. Hild and S. Roux, "Digital image correlation: from displacement measurement to identification of elastic properties – a review," *Strain*, vol. 42, no. 2, p. 69–80, 2006.

[134] LaVision, "Strain master 3D," 2004.

[135] A. E. Lord and D. N. Beshers, "Elastic stiffness coefficients of iron from 77° to 673°K," *Journal of Applied Physics*, vol. 36, no. 5, pp. 1620–1623, 1965.

[136] G. Thomas, "Electron microscopy investigations of ferrous martensites," *Metallurgical and Materials Transactions B*, vol. 2, no. 9, pp. 2373–2385, 1971.

[137] M. K. Miller, A. Cerezo, M. G. Hetherington, and G. D. W. S. FRS, *Atom Probe Field Ion Microscopy*. Clarendon Press, 1996.

[138] V. Bilyk, *Etude de la microstructure d'un acier martensitique brut de trempe et revenu par sonde atomique tri-dimensionnelle*. MSc., Universit\'e de Rouen, France, 2011.

[139] D. Blavette, A. Bostel, J. Sarrau, B. Deconihout, and A. Menand, "An atom-probe for 3-dimensional tomography," *Nature*, vol. 363, no. 6428, pp. 432–435, 1993. WOS:A1993LE93800053.

[140] W. Sha, L. Chang, G. Smith, L. Cheng, and E. Mittemeijer, "Some aspects of atom-probe analysis of Fe?C and Fe?N systems," *Surface Science*, vol. 266, pp. 416–423, Apr. 1992.

[141] F. Danoix, D. Julien, X. Sauvage, and J. Copreaux, "Direct evidence of cementite dissolution in drawn pearlitic steels observed by tomographic atom probe," *Materials Science and Engineering: A*, vol. 250, pp. 8–13, July 1998.

[142] X. Sauvage, N. Guelton, and D. Blavette, "Microstructure evolutions during drawing of a pearlitic steel containing 0.7 at.% copper," *Scripta Materialia*, vol. 46, no. 6, pp. 459–464, 2002.

[143] H. Kitahara, R. Ueji, N. Tsuji, and Y. Minamino, "Crystallographic features of lath martensite in low-carbon steel," *Acta Materialia*, vol. 54, no. 5, pp. 1279–1288, 2006.

[144] M. Richman and M. Cohen, "Electron microscopy of the fine structure in iron-nickel-carbon martensites," *Materials Science and Engineering*, vol. 3, no. 4, pp. 240–245, 1968.

[145] K. Shimizu and H. Okamoto, "High-voltage electron-microscopy study of metastable iron carbide in a eutectoid fe-c alloy," *Transactions of the Japan Institute of Metals*, vol. 15, no. 3, pp. 193–199, 1974.

[146] G. Thomas, *Transmission Electron Microscopy of Materials.* Techbooks, 1990.

[147] D. Williamson, K. Nakazawa, and G. Krauss, "A study of the early stages of tempering in an fe-1.2 pct alloy," *Metallurgical and Materials Transactions A*, vol. 10, no. 9, pp. 1351–1363, 1979.

[148] H.-C. Lee and G. Krauss, "Intralath carbide transitions in martensitic medium-carbon steels tempered between 200 and 300C," in *Gilbert R. Speich Symposium Proceedings on Fundamentals of Aging and Tempering in Bainitic and Martensitic Steel Products, October 25, 1992 - October 28, 1992*, (Montreal, Que, Can), pp. 39–43, Publ by Iron & Steel Soc of AIME, 1992.

[149] R. Padmanabhan and W. Wood, "Precipitation of [epsilon] carbide in martensite," *Materials Science and Engineering*, vol. 65, no. 2, pp. 289–297, 1984.

[150] L. Darken, "Diffusion of carbon in austenite with a discontinuity in composition," *Transactions of the American Institute of Mining and Metallurgical Engineers*, vol. 180, pp. 430–438, 1949.

[151] C. Zener, "Theory of strain interaction of solute atoms," *Physical Review*, vol. 74, no. 6, p. 639, 1948. Copyright (C) 2009 The American Physical Society; Please report any problems to prola@aps.org.

[152] Y. Wang, S. Denis, B. Appolaire, and P. Archambault, "Modelling of precipitation of carbides during tempering of martensite," *Journal De Physique Iv*, vol. 120, pp. 103–110, 2004.

[153] L. Chang, S. Barnard, and G. Smith, "Segregation of carbon atoms to dislocations in low-carbon martensites: studies by field ion microscopy and atom probe microanalysis," in *Gilbert R. Speich Symposium Proceedings on Fundamentals of Aging and Tempering in Bainitic and Martensitic Steel Products, October 25, 1992 - October 28, 1992*, (Montreal, Que, Can), pp. 19–28, Publ by Iron & Steel Soc of AIME, 1992.

[154] B. Soenen, A. K. De, S. Vandeputte, and B. C. De Cooman, "Competition between grain boundary segregation and cottrell atmosphere formation during static strain aging in ultra low carbon bake hardening steels," *Acta Materialia*, vol. 52, no. 12, pp. 3483–3492, 2004.

[155] J. Chipman, "Thermodynamics and phase diagram of the fe-c system," *Metallurgical and Materials Transactions B*, vol. 3, no. 1, pp. 55–64, 1972.

[156] B. Sandvik and C. Wayman, "Characteristics of lath martensite: Part i. crystallographic and substructural features," *Metallurgical and Materials Transactions A*, vol. 14, no. 4, pp. 809–822, 1983.

[157] M. F. Ashby, "The deformation of plastically non-homogeneous materials," *Philosophical Magazine*, vol. 21, no. 170, pp. 399–424, 1970.

[158] A. Deschamps and Y. Brechet, "Influence of predeformation and agEing of an Al–Zn–Mg alloy—II. modeling of precipitation kinetics and yield stress," *Acta Materialia*, vol. 47, pp. 293–305, Dec. 1998.

[159] H. Zurob, C. Hutchinson, Y. Brechet, and G. Purdy, "Modeling recrystallization of microalloyed austenite: effect of coupling recovery, precipitation and recrystallization," *Acta Materialia*, vol. 50, no. 12, pp. 3077–3094, 2002.

[160] H. Ohtani and C. McMahon Jr., "Modes of fracture in temper embrittled steels," *Acta Metallurgica*, vol. 23, no. 3, pp. 377–386, 1975.

[161] U. Kocks and H. Mecking, "Physics and phenomenology of strain hardening: the FCC case," *Progress in Materials Science*, vol. 48, no. 3, pp. 171–273, 2003.

[162] G. Baozhu, J. Losz, and G. Krauss, "Substructure and flow strength of low-temperature tempered medium carbon martensite," in *Proceedings of the International Conference on Martensitic Transformations*, (Nara, Japan), pp. 367–374, 1986.

[163] J. R. Rice and J.-S. Wang, "Embrittlement of interfaces by solute segregation," *Materials Science and Engineering: A*, vol. 107, pp. 23–40, 1989.

[164] P. Dumoulin, M. Guttmann, P. Maynier, and P. Chevalier, "Influence of segregated transition metals on intergranular brittleness of tempered martensitic steels," *Metal Science*, vol. 17, no. 2, pp. 70–74, 1983.

[165] M. Guttmann, "The role of residuals and alloying elements in temper embrittlement," *Philosophical Transactions of the Royal Society of London. Series A, Mathematical and Physical Sciences*, vol. 295, no. 1413, pp. 169–196, 1980.

[166] J. Low Jr. and R. Feustel, "Inter-crystalline fracture and twinning of iron at low temperatures," *Acta Metallurgica*, vol. 1, no. 2, pp. 185–192, 1953.

[167] C. McMahon Jr., "Intergranular brittleness in iron," *Acta Metallurgica*, vol. 14, no. 7, pp. 839–845, 1966.

[168] G. L. Krasko and G. Olson, "Effect of boron, carbon, phosphorus and sulphur on intergranular cohesion in iron," *Solid State Communications*, vol. 76, no. 3, pp. 247–251, 1990.

[169] R. Wu, A. J. Freeman, and G. B. Olson, "Effects of carbon on fe-grain-boundary cohesion: First-principles determination," *Physical Review B*, vol. 53, no. 11, p. 7504, 1996.

[170] D. McLean, *Grain boundaries in metals.* Clarendon Press, 1957.

[171] G. Hahn, "A model for yielding with special reference to the yield-point phenomena of iron and related bcc metals," *Acta Metallurgica*, vol. 10, no. 8, pp. 727–738, 1962.

[172] H. Fujita and S. Miyazaki, "Lüders deformation in polycrystalline iron," *Acta Metallurgica*, vol. 26, no. 8, pp. 1273–1281, 1978.

[173] N. Breyer, "The yield point phenomenon in strain-aged martensite," *Transactions of AIME*, vol. 236, pp. 1198 – 1202, 1966.

[174] J. Embury, "Structural aspects of the bauschinger effect," *Materials Forum*, vol. 10, no. 1, pp. 27–32, 1987. Compendex.

[175] H. Proudhon, W. J. Poole, X. Wang, and Y. Bréchet, "The role of internal stresses on the plastic deformation of the Al–Mg–Si–Cu alloy AA6111," *Philosophical Magazine*, vol. 88, no. 5, p. 621, 2008.

[176] J. D. Atkinson, L. M. Brown, and W. M. Stobbs, "The work-hardening of copper-silica: IV. the bauschinger effect and plastic relaxation," *Philosophical Magazine*, vol. 30, pp. 1247–1280, 1974.

[177] G. Moan and J. Embury, "A study of the bauschinger effect in Al?Cu alloys," *Acta Metallurgica*, vol. 27, no. 5, pp. 903–914, 1979.

[178] H. Mughrabi, "Dislocation wall and cell structures and long-range internal stresses in deformed metal crystals," *Acta Metallurgica*, vol. 31, no. 9, pp. 1367–1379, 1983.

[179] O. Pedersen, L. Brown, and W. Stobbs, "The bauschinger effect in copper," *Acta Metallurgica*, vol. 29, no. 11, pp. 1843–1850, 1981.

[180] O. Bouaziz, D. Barbier, J. Embury, and G. Badinier, "An extension of the Kocks–Mecking model of work hardening to include kinematic hardening and its application to solutes in ferrite," *Philosophical Magazine*, vol. 0, no. 0, pp. 1–9, 2012.

[181] C. Sinclair, W. Poole, and Y. Bréchet, "A model for the grain size dependent work hardening of copper," *Scripta Materialia*, vol. 55, no. 8, pp. 739–742, 2006.

[182] C. W. Sinclair, G. Saada, and J. D. Embury, "Role of internal stresses in co-deformed two-phase materials," *Philosophical Magazine*, vol. 86, no. 25, p. 4081, 2006.

[183] G. Masing, "Zur heyn'schen theorie der verfestigung der metalle durch verborgen elastische spannungen," *Wissenschaftliche Veroffentlichungen aus dem Siemens-Konzern*, vol. 3, no. 1, pp. 231–239, 1923.

[184] P. Bate and D. Wilson, "Analysis of the bauschinger effect," *Acta Metallurgica*, vol. 34, no. 6, pp. 1097–1105, 1986.

[185] C. Holste and H. Burmeister, "Change of long-range stresses in cyclic deformation.," *Physica Status Solidi (A) Applied Research*, vol. 57, no. 1, pp. 269–280, 1980.

[186] J. Polak, M. Klesnil, and J. Helesic, "Hysteresis loop - 3. stress-dip experiments.," *Fatigue of engineering materials and structures*, vol. 5, no. 1, pp. 45–56, 1982.

[187] R. Skelton, H. Maier, and H.-J. Christ, "The bauschinger effect, masing model and the ramberg-osgood relation for cyclic deformation in metals," *Materials Science and Engineering: A*, vol. 238, pp. 377–390, Nov. 1997.

[188] B. Raeisinia and W. J. Poole, "Modelling the elastic–plastic transition of polycrystalline metals with a distribution of grain sizes," *Modelling and Simulation in Materials Science and Engineering*, vol. 20, no. 1, p. 015015, 2012.

[189] S. Allain, O. Bouaziz, and M. Takahashi, "Toward a new interpretation of the mechanical behaviour of as-quenched low alloyed martensitic steels," *ISIJ International*, vol. 52, no. 4, pp. 717–722, 2012.

[190] L. M. Brown and W. M. Stobbs, "The work-hardening of copper-silica," *Philosophical Magazine*, vol. 23, pp. 1185–1199, 1971.

[191] L. M. Brown and W. M. Stobbs, "The work-hardening of copper-silica," *Philosophical Magazine*, vol. 23, pp. 1201–1233, 1971.

[192] J. Polak and M. Klesnil, "Hysteresis loop - 1. a statistical theory.," *Fatigue of engineering materials and structures*, vol. 5, no. 1, pp. 19–32, 1982.

[193] L. M. Brown, "Orowan's explanation of the bauschinger effect," *Scripta Metallurgica*, vol. 11, no. 2, pp. 127–131, 1977.

[194] R. Asaro, "Elastic-plastic memory and kinematic-type hardening," *Acta Metallurgica*, vol. 23, no. 10, pp. 1255–1265, 1975.

[195] L. Brown and D. Clarke, "Work hardening due to internal stresses in composite materials," *Acta Metallurgica*, vol. 23, no. 7, pp. 821–830, 1975.

[196] W. Stobbs and S. Paetke, "The bauschinger effect in cold drawn patented wire," *Acta Metallurgica*, vol. 33, no. 5, pp. 777–783, 1985.

[197] P. Withers, "Mapping residual and internal stress in materials by neutron diffraction," *Comptes Rendus Physique*, vol. 8, no. 7–8, pp. 806–820, 2007.

[198] I. Tamura, Y. Tomota, A. Akao, Y. Yamaoka, M. Ozawa, and S. Kanatani, "On the strength and ductility of two-phase iron alloys," *Transactions of the Iron and Steel Institute of Japan*, vol. 13, no. 4, pp. 283–292, 1973.

[199] A. Perlade, O. Bouaziz, and Q. Furnémont, "A physically based model for TRIP-aided carbon steels behaviour," *Materials Science and Engineering: A*, vol. 356, pp. 145–152, Sept. 2003.

[200] M. Roberts and W. Owen, "Solid solution hardening by carbon and nitrogen in ferrous martensites," tech. rep., Iron and Steel Institute (ISI), London, England, 1965.

[201] K. Zhu, O. Bouaziz, C. Oberbillig, and M. Huang, "An approach to define the effective lath size controlling yield strength of bainite," *Materials Science and Engineering: A*, vol. 527, no. 24–25, pp. 6614–6619, 2010.

[202] A. J. E. Foreman and M. J. Makin, "Dislocation movement through random arrays of obstacles," *Philosophical Magazine*, vol. 14, no. 131, pp. 911–924, 1966.

[203] S. Berbenni, V. Favier, X. Lemoine, and M. Berveiller, "A micromechanical approach to model the bake hardening effect for low carbon steels," *Scripta Materialia*, vol. 51, no. 4, pp. 303–308, 2004.

[204] U. Kocks, "Superposition of alloy hardening, strain hardening, and dynamic recovery," in *Proceedings of the International Conference on the Strength of Metals and Alloys*, (Aachen, Germany), pp. 1661–1680, Pergamon, 1979.

[205] Y. Chen, *The Effect of Interrupted Ageing on the Strength and Elongation of Precipitation Hardened Aluminium Alloys*. Ph.D. thesis, Monash University, Melbourne, 2012.

[206] J. Gil Sevillano, "An alternative model for the strain hardening of FCC alloys that twin, validated for twinning-induced plasticity steel," *Scripta Materialia*, vol. 60, no. 5, pp. 336–339, 2009.

[207] G. Michal, F. Ernst, H. Kahn, Y. Cao, F. Oba, N. Agarwal, and A. Heuer, "Carbon supersaturation due to paraequilibrium carburization: Stainless steels with greatly improved mechanical properties," *Acta Materialia*, vol. 54, no. 6, pp. 1597–1606, 2006.

[208] R. Roumina and H. Zurob *Unpublished results*, 2012.

[209] X. Peng, Y. Qin, and R. Balendra, "Finite element investigation into the torsion test in the range of large strains and deformations," *The Journal of Strain Analysis for Engineering Design*, vol. 36, no. 4, pp. 401–409, 2001.

[210] R. Sowerby, D. Uko, and Y. Tomita, "A review of certain aspects of the bauschinger effect in metals," *Materials Science and Engineering*, vol. 41, no. 1, pp. 43–58, 1979.

[211] D. Wilson, "Reversible work hardening in alloys of cubic metals," *Acta Metallurgica*, vol. 13, no. 7, pp. 807–814, 1965.

[212] D. Wilson and P. Bate, "Reversibility in the work hardening of spheroidised steels," *Acta Metallurgica*, vol. 34, no. 6, pp. 1107–1120, 1986.

[213] R. Woolley, "LXIV. the bauschinger effect in some face-centred and body-centred cubic metals," *Philosophical Magazine Series 7*, vol. 44, no. 353, pp. 597–618, 1953.

[214] N. Ibrahim and J. Embury, "The bauschinger effect in single phase b.c.c. materials," *Materials Science and Engineering*, vol. 19, no. 1, pp. 147–149, 1975.

Appendices

Appendix A

Measurement of the Ms Temperature by Dilatometry

Tubes 20 mm long and having an external diameter of 8 mm and a wall thickness of 1 mm were machined and then annealed in a Gleeble 3500 thermomechanical simulator, under high vacuum (10^{-3} mtorr). A dilatometer was attached to the center of the specimen, and the variation in diameter was recorded during the test. The specimen was annealed at 900°C for 5 minutes and quenched by running helium gas through the tube. The dilatation-temperature curve recorded during the test is plotted on figure A.1. The Ms temperature was measured as the temperature where the curve was observed to depart from linearity during cooling. The value given by this technique was 282°C.

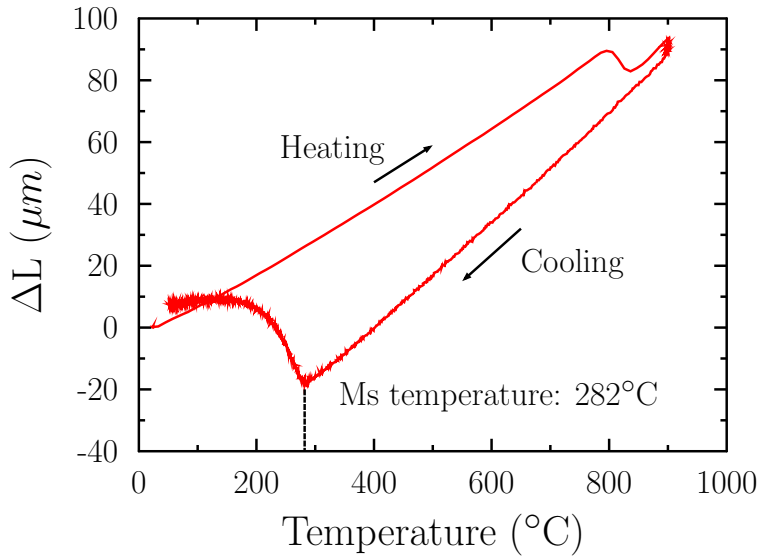

Figure A.1: Dilatation-temperature curve measured during the heat treatment.

Appendix B

Finite Element Analysis of a Torsion Test on a Tubular Specimen

The stress homogeneity accross the wall-thickness of a Lindholm-type torsion specimen was analyzed using the finite element method. The analysis was performed using the Abaqus software (explicit) [209] on specimens having the dimensions given in section 4.2. Given the axial symmetry of the specimen, the analysis was run using only one quarter of the specimen, and the axi-symmetric option of the Abaqus software was used. The experimentally measured equivalent stress-strain curve on specimens tempered one hour at 150°C (see chapter 6) was used as the input mechanical properties of the material. This stress-strain curve was thought to be representative of the mechanical behaviour of the water-quenched and tempered 300M martensitic steel.

The specimen was meshed using CGAX4R elements, as explained in [209]. The simulation was run in the exact same conditions as those described in [209], and the stresses at the outer and inner radii were plotted against applied twist angle (figure B.1). The results show that the maximum stress variation (the stress at the outer radius was $\sim 12\%$ higher than the stress at the inner radius) occurred approximately at the end of the linear-elastic regime. The stress differential was found to decrease rapidly after the elasto-plastic transition, until it reached 0.

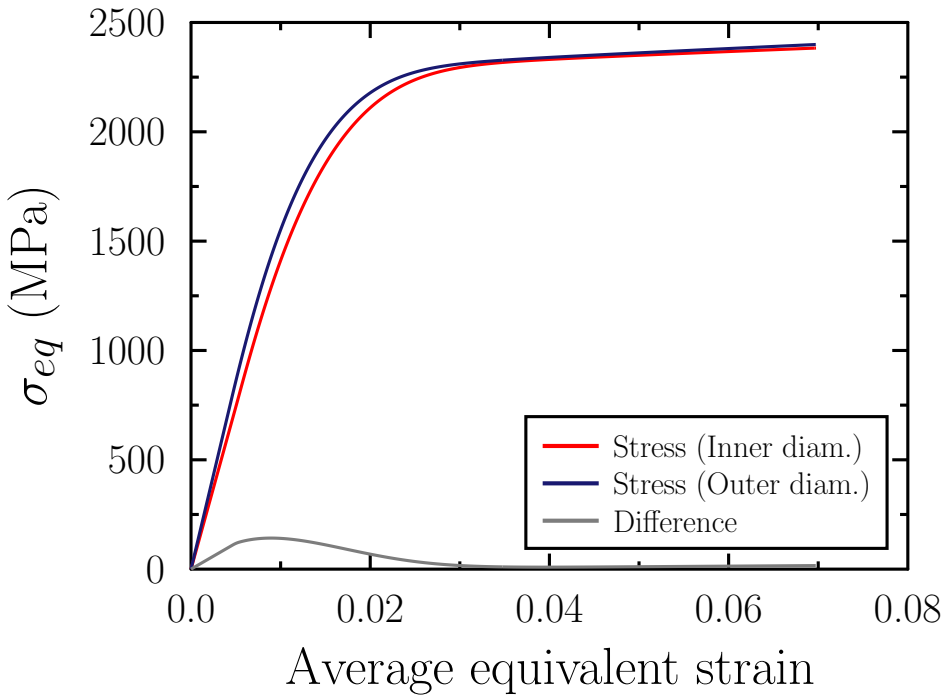

Figure B.1: Von Mises equivalent stress in the outer and inner fibers of a tubular specimen pulled in torsion.

Appendix C

Precipitation Model

The full precipitation model used in chapter 5 to predict the evolution of precipitation with tempering is presented here. This starts with the treatment of nucleation and growth, and continues with the treatment of growth and coarsening. The model used here has been adapted from ref. [158], and assumes that nucleation occurred heterogeneously on dislocations.

C.1 Nucleation and growth

The volumetric change in free energy is given as [152],

$$\Delta G_v = \frac{kT}{\nu_{at}} \left(C_p \ln \left(\frac{C_{eq}}{C} \right) + (1 - C_p) \ln \left(\frac{1 - C_{eq}}{1 - C} \right) \right) \tag{C.1}$$

where ν_{at} is the atomic volume of iron, C_p is the atomic fraction of carbon in the carbides, C is the current atomic fraction of carbon dissolved in martensite, C_{eq} is the equilibrium carbon solubility, k is the Boltzmann constant and T is the absolute temperature (K).

The critical precipitates radius R^* for nucleation can be calculated as [158],

$$R^* = -\frac{2\gamma}{\Delta G_v} \tag{C.2}$$

where γ is the interfacial energy. The corresponding driving force for nucleation writes,

$$\Delta G^* = \zeta \frac{16\pi}{3} \frac{\gamma^3}{(\Delta G_v)^2} \tag{C.3}$$

where ζ is a scaling parameter ($0 < \zeta < 1$) that takes into account the reduc-

tion in the energy barrier due to heterogeneous nucleation. The nucleation rate is taken as,

$$\frac{dN_n}{dt} = \left(1 - \frac{N}{N_{tot}}\right) N_{tot}\beta \exp\left(-\frac{\Delta G^*}{kT}\right) \tag{C.4}$$

where N is the number of nuclei and β is given as [158],

$$\beta = 4\pi \left(R^*\right)^2 D \frac{C_0}{20a^4} \tag{C.5}$$

where D is the diffusivity of carbon in martensite, a is the lattice parameter of iron and C_0 is the carbon composition available for precipitation. Here, it is assumed that C_0 depends on the dislocation density as [71],

$$C_0 = C_{nom} - \nu_{at}\frac{\rho}{a_{seg}} \tag{C.6}$$

where C_{nom} is the nominal carbon composition of the steel and ρ is the dislocation density.

In equation C.4, a correction term $1-N/N_{tot}$ has been added to take into account the possible saturation of the nucleation sites [159], N_{tot} being the total number of nucleation sites. Here, it was assumed that precipitation occurred on dislocations. Therefore, N_{tot} was related to the dislocation density as,

$$N_{tot} = \frac{\rho}{b} \tag{C.7}$$

where b is the Burgers' vector of the dislocations.

The evolution of the precipitate radius is given by,

$$\frac{dR_n}{dt} = \frac{D}{R}\left(\frac{C - C_{eq}\exp\left(\frac{R_0}{R}\right)}{C_p - C_{eq}\exp\left(\frac{R_0}{R}\right)}\right) + \frac{1}{N}\frac{dN_n}{dt}\left(1.05R^* - R\right) \tag{C.8}$$

where $R_0 = 2\gamma\nu_{at}/kT$ [158]. The first term on the right-hand side corresponds to the growth of existing precipitated and the second term corresponds to the arrival of new nuclei within the existing population of precipitates.

C.2 Growth and coarsening

The evolution of the precipitate radius during coarsening is [158],

$$\frac{dR_c}{dt} = \frac{4}{27}\left(\frac{C_{eq}}{1-C_{eq}}\right) D\frac{R_0}{R^2} \tag{C.9}$$

The evolution of the number density of precipitates during coarsening is [158],

$$\frac{dN_c}{dt} = \frac{4}{27}\left(\frac{C_{eq}}{1-C_p}\right) D\frac{R_0}{R^3}\left(\frac{R_0 C}{R\left(C_p - C\right)}\right)\left(\frac{3}{4\pi R^3} - N\right) - 3N \tag{C.10}$$

At any time, the solut balance must be respected,

$$C = \frac{C_0 - \frac{4}{3}\pi N R^3 C_p}{1 - \frac{4}{3}\pi N R^3} \tag{C.11}$$

In order to go continuously from the growth stage to the coarsening stage, a coarsening volume fraction is defined [158],

$$f = 1 - erf\left(4\left(\frac{R}{R^*} - 1\right)\right) \tag{C.12}$$

Then the evolution of the precipitate radius is given as,

$$\frac{dR}{dt} = (1-f)\frac{dR_n}{dt} + f\frac{dR_c}{dt} \tag{C.13}$$

The evolution of the number density of precipitates during the transition regime has to be determined. A simple criterion is obtained for the transition regime is given when the number density decrease due to coarsening $-\frac{dN_c}{dt}$ becomes higher than the number density increase $\frac{dN_n}{dt}$ due to nucleation. Therefore, if $-\frac{dN_c}{dt} \geq \frac{dN_n}{dt}$, we have,

$$\frac{dN}{dt} = \frac{dN_c}{dt} f \tag{C.14}$$

Otherwise,

$$\frac{dN}{dt} = \frac{dN_n}{dt} \tag{C.15}$$

Appendix D

Measurement of the Back-Stress

A common way to quantify the Bauschinger effect is to measure the back-stress σ_b [107], which is a measure of the internal stress in the softest phase of the material [184, 190, 191]:

$$\sigma_b = \frac{1}{2}(\sigma_f - \sigma_r) \tag{D.1}$$

Where σ_f is the flow stress of the material at the point of strain reversal, and σ_r is the yield strength after strain reversal (see figure D.1). In the case where σ_b is equal to zero, the material presents no plastic anisotropy and the Bauschinger effect is null. In this hypothetical case, the plastic deformation occurs homogeneously during plastic deformation.

In model copper-silica alloys, permanent softening was observed and the back-stress in the copper matrix was estimated, according to equation D.1 as one half of the permanent softening [190, 191]. In the present case, no permanent softening was observed. Therefore, an alternative method for estimating σ_r had to be established [177]. This was done by using an offset strain, as shown in figure D.1. However, the estimation of σ_b made in this way depends on the strain offset used, as pointed out by Sowerby et al. [210]. To evaluate the sensitivity of the back-stress measurement to the strain offset, it was decided to estimate the back-stress using different offset values for determining σ_r, e.g. 0.05%, 0.1%, 0.2% and 0.3%.

Figure D.2 shows that the the back-stress varied quite substantially with the strain offset chosen to evaluate σ_r. For instance, the maximum value of the back-stress in specimens tempered one hour at 150°C varied from $\sim$ 890

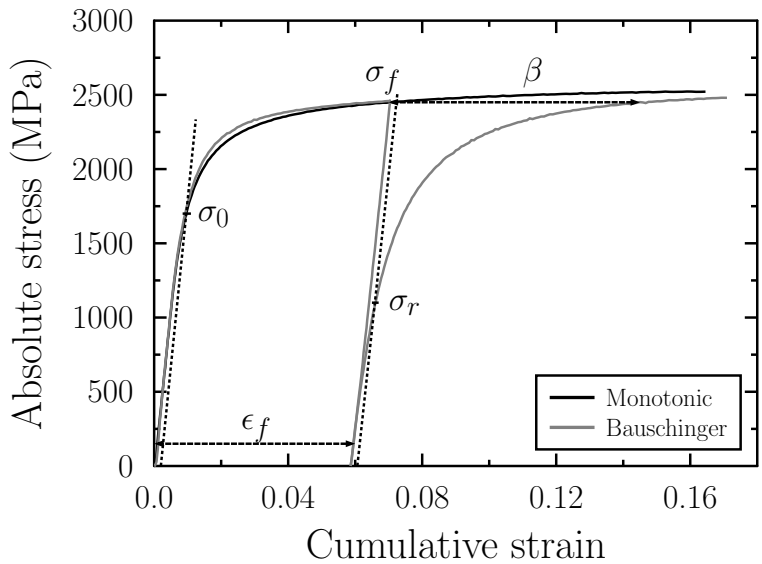

Figure D.1: Example of a stress strain curve obtained in a Bauschinger trial and plotted in terms of cumulative strain and absolute stress. The data extracted to calculate the different Bauschinger effect parameters are indicated.

MPa to $\sim$ 580 MPa when the offset varied from 0.05% to 0.3%. As shown in figure D.2, the same trends were observed in the other conditions tested. As discussed by Moan and Embury [177], who studied the Bauschinger effect in age-hardened aluminium alloys, it is necessary to measure the back-stress with another technique (e.g. by X-ray diffraction for instance [211]) to be able to choose consistently the offset to be used in the determination of σ_r. This cross-correlation technique works, however, only if the two soft and hard phases of the material can be easily identified as it is the case, for instance, in precipitation hardened alloys. This clear distinction between hard and soft phases allows for the estimation of the back-stress in the soft matrix as a function of pre-strain using X-ray diffraction data [211, 212]. In the present case, the hard and soft phases are not as easily identified. While the absolute value of σ_b depends on the selected offset, it can be seen that this evolution with forward pre-strain varies in the same way regardless of the offset.

Figure D.3 shows a comparison of the evolution of the back-stress with forward pre-strain for all studied conditions. This figure shows that the back-stress first increased with the forward pre-strain and then reached a

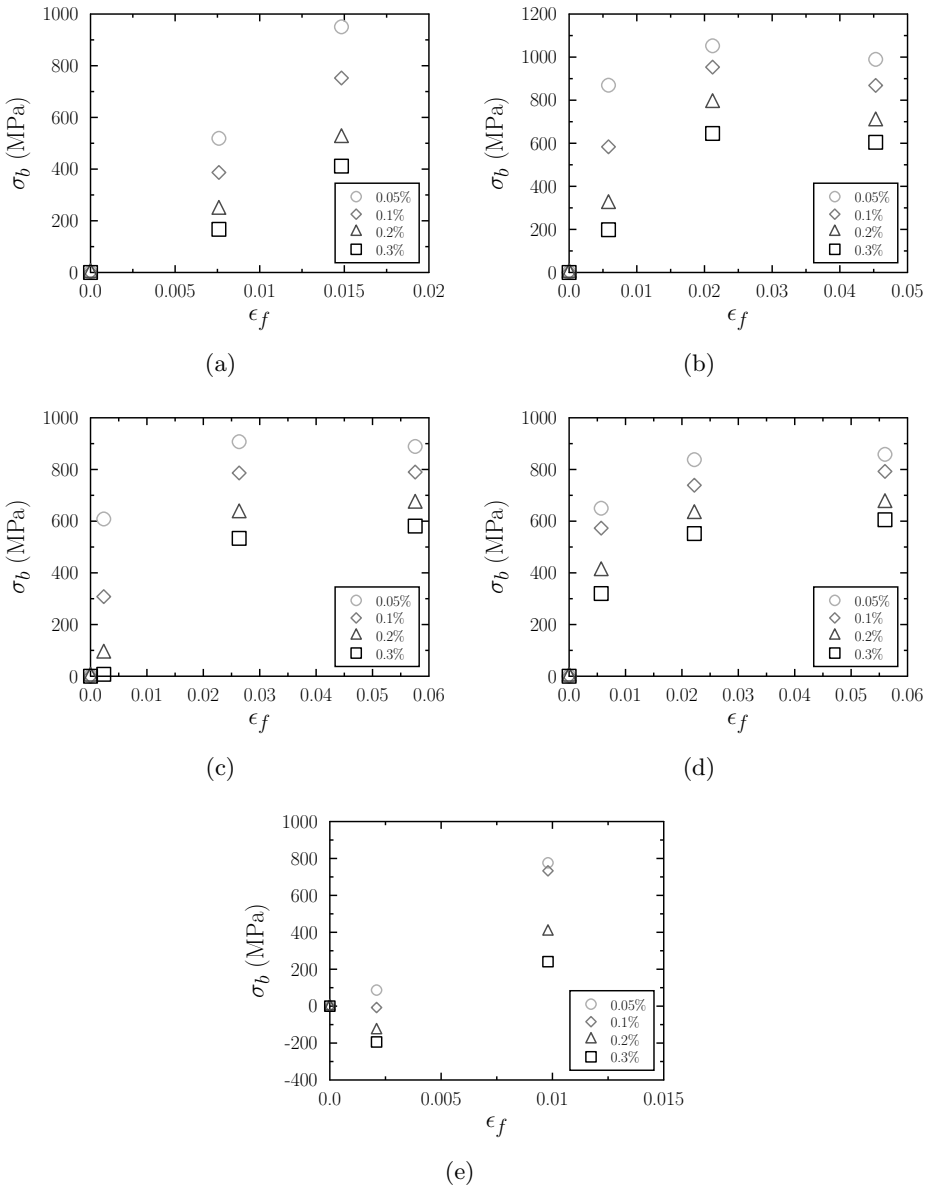

Figure D.2: Evolution of the back-stress as a function of forward pre-strain for each condition a) after tempering 3 hours at 120°C, b) after tempering 5 hours at 120°C, c) after tempering 1 hour at 150°C, d) after tempering 1 hour at 350°C, and e) in the as-helium-quenched condition.

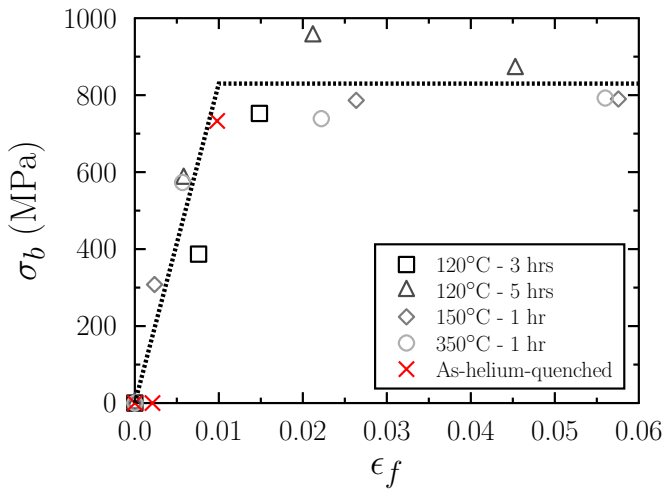

Figure D.3: Comparison of the back-stress in the conditions studied here.

saturation value. This trend is generally observed in polycrystalline metallic materials [175, 177, 180, 213, 214]. The saturation value did not seem to evolve drastically with tempering condition (figure D.3), but this must be considered with the fact that the macroscopic hardening rate did evolve, i.e. the relative contribution of the back-stress to the overall work hardening was not the same from one condition to another.